Inelastic J/ψ photoproduction in electron–proton collisions at HERA

Timothy C. Y. Yip

University of Oxford

Wolfson College



Submitted for the degree of Doctor of Philosophy

Trinity Term 1996

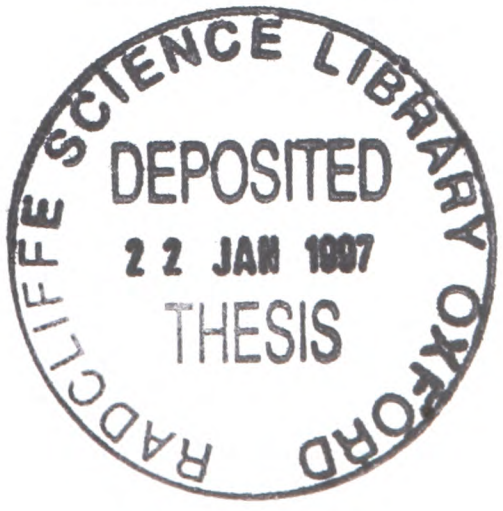

OHIO STATE UNIVERSITY SCIENCE LIBRARY
DEPOSITED
2 2 JAN 1957
THESIS

Inelastic J/ψ photoproduction in electron–proton collisions at HERA

Timothy C. Y. Yip

University of Oxford

Wolfson College

Submitted for the degree of Doctor of Philosophy
Trinity Term 1996

Abstract

The development of a neural network based electron finder designed for the ZEUS calorimeter is described. A study of elastic and inelastic J/ψ meson production in electron–proton collisions at HERA using the ZEUS detector is presented. During the 1993 and 1994 running periods, the ZEUS detector collected ~ 500 nb^{-1} and ~ 3 pb^{-1} of data respectively. The direct inelastic J/ψ photoproduction cross–section is measured for both running periods and an attempt is made to extract the gluon density inside the proton using the 1994 inelastic J/ψ sample.

Acknowledgements

It gives me great pleasure to thank my supervisor, Roger Cashmore, for his invaluable comments and interest in my work, despite being the busiest person in the whole world! I am also extremely grateful to Mandy Cooper–Sarkar for acting as my supervisor during Roger's absence, both in my first and final years, and for reading through my whole thesis on holiday and on countless other occasions.

I am much indebted to my undergraduate tutors, Neville Harnew and Caroline Fraser, who sparked my interest in physics and without whom, this D.Phil. would have never happened.

Thanks also go to Chandi Nath, Val Noyes, Roman Walczak, Ken Long, Robin Devenish, Christine Sutton, Dave Bailey and the rest of the Oxford ZEUS group for the supportive working environment, both in Oxford and at DESY, to Pete Gronbech and Ian McArthur for continually upgrading our computer system and for always being keen to show me their latest 'toys' and to the Particle Physics and Astronomy Research Council for the grant.

Special thanks go to Ling Wai Hung for always having time to answer my questions, the rest of the inelastic J/ψ group for showing me what 'teamwork' really meant, Arnulf Quadt for introducing me to the lighter side of Germans... during 'Karneval' and for answering the questions I was too embarrassed to ask Wai, all my friends at the Tangun gym in Hamburg for keeping me sane and teaching me German and an extra big thank you to all my friends I have met in the past seven years at St. Anne's, Wolfson and the rest of the University for giving me such a memorable time.

Finally, I would like to thank my grandparents, for always being interested, my brother, for always being there to talk to and especially my parents for their constant encouragement and support.

Contents

1 The HERA accelerator and ZEUS detector **1**

1.1 The HERA accelerator 1

1.2 The ZEUS detector 4

1.2.1 Overview of the ZEUS detector 4

1.3 Inner Tracking Detectors 8

1.3.1 Central Tracking Detector 8

1.3.2 Vertex Detector 11

1.3.3 Forward and Rear Tracking Detectors 12

1.4 Calorimeter 13

1.5 Muon Detectors 15

1.6 Luminosity Monitor 17

1.7 C5 Counter 18

1.8 Small Angle Rear Tracking Detector 18

1.9 ZEUS trigger and Data Acquisition System 18

2 Physics at HERA **23**

2.1 Kinematics of electron–proton scattering 23

2.2 The electron–proton differential cross–section 26

2.3 The Quark Parton Model 26

2.4 Quantum Chromodymamics 28

2.5 Measurement of the gluon density at HERA 33

2.5.1 F_2 structure function fits 33

2.5.2 F_L structure function fits 34

2.5.3 Dijet rates in BGF photoproduction 37

2.5.4 Elastic J/ψ photoproduction 40

2.5.5 Heavy flavour production 42

2.6 Properties of the J/ψ meson and some production mechanisms 42

2.6.1 The decay modes of J/ψ 42

2.6.2 J/ψ production mechanisms at HERA 44
2.7 Summary 47

3 Searching for $J/\psi \to e^+e^-$ **48**
3.1 Kinematics of J/ψ production 48
3.2 Reconstruction of kinematic variables in photoproduction 49
3.3 Track reconstruction 50
3.4 Electron identification 51
3.5 Interaction of charged particles with matter 52
3.5.1 Ionisation loss of charged particles 52
3.5.2 Bremsstrahlung 55
3.6 Background from $\gamma \to e^+e^-$ conversions 58
3.7 Monte Carlo generators 60

4 Neural Network Electron Identification **63**
4.1 Introduction 63
4.2 Input for the neural network 64
4.3 The Theory of Neural Networks 67
4.4 Training and Testing the Neural Network 69
4.5 Testing the Neural Network on Test Beam Data 73
4.6 Conclusions 75

5 The search for $J/\psi \to e^+e^-$ in 1993 data **77**
5.1 1993 Triggers 77
5.1.1 First Level Trigger (FLT) 78
5.1.2 Third Level Trigger (TLT) 80
5.2 Pre–selection of 1993 data 84
5.3 Elastic $J/\psi \to e^+e^-$ selection 87
5.4 Inelastic $J/\psi \to e^+e^-$ selection 90
5.5 dE/dx 101
5.6 Monte Carlo studies 109
5.7 Production mechanisms entering the signal 113
5.7.1 Resolved photon J/ψ production 113
5.7.2 Elastic ψ' production 116
5.8 Results 119
5.8.1 Acceptance and cross–section calculations 119
5.8.2 Systematic uncertainties 120

5.9 Conclusions 122

6 The search for $J/\psi \to e^+e^-$ in 1994 data **124**

6.1 Pre–selection of 1994 data 124
6.2 Elastic $J/\psi \to e^+e^-$ selection 126
6.3 Inelastic $J/\psi \to e^+e^-$ selection 129
6.4 1994 Triggers and Selection 139
6.4.1 First Level Trigger (FLT) 139
6.4.2 Second Level Trigger (SLT) 142
6.4.3 Third Level Trigger (TLT) 144
6.5 γp centre–of–mass energy, W, cut 147
6.6 Production mechanisms entering the signal 148
6.6.1 Resolved photon J/ψ production 148
6.6.2 Elastic ψ' production 150
6.7 In–depth view of an inelastic J/ψ event 152
6.8 dE/dx 154
6.9 Monte Carlo Studies 161
6.10 Results 169
6.10.1 Cross–section calculation 169
6.10.2 Systematic uncertainties 170
6.11 Conclusions 171

7 Extraction of the gluon density in the proton **173**

7.1 Colour singlet model 174
7.2 Kinematics 177
7.2.1 Kinematical limits 179
7.3 Extraction of the gluon density in leptoproduction 180
7.4 Extracting the gluon density using 1994 data 184
7.4.1 Possible sources of error 188
7.5 Conclusions 189

A The integrated photon flux **191**

B Derivation of kinematic formulae **193**

C Inelastic J/ψ photoproduction cross–section **197**

Bibliography **202**

Chapter 1

The HERA accelerator and ZEUS detector

This chapter will provide an introduction to the HERA accelerator and various components of the ZEUS detector.

1.1 The HERA accelerator

The Hadron Elektron Ring Anlage (HERA) was constructed at the German National Particle Physics Laboratory, DESY, in Hamburg between May 1984 and November 1990 and is the world's first electron–proton collider. It consists of two independent accelerator rings in a tunnel of 6.3 km circumference. These were designed to store beams of 820 GeV protons and 30 GeV electrons. Collisions are possible with zero crossing angle at four interaction regions located around the ring as shown in figure 1.1, giving a nominal centre–of–mass energy of 314 GeV. The H1 and ZEUS detectors have been built around the interaction points in the north and south halls respectively. Basic details of the design of HERA are given in tables 1.1 and 1.2.

Superconducting magnets, producing a 4.68 T magnetic field, are required to confine the protons of energy 820 GeV within the HERA proton ring. However, a much lower

magnetic field of 0.164 T is required to confine the 30 GeV electrons within the electron ring, and so conventional magnets are used. Conventional and superconducting RF cavities are used in the electron ring to replace the energy lost to synchrotron radiation[1] by the electrons. In 1993, not all of the accelerator cavities were installed and so the electron beam energy was limited to 26.67 GeV.

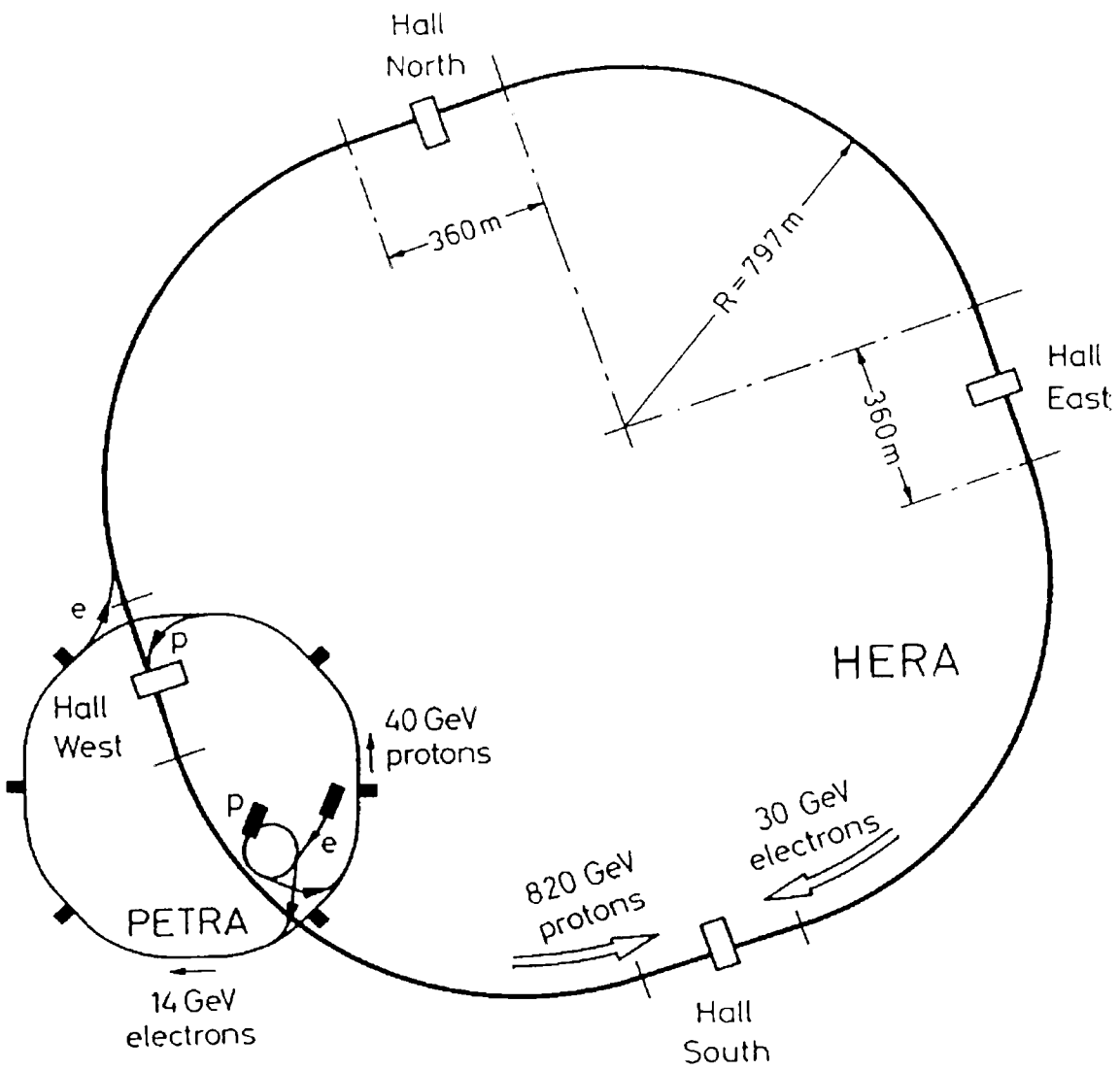

Figure 1.1: Plan of HERA at DESY, Hamburg

The design luminosity of 1.5×10^{31} cm^{-2}s^{-1} is reached by bunching both the electron and proton beams into 220 buckets, 28.8 m apart. Of these, 210 are filled with particles and the remaining 10 are left empty for background studies since no genuine ep collisions

[1]See section 3.5.2.

General HERA design details:	
Construction time	May 1984 – November 1990
Circumference of tunnel	6336 m
Depth underground	10 – 25 m
Inner diameter of tunnel	5.2 m
Number of experimental halls	4
Number of experiments (first stage)	2 (H1 and ZEUS)
Cost of collider	DM 1.01 billion
Cost of experiments (first stage)	DM 240 million

Table 1.1: Design details of HERA.

Details of the HERA beams:	Design	Attained in 1992	Attained in 1993
Proton beam energy (GeV)	820	820	820
Electron beam energy (GeV)	30	26.7	26.7
# Proton bunches			
(paired/unpaired)	210/0	9/1	84/6
# Electron bunches			
(paired/unpaired)	210/0	9/1	80/10
Proton beam current (mA)	160	1.5	20.4
Electron beam current (mA)	58	3.5	25
Proton beam lifetime (hours)	> 10	> 100	> 1000
Electron beam lifetime (hours)	> 5	~ 4	20
Peak luminosity ($cm^{-2}s^{-1}$)	1.5×10^{31}	2.0×10^{29}	1.5×10^{30}
Integrated luminosity/year:			
delivered to ZEUS (pb^{-1})	100	~ 0.06	1.088
recorded by ZEUS (pb^{-1})	100	0.027	0.6

Table 1.2: Design values of the HERA beams and those attained during the 1992 and 1993 running periods.

take place. The resulting bunch crossing interval of 96 ns places stringent demands on both the detectors and their readout.

Figure 1.2 shows an enlarged view of the particle injection system used at HERA. Negatively charged hydrogen ions are injected into a 50 MeV linear accelerator and then enter the DESY III synchrotron where they are stripped and captured into bunches. The resulting proton bunches are accelerated to 7.5 GeV before being transferred to the PETRA ring. When 70 bunches, 28.8 m apart have been accumulated, they are accelerated to 40 GeV before being injected into the HERA proton storage ring.

The electrons follow a similar injection process. They are accelerated to 500 MeV in a linear accelerator and injected into a small storage ring (PIA) where they are captured into a 60 mA single bunch. These single bunches are injected into the DESY II synchrotron, accelerated to 7 GeV, transferred to the PETRA ring and further accelerated to 14 GeV before finally being injected into the HERA electron storage ring.

1.2 The ZEUS detector

1.2.1 Overview of the ZEUS detector

ZEUS is a multi–purpose detector designed to record physics events at HERA. The general layout of the detector is shown in figure 1.3 where it is seen that the detector is composed of many components. Some of the components relevant to this thesis will be described in this chapter and a more complete description can be found in [1]. The design of the detector is deliberately asymmetric with more instrumentation in the forward (proton) direction. This is due to the greater density of high momentum tracks in the forward direction because of the imbalance in beam energies, which results in a boost of the centre–of–mass into the forward direction.

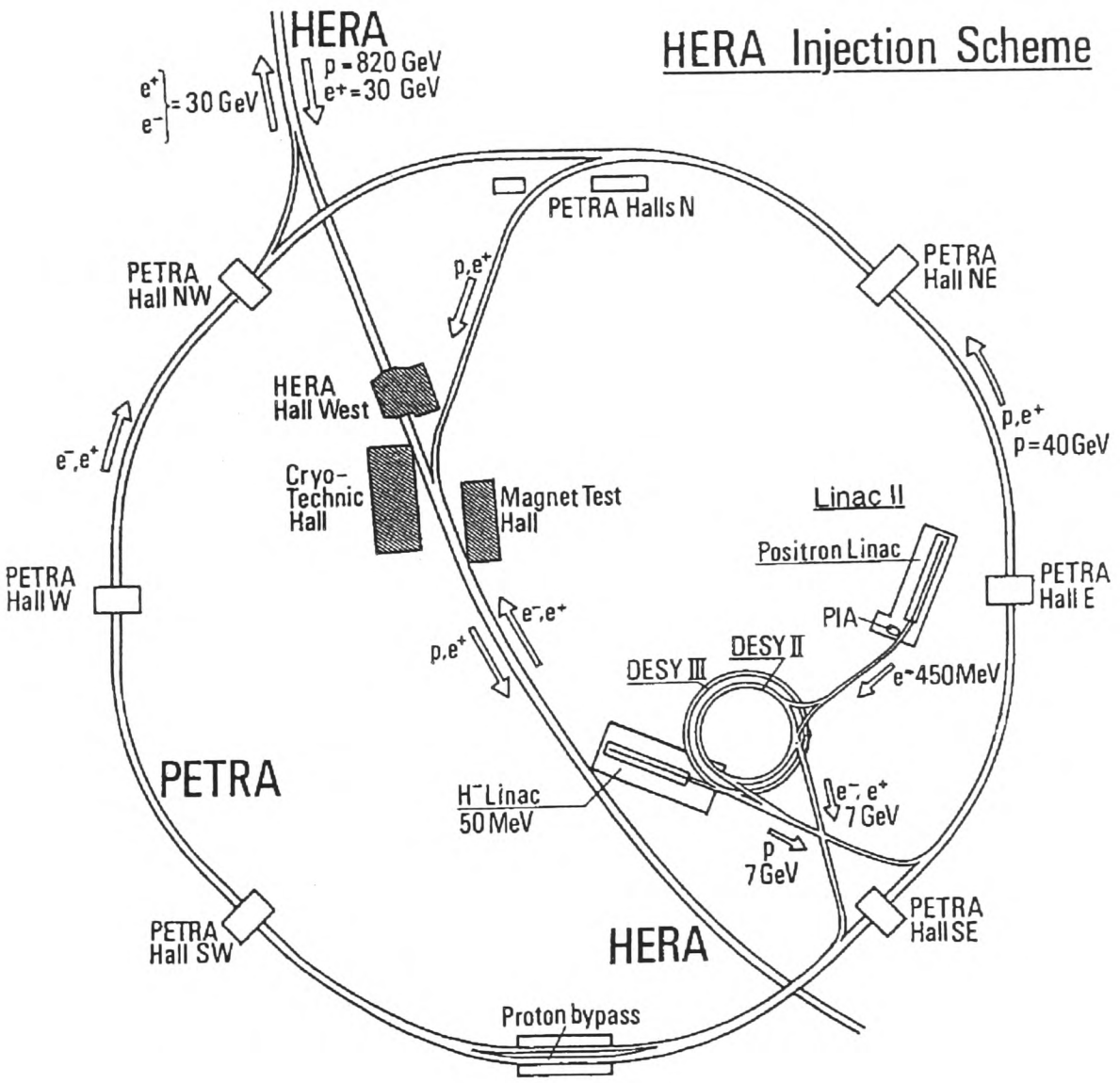

Figure 1.2: The HERA injection system

The ZEUS coordinate system is defined with the positive z–axis pointing along the proton beam direction, the y–axis pointing vertically upwards and the x–axis pointing towards the centre of the HERA ring.

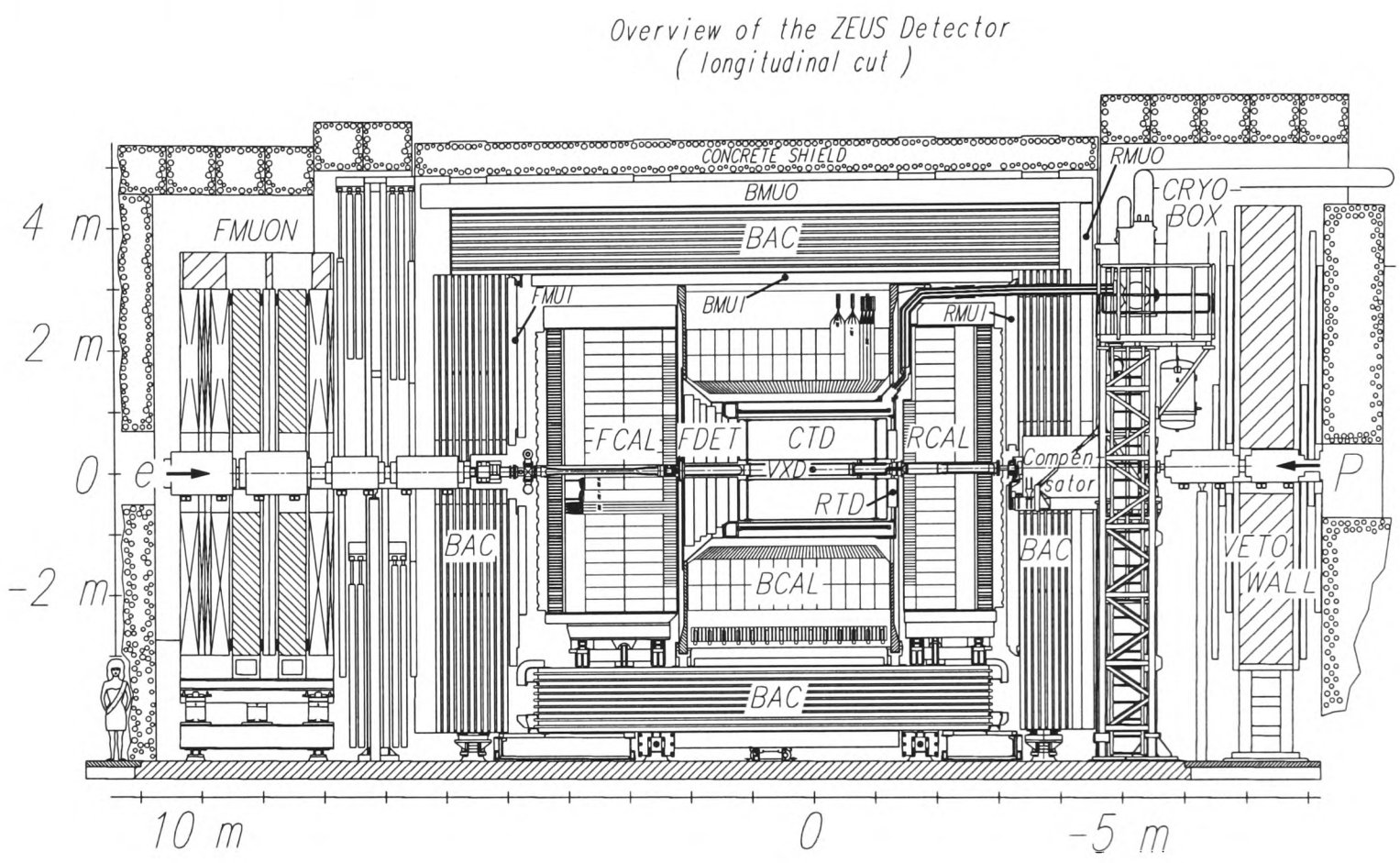

Figure 1.3: The general layout of the ZEUS detector.

An inner tracking system around the interaction point is used to track charged particles. It is composed of a vertex detector (VXD) and a Central Tracking Detector (CTD), both of which are cylindrical drift chambers. In addition, forward and rear tracking detectors (FDET and RTD respectively) aid in charged particle detection when the particles are travelling close to the beam pipe. These are both planar drift chambers.

This inner tracking detector is surrounded by a thin superconducting solenoid which produces a magnetic field of 1.43 T, allowing the measurement of the momenta of charged particles from the curvature of their tracks. This in turn is surrounded by a virtually hermetic uranium–scintillator calorimeter except for holes of 20×20 cm

required at each end to accommodate beam pipe. The calorimeter is divided into three parts to cover different regions of the polar angle, θ: forward calorimeter (FCAL $2.2^o \leq \theta \leq 39.9^o$), barrel calorimeter (BCAL $36.7^o \leq \theta \leq 129.1^o$) and rear calorimeter (RCAL $128.1^o \leq \theta \leq 176.5^o$). Each of these three calorimeters is divided into the inner electromagnetic and outer hadronic components.

Finally, the calorimeter is surrounded by an iron return yoke for the magnet which is instrumented with proportional counters. The instrumentation allows the iron to act as both a muon detector and a backing calorimeter (BAC). This measures any energy from energetic hadrons which punch through the main detector. Iron toroids and tracking chambers allow muon detection in the forward direction (FMUON).

The Leading Proton Spectrometer (LPS) is located between 24 m and 90 m from the ep interaction point in the proton beam direction. It is composed of six silicon microstrip detectors in Roman pots and is used to detect very small angle scattered protons down to $\theta \approx 0.57^o$. The momentum resolution is dependent on how many of the stations are hit. When the three furthest stations are hit, a resolution of $\frac{\sigma_p}{p} \approx 0.15\%$ (at a momentum of $\sim$ 820 GeV) is possible, whereas when two stations are hit, a resolution of $\frac{\sigma_p}{p} \approx 2\%$ is obtained.

The veto wall (VETO) is an 87 cm thick iron shield, mounted 7.5 m from the interaction point on the opposite side to the LPS in the electron direction. This protects the ZEUS detector from collisions between protons and gas molecules in the beam pipe which occur upstream in the proton beam. Scintillators, used for proton beam gas related background rejection, are also mounted on the VETO. Two lead–scintillator calorimeters, an electron detector at $z = -34.7$ m and a photon detector at $z = -107$ m are used to measure the luminosity delivered to ZEUS and to identify very low momen-

tum transfer (low Q^2) events.

The remainder of this chapter will discuss in more detail various parts of the ZEUS detector and the triggering system used at ZEUS.

1.3 Inner Tracking Detectors

The inner tracking detectors were designed to detect charged particles in the angular range $7.5^o \leq \theta \leq 170^o$ with a transverse momentum resolution of:

$$\frac{\sigma(p_t)}{p_t} = 0.003\, p_t \tag{1.1}$$

1.3.1 Central Tracking Detector

The Central Tracking Detector (CTD) [2] is a cylindrical drift chamber 2 m in length, with inner and outer radii of 16.2 cm and 85 cm respectively and covering an angular region $15^o \leq \theta \leq 164^o$. It contains 4608 sense wires arranged into 9 superlayers with each superlayer further divided into cells, consisting of eight wires. In addition, 19,584 field wires are used to shape the electric field throughout the chamber. The layout of these wires is shown in figure 1.4 where a cross–section of an octant of the CTD is seen. The wires in the odd–numbered 'axial' superlayers are parallel to the beam axis, whereas those in the even–numbered 'stereo' superlayers are inclined at a small stereo angle of around 5° with respect to the beam axis (the exact angles are shown in figure 1.4). This arrangement of axial and stereo superlayers is designed to give roughly equal resolutions in the azimuthal and polar angular reconstruction of tracks. The resolution in the z–coordinate using these stereo superlayers is around 1.4 mm.

The CTD was designed to operate in a 1.8 T magnetic field using a ratio of 50:50 argon:ethane gas mixture in the chamber at atmospheric pressure. However, during the

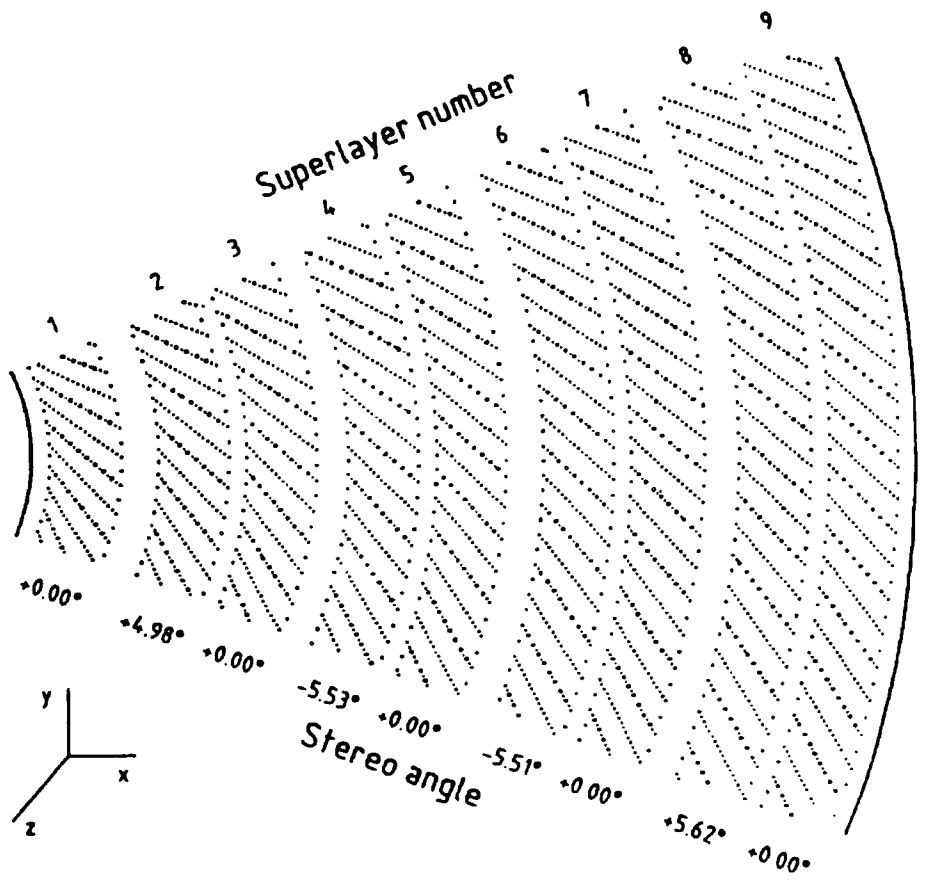

Figure 1.4: The layout of an octant of the CTD. The larger dots represent sense wires and the remainder representing field wires. The superlayer numbering and their respective stereo angles are also shown.

1992–4 running periods, the magnetic field was 1.43 T and in 1994, a mixture of argon, ethane and CO_2 in the ratio 90:2:8 with a small amount (0.84%) of ethanol[2] was used. This combination gave similar values of gain, ionisation drift direction and velocity to the design values. The Lorentz angle is defined as the angle of the drift of ionisation electrons with respect to the electric field direction. It has a value of around 45°. Due to the short inter–bunch crossing times of 96 ns at HERA, a 'fast' gas ($\sim 50\mu$m/ns) is used in the chamber giving a maximum ionisation drift time of $\sim$ 500 ns corresponding to the maximum drift length of $\sim$ 2.5 cm in a cell.

It is seen in figure 1.4 that each cell is inclined at 45° to the radial direction. High momentum charged tracks will essentially traverse the CTD radially and given a 45° Lorentz angle, ionisation from these tracks will drift perpendicular to the tracks themselves in the azimuthal direction. The 45° inclination of the cells therefore has several advantages in measuring high momentum charged tracks:

- Tracks traversing the CTD will always cross several sense wire planes and at least one drift time measurement will be less than the inter–bunch crossing time of 96 ns.

- Since high momentum tracks will cross several sense wire planes, the left–right ambiguity, arising from the fact that it is not known from which side ionisation hitting a sense wire originates, is reduced.

- Ionisation hitting a particular sense wire from different points on a track will have travelled the same distance when the track and drift direction are perpendicular. The ionisation will therefore arrive simultaneously to give a narrow pulse on the

[2]The ethanol was added to prevent whisker growth on the chamber wires.

sense wire, improving the position resolution.

Thus the CTD was designed to give optimum position resolution for high momentum tracks. However, since the momentum of charged tracks is measured by their curvature in the magnetic field, the momentum resolution decreases with increasing transverse momentum (see equation 1.1).

All the sense wires in the CTD are read out by a 104 MHz[3] Flash Analogue to Digital Converter (FADC) system. This was designed to give a resolution in the $r\phi$ plane of $100 - 120\,\mu$m and a resolution of $\sim 190\,\mu$m was achieved in 1994 (using the different gas mixture mentioned above). By looking at the heights of the pulses on the sense wires, the $\frac{dE}{dx}$ of a track can also be calculated to assist in particle identification. This is used extensively in the analysis presented in this thesis and will be covered in greater detail in section 3.5.

A second independent fast z–by–timing readout system is also implemented on all wires of superlayer 1 and alternate wires of superlayers 3 and 5. This essentially compares the arrival times of signals to the two ends of a sense wire from which a z–coordinate for the track is obtained with a design resolution $\sigma_z \simeq 3$ cm. The z–by–timing provides fast information for the trigger as well as being an independent tracking system.

1.3.2 Vertex Detector

The vertex detector (VXD) [3] is a high precision axial drift chamber, covering an angular region $8.6^o < \theta < 165^o$, situated between the beam pipe and inner wall of the CTD. It has an active radius of 10.65 cm to 14.25 cm and its length extends from

[3]Equivalent to every 9.6 ns

$z = -50$ to $+90$ cm. It consists of 120 drift cells, each one containing 12 sense wires. Dimethyl–ether with a trace of oxygen is used as the drift gas which provides a 'slow' drift velocity of around 5 μm/ns. Resolutions in the $r\phi$ plane of around 50 μm in the centre of a cell (compared to a design value of 30–40 μm) and 150 μm at the edge of a cell have been achieved. The VXD was designed to be used in conjunction with the CTD to improve the measurement of the track momentum and distance of closest approach to the event vertex, allowing the measurement of short lived particle decays.

1.3.3 Forward and Rear Tracking Detectors

The forward tracking system (FDET) was designed to detect particles emitted in the angular region $6^o < \theta < 25^o$ where the acceptance of the CTD becomes small. It consists of three Forward Tracking Detectors (FTDs), spaced 210 mm apart, sandwiching two Transition Radiation Detectors (TRDs).

The FTDs each contain three planes of wires spaced 7 mm apart, normal to the beam axis and with each plane inclined at 120° with respect to the next plane, allowing 3D charged track reconstruction.

The two TRDs, occupying the space between the FTDs, detect X–rays emitted when relativistic particles cross boundaries between plastic radiator layers and Xenon / CO_2 filled drift chambers, due to their differing refractive indices. By measuring the intensity of the X–rays, test beam results have shown that it is possible to separate electrons from hadrons with 1.5% of pions being mis–identified as electrons and 90% of electrons being correctly identified, for particles with momenta 2 – 10 GeV.

The Rear Tracking Detector (RTD) consists of a single chamber of identical design to the FTD chambers and covering an angular region $160^o < \theta < 170^o$.

During 1994, the RTD was fully read–out whereas the electronics for the FDET were commissioned near the end of the running period.

1.4 Calorimeter

The ZEUS uranium calorimeter was designed to accurately measure jets with high particle densities and to separate between leptons and hadrons. As jets contain electromagnetic as well as hadronic components, it is important that the device is compensating, meaning that it has an equal response to electromagnetic and hadronic showers. Another important consideration in the design of the calorimeter is achieving good angular resolution and jet separation and to this end, it is finely segmented into around 6000 cells.

The calorimeter is especially important for the measurement of neutral particles which are not registered in the tracking detectors and also for high momentum particles where the momentum resolution of the CTD becomes poor (see equation 1.1). One of the most important design aspects is the hermeticity of the calorimeter (apart from the two small beam pipe holes). For example, from missing transverse energy, it is possible to infer the presence of neutrinos which pass undetected through the detector.

The calorimeter is divided into towers of 20×20 cm, each with either two or three sections. Towers in the FCAL and BCAL have an inner electromagnetic (EMC) section and two outer hadronic (HAC) sections, whereas those in the RCAL have an inner EMC section and only one outer HAC section. The EMC sections are further divided into four 5×20 cm cells in the FCAL and BCAL and two 10×20 cm cells in the RCAL. This bias towards more instrumentation in the forward direction is directly related to the forward going centre–of–mass of the ep interaction. The regions of the FCAL and

RCAL shielded from the interaction point by the overlap with the BCAL do not have EMC sections.

Figure 1.5 shows an FCAL module. The individual towers and cells can be seen. Each cell is composed of alternate layers of depleted uranium (DU) and plastic scintillator tiles. Hadrons entering the calorimeter lose energy into the binding energy required to break up the heavy uranium nuclei. However, in a process known as self–compensation, part of the shower energy produces spallation neutrons in the break up of the uranium nuclei. These spallation neutrons scatter off hydrogen atoms in the plastic scintillator and the recoiling protons produce light in the scintillator by ionisation thereby compensating for some of the energy lost into the binding energy. The thicknesses of the uranium and scintillator plates are chosen so that the energy lost and gained by the two processes cancel out. This self–compensation process results in the calorimeter having a high energy resolution for hadrons. In test beam data, the following errors have been achieved (sampling in quadrature with systematic):

$$\frac{\sigma(E)}{E} = \frac{35\%}{\sqrt{E}} \oplus 2\% \qquad \text{(for hadrons)} \tag{1.2}$$

$$\frac{\sigma(E)}{E} = \frac{18\%}{\sqrt{E}} \oplus 1\% \qquad \text{(for electrons)} \tag{1.3}$$

The EMC sections are each 25 radiation lengths deep so that electromagnetic showers are fully contained. This depth is equivalent to one nuclear interaction length for hadrons. The HAC sections vary in depth from 3 interaction lengths in the rear to 6 interaction lengths in the forward direction.

The scintillator layers in each cell are coupled to two wavelength shifters, one on either side of the cell which are in turn linked to two photomultiplier tubes (PMTs) positioned at the back of the towers. The PMTs then produce a signal proportional

to the energy of the incident particle. Two wavelength shifters are used to allow determination of the position of the energy deposit within a cell. The scintillator layers produce UV light which the wavelength shifters turn to green light to which the PMTs are much more sensitive.

The signals from the scintillator layers have a very fast response time of the order of a nanosecond allowing the trigger to reject backgrounds from beam gas interactions and cosmic rays.

There are slots after the 4th and 7th scintillator layers of the FCAL and only after the 4th scintillator layer in the BCAL and RCAL to accommodate the Hadron Electron Separator (HES). This was designed to identify electrons within dense jets by improving the segmentation of the calorimeter using silicon diodes. Only the rear HES was installed in 1994.

1.5 Muon Detectors

Muons are highly penetrating at the energies typically reached at HERA and so the ZEUS detector has an extensive muon detection system as its outermost component.

The forward muon detector (FMUON) detects and measures high momenta muons independent of the CTD. It consists of two iron toroids sandwiched between limited streamer tube (LST) planes, which measure the $r\phi$–coordinate, and drift chamber planes, which measure the polar angle θ. The toroids each provide a magnetic field of up to 1.7 T to allow momentum measurements with a design resolution of $\sigma_p/p = 20\%$ at 100 GeV.

The barrel and rear muon detectors lie inside and outside the magnetized iron yoke (BMUI/BMUO and RMUI/RMUO) with each consisting of two orthogonal LST layers.

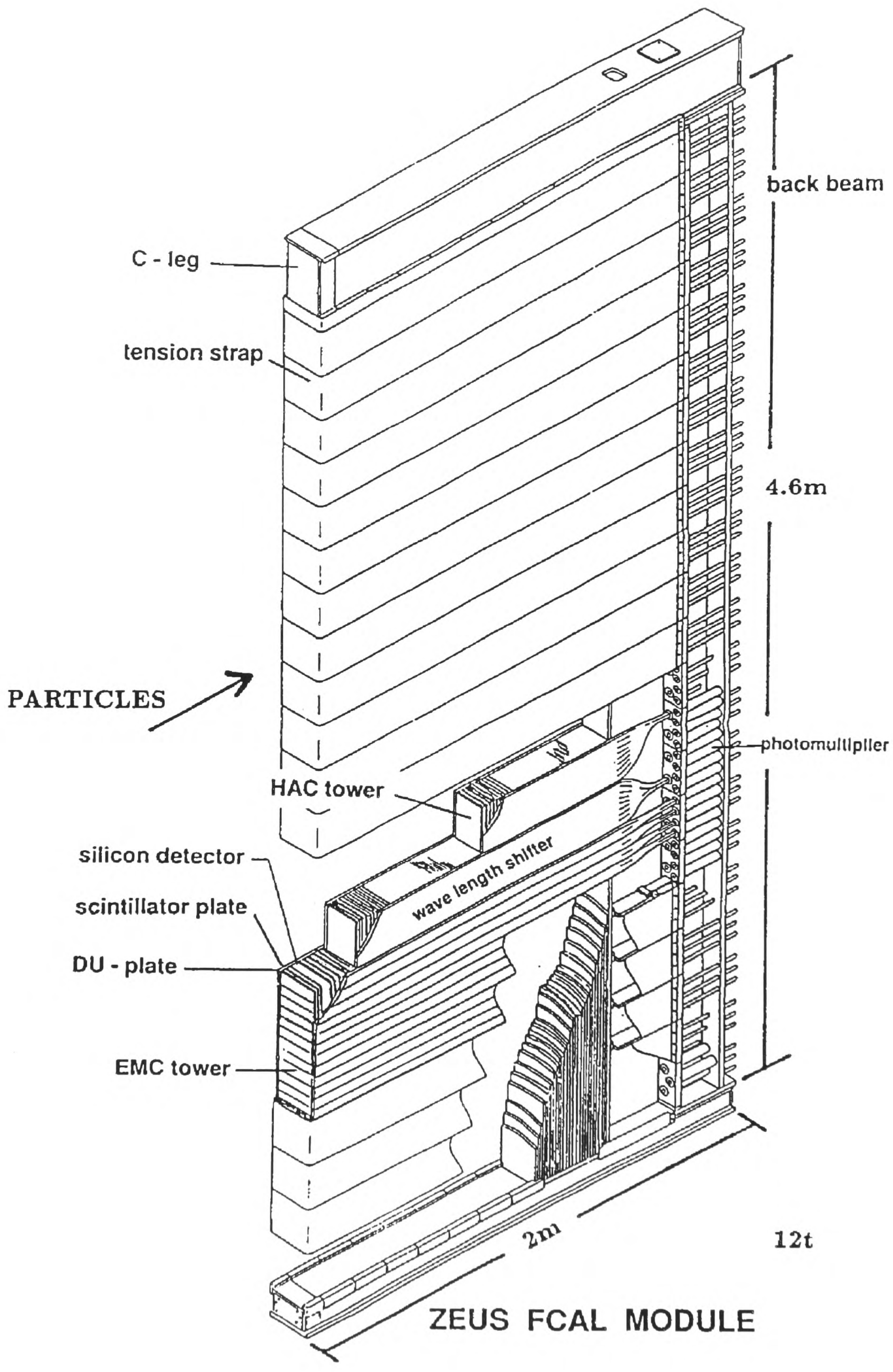

Figure 1.5: An FCAL module showing segmentation into towers and the structure of the towers with alternate depleted uranium (DU) and scintillator layers. The layers are connected to the photomultiplier tubes at the back of the towers by two wavelength shifter bars.

They identify particles punching through the calorimeter and measure their momenta by looking at the change in direction of the particles on passing through the yoke. The design resolution in this barrel and rear direction is $\sigma_p/p = 30\%$ at 20 GeV.

1.6 Luminosity Monitor

The luminosity delivered to the ZEUS detector is measured using the luminosity monitor (LUMI) which consists of an electron detector at $z = -34.7$ m and a photon detector at $z = -107$ m. Both are lead–scintillator calorimeters with the photon detector having an additional 3 radiation length carbon filter to absorb synchrotron radiation and a Čerenkov counter to veto electrons from synchrotron photons converting in the filter. Electrons, scattered at polar angles $\theta \leq 6$ mrad and with between 20% to 90% of the incident electron beam energy, are deflected by the beam magnets into the electron calorimeter. The photon detector has an acceptance of $\theta \leq 0.5$ mrad.

The LUMI operates by measuring the rate of the bremsstrahlung process $ep \rightarrow ep\gamma$, which can be calculated precisely in QED (see section 3.5.2). This has a signature of a photon and electron in coincidence with $E_\gamma + E_e = E_{beam}$. Despite the filters to absorb synchrotron radiation, some does reach the photon detector, but this background can be measured using the unpaired electron pilot bunches and subtracted from the overall rate to give a rate for colliding bunches.

The LUMI detector is also used to tag very low Q^2 quasi–photoproduction events where the incident electron is scattered through a very small angle and is not seen in the main detector.

1.7 C5 Counter

The C5 collimator, positioned at $z = -3.2$ m behind the RCAL, is one of a series of collimators both down and upstream of ZEUS installed to protect the detector from damaging synchrotron radiation[4] and beam gas background. The C5 collimator is instrumented with tungsten layers and read out by silicon diodes. In 1994, when positrons replaced electrons in the incident beam, the C5 counter timed the proton and positron bunches with respect to each other. This information was fed into the ZEUS trigger to veto background events.

1.8 Small Angle Rear Tracking Detector

The Small Angle Rear Tracking Detector (SRTD) was installed in 1994 and is a scintillator–strip device positioned at $z = -1.46$ m on the inner side of the RCAL around the beam pipe. It covers an area of 68×68 cm giving a nominal angular range of 161.8^o – 176.1^o with 100% acceptance in the range 166.9^o – 174.5^o. It consists of 272 scintillator strips each 10 mm wide and 5 mm thick. These are arranged in two orthogonal layers to give an electron position resolution of $\sim$3 mm. A schematic view of the SRTD with the arrangement of the scintillator strips is shown in figure 1.6.

1.9 ZEUS trigger and Data Acquisition System

Bunches cross at the interaction regions of HERA every 96 ns, equivalent to 10^7 times a second. However, genuine ep interactions do not occur at every bunch crossing and the actual rate of ep events is very low in comparison to the rate of background interactions. The two main sources of background are 'beam gas' collisions when residual

[4] See section 3.5.2.

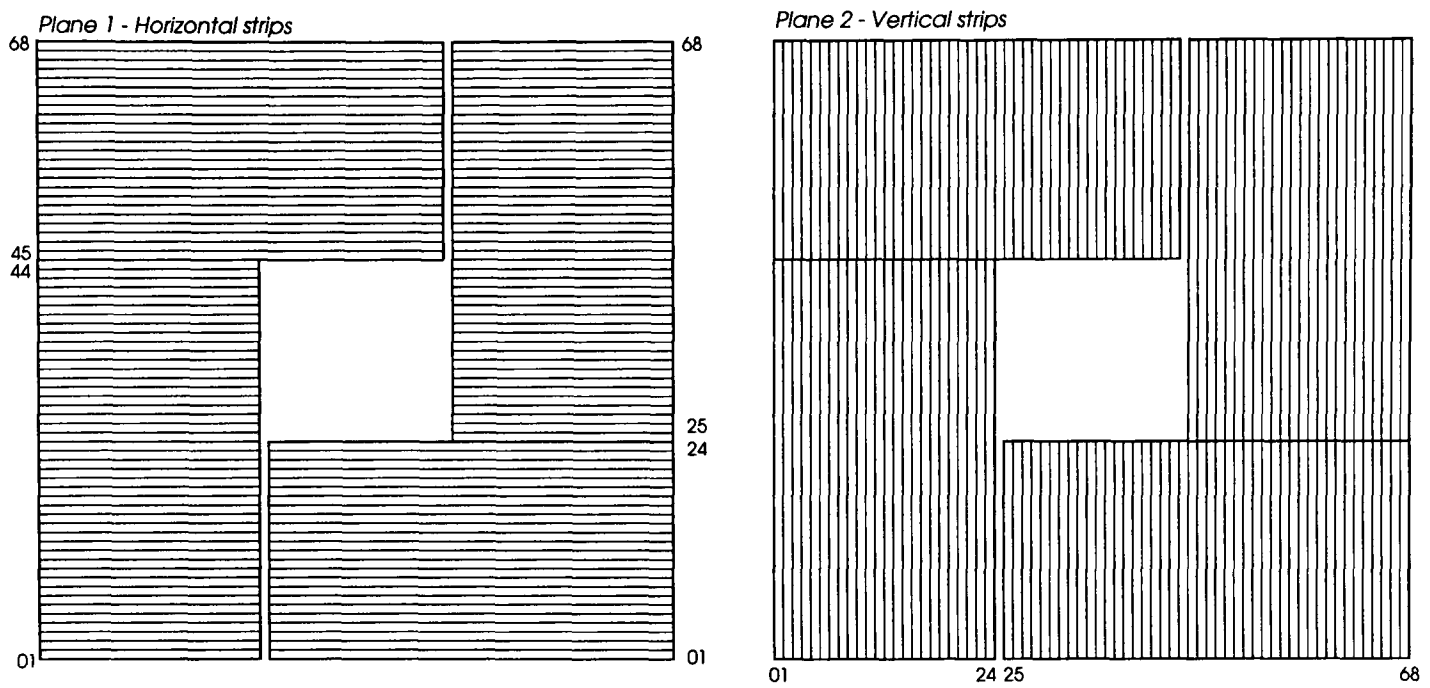

Figure 1.6: Schematic view of the SRTD showing the arrangement of the 272 scintillator strips in two layers with the horizontal strips on the left and the vertical strips on the right. The numbering scheme of the SRTD is also shown.

gas molecules in the beam pipe collide with the proton beam and beam–scraping interactions when the proton beam collides with parts of the machine. Other sources of background include cosmic rays passing through the detector and synchrotron radiation from the electron beam.

The ZEUS trigger was designed to select out the useful events from this large background in real time. A three level trigger system is used to reduce the output rate to a few Hz. An upper limit of 3–5 Hz on this output rate is imposed by the rate at which events can be written onto tape. Figure 1.7 shows a schematic view of the trigger system.

The First Level Trigger (FLT) operates a deadtime–free pipeline system, synchronised with the 96 ns bunch crossing interval and the HERA clock. The FLT is composed of component FLTs operating on dedicated hardware for individual components within the ZEUS detector. These send their decisions as to whether or not to accept an event

to the Global First Level Trigger (GFLT). The GFLT combines these inputs into 64 trigger slots, each containing a single bit, and accepts the event approximately 5 μs after the respective beam crossing if any one of these 64 slots is triggered. The fast clear (see figure 1.7) bases a veto decision on calorimeter energy sums. It was not operational in 1994.

With a 96 ns bunch crossing interval, one can see why the pipelining procedure is required. Some of the FLT slots have a pre–scale factor different from unity. This specifies what fraction of events passing the selection algorithm for a particular slot, generate an acceptance for the slot. This is useful for slots which have too high an acceptance rate. The FLT reduces the event rate to around 1 kHz.

Events accepted by the FLT are passed onto the software buffers and component Second Level Triggers (SLTs). With a longer processing time, the SLTs are no longer required to be synchronised with the HERA clock. The component SLTs run on detailed software algorithms in contrast to the FLT. They pass their decisions to the Global Second Level Trigger (GSLT) which then reduces the event rate by an order of magnitude using timing cuts and more sophisticated physics filters based on the component SLT decisions.

All components transfer their data to an Event Builder (EVB) on acceptance by the GSLT. This combines all the data into a single event record which is passed onto the Third Level Trigger (TLT). Here, a fast version of the off–line detector reconstruction is run on a farm of Silicon Graphics machines. Kinematic properties can be calculated, further timing cuts are applied and physics pre–selection filter slots are filled. Events passing any one of these physics filters are then transferred to the full off–line reconstruction. Here, more accurate information from all the components of the detector

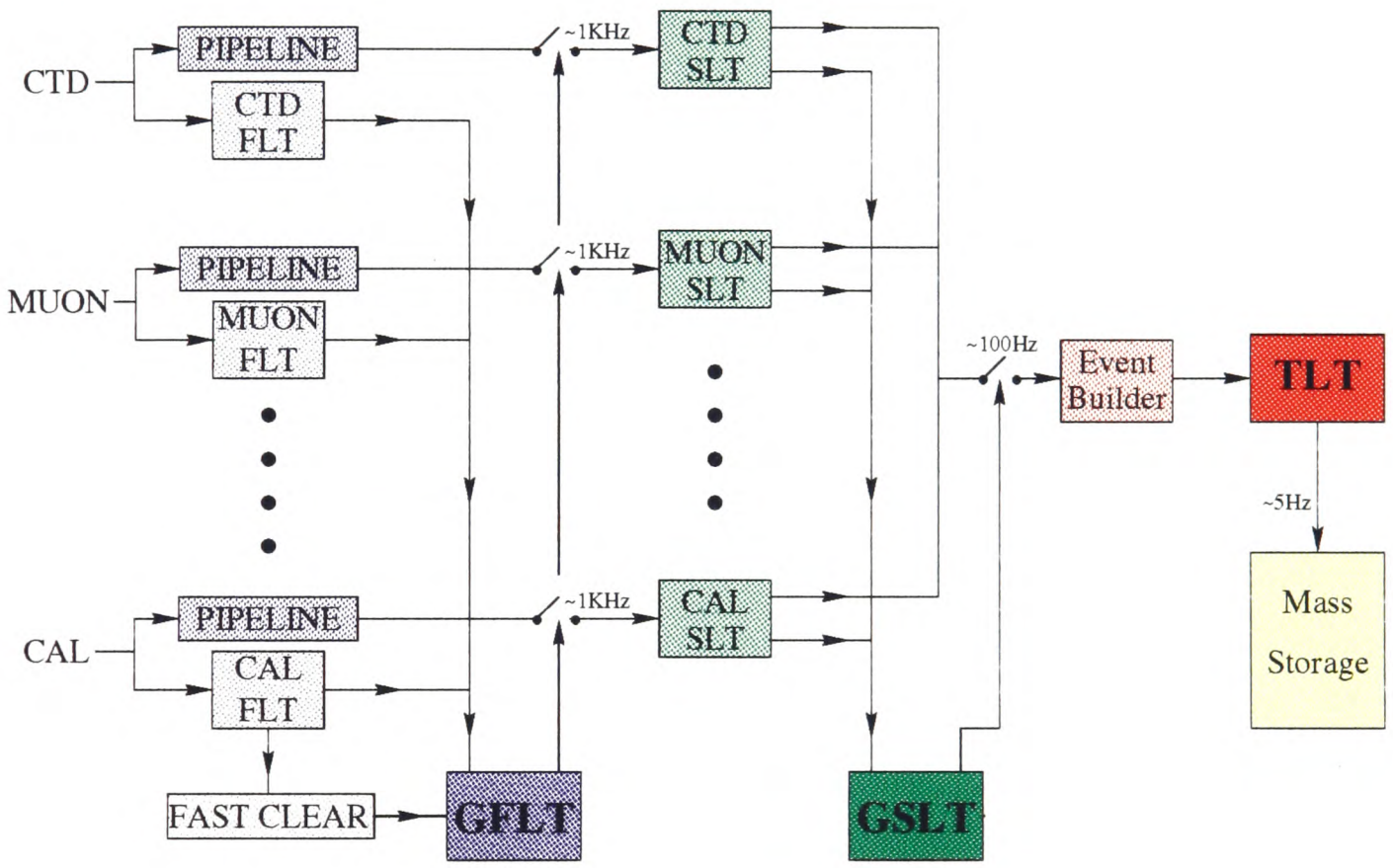

Figure 1.7: Schematic view of the three level trigger system operated at ZEUS also showing the event rates at each level.

is used to reprocess the data giving improved calibrations and all this information is written onto magnetic tape at a rate of a few Hz.

A more detailed description of the algorithms for the trigger slots relevant to the analysis presented in this thesis will be given in chapters 5 and 6.

Chapter 2

Physics at HERA

This chapter will introduce the kinematical variables used for electron–proton scattering at HERA. The Quark Parton Model (QPM) and Quantum Chromodynamics (QCD) will be described. Methods available at HERA to extract the gluon density in the proton will be summarised and finally, the J/ψ meson will be introduced with possible production mechanisms at HERA mentioned.

2.1 Kinematics of electron–proton scattering

Figure 2.1 shows a generic ep scattering event at HERA, assuming a scattered lepton emerges. The four–momenta of the particles are labelled. The incident electron and proton, the final state lepton and the final hadronic system, X, have four–momenta l, p, l' and p_X respectively. The four–momentum transfer from the electron is $q = (l - l')$ and we define:

$$Q^2 = -q^2 = -(l - l')^2 \tag{2.1}$$

The incident electron and proton are highly relativistic at HERA and so their masses can be safely neglected. The total centre–of–mass energy squared, s, is given by:

$$s = (p + l)^2 \simeq 2p.l \simeq 4E_e E_p \tag{2.2}$$

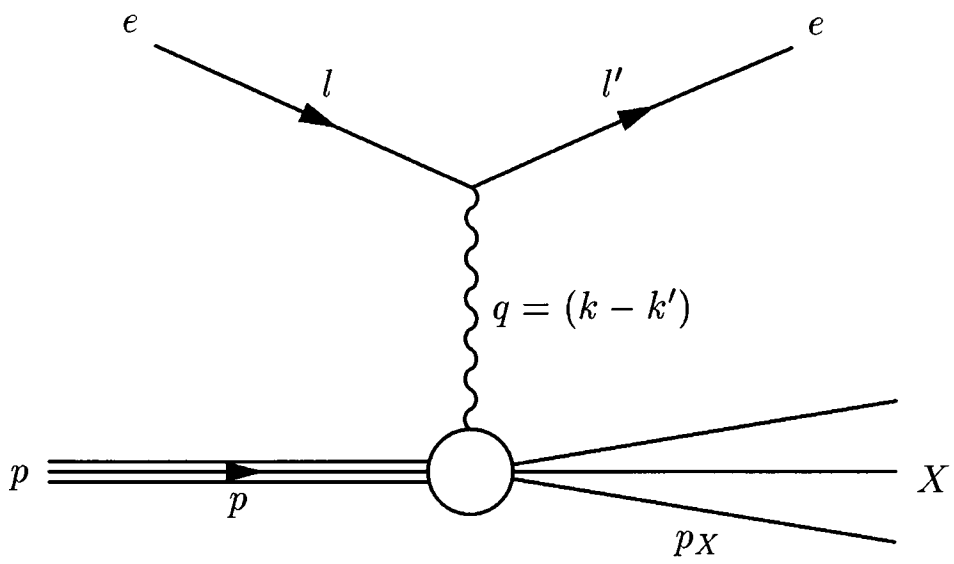

Figure 2.1: A generic ep interaction at HERA with the momentum labels of the particles shown.

where E_e and E_p are the initial electron and proton energies respectively. Finally, two Lorentz invariant scalars, the Bjorken variable, x, and the inelasticity parameter, y, are often used to describe events. These are defined by:

$$x = \frac{Q^2}{2p.q} \tag{2.3}$$

$$y = \frac{p.q}{p.l} \tag{2.4}$$

Both these scalars lie between 0 and 1. It is seen that $s \simeq 2p.l = 2p.q/y = Q^2/xy$, giving the important relation:

$$Q^2 = sxy \tag{2.5}$$

Thus only two of the variables Q^2, x and y are independent. The variable, y, can also be written in terms of E and E', the initial and final electron energies in the proton rest frame respectively:

$$y = \frac{E - E'}{E} \tag{2.6}$$

So, y is equal to the fractional energy loss of the electron in the proton rest frame.

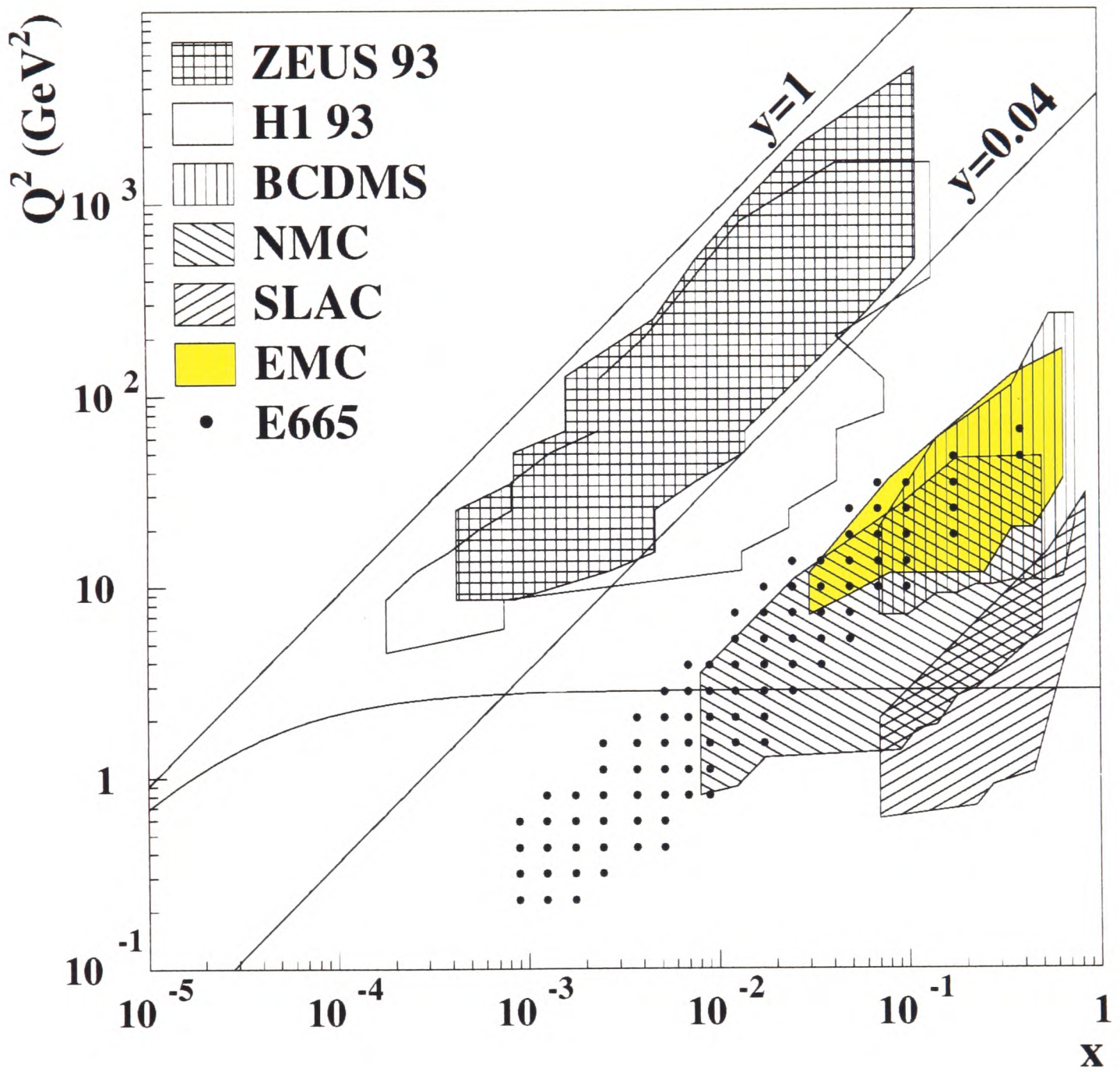

Figure 2.2: The regions covered in the xQ^2 plane by the 1993 DIS data from the ZEUS and H1 experiments at HERA. Also shown are the regions covered by previous fixed target experiments. The kinematic limit $y = 1$ is shown together with the cut $y = 0.04$ used at ZEUS.

Figure 2.2 shows the regions covered in the xQ^2 plane by the 1993 selected DIS data from both the ZEUS and H1 experiments, The regions covered by previous fixed–target experiments are also shown. It is seen that measurements of the proton structure are possible at HERA in a completely new region of very low x and high Q^2 which is quite far removed from previous data. In order to bridge the gap in the future, HERA may be run at lower centre–of–mass energies by lowering the proton and/or electron beam energies.

2.2 The electron–proton differential cross–section

The differential cross–section for the inelastic ep scattering process shown in figure 2.1 can be written quite generally as:

$$\frac{d\sigma_{ep}}{dx\,dQ^2} = \frac{4\pi\alpha^2}{x\,Q^4}\left\{xy^2\,F_1(x,\,Q^2) + (1-y)\,F_2(x,\,Q^2) \pm \left(y - \frac{y^2}{2}\right)\,x\,F_3(x,\,Q^2)\right\} \quad (2.7)$$

where α is the electromagnetic fine structure constant. The structure function, $F_3(x,\,Q^2)$, accounts for the parity violating exchange of the weak Z^o boson. This term is negligible for $Q^2 \ll M_Z^2$. The three structure functions, $F_1(x,\,Q^2)$, $F_2(x,\,Q^2)$ and $F_3(x,\,Q^2)$ are used to parameterise our ignorance of the structure of the proton. The y dependence in the differential cross–section is a result of helicity conservation at the photon–quark vertex. It is clearly the objective of experiments such as HERA to measure and understand these structure functions.

2.3 The Quark Parton Model

In the Quark Parton Model (QPM), the proton is assumed to be composed of partons (quarks and gluons), each carrying a fraction, x, of the momentum of the proton. Therefore, the partons all have zero transverse momentum. This is only possible in

a frame where the proton has infinite momentum so that all the parton masses and transverse momenta can be neglected.

For ep interactions depicted in figure 2.1, the virtual photon scatters elastically off a parton of momentum xp as shown in figure 2.3. For such elastic collisions, the relation $Q^2 = 2(xp).q$ holds. Thus, $x = Q^2/2p.q$ which is exactly the Bjorken x variable associated with the virtual photon (see equation 2.3).

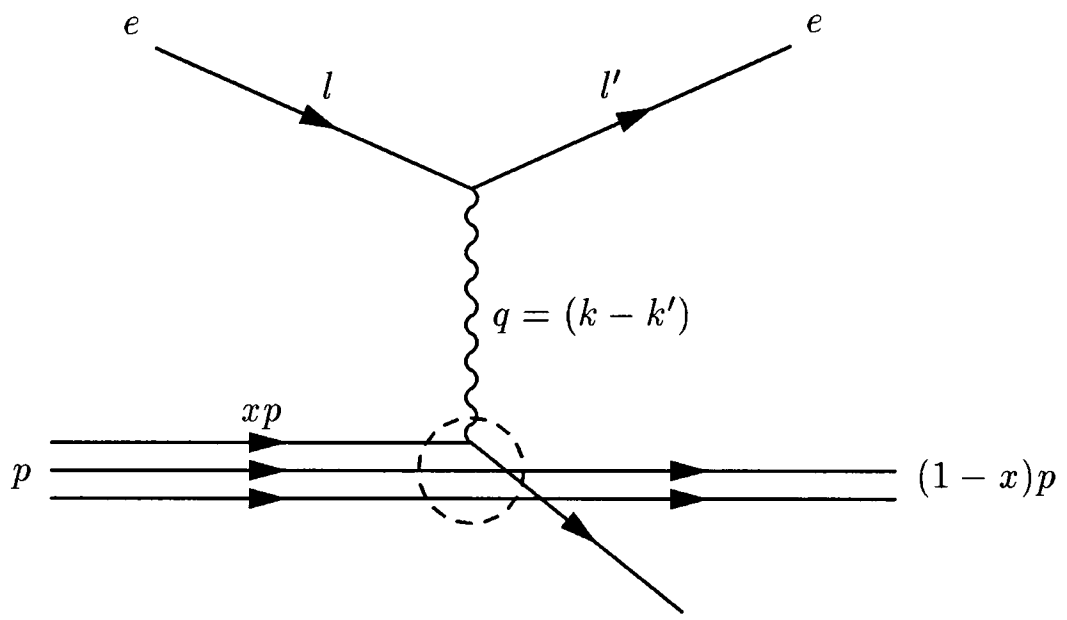

Figure 2.3: An ep interaction in the Quark Parton Model where the virtual photon scatters elastically off one of the constituent partons in the proton carrying momentum xp.

In the electron–parton centre–of–mass frame, the electron scattering angle, θ_{ep_e} is directly related to the y variable by:

$$y = \frac{1}{2}(1 - cos\,\theta_{ep_e}) \tag{2.8}$$

The QPM also enables the proton structure functions to be written exactly since the virtual photon scatters *elastically* off only the charge carrying partons. It is therefore

only the quarks which participate in the ep scattering and we have:

$$F_2(x) = \sum_q e_q^2 \, x q(x) \tag{2.9}$$

$$2x \, F_1(x) = F_2(x) \tag{2.10}$$

where : e_q = quark charge (in units of e)

$q(x)\,dx$ = probability of a quark having a fractional momentum in the range x to $x + dx$

The sum in equation 2.9 runs over all quark and antiquark flavours. The quark density is defined as $q(x)$ and $x\,q(x)$ is the quark momentum density. The most important point to note is that the proton structure functions in equations 2.9 and 2.10 are sole functions of x and independent of Q^2. This property is known as Bjorken scaling. The Callan–Gross relation, $2x\,F_1(x) = F_2(x)$, is a direct consequence of the quarks having spin$-\frac{1}{2}$.

Early deep inelastic scattering experiments confirmed the scaling of the structure functions, however, as the proton was probed in more detail, it was found that the quark densities did in fact depend on the scale at which they were being probed. Also, when F_2 was integrated over the whole momentum range ($0 < x \leq 1$), it was found that the quarks only accounted for around half the momentum of the proton. The remaining half is carried by electrically neutral partons which do not interact with the virtual photon, and hence do not contribute to F_2.

2.4 Quantum Chromodymamics

The current theory which is believed to explain all the features of the data in principle, is Quantum Chromodymamics (QCD). It differs from the QPM in that the constituent quarks interact with one another via the exchange of electrically neutral gluons (much

like the exchange of photons in QED). It is these gluons which are believed to carry the missing momentum fraction of the proton.

The quarks and gluons both carry a colour charge (in contrast to QED where the photons are electrically neutral). This allows radiation of gluons by gluons in addition to the radiation of gluons by quarks and quarks by gluons. This property causes the strong coupling constant of QCD, α_s, to 'run' so that: $\alpha_s = \alpha_s(Q^2)$. At small distances or equivalently, at high Q^2, $\alpha_s(Q^2)$ becomes sufficiently small for the perturbative techniques, familiar from QED, to be applied.

QCD therefore introduces higher order diagrams to the generic ep interaction shown in figure 2.1. Figure 2.3 shows the leading order $\mathcal{O}(\alpha^2)$ diagram where the virtual photon interacts with a quark from the incident proton, but the quark may also radiate a gluon before or after the virtual photon interaction as shown in figures 2.4a and b. Alternatively, the gluon content in the proton can interact with the virtual photon by splitting into a $q\bar{q}$ pair as shown in figure 2.5. It is clear that this process is proportional to the gluon density in the proton and by isolating such processes, the gluon density can, in theory, be measured. This will be attempted in the final chapter of this thesis.

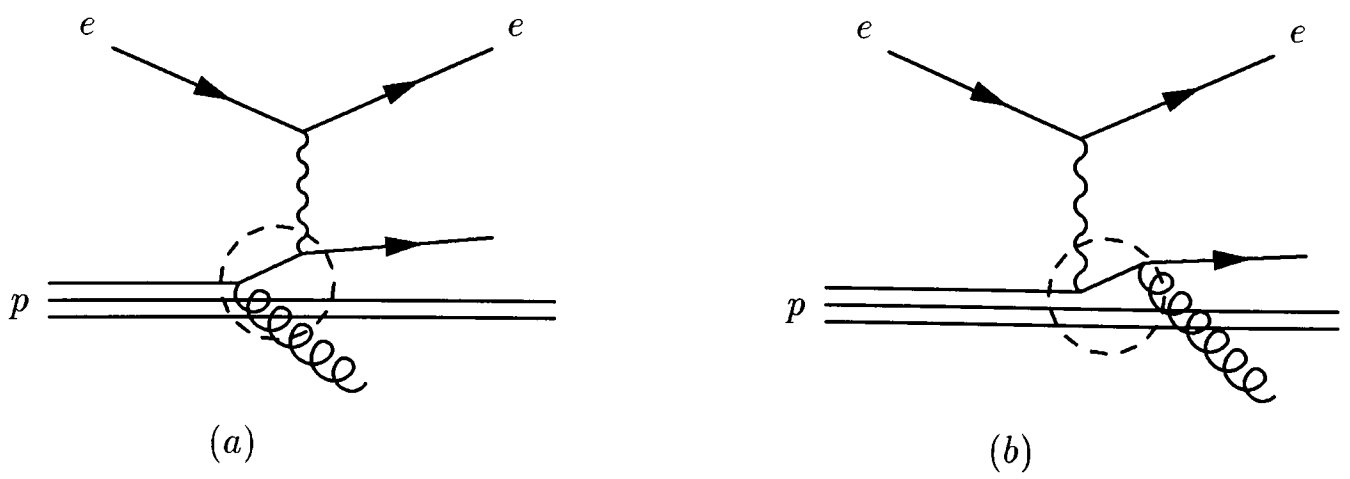

Figure 2.4: Diagrams showing $\mathcal{O}(\alpha^2\alpha_s)$ terms to the ep scattering cross–section where the struck quark radiates a gluon a) before and b) after the virtual photon interaction.

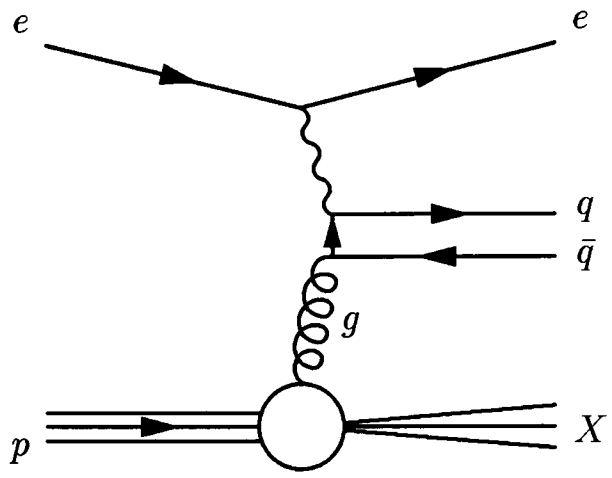

Figure 2.5: Diagram showing a $\mathcal{O}(\alpha^2\alpha_s)$ term to the ep interaction where a gluon from within the proton, splits into a $q\bar{q}$ pair before interacting with the virtual photon.

Figures 2.4 and 2.5 show $\mathcal{O}(\alpha^2\alpha_s)$ contributions to the ep cross–section. The inclusion of such Feynman diagrams results in scaling violations in the structure functions: $F_{1,2}(x) \neq F_{1,2}(x, Q^2)$, because the struck quark will no longer be collinear with the photon, as predicted in the QPM since the quark can recoil against a radiated gluon. Experiments such as that performed by the EMC collaboration at CERN, have measured an excess of large transverse momentum hadron jets over QPM predictions, in accordance with QCD predictions of quark and gluon jets recoiling against one another.

The scaling violations of the structure functions can be qualitatively explained as the virtual photon probing the proton structure in more detail with increasing Q^2. As the resolution increases with Q^2, QCD predicts that we should begin to 'see' a cloud of partons surrounding each quark. As the number of resolved partons which share the proton's momentum increases, the probability of finding a parton carrying a high fraction, x, of the proton momentum decreases. Conversely, the probability of finding a parton carrying a small fraction, x, of the proton momentum increases. This is seen in figure 2.6 where the $F_2(x, Q^2)$ structure function is plotted against x in bins of constant Q^2 for data collected by the ZEUS experiment in 1994. The structure function is seen

to rise with Q^2 in the very low x region. The steep rise in $F_2(x, Q^2)$ with decreasing x implies a very high parton density with low momenta. Also shown in figure 2.6 is the next–to–leading order (NLO) QCD fit to the structure functions.

By calculating the matrix elements for diagrams such as figures 2.4 and 2.5, it is possible to derive the Altarelli–Parisi evolution equations for the change in the quark, $q_i(x, Q^2)$, and gluon, $G(x, Q^2)$ densities with Q^2:

$$\frac{d\,q_i(x, Q^2)}{d\,ln\,Q^2} = \frac{\alpha_s}{2\pi} \int_x^1 \frac{dy}{y} \left\{ q_i(y, Q^2)\, P_{qq}\left(\frac{x}{y}\right) + G(y, Q^2)\, P_{qg}\left(\frac{x}{y}\right) \right\} \tag{2.11}$$

$$\frac{d\,G(x, Q^2)}{d\,ln\,Q^2} = \frac{\alpha_s}{2\pi} \int_x^1 \frac{dy}{y} \left\{ \sum_i q_i(y, Q^2)\, P_{gq}\left(\frac{x}{y}\right) + G(y, Q^2)\, P_{gg}\left(\frac{x}{y}\right) \right\} \tag{2.12}$$

where :

$$P_{qq}(z) = \frac{4}{3}\left\{\frac{1+z^2}{1-z}\right\} \tag{2.13}$$

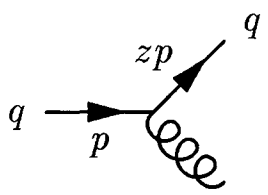

$$P_{qg}(z) = \frac{1}{2}\left\{z^2 + (1-z)^2\right\} \tag{2.14}$$

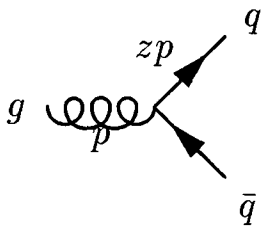

$$P_{gq}(z) = \frac{4}{3}\left\{\frac{1+(1-z)^2}{z}\right\} \tag{2.15}$$

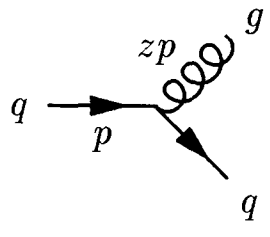

$$P_{gg}(z) = 6\left\{\frac{1-z}{z} + \frac{z}{1-z} + z(1-z)\right\} \tag{2.16}$$

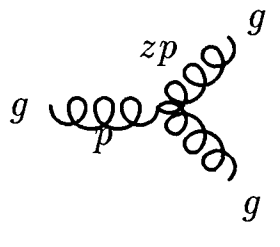

The sum in equation 2.12 runs over the $2n_f$ quark and antiquark flavours. The splitting function $P_{qq}(z)$ represents the probability of a quark emitting a gluon and becoming

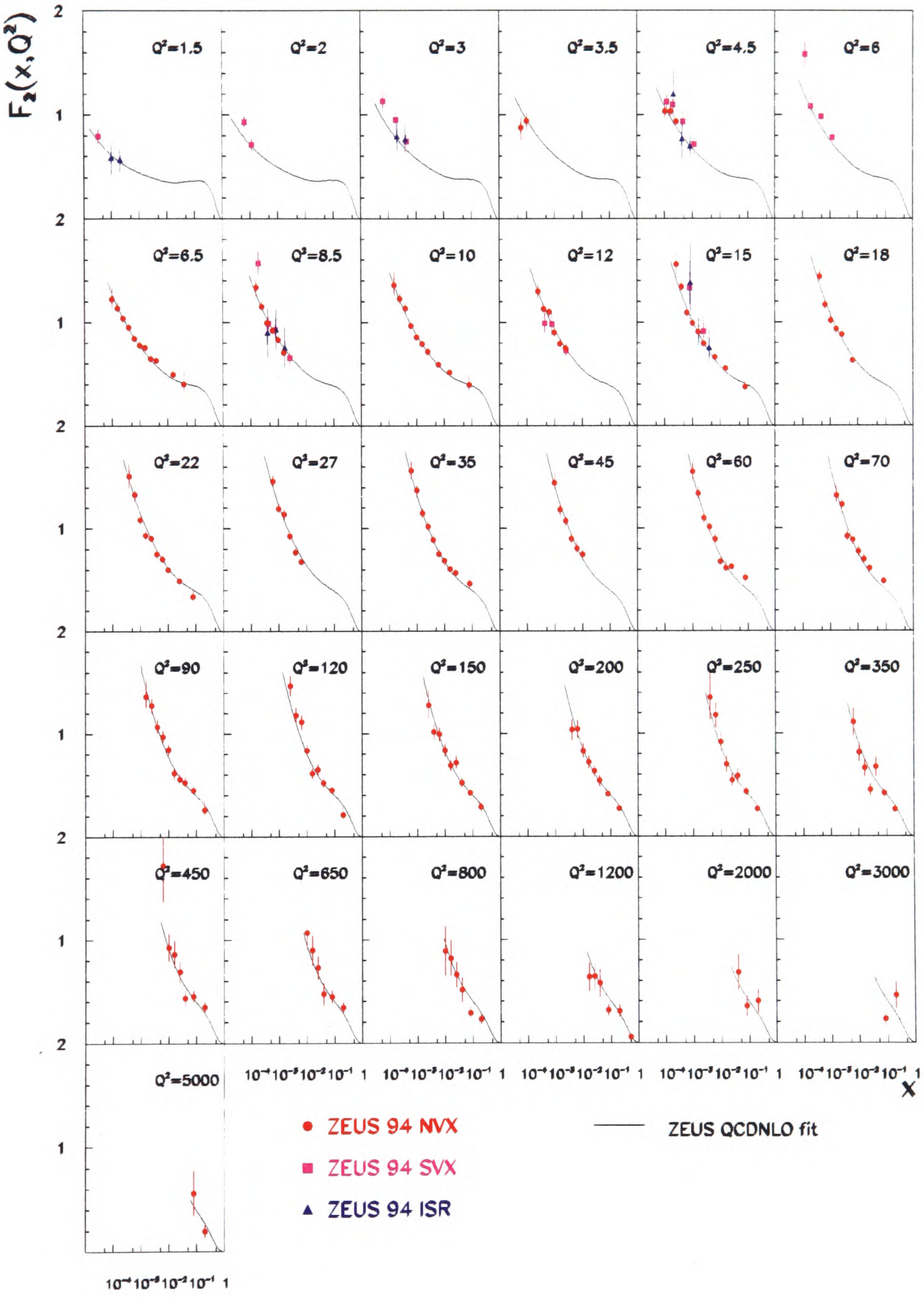

Figure 2.6: The F_2 structure function as measured by the ZEUS collaboration in 1994 as a function of x in bins of constant Q^2. The nominal vertex (NVX), shifted vertex (SVX) and initial state radiation (ISR) data sets are used. The structure function is seen to rise steeply at low x. The fit of the structure function using next–to–leading order (NLO) is also shown.

a quark with a fraction z of the original momentum as suggested by the diagram in equation 2.13. The other splitting functions, $P_{qg}(z)$, $P_{gq}(z)$ and $P_{gg}(z)$ have similar probability interpretations as indicated by the diagrams. Equations 2.13 to 2.16 for the splitting functions are the results of leading order calculations. The Altarelli–Parisi equations state, in mathematical terms, that a parton with momentum fraction, x, could have come from a parton with a larger momentum fraction, y, (where $x \leq y \leq 1$) with a probability proportional to α_s and the respective splitting function.

2.5 Measurement of the gluon density at HERA

In this section, various methods for extracting the gluon density available at HERA will be discussed. The extraction from direct inelastic J/ψ photoproduction data will be attempted in the final chapter of this thesis.

Measurements of the parton densities in the proton are not only essential to further our understanding of the nucleon structure, but also to understand the physics of present and future hadron colliders such as the Tevatron and LHC respectively.

Fixed target experiments in the past with lepton or photon beams, have provided useful information on the valence and sea quark distributions, but the gluon distribution has been poorly measured in these experiments, despite the gluons carrying around half the momentum of the proton. This is because such experiments have been limited to the kinematical region $x > 10^{-2}$.

2.5.1 F_2 structure function fits

The QCD evolution equations 2.11 and 2.12 relate the change with Q^2 of the parton densities within the proton. These results can also be extended to give the GLAP

evolution equation [4, 5] for the scaling violation of the F_2 structure function:

$$\frac{d\,F_2(x,\,Q^2)}{d\,ln\,Q^2} = \frac{\alpha_s}{2\pi}\int_x^1 \frac{x\,dy}{y^2}\left\{F_2(y,\,Q^2)\,P_{qq}\left(\frac{x}{y}\right) + 2\sum_i e_{q_i}^2\,y\,G(y,\,Q^2)\,P_{qg}\left(\frac{x}{y}\right)\right\} \quad (2.17)$$

Thus by measuring the F_2 structure function, it is possible to extract the Q^2 dependence of the parton densities provided their x dependence is known from data at a fixed Q^2 value.

A common technique [6] used at both the ZEUS and H1 collaborations at HERA is to parameterise the x dependence of the parton densities at a fixed $Q^2 = Q_o^2$. A fit to the data is then performed on all the free parameters. The gluon momentum density was parameterised as follows:

$$x\,G(x, Q_o^2) = A_g\,x^{\delta_g}(1-x)^{\eta_g} \quad (2.18)$$

with $Q_o^2 = 7\,\mathrm{GeV}^2$. A fit was done on the F_2 structure function measured at ZEUS in 1994 (see figure 2.6) to next–to–leading order (NLO). The preliminary results for the gluon density are shown in figure 2.7. Also shown is the gluon density from the 1993 fit to the F_2 data. The central values for the fit parameters are: $A_g = 1.01$, $\delta_g = -0.35$ and $\eta_g = 5.22$.

2.5.2 F_L structure function fits

The longitudinal structure function, F_L is defined as:

$$F_L(x,\,Q^2) = F_2(x,\,Q^2) - 2x\,F_1(x,\,Q^2) \quad (2.19)$$

Measurements of F_L give deviations from the Callan–Gross relation (see equation 2.10), predicted by the QPM. The leading order QCD calculation for F_L gives the result:

$$F_L(x,\,Q^2) = \frac{\alpha_s}{\pi}\int_x^1 \frac{x\,dy}{y^2}\left\{\frac{4}{3}\frac{x}{y}\,F_2(y,\,Q^2) + 2\sum_i e_{q_i}^2\,\left(1-\frac{x}{y}\right)\,y\,G(y,\,Q^2)\right\} \quad (2.20)$$

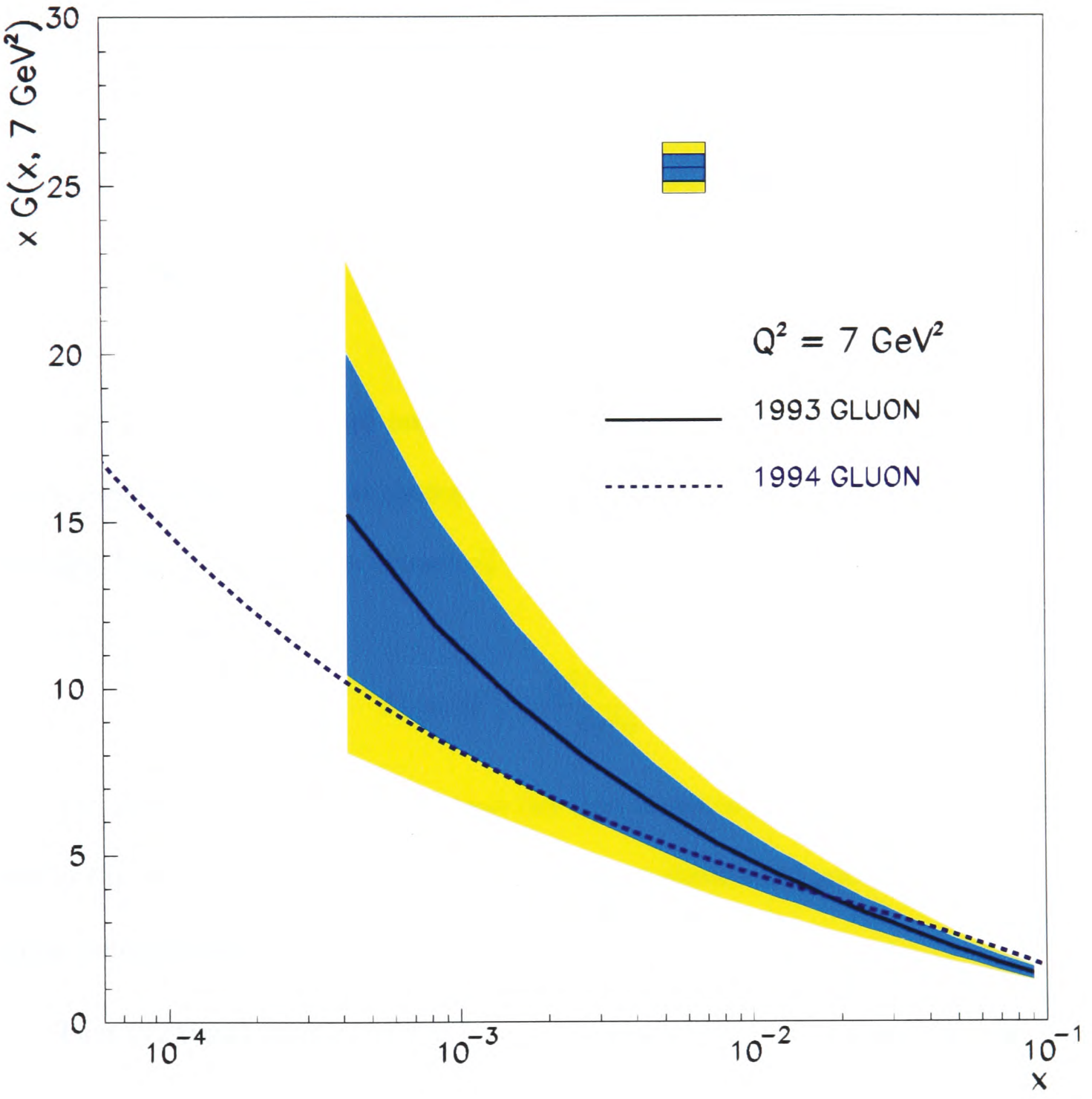

Figure 2.7: The gluon density in the proton extracted from fits to the F_2 structure function measured at ZEUS in 1993 and the preliminary results from 1994. The blue and yellow shaded regions show the statistical and systematic errors on the 1993 result respectively.

and it is seen that F_L is a very sensitive probe of the gluon density. The differential cross–section, $\frac{d^2\sigma^{ep}}{dx\,dQ^2}$, can be written as the sum of the transverse and longitudinal virtual photon–proton cross–sections, $\sigma_T^{\gamma^* p}$ and $\sigma_L^{\gamma^* p}$ respectively:

$$\frac{d^2\sigma^{ep}}{dx\,dQ^2} = \Gamma(\sigma_T^{\gamma^* p} + \epsilon\sigma_L^{\gamma^* p}) \tag{2.21}$$

where :

$$\epsilon = \frac{2(1-y)}{1+(1-y^2)} \tag{2.22}$$

$$\Gamma = \frac{\alpha}{2\pi}\frac{1+1-y^2}{x\,Q^2} \tag{2.23}$$

ϵ is the relative longitudinal polarisation of the virtual photon and Γ is the flux of transversely polarised virtual photons. Thus by plotting $\frac{1}{\Gamma}\frac{d^2\sigma^{ep}}{dx\,dQ^2}$ against ϵ and fitting a straight line, it is possible to extract $\sigma_T^{\gamma^* p}$ and $\sigma_L^{\gamma^* p}$. The longitudinal structure function is then given by:

$$F_L(x, Q^2) = \frac{Q^2(1-x)}{4\pi^2\alpha}\sigma_L^{\gamma^* p} \tag{2.24}$$

The gluon density within the proton can then be extracted using the same methods as for the F_2 fits, namely, to parameterise the gluon density and perform a fit to the F_L data using equation 2.20.

Thus to extract the gluon density through F_L measurements, the differential cross–section must be measured as a function of y for fixed values of x and Q^2. Two methods have been suggested to achieve this:

1. Changing the *ep* centre–of–mass energy by lowering the proton beam energy.

2. Relying on initial state radiation of the incident electron to provide a sample of events with a reduced electron energy.

In practice, it is very difficult to measure F_L because of the limited precisions of the F_2 measurements. The current results on F_2 from the ZEUS experiment do not provide sufficient precision to measure F_L. A minimum integrated luminosity of around 5 pb^{-1} at two different centre–of–mass energies is required to extract the gluon density from F_L measurements. In 1994, ~ 3 pb^{-1} of data was taken by the ZEUS experiment.

2.5.3 Dijet rates in BGF photoproduction

The interactions between almost real photons ($Q^2 \approx 0$) and protons at HERA produce jets with high transverse energy [7, 8]. Two processes are responsible for jet production at LO. In figure 2.8a, the photon interacts directly with a parton in the proton to produce two jets in a process known as direct photoproduction, whereas in figure 2.8b, the photon first fluctuates into a hadronic state before interacting with the parton, a process known as resolved photoproduction. It is possible to separate these two processes by measuring

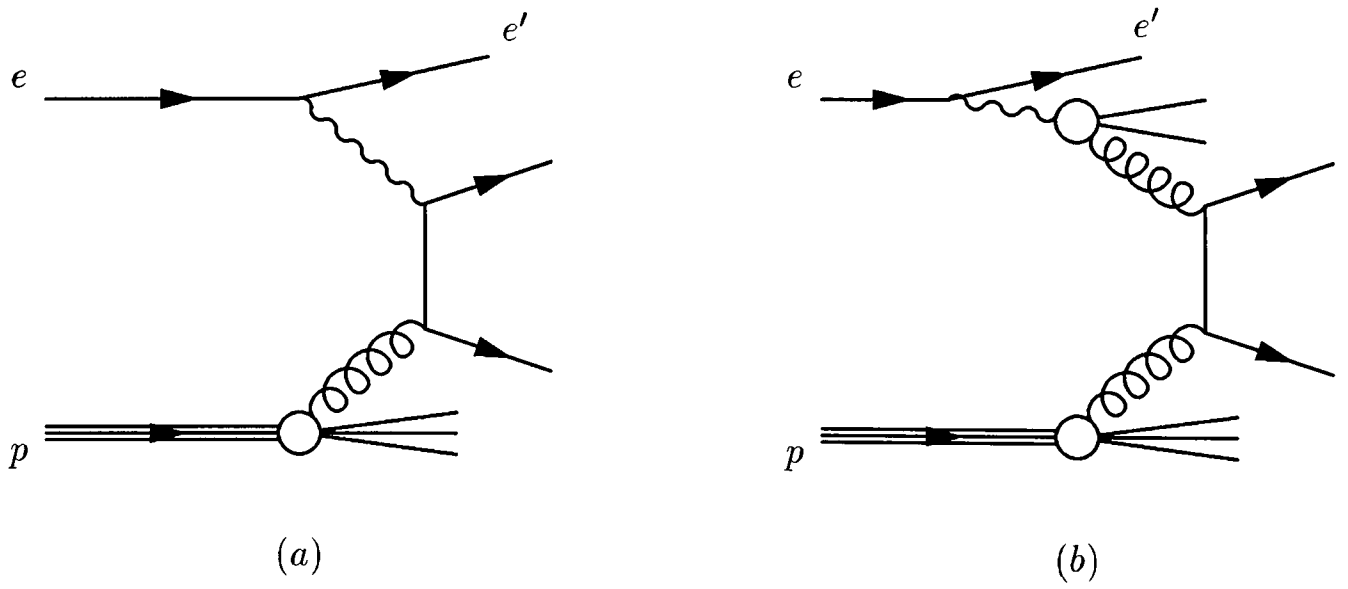

Figure 2.8: Diagrams showing the leading order diagrams for dijet production at HERA via the a) direct and b) resolved photoproduction processes.

the fraction, x_γ, of the photon energy observed in the highest two transverse energy, E_T^{Jet}, jets. The high x_γ region is populated mainly by events from the direct process whereas the resolved events occupy the lower x_γ region.

The differential dijet cross–section for the direct process is sensitive to the gluon distribution in the proton. It has been measured by the ZEUS collaboration [9] for $x_\gamma \geq 0.75$ with a cut $E_T^{Jet} > 6$ GeV for $y = E_\gamma/E_e$ in the range $0.04 < y < 0.95$. Also, the pseudorapidities, $\eta_i = -ln\{tan(\theta_i/2)\}$, of the two jets were constrained by $|\Delta\eta| < 0.5$.

The dijet differential cross–section for direct events can be calculated to LO using QCD [10] giving:

$$\left.\frac{d^3\sigma}{d\eta_1\, d\eta_2\, dp_t^2}\right|_{\eta_1=\eta_2} = \frac{\pi\alpha\alpha_s}{4p_t^4}\, y f_{\gamma/e}(y) \left[\sum_i e_i^2\, xG(x,\mu^2) + \frac{10}{3} F_2(x,\mu^2)\right] \qquad (2.25)$$

where : $\eta_1,\ \eta_2$ = Laboratory pseudorapidities of the two jets

p_t = Transverse momentum of the interacting parton in the proton.

$f_{\gamma/e}(y)$ = Flux of effectively real photons with energy fraction, y.

The scale, μ, is conventionally taken to be $\frac{1}{2}E_T^{Jet}$. The choice of scale at which $xG(x,\mu^2)$ is probed is unclear. The γg centre–of–mass energy is $\sqrt{\hat{s}} = 2E_T^{Jet}$ since both jets have equal pseudorapidity, so the scale must be chosen to be $\mu \propto E_T^{Jet}$. The gluon density is taken to have some simple functional form with few free parameters. The LO cross–section is then fitted to the data by adjusting the free parameters. Figure 2.9 shows the preliminary gluon density results extracted from dijet events collected at ZEUS during the 1994 running period with various parton parameterisations. Because the gluon density is probed only down to $x \approx 10^{-2}$, all the structure functions lie well within the error bars in this well known kinematical region.

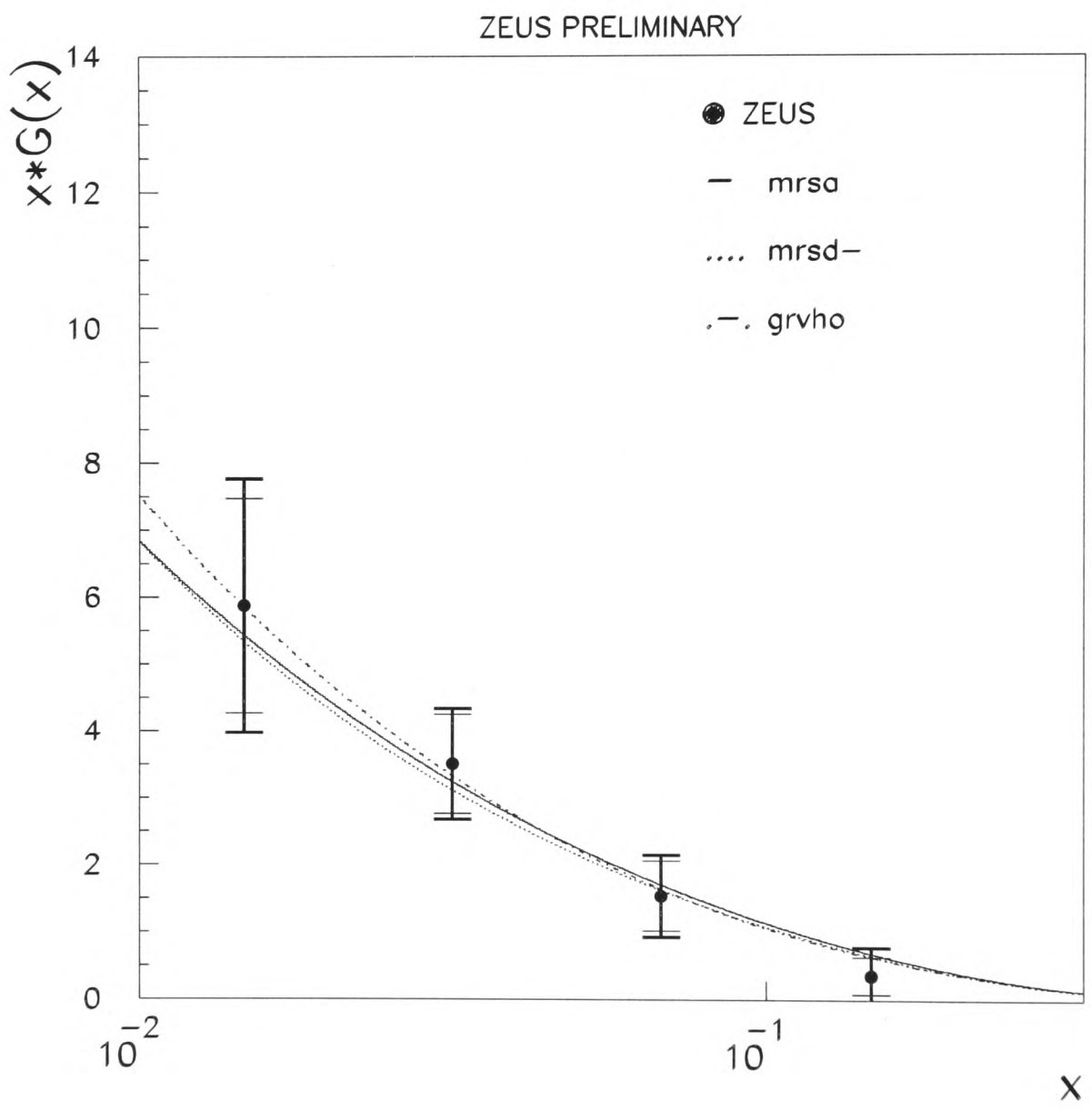

Figure 2.9: The preliminary results for the gluon density in the proton extracted from fits to the dijet differential cross–section measured at ZEUS in 1994. The thick and thin error bars show the statistical and systematic errors respectively. Various parameterisations of the gluon density are also shown and the measured results do not distinguish between them.

2.5.4 Elastic J/ψ photoproduction

Elastic J/ψ photoproduction ($ep \rightarrow ep\,J/\psi$) has been described [11, 12, 13] as a sequence of three distinct events as illustrated in figure 2.10. Firstly, the photon fluctuates into a $c\bar{c}$ pair. The $c\bar{c}$ pair then scatters off the proton via the exchange of two gluons in a colour singlet state. Finally, the scattered $c\bar{c}$ pair turns into a J/ψ vector meson.

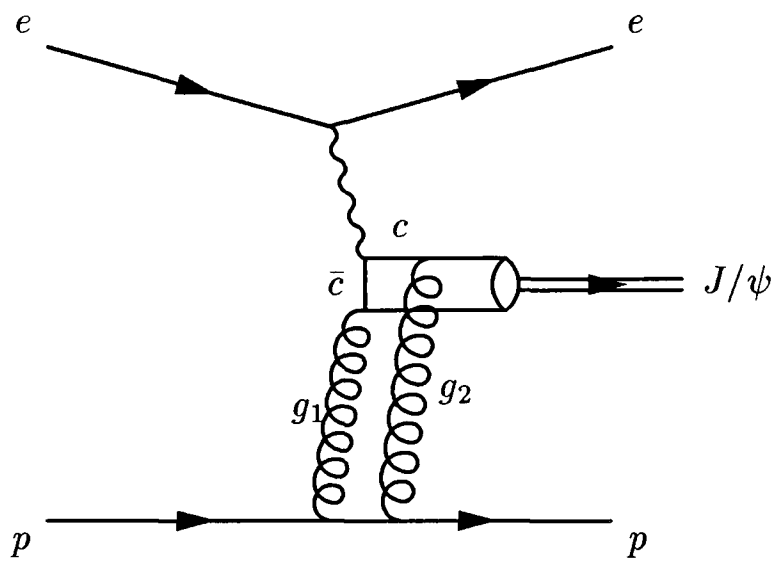

Figure 2.10: Elastic J/ψ photoproduction shown as a three stage process. The photon fluctuates into a $c\bar{c}$ pair which couples with the proton via exchange of two gluons. The J/ψ is then formed after the scattering has occured.

The cross–section calculated according to this model [11] is found to be proportional to the square of the gluon density in the proton:

$$\sigma(\gamma p \rightarrow J/\psi\, p) \propto \left[x_g G(x_g, Q^2)\right]^2 \tag{2.26}$$

The cross–section is therefore very sensitive to the gluon density. The range $\sim 10^{-3.5} < x_g < 10^{-2}$ is probed at $Q^2 = \mathcal{O}(M^2_{J/\psi})$. Both the ZEUS and H1 collaborations have published measurements on the gluon density in this x_g range with Q^2= 20 GeV^2 [14]. Figure 2.11 shows the gluon density extracted from the 1994 elastic J/ψ sample at ZEUS measured at $Q^2 = 2.5$ GeV^2. Also shown are the LO and NLO ZEUS results from the F_2 scaling violations described above, evolved back to $Q^2 = 2.5$ GeV^2 for comparison.

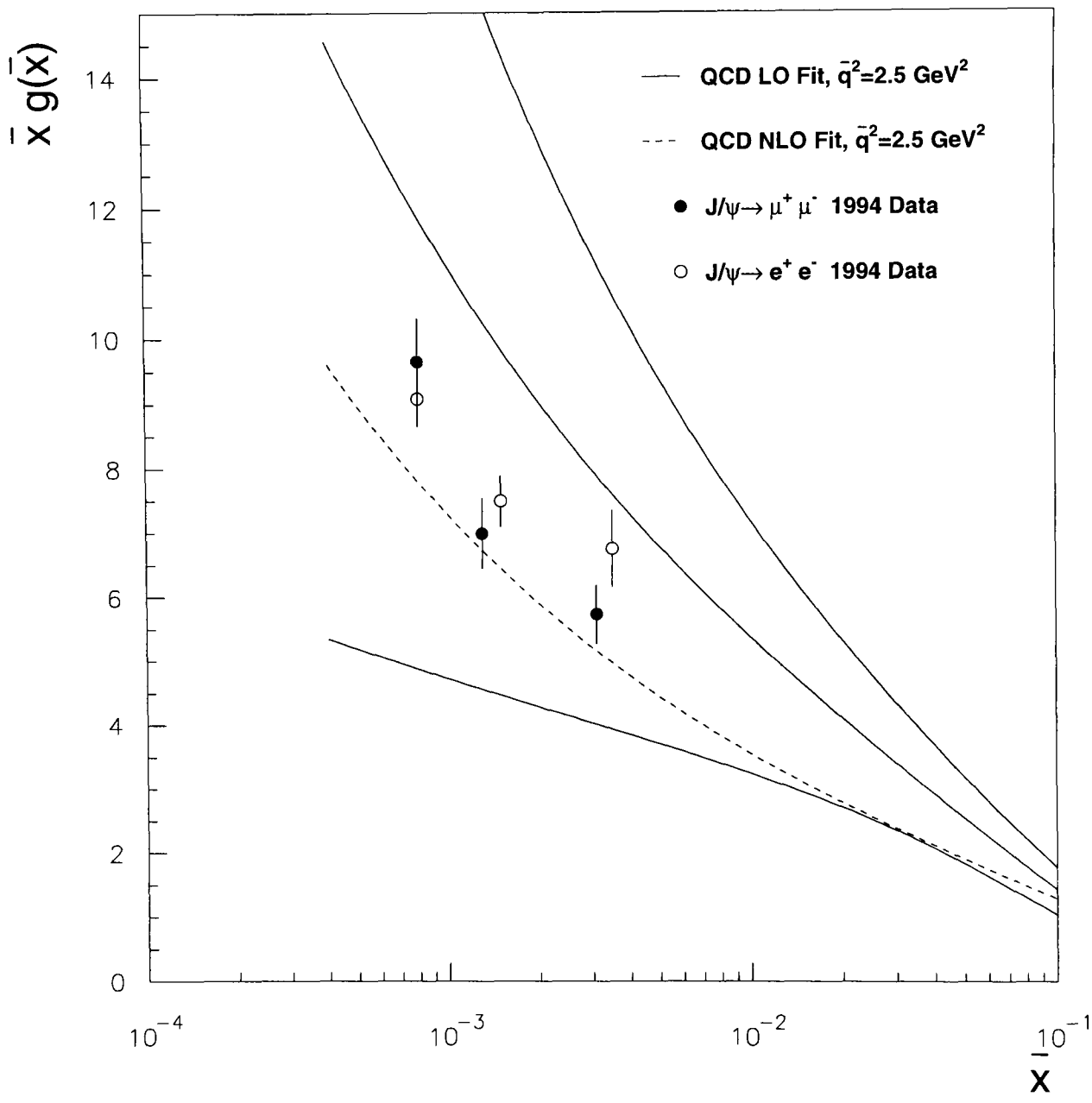

Figure 2.11: The gluon density in the proton extracted from the ZEUS 1994 elastic J/ψ sample. The errors are purely statistical. The dashed line shows the gluon density obtained from a NLO fit to the ZEUS F_2 data. The three solid lines show the upper, central and lower limits for the gluon density obtained from a LO fit to the ZEUS F_2 data.

2.5.5 Heavy flavour production

With a design luminosity of 100 pb^{-1}/year (3 pb^{-1} collected by ZEUS in 1994), there are expected to be around 10^8 $c\bar{c}$ pairs/year produced at HERA (and 10^6 $b\bar{b}$ pairs/year) via the mechanism shown in figure 2.5. This provides a possibility to measure the gluon density in the proton directly. This thesis concentrates on inelastic J/ψ photoproduction and in the final chapter, a method used to extract the gluon density using inelastic J/ψ events will be described and an attempt will be made to extract the gluon density using inelastic J/ψ's obtained from the ZEUS data.

2.6 Properties of the J/ψ meson and some production mechanisms

This section will begin with a brief reminder of the properties of the J/ψ followed by possible production mechanisms in electron–proton collisions at HERA.

2.6.1 The decay modes of J/ψ

The J/ψ meson is the 1^3S bound $c\bar{c}$ state with spin–parity $J^P = 1^-$. It has a mass $M_{J/\psi} = 3096.88 \pm 0.04$ MeV and a full width $\Gamma = 88 \pm 5$ keV [15]. In contrast, the $\psi''(3770)$ has a much larger full width of $\Gamma = 23.6 \pm 2.7$ MeV, decaying dominantly to two charmed mesons such as $D^+(c\bar{u})$ and $D^-(\bar{c}u)$ as shown in figure 2.12a. The narrow width of the J/ψ is due to the fact that it is forbidden to decay into two charmed mesons by the conservation of energy since $M_{J/\psi} < 2m_D$ ($m_D = 1864.6 \pm 0.5$ MeV). Likewise, the 2^3S excited state of the $c\bar{c}$ system, the $\psi'(3686)$, lies just below the mass threshold to decay into two charmed mesons. It also has a much narrower full width than the ψ'' of $\Gamma = 277 \pm 31$ keV.

Therefore, the J/ψ can only decay via the strong interaction into a colourless combination of non-charmed mesons such as $J/\psi \rightarrow \pi^+\pi^o\pi^-$. as shown in figure 2.12b. However, such decays are suppressed by the 'Zweig rule' which asserts that disconnected quark lines are highly suppressed relative to connected ones. The origin of this rule lies in the fact that all mesons are colour singlet states and so the connection between the initial and final quark states in QCD must be via a colour singlet gluon combination. Therefore, at least two gluons must be exchanged. However, the J/ψ has a charge conjugation quantum number, $C = -1$ and so there must be an odd number of gluons exchanged (which also have charge conjugation number, $C = -1$). Thus a three gluon exchange is the simplest possibility giving an α_s^3 term in the full width. However, the large mass of the J/ψ assists decays into the much lighter pions by providing a large available phase space.

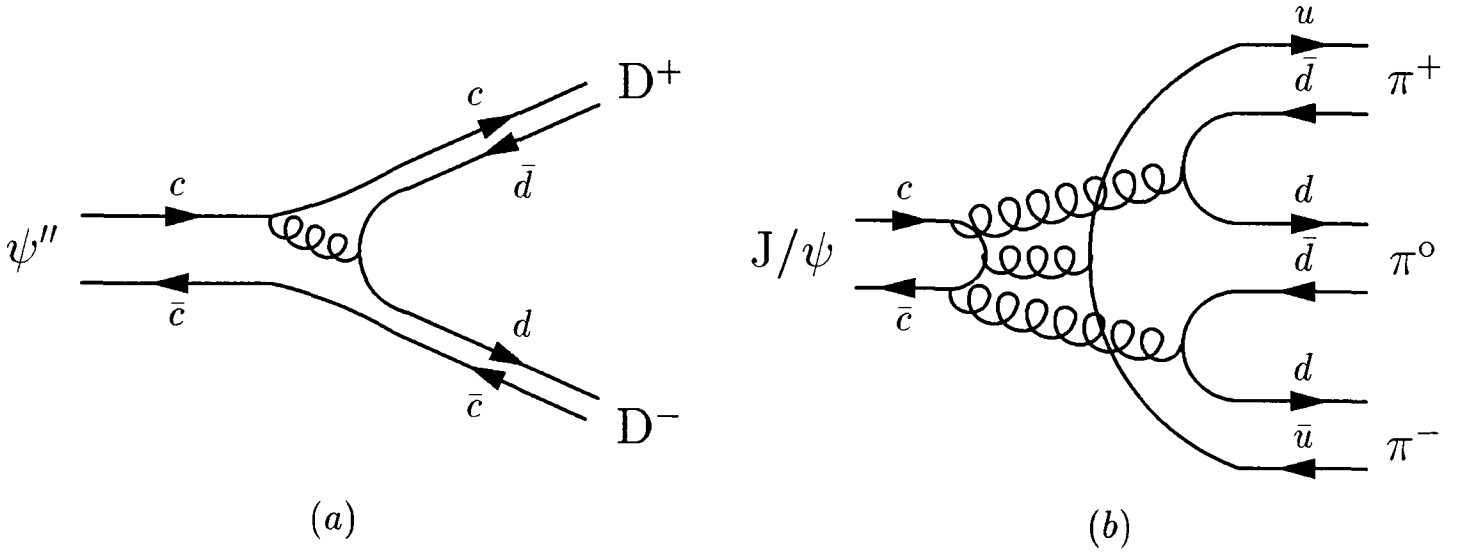

Figure 2.12: a) The dominant decay mode of the $\psi''(3770)$ into two charmed mesons such as $D^+(c\bar{u})$ and $D^-(\bar{c}u)$. b) Strong decay of the J/ψ is Zweig suppressed and the lowest order strong decay is via the exchange of three gluons.

The J/ψ can also decay electromagnetically, annihilating into a virtual photon which can then hadronize or decay into a lepton–antilepton pair (except the $\tau^+\tau^-$ pair which is above the mass threshold). The decay modes and branching fractions are summarised in table 2.1.

J/ψ(1S) decay modes	Branching fractions (Γ_i/Γ)
hadrons	$(86.0 \pm 2.0)\%$
virtual $\gamma \rightarrow$ hadrons	$(17.0 \pm 2.0)\%$
e^+e^-	$(5.99 \pm 0.25)\%$
$\mu^+\mu^-$	$(5.99 \pm 0.25)\%$

Table 2.1: Decay modes and branching fractions of J/ψ.

2.6.2 J/ψ production mechanisms at HERA

At HERA, J/ψ's are expected to be produced from the interaction of the incident proton and an exchanged virtual photon. At centre–of–mass energies $W_{\gamma p} \leq 15$ GeV, the four production mechanisms listed below in equations 2.27 – 2.30 have been observed by photo– and muon–production experiments [16] – [21]. The basic processes are illustrated in figures 2.13 – 2.16.

- **Beam and target elastic (elastic):**

$$\gamma + p \rightarrow J/\psi + p \tag{2.27}$$

- **Beam elastic and target inelastic (diffractive dissociative):**

$$\gamma + p \rightarrow J/\psi + X \tag{2.28}$$

- **Beam inelastic and target elastic (diffractive inelastic):**

$$\gamma + p \rightarrow J/\psi + X + p \tag{2.29}$$

- **Beam and target inelastic (direct inelastic):**

$$\gamma + p \rightarrow J/\psi + X \tag{2.30}$$

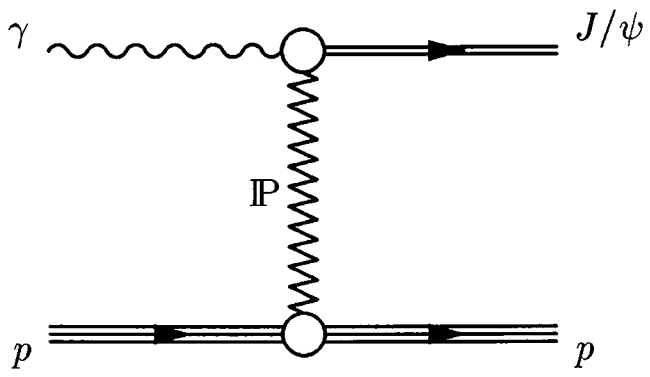

Figure 2.13: Diagram of the beam and target elastic (elastic) production mechanism.

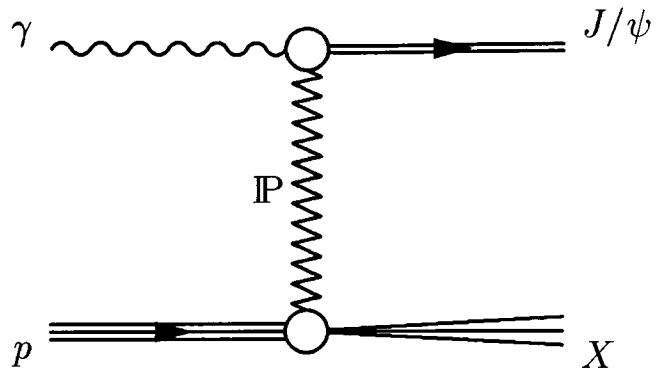

Figure 2.14: Diagram of the beam elastic, target inelastic (diffractive dissociative) production mechanism.

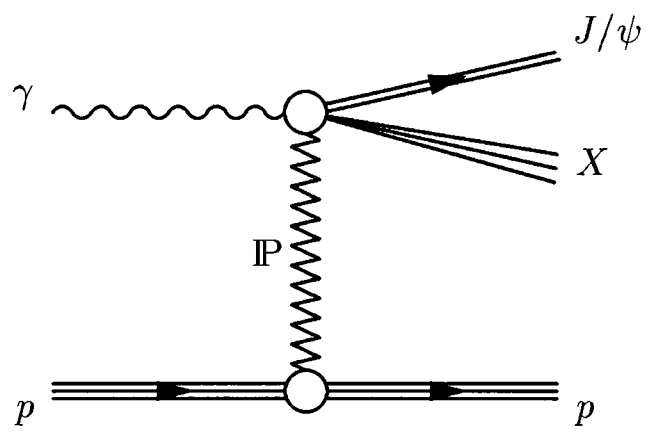

Figure 2.15: Diagram of the beam inelastic, target elastic (diffractive inelastic) production mechanism.

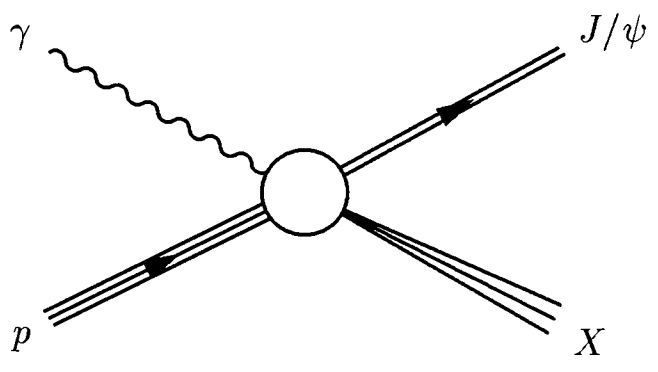

Figure 2.16: Diagram of the beam and target inelastic (direct inelastic) production mechanism.

A possible model for the diffractive inelastic process is illustrated in figure 2.17. The photon–gluon–fusion mechanism for the direct inelastic process is shown in figure 2.18. This analysis will concentrate heavily on the latter production mechanism and in the final chapter, an attempt will be made to extract the gluon density from within the proton using direct inelastic J/ψ events.

At the higher energies attainable at HERA, additional inelastic production mechanisms will become important. For example, a low Q^2 photon will not only couple

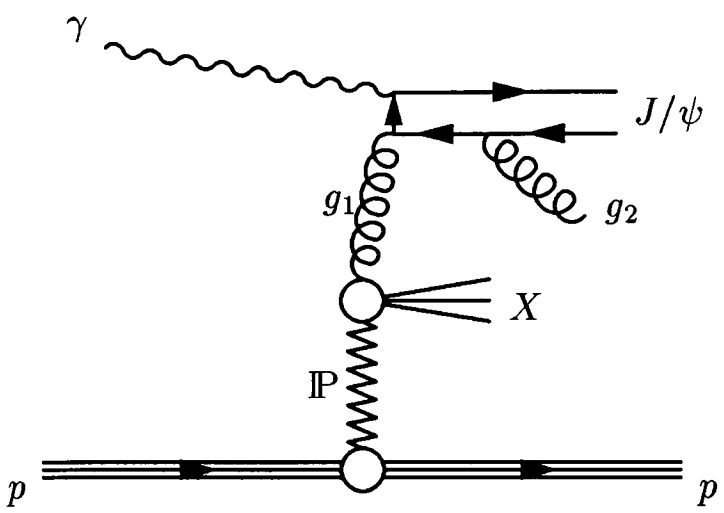

Figure 2.17: Diagram showing a possible model for the diffractive inelastic production mechanism.

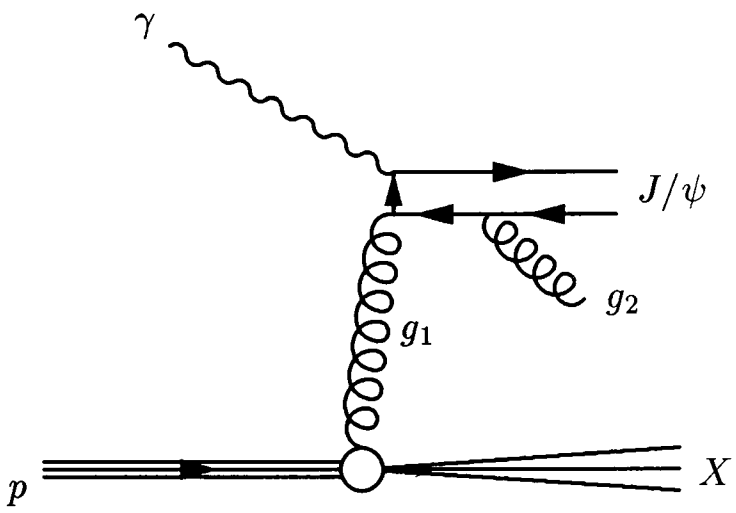

Figure 2.18: Diagram showing a possible model for the direct inelastic production mechanism.

directly with the partons in the proton, but it may also behave like a hadron giving rise to the 'resolved photon' contributions. In these processes, the virtual gluons or quarks in the photon interact to form the J/ψ and their contribution is expected to increase rapidly with centre–of–mass energy. The diagram for one such process (see equation 2.31) is illustrated in figure 2.19. Listed below are some other possible J/ψ production mechanisms:

- **resolved photon contributions: direct J/ψ production**

$$g + g \rightarrow J/\psi + g \tag{2.31}$$

$$g + g \rightarrow J/\psi + \gamma \tag{2.32}$$

- **resolved photon contributions: χ decays**

$$\begin{aligned} g + g \rightarrow \quad & \chi_{0,2} \quad \rightarrow J/\psi + \gamma \\ (gg, q\bar{q}) \rightarrow \quad & \chi \quad (\rightarrow J/\psi + \gamma) + g \\ gq \rightarrow \quad & \chi \quad (\rightarrow J/\psi + \gamma) + q \end{aligned} \tag{2.33}$$

- **two photon contributions:**

$$\gamma + \gamma \rightarrow \chi_{0,2}(\rightarrow J/\psi + \gamma) \tag{2.34}$$

- **b decays:**

$$(\gamma, g) + g \rightarrow b\bar{b} \rightarrow J/\psi + X \tag{2.35}$$

- **double charm production:**

$$(\gamma, g) + g \rightarrow J/\psi + c\bar{c} \tag{2.36}$$

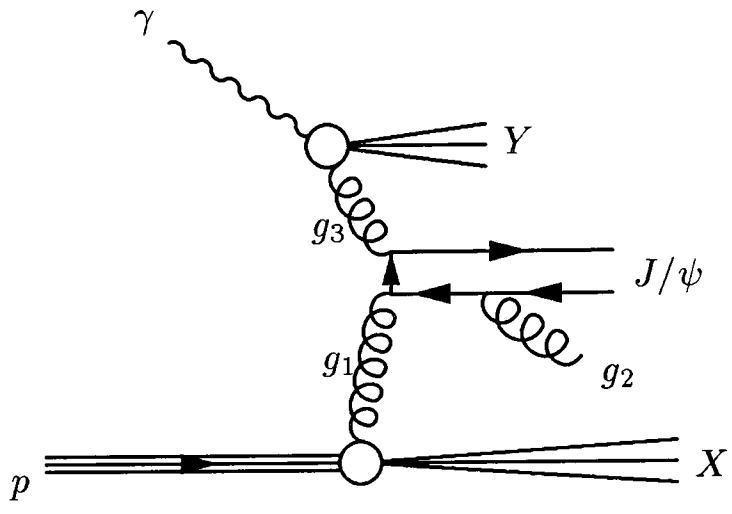

Figure 2.19: Diagram showing a resolved photon process where the gluon content of the photon interacts with the gluon in the proton. The subsequent colour flows between the states X, Y and g_2 are not shown. If the gluons g_1 and g_3 are in a colour singlet state, the final gluon, g_2 will not be emitted.

2.7 Summary

This chapter has discussed the Quark Parton Model, Quantum Chromodynamics and has described some of the approaches possible at HERA, to extract the gluon density in the proton. The J/ψ has been introduced with various production mechanisms possible at HERA.

It will be interesting to compare the results from the different extraction methods which will provide a test of QCD and the universality of the gluon density. The rest of this thesis will be concerned with obtaining a sample of J/ψ events from the data taken at HERA. In the final chapter of this thesis, an attempt will be made to extract the gluon density using a sample of inelastic J/ψ events.

Chapter 3

Searching for $J/\psi \to e^+e^-$

This chapter will describe the kinematics of J/ψ production and the methods for extracting the kinematical variables from the data. This thesis is concerned with J/ψ's decaying via the electron channel. Methods for identifying electrons and possible backgrounds will be discussed. Finally, the Monte Carlo generators used in this analysis will be described.

3.1 Kinematics of J/ψ production

For J/ψ production, the four–momenta are defined as:

$$e(l) + p(p) \longrightarrow e(l') + J/\psi(p_{J/\psi}) + X(p_X) \tag{3.1}$$

The event is described by the variables defined in section 2.1:

$$E_e; \qquad E_p; \qquad q = l - l'; \qquad Q^2 = -q^2; \qquad s = (p+l)^2; \qquad y = \frac{p.q}{p.l} \tag{3.2}$$

where E_e and E_p are the initial electron and proton energies respectively, q is the four–momentum transfer and $\sqrt{s}$ is the total centre–of–mass energy. The sub-process $\gamma + p \to J/\psi + X$ is described by the variables:

$$s_{\gamma p} = W^2 = (p+q)^2; \qquad M^2 = p_X^2; \qquad z = \frac{p.p_{J/\psi}}{p.q} \tag{3.3}$$

where z is the elasticity variable, so–called because it is a measure of the elasticity of the scattering off the proton. For the elastic J/ψ production mechanism in equation 2.27 and figure 2.13, the colourless object emitted from the proton carries little four–momentum, the proton remains intact. The four–momentum of the J/ψ comes mainly from the virtual photon: $p_{J/\psi} \approx q$ and $z \approx 1$. In contrast, for the direct inelastic J/ψ production mechanism in equation 2.30 and figure 2.18, the incident proton breaks up emitting a gluon. Since the proton is boosted in the forward direction in the laboratory frame, the emitted gluon will also be going forward. The four–momentum of this gluon contributes to the four–momentum of the J/ψ in the forward direction and the larger this contribution, the smaller the elasticity, z.

3.2 Reconstruction of kinematic variables in photoproduction

We will be looking at J/ψ's in direct photoproduction (with $Q^2 \approx 0$) where the scattered electron will usually be lost down the beam pipe making it impossible to measure its four–momentum (a small percentage of scattered electrons may be tagged by the LUMI[1] detectors). Other methods of reconstructing some of the above quantities used in this analysis will therefore be required.

To reconstruct the γp centre–of–mass energy, W, we first of all neglect the proton mass and assume $Q^2 = 0$. Then:

$$W^2 = (p+q)^2 \approx 2p.q = 2E_p(E - p_z)_\gamma$$

since $p = (E_p, 0, 0, E_p)$. However, the photon $(E - p_z)$ is precisely equal to the total $(E - p_z)$ of the γp system before the photon–proton interaction as the proton has zero

[1]The LUMI detector is described in section 1.6.

$(E - p_z)$. Since $(E - p_z)$ is conserved in the interaction, then $(E - p_z)_\gamma$ is equivalent to the total $(E - p_z)$ after the interaction, assuming of course, that the scattered electron is lost down the beam pipe and so does not contribute to $(E - p_z)_{total}$. So, we are left with:

$$W^2 \approx 2E_p(E - p_z)_{total} \tag{3.4}$$

Having established $p.q = E_p(E - p_z)_{total}$, it is now apparent that:

$$z = \frac{p.p_{J/\psi}}{p.q} = \frac{(E - p_z)_{J/\psi}}{(E - p_z)_{total}} \tag{3.5}$$

$$y = \frac{p.q}{p.l} = \frac{(E - p_z)_{total}}{2E_e} \tag{3.6}$$

3.3 Track reconstruction

The analysis presented in this thesis relies heavily on the detection and measurement of the charged electron[2] tracks from the decay of the J/ψ.

The algorithm VCTRAK [22] reconstructs tracks using hits in the vertex detector and axial superlayers of the CTD. It begins by taking hits in the outer axial superlayer of the CTD and guiding the trajectory inwards using a virtual hit at $x = y = 0$ and gathering other hits along the trajectory. The resulting trajectory is circular in the xy plane. This procedure is repeated to look for further tracks amongst the remaining hits.

The second stage of the algorithm then involves taking the inner hits of each trajectory and extrapolating a track outwards in three dimensions using the full z–by–timing and stereo hit information. An ideal helix is formed, allowing the track momentum to be determined. The error on the track parameters is calculated by considering the distance between this ideal helix and the hits associated to the particular track.

[2]The term 'electron' will be used in a loose sense throughout this thesis to refer to both the decay electrons and positrons from the J/ψ, since they both behave identically in the detector aside from bending in opposite directions in the magnetic field of the CTD.

3.4 Electron identification

Since the analysis presented in this thesis studies the J/ψ decaying in the electron channel, it is important to be able to identify electrons in the detector. In this section, some of the variables used to identify electromagnetic energy deposits in the calorimeter are introduced. A neural network based electron finder which looks at all aspects including the shape of these energy deposits will be described in the next chapter. In section 3.5, the energy loss of charged particles passing through matter by ionisation will be described. This provides an independent means of identifying charged particles and in particular electrons, by measuring the amount of ionisation along their tracks.

The energy deposited by electromagnetic objects in the calorimeter tend to be more compact than those deposited by hadronic objects of the same energy. In this analysis, loose cuts will be made on the size of these energy deposits for the candidate decay electrons to reject obvious non–electromagnetic clusters. The definitions of the quantities used to measure the size of the deposits will now be given.

Consider an energy deposit consisting on n cells with position vectors $\mathbf{r}_i$ and energies E_i for $i = 1, ..n$. The shower radius of the energy deposit is defined as the energy weighted rms radius of the deposit:

$$\text{Shower radius} = \sqrt{\left(\frac{\sum_i E_i\, \mathbf{r}_i^2}{\sum_i E_i}\right) - \left(\frac{\sum_i E_i\, \mathbf{r}_i}{\sum_i E_i}\right)^2} \tag{3.7}$$

Suppose the energy deposit has an energy weighted centre $\mathbf{R}$, then the shower length is defined as the energy weighted rms distance of all the cells belonging to the deposit from the energy weighted centre:

$$\text{Shower length} = \sqrt{\left(\frac{\sum_i E_i\, |\mathbf{r}_i - \mathbf{R}|^2}{\sum_i E_i}\right)} \qquad \text{where :} \quad \mathbf{R} = \frac{\sum_i E_i\, \mathbf{r}_i}{\sum_i E_i} \tag{3.8}$$

Finally, we define a cylindrical coordinate system where the z–axis is along the vector from the interaction vertex to the energy weighted centre, $\mathbf{R}$, of the energy deposit. The x and y axes are arbitrary. We convert the coordinates of all cells in the deposit to this new cylindrical coordinate system, (ρ_i, θ_i, z_i) and define the shower width of the deposit as:

$$\text{Shower width} = \sqrt{2\pi} \times \frac{\sum_i E_i \, \rho_i}{\sum_i E_i} \tag{3.9}$$

3.5 Interaction of charged particles with matter

3.5.1 Ionisation loss of charged particles

This section deals with the energy loss of charged particles through matter. This energy loss is not only dependent on the energy of the particles, but also on the type of particle. Therefore, by measuring the energy loss of particles along their tracks, it is possible to identify them. This will be a very useful tool in the analysis presented in this thesis.

Charged particles traversing a medium, lose energy by exciting or ionising the atoms in the medium. The Bethe–Bloch formula[3] for the mean rate of energy loss of a charged particle is derived using quantum mechanics, taking into account the wave nature of the particle and the discrete nature of the energy transferred between the particle and the atomic electrons in the medium:

$$\frac{dE}{dx} = \frac{4\pi n_e z^2 e^4}{m_e v^2} \left[ln \left(\frac{2m_e c^2 \beta^2 \gamma^2}{I} \right) - \beta^2 \right] \tag{3.10}$$

[3] A semi–classical derivation of the Bethe–Bloch formula is given in [23] and [24].

where :	m_e	=	Electron mass
	z	=	Charge of incident particle in units of e
	v	=	Speed of incident particle
	β	=	v/c
	γ	=	$(1-\beta^2)^{-1/2}$
	n_e	=	Number of atomic electrons per unit volume
	I	=	Mean ionisation potential per electron

The mean ionisation potential per electron, I, depends on the atomic number, Z, of the atoms in the material, but it can be approximated for atoms with atomic number greater than around 20 by $I/Z \simeq 10$ eV.

As expected for an electromagnetic interaction, the energy loss is dependent only on the charge, ze, and speed, v, of the incident particle and independent of its mass M.

At non–relativistic energies, $\gamma \rightarrow 1$ and $\beta \rightarrow 0$ so that $\frac{dE}{dx} \sim \frac{1}{v^2}$. As the particle energy increases into the relativistic regime, the $ln\,\gamma$ term in equation 3.10 begins to dominate and the $\frac{dE}{dx}$ value passes through a minimum at around $\beta\gamma = p/Mc \sim 3$ and rises logarithmically thereafter. This rise is associated with the fact that the transverse electric field of the particle is proportional to γ and so distant collisions become more important with increasing energy.

The relativistic rise does not continue indefinitely. The Bethe–Bloch equation considers the interaction of the incident particle with an isolated atom. However, there is an upper limit imposed on the impact parameter due to the screening of the incident particle's electric field by the atomic electrons. A theory of this dielectric screening has been developed by Fermi [25] and it is affected by the density of the medium. It causes the energy loss to become constant at very large γ, a region known as the Fermi

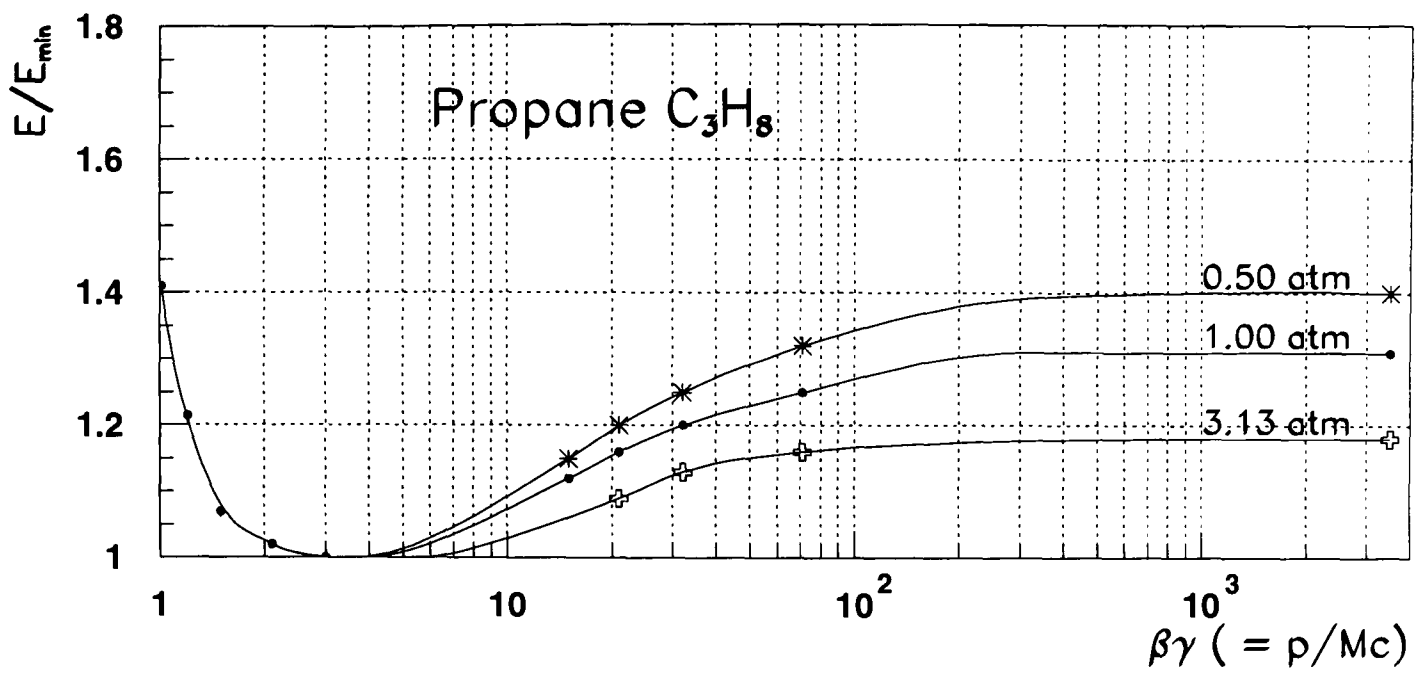

Figure 3.1: Measured mean energy losses in propane as a function of $\beta\gamma$ at various gas pressures.

plateau. Equation 3.11 is a modified version of the Bethe–Bloch equation which takes this density effect into account with an additional correction factor, $\delta(\gamma)$. Sternheimer [26] – [28] has developed a successful model for calculating $\delta(\gamma)$ in terms of the atomic properties of the medium.

$$\frac{dE}{dx} = \frac{4\pi n_e z^2 e^4}{m_e v^2}\left[ln\left(\frac{2m_e c^2\beta^2\gamma^2}{I}\right) - \beta^2 - \frac{\delta(\gamma)}{2}\right] \tag{3.11}$$

Measurements [29] of $\frac{dE}{dx}$ values in propane as a function of $\beta\gamma(= p/Mc)$ at various gas pressures are shown in figure 3.1. The $\frac{1}{v^2}$ drop is seen at low momenta followed by the minimum at $\beta\gamma \sim 3$ and then the relativistic rise which flattens off at very relativistic velocities. Note that the plateau value of $\frac{dE}{dx}$ at these very high energies decreases with increasing pressure due to the density effect. The ionisation losses of high energy protons and pions in high pressure hydrogen gas have also been measured [30] and have shown that the energy loss in the Fermi plateau region remains constant for γ values up to 1800.

The equation for the ionisation energy loss of charged particles is slightly different for

electrons because the Møller scattering cross–section of identical particles $e^-e^- \rightarrow e^-e^-$ must be used. However, for highly relativistic particles ($\beta \sim 1$), the equation for the energy loss is the same to first order.

The dependence of $\frac{dE}{dx}$ on $p/Mc = \beta\gamma$ allows particles of known momentum to be distinguished. For example, a 1 GeV electron and pion will have $\beta\gamma$ values of around 2000 and 7 respectively and so the $\frac{dE}{dx}$ value of the electron will lie on the Fermi plateau, whereas all other hadrons will be expected to have a lower $\frac{dE}{dx}$ value on the relativistically rising part of the curve.

In the ZEUS detector, the $\frac{dE}{dx}$ value of charged particles is measured in the CTD by measuring the pulse heights on the chamber wires and taking a truncated mean of these values. This involves discarding the largest 40% or so of the pulse heights and taking the average of the remainder. This method is used because the pulse heights are expected to follow a Landau distribution with a long high energy loss tail and taking the truncated mean is found to give a better resolution than averaging all the data.

3.5.2 Bremsstrahlung

Electrons lose energy in matter by exciting or ionising the atoms in the medium just as heavier charged particles do. However, because of their small mass, the main source of energy loss for high energy relativistic electrons encountered at HERA, is from the production of radiation in a process known as bremsstrahlung or synchrotron radiation for circular acceleration.

In the electron decay channel of the J/ψ the two decay electrons each have a momentum of $\frac{1}{2}M_{J/\psi}$ (ignoring the electron mass) in the J/ψ rest frame and are highly relativistic. It is therefore necessary to consider bremsstrahlung of the decay electrons

when their invariant mass is calculated in an attempt to reconstruct the J/ψ mass. It will be seen in chapters 5 and 6 that a tail in the e^+e^- invariant mass is seen due to bremsstrahlung of the decay electrons.

A semi–classical approach to the bremsstrahlung cross section is given in [24]. The cross section is calculated to be:

$$\frac{d\sigma}{dk} \simeq 5\,\frac{e^2}{\hbar c}\,z^4 Z^2 \left(\frac{m_e c}{Mv}\right)^2 \frac{r_e}{k}\,ln\left(\frac{Mv^2\gamma^2}{k}\right) \tag{3.12}$$

where : k = Wavenumber of radiation

Z = Atomic number of atoms in the material

M = Mass of incident particle

r_e = Classical radius of electron $(= e^2/mc^2)$

It is seen that the bremsstrahlung cross section varies inversely with the square of the particle mass, M, and so at HERA energies, this radiation loss has only been an important factor for electrons. The cross section falls off with increasing photon energy approximately as $1/k$. This would imply that the cross section for low energy photon production increases without limit as $k \rightarrow 0$. This infrared divergence does not in fact occur since equation 3.12 is not valid in this limit.

It is also seen in equation 3.12 that the cross section depends on the medium through the factor Z^2. There are Z atomic electrons per atom and so their contribution to the bremsstrahlung will vary as Z, whereas the contribution from the nuclei will vary as Z^2. Thus the bremsstrahlung cross section is dominated by interactions between the incident particle and the Coulomb field of the nuclei in all but the lightest elements. This is in contrast to the energy loss through ionisation, where the dominant interaction is with the electrons. The atomic electrons do however play an important role in bremsstrahlung

by screening the nuclear charge, thus limiting the effective charge seen by the incident particle.

At high energies, the mean angle of photon emission relative to the initial electron direction is found to be [31]:

$$\langle \theta_\gamma \rangle \simeq \frac{mc^2}{E} \tag{3.13}$$

where E is the initial electron energy. Thus, it is independent of the photon energy and most of the radiation lies inside a narrow cone round the electron direction with the cone becoming narrower as the electron energy increases.

The rate of energy loss due to bremsstrahlung is found to be proportional to the incident electron energy:

$$\left(\frac{dE}{dx}\right)_{rad.} = \frac{E}{X_o} \tag{3.14}$$

where X_o is defined as the radiation length of the particular medium.

Since the energy loss due to ionisation is approximately constant for fast electrons, there exists a critical electron energy, E_{crit}, where the energy loss due to ionisation and radiation are equal. The ratio of the radiation to ionisation energy loss is given approximately by:

$$\frac{\left(\frac{dE}{dx}\right)_{rad.}}{\left(\frac{dE}{dx}\right)_{ion.}} \simeq \frac{ZE}{1600mc^2} \tag{3.15}$$

so that:

$$E_{crit} \simeq \frac{1600}{Z}\, mc^2 \tag{3.16}$$

Taking Z to be around 20, $E_{crit} \sim 0.04$ GeV for electrons and ~ 10 GeV for the lightest of hadrons, the pions. Thus, at energies of a few GeV encountered at ZEUS, electrons predominantly lose energy in the CTD via radiation, whereas ionisation is the main source of energy loss for hadrons.

When the $\frac{dE}{dx}$ values of particles are measured at ZEUS, it is actually the ionisation energy loss which is measured by the pulse sizes on the sense wires of the CTD. The energy losses due to bremsstrahlung are not seen in this measurement. Due to the small mass of the electrons, they remain highly relativistic after bremsstrahlung and so their energy loss due to ionisation remains on the Fermi plateau. Therefore, the results in the previous section for identifying particles by measuring their energy loss, $\frac{dE}{dx}$ remain valid in spite of this extra source of energy loss.

3.6 Background from $\gamma \rightarrow e^+e^-$ conversions

Photons convert to e^+e^- pairs in material at a rate increasing with the number of radiation lengths of the material being traversed. In view of this, the beam pipe and inner walls of the CTD and VXD were made as thin as possible, however, the large number of photons from the $\pi^o \rightarrow 2\gamma$ decay and from bremsstrahlung of charged particles (mainly electrons) lead to a large number of conversion electrons. These provide a source of background in the search for $J/\psi \rightarrow e^+e^-$. However, the energy of photons produced in ep interactions is in general small, peaking at around 0.5 GeV. Therefore, the conversion electrons from a photon can usually only provide a background to the J/ψ signal when combined with a more energetic electron candidate not originating from a photon conversion to produce a reconstructed mass closer to that of the J/ψ at 3.1 GeV. The momentum spectrum of the conversion electrons peaks at zero and falls off rapidly. This is due to the energy spectrum of the photons which itself peaks at zero. A cut requiring a minimum transverse momentum of the two electron tracks is an effective method to remove most of the background from conversion electrons.

The algorithm CONVERT2 [32] was designed to identify photon conversions. A

fairly detailed description will be given here as it will be used in this analysis not only to remove conversion electrons, but also to select a clean source of electrons. Since the $\frac{dE}{dx}$ values of tracks are used extensively in this thesis to distinguish electromagnetic from hadronic charged tracks, this clean source of electrons from conversion photons will enable us to study the $\frac{dE}{dx}$ values of electron tracks and their variation with track momenta and other track variables.

All pairs of oppositely charged tracks are considered as photon conversion candidates and like–signed pairs are kept for background studies. The tracks are extrapolated back to their point of closest approach in the xy plane. The difference in polar angle, THDIF, is required to be less than 0.4 radians and the track separation in the xy plane, XYDIF, is required to be less than 1.0 cm. If both tracks have stereo[4] hits, these cuts are tightened to 0.1 radians and 0.4 cm respectively. A dimensionless quantity DistB is calculated for all track pairs passing these two cuts:

$$\text{DistB} = \sqrt{\left(\frac{\text{XYDIF}}{\sigma(xy)}\right)^2 + \left(\frac{\text{THDIF}}{\sigma(\theta)}\right)^2} \tag{3.17}$$

where $\sigma(xy)$ and $\sigma(\theta)$ are the rms xy and polar angle resolutions respectively estimated from data and Monte Carlo for two samples: both tracks with and without hits in the vertex detector (VXD).

Each track is combined with all the other tracks in the event and it is paired with the track giving the minimum DistB value. If the tracks are like–signed, the sign of DistB is reversed and the pair is saved for background studies.

The flag, IGCTAG, is used to select photon conversions into electron pairs. It is defined as follows:

[4]The stereo superlayers in the CTD are the even numbered ones inclined at a small angle to the beam axis. See section 1.3.1.

IGCTAG = 1: Electron pairs must satisfy |DistB|< 25 cm and have a conversion radius greater than 5 cm where the conversion radius is defined as the distance in the xy plane from the vertex to the point of conversion.

IGCTAG = 2: In addition to IGCTAG = 1, the event must come from the main vertex ($| z_{vertex} | < 50$ cm). The angle, θ, between the photon direction (reconstructed from the electron tracks) and the vector between the vertex and conversion point must satisfy $cos\,\theta > 0.95$ and when these two vectors are projected onto the xy plane, the angle between them, θ_{xy}, must also satisfy $\cos\,\theta_{xy} > 0.98$. Finally, no hits associated with the two tracks are allowed in the VXD if the conversion took place outside the VXD active area.

IGCTAG = 3: In addition to IGCTAG = 2, stereo hits and a $p_t > 50$ MeV are required for both tracks.

If none of the above conditions are met, the IGCTAG flag is set to zero. The CONVERT2 algorithm will be used in this analysis and cuts will be applied to both DistB and IGCTAG to select photon conversions and to reduce background.

3.7 Monte Carlo generators

Two Monte Carlo generators are used in the analysis presented in this thesis:

- **HERWIG:** [33] this is a general purpose event generator for high energy hadronic processes with a particular emphasis on the detailed simulation of QCD parton showers. It is capable of simulating hard lepton–lepton, lepton–hadron and

hadron–hadron scattering and soft hadron–hadron collisions. Heavy flavour production and decay with QCD coherence effects are included. HERWIG uses the Colour Singlet Model[5] to simulate direct γg interactions. Initial state radiation of the incoming gluon is included which tends to lower the production cross–section. The parton distributions for the proton can be chosen for the generator.

- **EPJPSI:** [34] this can generate J/ψ events through the resolved photon or the direct inelastic production mechanisms using the Colour Singlet Model. Elastic J/ψ events can also be generated via single pomeron exchange. Diffractive inelastic J/ψ events are generated by the exchange of one pomeron. The gluon content of the pomeron then interacts with the virtual photon. Again, the parton distributions in the proton (and in the photon for resolved processes) can be chosen.

In this analysis, the MRSD0′ and MRSD−′ proton structure functions will be used [35, 36]. These distributions are fitted to the high x ($> 10^{-2}$) muon and neutrino deep inelastic fixed target data from the NMC[37], CCFR[38] and CDHSW[39] experiments. The two structure functions are essentially identical in this high x region and they can only be distinguished by experiments such as HERA which probe to lower x regions. The gluon distributions at low x with the starting scale of evolution at $Q^2 = 4$ GeV, as predicted by these two structure functions vary as:

$$\text{MRSD0}' \quad : \quad x\,g(x) \sim x^{o}$$

$$\text{MRSD}-' \quad : \quad x\,g(x) \sim x^{-\frac{1}{2}}$$

[5]The Colour Singlet Model will be described in chapter 7.

The MRSD0′ and MRSD−′ forms for the low x behaviour arise from expectations of Regge theory[40] and BFKL[41, 42] respectively.

Chapter 4

Neural Network Electron Identification

4.1 Introduction

SINISTRA [43] is a neural network based electron finder developed for energies above 5 GeV. It is presently used to identify the scattered electron in the Deep Inelastic Scattering (DIS) analysis of the ZEUS data. By recognising showering properties in the segmented ZEUS calorimeter, it has been shown to be more efficient than current electron finders in this energy region. This chapter describes a study on the application of SINISTRA to the identification of isolated electrons in the lower energy region 0.5 – 7.0 GeV and the ability of SINISTRA to distinguish between electrons and pions which can often leave similar patterns of energy at these low particle energies.

At the time of writing, the standard calorimeter based electron finder used at ZEUS, known as LOCAL, was based on the lateral size of the calorimeter deposits and the ratio of energy deposited in the electromagnetic (EMC) section to the total energy in the deposit. This latter ratio peaks at unity for electromagnetic particles, whereas for hadrons, it peaks close to zero but extends up to unity. The overlap in the electromagnetic and hadronic distributions increases with decreasing particle energy. Similarly, the lateral

size of electromagnetic clusters is smaller than hadronic clusters, however, the separation in this lateral size also becomes less distinct with decreasing particle energy. As a result, the LOCAL electron finder was only designed to find electrons down to 2 GeV. It will be seen in the following chapters that the decay electrons from J/ψ produced via direct inelastic photoproduction at HERA typically have an energy distribution peaking at below 2 GeV. This was the motivation behind the development of an electron finder capable of separation down to 0.5 GeV.

This chapter begins with a description of the input parameters used to train the neural network. This is then followed by the theory of the neural network used in this study. To train the neural network, single electrons and pions were generated and passed through a detailed Monte Carlo of the ZEUS detector. The neural network was then trained to distinguish between them. The chapter is concluded with a description of a test of the neural network using a separate independent sample of Monte Carlo data and CERN test beam data.

4.2 Input for the neural network

The neural network functioned by recognising the characteristic patterns of energy deposits from electrons and pions in the ZEUS calorimeter. Therefore a method of defining the boundaries of any particular cluster was required.

The 'ISLANDS' algorithm is used by the low–energy neural network to identify individual clusters of energy deposits as in the higher energy regime (above 5 GeV). Each calorimeter tower has a pointer directed to the highest energy neighbouring tower. Each local maximum in tower energy forms the centre of a cluster. The cluster is then expanded by including all towers with pointers pointing towards the local maximum,

either directly, or indirectly via pointers of neighbouring towers. Therefore all towers in the calorimeter containing energy are included in one of the island clusters with single isolated energy towers forming their own islands. An example of the ISLANDS algorithm is shown in figure 4.1. The energies of towers in the calorimeter are shown and the algorithm groups them into two clusters. The two local maxima in tower energy are marked with an asterisk.

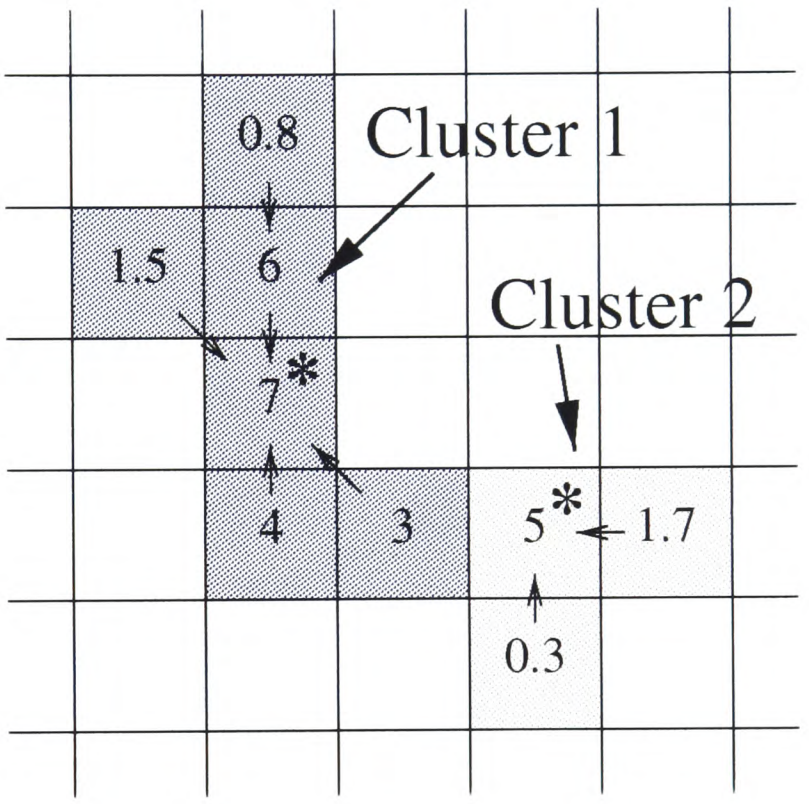

Figure 4.1: Example of the ISLANDS clustering. The energies of the towers in the calorimeter are shown together with pointers directed to the highest energy neighbour. Hence, the two local maxima in tower energy, marked with asterisks, have no pointers. Two ISLAND clusters are formed around these local maxima (shown shaded).

The input to the neural network has to consist of a large enough block of calorimeter towers so as to contain entire electromagnetic showers, but their size is limited by the requirement not to include neighbouring energy deposits from other particles. Each calorimeter tower measures 20 $\times$ 20 cm and it was found that most islands belonging to electromagnetic particles were contained within a 3 $\times$ 3 tower block and hence this was taken as the input for the neural network.

Each of these 3 × 3 blocks is centered around the centre of each island, found using the 'ELECPO' algorithm. This was designed to get the best position for electromagnetic showers by combining the positions of all the cells in the shower weighted by their individual energies.

In each of the towers in the RCAL, there are 6 photomultiplier tubes (PMT) whereas in the BCAL and FCAL, there are 12 tubes per tower. In order to achieve a single geometry for the whole calorimeter, the extra information provided by the FCAL and BCAL is reduced to the format of the RCAL as shown in figure 4.2. Thus, each block of 3×3 towers is described by 54 energy values.

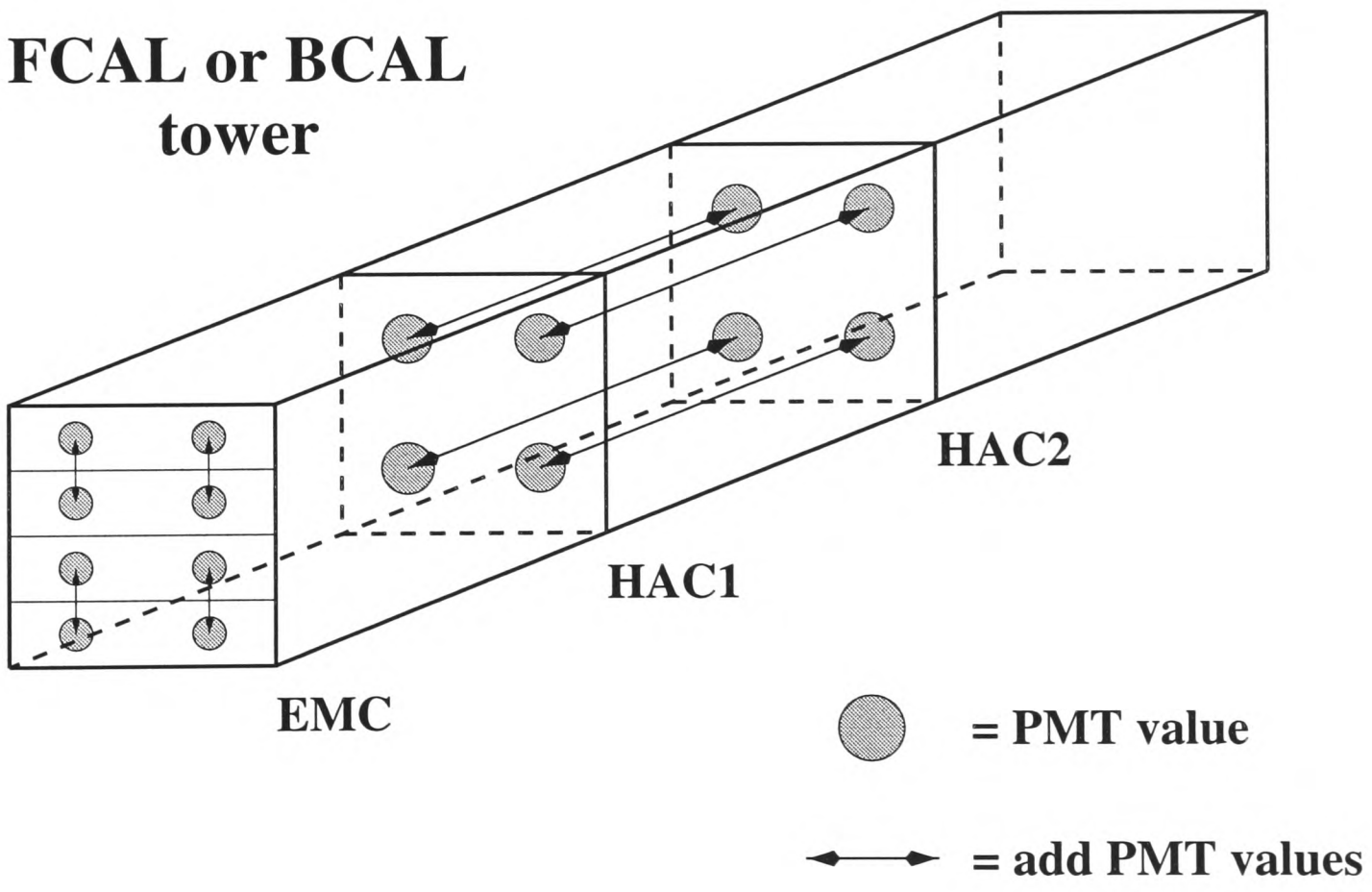

Figure 4.2: Schematic diagram showing the photomultiplier (PMT) measurements made in the FCAL and BCAL. These are reduced to the format of the RCAL for input to the neural network by adding the PMT values as shown.

The pattern of energy deposit in the calorimeter will also depend on a particle's angle of incidence into the calorimeter. The position **X**, of the energy weighted centre

of each island is found by summing over all cells in the island:

$$\mathbf{X} = \frac{\sum_{cells} E_{cell}\mathbf{X}_{cell}}{\sum_{cells} E_{cell}} \tag{4.1}$$

The angle of incidence of the island, α, is defined as the angle between the position vector $\mathbf{X}$ and the incident proton direction. The final input parameter for the neural network is then $cos(\alpha)$ for each island.

Therefore, there are 55 input values for the neural network consisting of 54 energy values and the cosine of the incident angle.

4.3 The Theory of Neural Networks

A neural network which projects L dimensions into a space of N dimensions ($L \gg N$) will be used in this analysis. In this case, there are 54 calorimeter energy values and the cosine of the incident angle giving a total of $L = 55$ input values to the neural network. Since we only want to separate electromagnetic and hadronic energy showers in the calorimeter, we have only the single output value from the neural network ($N = 1$).

The neural network first of all projects the L input values, represented by the vector $\mathbf{I}(L = 55)$, into M hidden variables ($M < L$) and these are in turn projected into the $N = 1$ output value. This neural network therefore has 3 *layers*. The M hidden variables remain unseen by the user as suggested by their name. They are represented by the vector $\mathbf{H}(M)$ and are chosen by the neural network to best separate between the different distributions. The neural network internally introduces a matrix B_{jk} which is used to define the M hidden variables as follows:

$$H_j = \sum_{k=1}^{55} B_{jk} I_k \qquad \forall j = 1, 2, \ldots M \tag{4.2}$$

Two further vectors $\mathbf{A}(M)$ and $\alpha(M)$ are introduced together with the parameters β and t. These are used to define the single output value, O, of the neural network which has a range of between -1 and $+1$ as seen in the following equation:

$$O = tanh\left(\frac{\sum_{j=1}^{M} A_j tanh\left(\frac{H_j - \alpha_j}{t}\right) - \beta}{t}\right) \tag{4.3}$$

The value of t is chosen so that the argument of the $tanh$ function is of the order unity. The vectors and matrices A_j, B_{jk}, α_j and the scalar β are initially chosen at random between $+1$ and -1 with the normalisation:

$$\sum_{j=1}^{M} A_j^2 = 1; \qquad \sum_{k=1}^{L} B_{jk}^2 = 1 \qquad \forall j \tag{4.4}$$

In this case, the neural network is used to separate electromagnetic and hadronic energy showers in the calorimeter, so a target vector, T, for the output value is defined as follows:

$$\begin{aligned} T = -1 \quad &: \quad \text{electromagnetic particles} \\ T = +1 \quad &: \quad \text{hadronic particles} \end{aligned}$$

Each input vector to the neural network is called a pattern. In this study, the neural network will be trained using 1000 electromagnetic and 1000 hadronic patterns giving 2000 patterns in total. There are therefore 2000 input vectors, $\mathbf{I}_p(L = 55)$ for $p = 1, 2, \ldots 2000$, and using equations 4.2 and 4.3, the corresponding 2000 output values O_p can be calculated.

The neural network achieves separation of electromagnetic and hadronic clusters by adjusting the degrees of freedom (A_j, B_{jk}, α_j, β and t) so as to minimise the error function, E, defined as follows:

$$E = \frac{1}{2}\sum_{p=1}^{2000}(O_p - T_p)^2 \tag{4.5}$$

where : E = Error function

O_p = Neural network output value for p^{th} pattern

T_p = Target vector for p^{th} pattern

The target vector, $T_p = -1$ or $+1$ depending on whether the pth pattern is the result of an electromagnetic or hadronic particle respectively. It can be seen from equation 4.5 that by choosing suitable degrees of freedom (A_j, B_{jk}, α_j, β and t) to minimise the error function, E, the output values of the 2000 patterns O_p are shifted towards their respective target vectors, T_p. For perfect separation between electromagnetic and hadronic objects, $E = 0$ and $O_p = T_p \quad (\forall p)$. However in practice, perfect separation is never achieved and for partial separation, the output vectors are distributed between -1 and $+1$ with the majority of electromagnetic patterns having $O_p < 0$ and the majority of hadronic patterns having $O_p > 0$.

The fractional error function, f, defined in equation 4.6, is obtained by dividing the error function by the number of patterns (in this case 2000). It will be used in the next section to monitor the training of the neural network.

$$f = \frac{E}{2000} \tag{4.6}$$

The parameter t in equation 4.3, known as the temperature of the neural network, should approach zero as the error function approaches the global minimum since as $t \to 0$ then the argument of the *tanh* function in equation 4.3 $\to \pm\infty$ and so $O_p \to \pm 1$. For perfect separation, the temperature $t = 0$.

4.4 Training and Testing the Neural Network

1000 single isolated electrons and 1000 single isolated pions with energies in the range 0.5 – 7.0 GeV were generated in all directions and passed through a detailed Monte

Carlo of the ZEUS detector. These were then used to train the neural network. The ratio of electrons to pions was chosen to be unity so as not to bias the training.

The temperature, t, and the fractional error function, f, were followed as the training progressed and they are plotted in figures 4.3a and b against the number of iterations of the neural network. The temperature, t, is seen to approach close to zero indicating a global minimum in the error function has been reached, but it never reaches zero indicating that perfect separation has not been achieved. The fractional error function, f, is seen to start at around 50% in accordance with the random starting parameters and then fall and stabilise after around 50 iterations to a non–zero value, again indicating the partial separation.

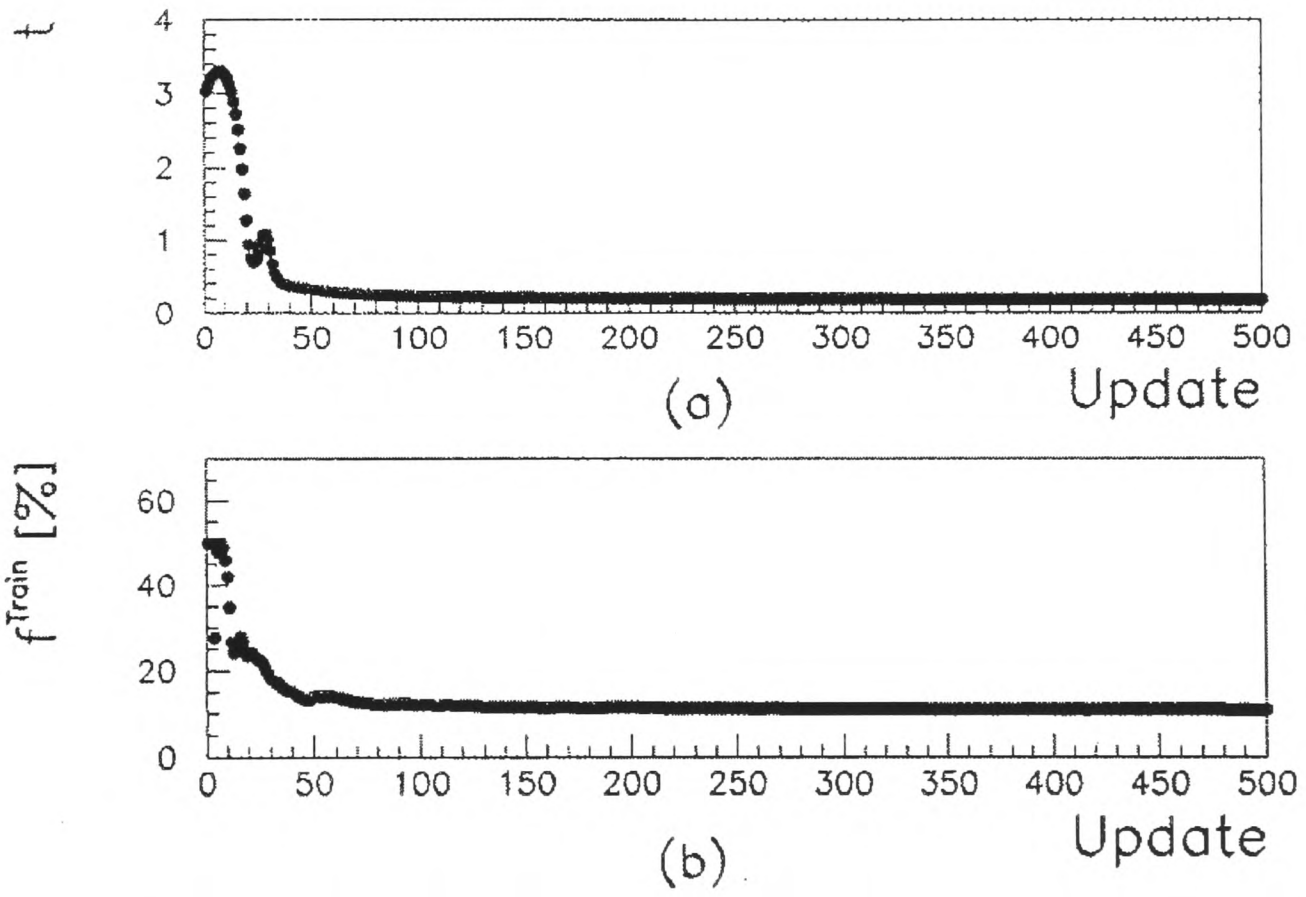

Figure 4.3: a) The temperature, t, and b) fractional error function, f of the neural network for the training sample plotted against the number of iterations.

Further independent sample of 1000 single isolated electrons and 1000 single isolated

pions were generated to test the trained neural network. The quantity δf is defined as the absolute difference in the number of mis–identified electrons in the test and training Monte Carlo samples divided by the square root of the number of patterns $= \sqrt{2000}$ (see equation 4.7). It therefore gives a measure of whether the training of the neural network is biased towards the training sample.

$$\delta f = \frac{|\text{No. mis}-\text{identified electrons in the test } - \text{ no. mis}-\text{identified in the training samples}}{\sqrt{\text{No. of patterns}}} \tag{4.7}$$

Assuming the probability of mis–identifying an electron is around 0.1 (this figure will be justified below), then one standard deviation in the number of mis–identified electrons would be of the order $\sqrt{2000 \times 0.9 \times 0.1} \simeq 13$. δf is plotted in figure 4.4 and it is seen that it falls to around 0.1 after 500 iterations and so the difference in the number of mis–identified electrons in the test and training samples is around $0.1 \times \sqrt{2000} \simeq 5$. This is well within one standard deviation and the trained neural network is not biased towards the training sample.

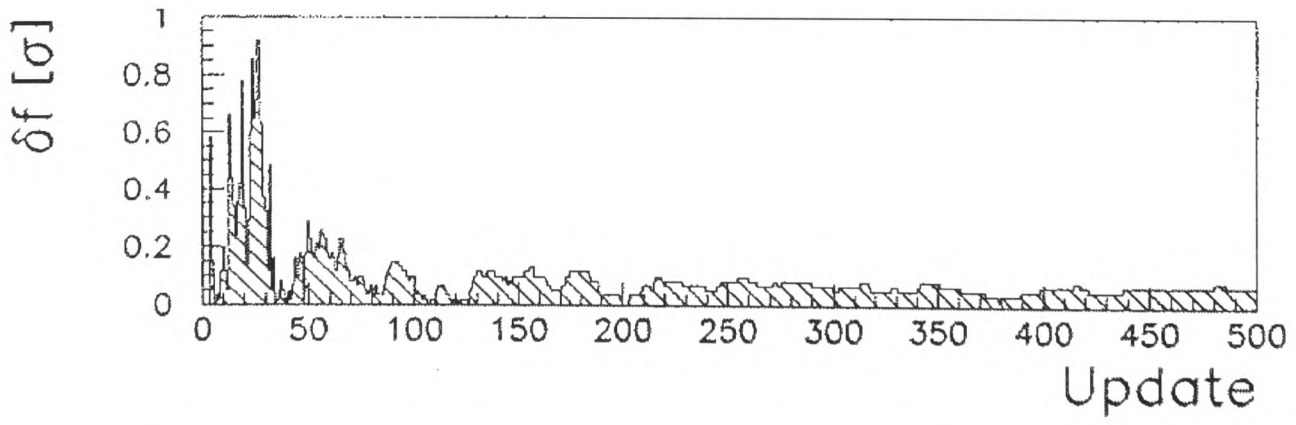

Figure 4.4: Plot of δf against the number of iterations for the test sample.

The neural network output value is plotted against the cluster energy for the electrons (in figure 4.5a) and pions (in figure 4.5b) in the test sample for cluster energies up to 5 GeV. A separation is seen between the electromagnetic and hadronic clusters

which becomes less distinct with decreasing cluster energy. This is seen more clearly in figures 4.6a and b, where the efficiency and purity (defined below) are plotted in bins of cluster energy.

$$\text{Efficiency} = \frac{\text{No. of correctly identified electrons}}{\text{Total no. of electrons}} \tag{4.8}$$

$$\text{Purity} = \frac{\text{No. of correctly identified electrons}}{\text{Total no. of clusters identified as electrons}} \tag{4.9}$$

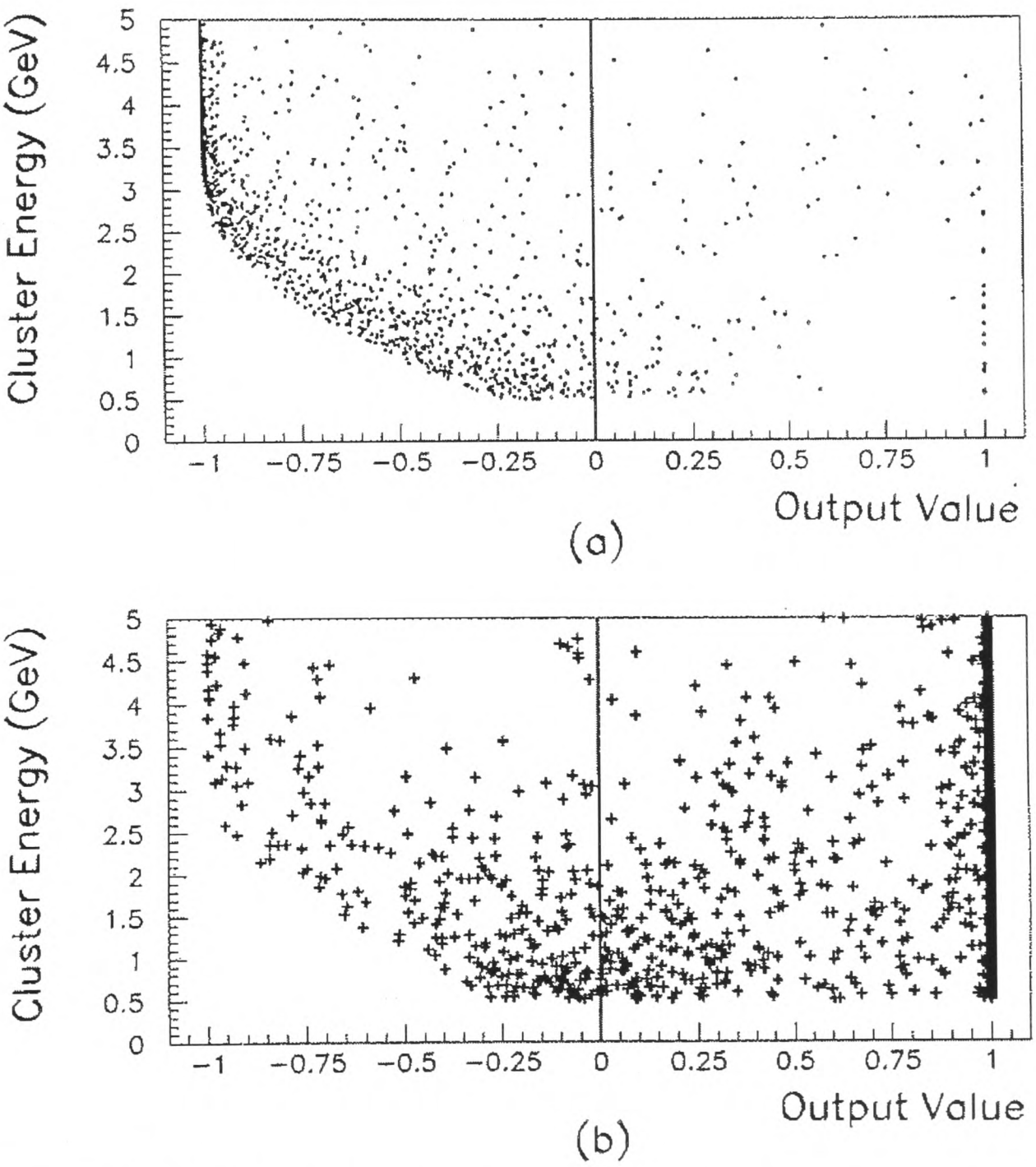

Figure 4.5: Plots of the cluster energy against the neural network output value for the a) electron and b) pion Monte Carlo test samples.

In this study, patterns are identified as electromagnetic if they have a negative neural

network output value and hadronic if the output value is positive. However, note that this cut on the output value is arbitrary and need not be at zero if different efficiency and purity characteristics are required for the electron finder.

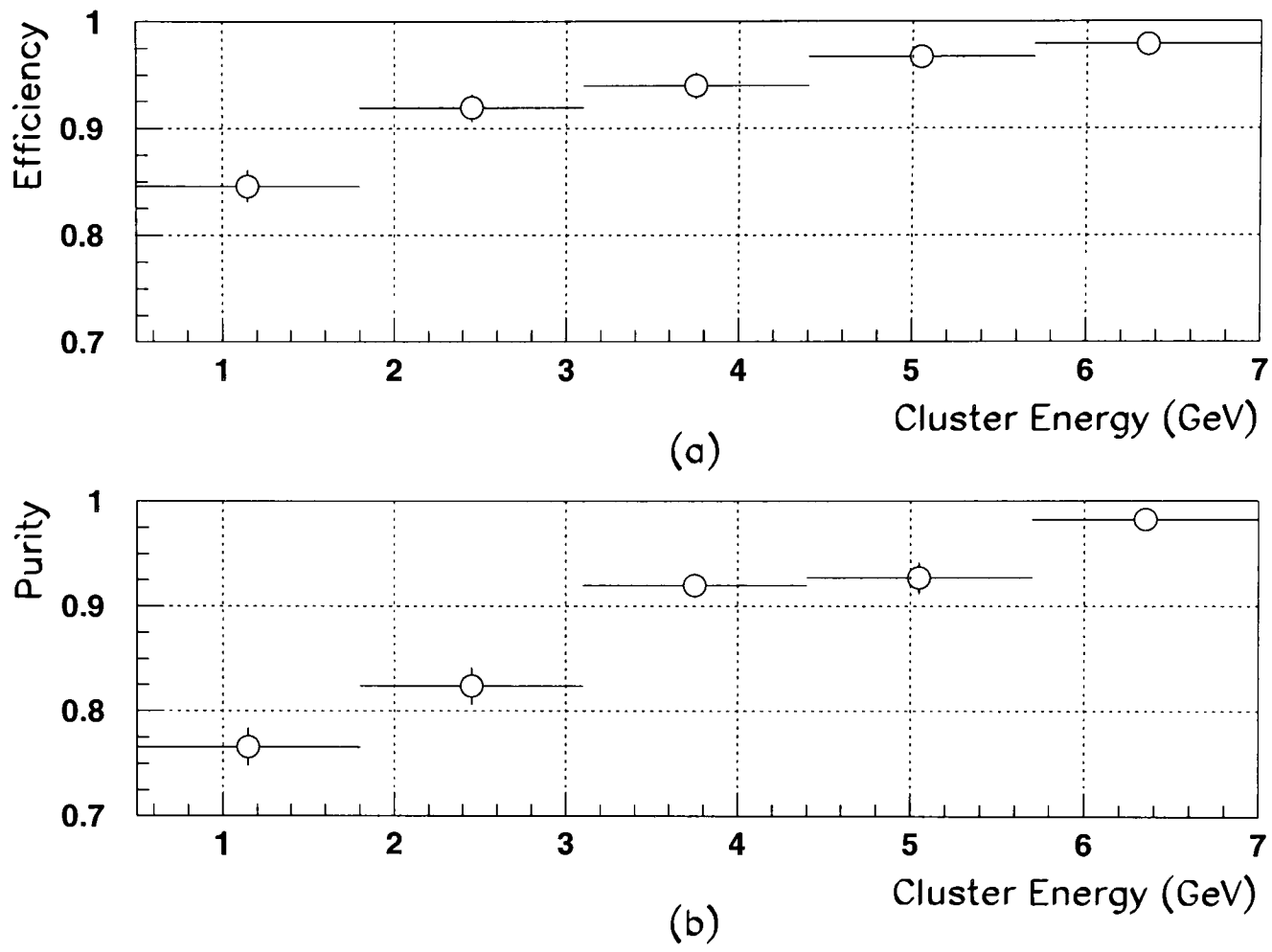

Figure 4.6: Plots of the a) efficiency and b) purity of the neural network as a function of the cluster energy.

4.5 Testing the Neural Network on Test Beam Data

At this stage, only Monte Carlo data has been used in the training and testing of the neural network and so it has been assumed that the showering of particles in the calorimeter in the Monte Carlo accurately reproduces that in the data. To check this assumption, it is useful to test the performance of the neural network on some real data. The neural network is run over two sets of CERN test beam data:

- 6 GeV electrons with 1 radiation length of dead material in front of calorimeter.

- 3 GeV electrons with 2 radiation lengths of dead material in front of calorimeter.

In the ZEUS detector, there are at least two radiation lengths of dead material (CTD walls, magnets etc.) in front of the calorimeter, and this of course depends on the angle at which particles pass through the material. Figures 4.7a and b, show lego plots of the cluster energy on the $y-$axis against the neural network output value on the $x-$axis for the 6 and 3 GeV electrons respectively. The efficiency of the neural network can be calculated by finding the fraction of events with a negative output value, and this is found to be 99% and 92% for the 6 and 3 GeV data samples respectively. Comparing this with the efficiency obtained from the Monte Carlo test sample in figure 4.6a, efficiencies of 98% and 92% are expected for these two energy bins thus agreeing well with the CERN test beam data. Unfortunately, no CERN test beam pion data existed at the time of the study, so the purity found from Monte Carlo data could not be checked with real data.

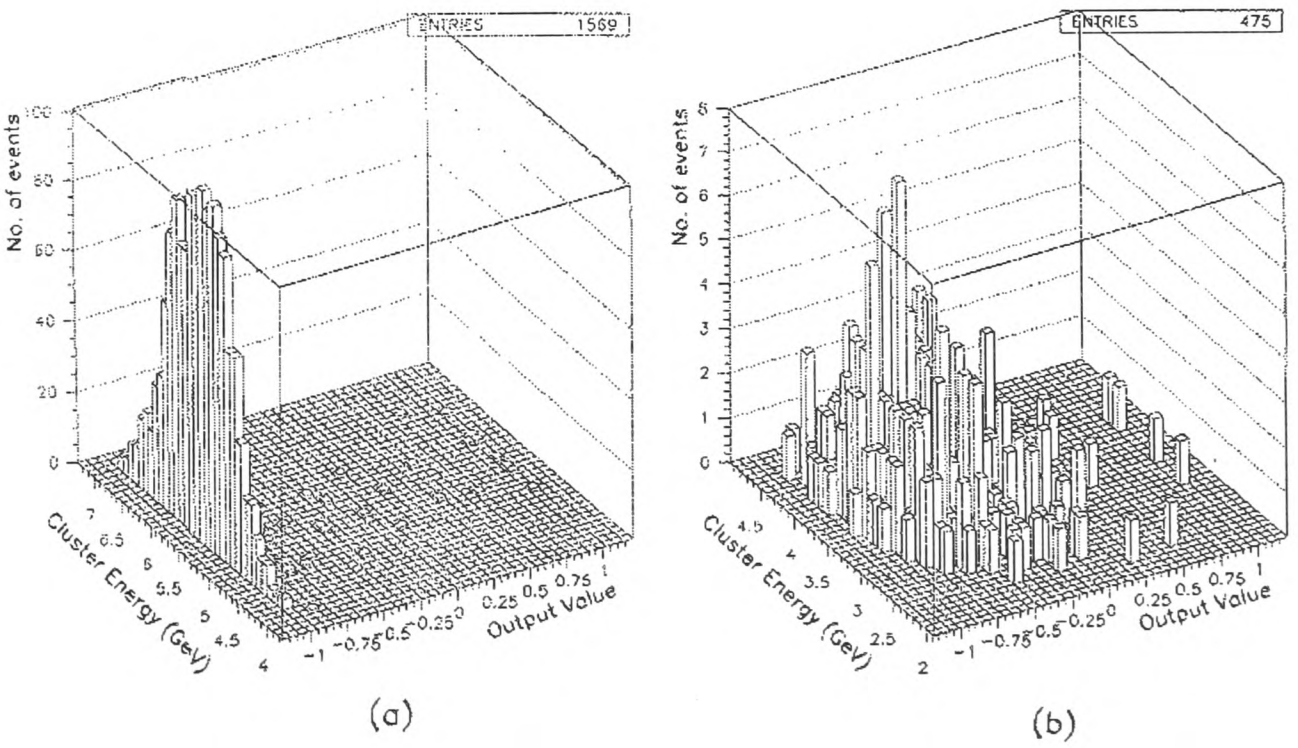

Figure 4.7: Lego plots of the cluster energy against the neural network output values for the a) 6 and b) 3 GeV CERN test beam electron data.

4.6 Conclusions

As mentioned at the start of this chapter, no electron finders had been developed at the time of writing for energies below 2 GeV. This chapter has described the development and testing of a neural network based electron finder designed to operate between 0.5 and 7 GeV. Monte Carlo generated data was used to train and test the neural network with further checks being made using CERN test beam data. The results from the neural network have been good with almost 90% of the Monte Carlo electrons found with a purity of around 80%.

In this study, no track information was used and there is potential for further work to incorporate this as extra input parameters for the neural network. However, at the time of the study, the Monte Carlo did not reproduce the track $\frac{dE}{dx}$ information of the data and so a neural network with such an input parameter could not be trained or tested on Monte Carlo generated data.

The following two chapters deal with the search for the J/ψ through the electron channel using data collected in the 1993 and 1994 running periods. The neural network described in this chapter will be used to select electromagnetic clusters in the analysis using the 1993 data but not the 1994 data.

The reason for this was the significant improvement in the understanding of the CTD during the 1994 running period and the use of a more stable drift gas composition in the chamber. This resulted in a far greater resolution in the measured $\frac{dE}{dx}$ values of the tracks, which provided a very strong handle for selecting electrons. After a cut on the $\frac{dE}{dx}$ values of tracks had been used in the 1994 analysis, all of the energy deposits matched to the selected tracks also passed the neural network cut for selecting electromagnetic

clusters. It was therefore decided that it was unnecessary to use the neural network in the 1994 analysis. In contrast, the neural network provided valuable information in the 1993 analysis where the $\frac{dE}{dx}$ resolution was much poorer.

Chapter 5

The search for $J/\psi \to e^+e^-$ in 1993 data

This chapter begins with a description of the triggers relevant to the J/ψ analysis using 1993 data from the ZEUS experiment. This is followed by a loose pre–selection and then by the final selections used to obtain a sample of elastically and inelastically produced J/ψ. Monte Carlos describing J/ψ production through various channels are examined and finally, a cross–section is calculated for J/ψ produced through the direct inelastic channel.

5.1 1993 Triggers

This analysis uses most of the data from the 1993 running period, starting when the triggers had reached a stable configuration. The trigger configuration used was the first to include the inelastic J/ψ BGF05 third level trigger (TLT) in which J/ψ candidates were identified by requiring two oppositely charged tracks matched to electron or muon – like calorimeter objects.

No Second Level Triggers (SLT) were explicitly selected in this analysis. However, for an acceptance calculation, an SLT selection had to be made and later, we will select

the Data Summary Tape (DST) filter TSTAM11 bit 23 which requires any of the SLTs to be triggered. A detailed description of the triggers used in this analysis follows.

5.1.1 First Level Trigger (FLT)

First of all, J/ψ's decaying into an electron–positron (e^-e^+) pair must be identified. Beginning with the first level trigger (FLT), those triggers requiring energy deposits in the electromagnetic (EMC) part of the calorimeter are selected. A description of the FLTs used in the analysis follows. These are referred to as slots 40, 41, 45, 50, 54 and 58.

- **Slot 40:**

  The total energy of all the EMC cells with energy above 464 MeV, excluding those cells in the first three rings around the forward beam pipe and the first ring around the rear beam pipe must be greater than or equal to 10068 MeV.

- **Slot 41:**

  The total energy of all the EMC cells with energy above 464 MeV in the barrel calorimeter (BCAL) must be greater than or equal to 3404 MeV.

- **Slot 45:**

  The total energy of all the EMC cells with energy above 464 MeV in the rear calorimeter (RCAL), excluding those cells in the first ring around the rear beam pipe must be greater than or equal to 2032 MeV.

- **Slot 50:**

  Each EMC tower[1] is assigned a 3-bit number which is set to 1, 2, 3, 4, 5 or 6 if the EMC energy is greater than 0.625, 1.25, 2.50, 5.0, 10.0 or 20.0 GeV, respectively.

[1]The ZEUS calorimeter is divided into towers as described in section 1.4.

The 3-bit number is set to 7 if the energy overflows and zero for energies less than 0.625 GeV. The quantity REMC_threshold_sum is obtained by summing the bits of all the RCAL EMC towers and this sum must be greater than 3750 MeV to pass this trigger.

- **Slot 54 (Elastic Rho):**

  This trigger consists of three parts, all of which have to be satisfied for an event of be accepted.

  - Total energy in the RCAL $\geq$ 464 MeV.
  - Any track in the CTD.
  - FCAL_bp_threshold_sum $\leq$ 3750 MeV (calculated as REMC_threshold_sum mentioned in slot 50 but using cells in the first three rings around the FCAL beam pipe).

  Beam related background is rejected using the VETO and C5 detectors, described in sections 1.2 and 1.7 respectively. They detect proton beam gas related background where the proton bunches collide with residual gas particles in the beam pipe upstream of the ZEUS detector. The products of this beam gas collision then stream into the detector.

- **Slot 58 (Elastic J/ψ):**

  This slot consists of four parts, all of which have to be satisfied for an event of be accepted. Beam related background is again rejected using the C5 and vetowall detectors.

  - Total energy in the calorimeter $\geq$ 2032 MeV (excluding the cells in the first three forward EMC, first four forward HAC and first rear ring around the

beam pipe) or FCAL_out_of_bp_threshold_sum $\geq$ 2500 MeV (calculated as described in slot 54, but for FCAL cells outside the first three rings around the beam pipe).

- The track multiplicity must be 1, 2 or 3.
- The FCAL_bp_threshold_sum $\leq$ 3750 MeV.
- There must be no more than 3 out of the 16 CAL trigger regions with transverse energy $E_t \geq 696$ MeV.

5.1.2 Third Level Trigger (TLT)

The important TLTs for this analysis are the charm, elastic J/ψ, and inelastic J/ψ triggers also known as the BGF03, BGF04 and BGF05 triggers respectively. The acronym refers to Boson Gluon Fusion. All the BGF triggers have the following common cuts:

- Vertex closest to the interaction point has $|z| < 75$ cm.
- The highest multiplicity vertex has $z > -100$ cm and the number of CTD tracks ≥ 8. This removes proton beam gas events.
- $E_{tot} - P_z < 100$ GeV where E_{tot} is the total energy in the calorimeter after UNO suppression[2] and P_z is the sum of the $z-$component of the energy deposits in each cell.
- $P_z/E_{tot} < 0.94$

The charm trigger, BGF03:

This trigger looks for two oppositely–signed, high transverse momentum tracks, consis-

[2] In UNO suppression, EMC and HAC cells with energy less than 50 MeV and 110 MeV respectively, are not included in the sum.

tent with the decay of two charmed mesons (due to their large mass). The trigger has several branches all of which have to be passed for an event to be accepted. The trigger is defined as follows:

- $E_{tot} - P_z > 3.0$ GeV
- $P_z/E_{tot} < 0.9$
- $min(P_{t+}, P_{t-}) > 0.5$ GeV and $P_{t+} + P_{t-} > 1.3$ GeV, where P_{t+} and P_{t-} are the maximum transverse momenta of all the positive and negative tracks, in the angular region $0.2618 < \theta < 2.880$ rad, respectively.
- Any of the following:
  - Energy in the LUMI electron calorimeter > 5 GeV (see section 1.6). This condition looks for the scattered electron in the LUMI detector.
  - $P_z/E_{tot} < 0.8$
  - $E_{tot} - P_z > 15$ GeV
  - Total transverse energy of calorimeter cells outside a cone of polar angle $\theta = 10^o$ is greater than 5 GeV.

The elastic J/ψ trigger, BGF04:

This trigger is designed to search for low charge multiplicity events with most of the energy deposited in the EMC sections of the calorimeter. The trigger requirements are:

- HAC energy < 1.0 GeV
- EMC energy > 1.5 GeV

- BEMC energy $>$ 10 $\times$ BHAC energy or BHAC energy $<$ 0.2 GeV

- REMC energy $>$ 10 $\times$ RHAC energy or RHAC energy $<$ 0.2 GeV

- Number of tracks with $P_t > 0.2$ GeV less than 5

- At least two oppositely charged tracks with $P_t > 0.4$ GeV.

The inelastic J/ψ trigger, BGF05:

This trigger is designed to tag events with two oppositely charged electron or muon candidates, consistent with leptonically decaying J/ψ. The requirements for the electron channel are listed below:

- Number of electron candidates ≥ 2. An electron candidate is defined as an island-cluster[3] with the following properties:
  - number of EMC cells ≤ 8
  - number of HAC cells ≤ 3
  - EMC energy ≥ 0.5 GeV
  - EMC energy / Cluster energy > 0.9
- Each track passing all of the following cuts is selected:
  - χ^2 per degree of freedom < 3
  - momentum > 0.5 GeV
  - z position of the closest point on the helix to the z axis, $z_h < 80$ cm

[3] See section 4.2.

– transverse distance of the closest point on the helix to the z axis, $d_h < 10$ cm (see figure 5.1).

- The number of selected tracks matched to electron island–clusters ≥ 2. There is assumed to be a constant magnetic field, $\mathbf{B_z}$, along the $z-$axis in a cylinder defined by $r < 80$ cm and $|z| < 110$ cm (see figure 5.1). Outside this cylinder, the magnetic field is assumed to vanish. A track from a charged particle therefore follows a helix within the cylinder and a straight path outside with the track exit momentum, $\mathbf{p_{exit}}$, at the cylinder exit point, $\mathbf{r_{exit}}$. A vector is formed between the electron cluster position, $\mathbf{r_{clus}}$, and the cylinder exit point: $\mathbf{r_{TC}} = \mathbf{r_{clus}} - \mathbf{r_{exit}}$. The angle between this vector and the track exit momentum is defined as $\theta_{\rm TC}$:

$$cos\ \theta_{\rm TC} = \frac{|\mathbf{p_{exit}} \cdot \mathbf{r_{TC}}|}{|\mathbf{p_{exit}}| \times |\mathbf{r_{TC}}|}$$

  The track and electron cluster are said to be matched if $cos\ \theta_{\rm TC} \geq 0.9$ or equivalently, $\theta_{\rm TC} \leq 26^o$.

- Transverse momentum of the matched track–cluster electron candidates > 0.4 GeV

- At least one positive and one negative matched track.

Note that both the charm BGF03 and the elastic J/ψ BGF04 triggers have minimum transverse momentum cuts for both positive and negative tracks. They will therefore discriminate against like–signed background events since these will only be accepted if there is an additional third oppositely–signed track satisfying the transverse momentum requirements.

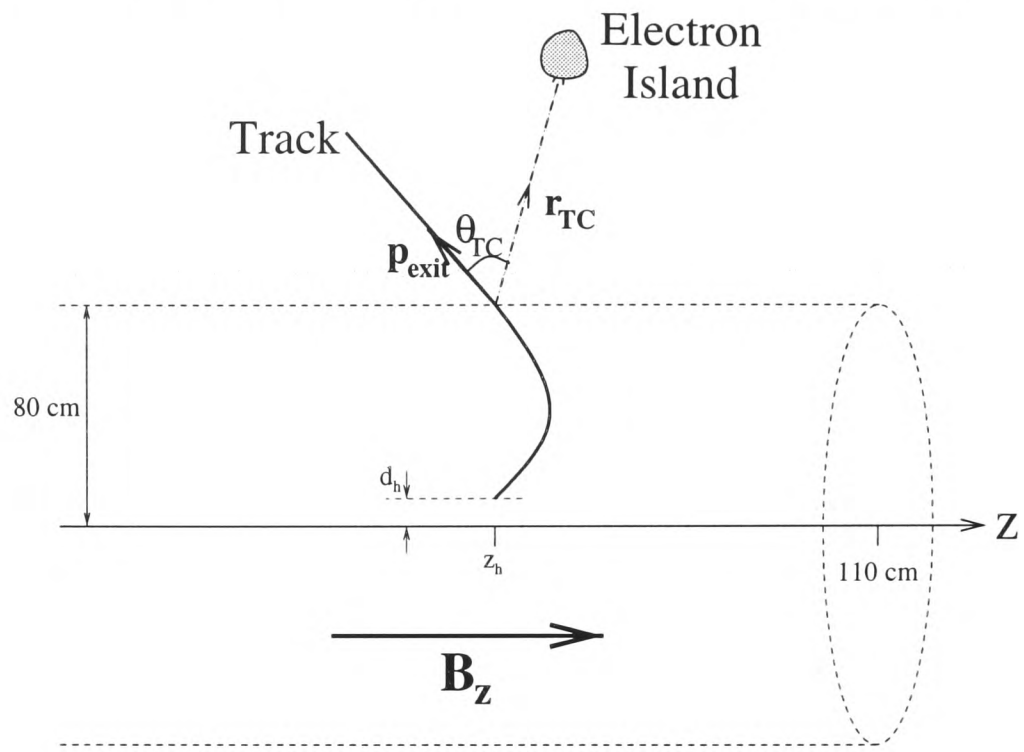

Figure 5.1: Schematic two dimensional diagram showing the track–cluster matching used in the BGF05 inelastic J/ψ trigger.

The inelastic J/ψ BGF05 trigger requires two oppositely charged electron or muon candidates. This will therefore also discriminate against the like–signed background events with an additional third oppositely–signed electron or muon candidate required to pass the trigger.

5.2 Pre–selection of 1993 data

In the offline reconstruction, events passing the TLT BGF05 trigger and any of the first and second level triggers, are tagged by the Data Summary Tape (DST) filter TSTAM11 bit 23 but with the TLT BGF05 code now using the full Flash Analogue to Digital Converter (FADC) tracking information (in the TLT, the FADC information was used only up to superlayer 5 of the CTD).

For the pre–selection of the 1993 data, only events passing the EVTAKE[4] routine

[4] The EVTAKE routine accepts only 'good' physics runs for analysis. For example runs where the calorimeter is open, luminosity is wrong or the magnets, calorimeter modules or CTD are off are rejected.

and the following trigger bits are considered.

- TSTAM11 bit 23
- FLT slots 40, 41, 45, 50, 54 or 58
- TLT BGF 3, 4 or 5

The total luminosity of the 1993 data analysed is 483.0 nb^{-1}. There are 1,526,000 events of which 1,481,000 passed EVTAKE. Of these, 214,000 passed the DST TSTAM bit 23. The FLT and TLT triggers further reduced this total to 113,000.

The next stage of the selection procedure involves identifying electron candidates using the ISLANDS algorithm[5] and demanding that the ratio of energy in EMC (including HAC0 cells) to total energy > 0.9 and that the shower radius[6] ≤ 25 cm.

Tracks, found using the VCTRAK algorithm[7], are then selected which:

- start in the vertex detector or superlayer 1 of the CTD and end in superlayer 3 or more.
- have an absolute pseudorapidity[8] $|\eta| \leq 2.0$
- have a transverse momentum, $P_t > 0.6$ GeV. This cut is very effective in removing background from conversion electrons (see section 3.6). It has the further advantage of being well within the understood reconstruction region of the CTD[9].

[5]The ISLANDS algorithm is described in section 4.2.

[6]The shower radius is defined in equation 3.7 in section 3.4.

[7]See section 3.3 and [22] for a description of the VCTRAK algorithm. This algorithm will be used to find all tracks in the rest of this analysis.

[8]The pseudorapidity of a track is defined as $\eta = -ln\{tan(\theta/2)\}$.

[9]For 1993 data, the so–called 'Foster cuts' recommend only tracks with transverse momentum, $P_t > 0.2$ GeV and absolute pseudorapidity $|\eta| \leq 1.5$ should be trusted. The cut in pseudorapidity falls outside these conditions and will be tightened later on. The reason behind this is to give an indication of how many events are removed by the tightening of this cut.

Attempts are made to match these selected tracks and clusters by calculating the closest distance of approach of all the selected tracks to all the selected clusters. The TRKCLUX routine calculates this distance using the VCATCAL tables for the track and the ELECPO routine to give the island centres (see section 4.2). The VCATCAL tables provide the entry point of each track into the calorimeter and the track momentum vector there. The track is extended from this entry point along the momentum vector and the closest distance to the island centre is calculated. Tracks and clusters are said to be matched if this distance is less than 35 cm and if the ratio of island energy to track momentum lies between 0.4 and 1.6. Each matching must be unique, so that a single cluster cannot be matched to more than one track and vice versa. In the case of an ambiguity, the closest pair is chosen.

Provided there are two or more matched track–clusters, a loop is performed over all pairs of track–clusters and a reconstructed mass calculated from the track variables. An event is accepted provided there is at least one pair for which this mass is greater than 2 GeV and the separation along the $z-$axis of the two tracks at their respective closest points to the beam line, is less than 40 cm.

In the 483.0 nb^{-1} of data analysed, 24,203 events pass the pre–selection cuts in which there are 36,632 J/ψ candidates. Therefore, a significant fraction of events have more than two matched track–cluster electron candidates giving more than one J/ψ candidate per event. The reconstructed mass distribution of these candidates in figure 5.2 (where there is an additional upper mass cut of 5 GeV) shows no sign of an enhancement in the J/ψ mass region because of the large background.

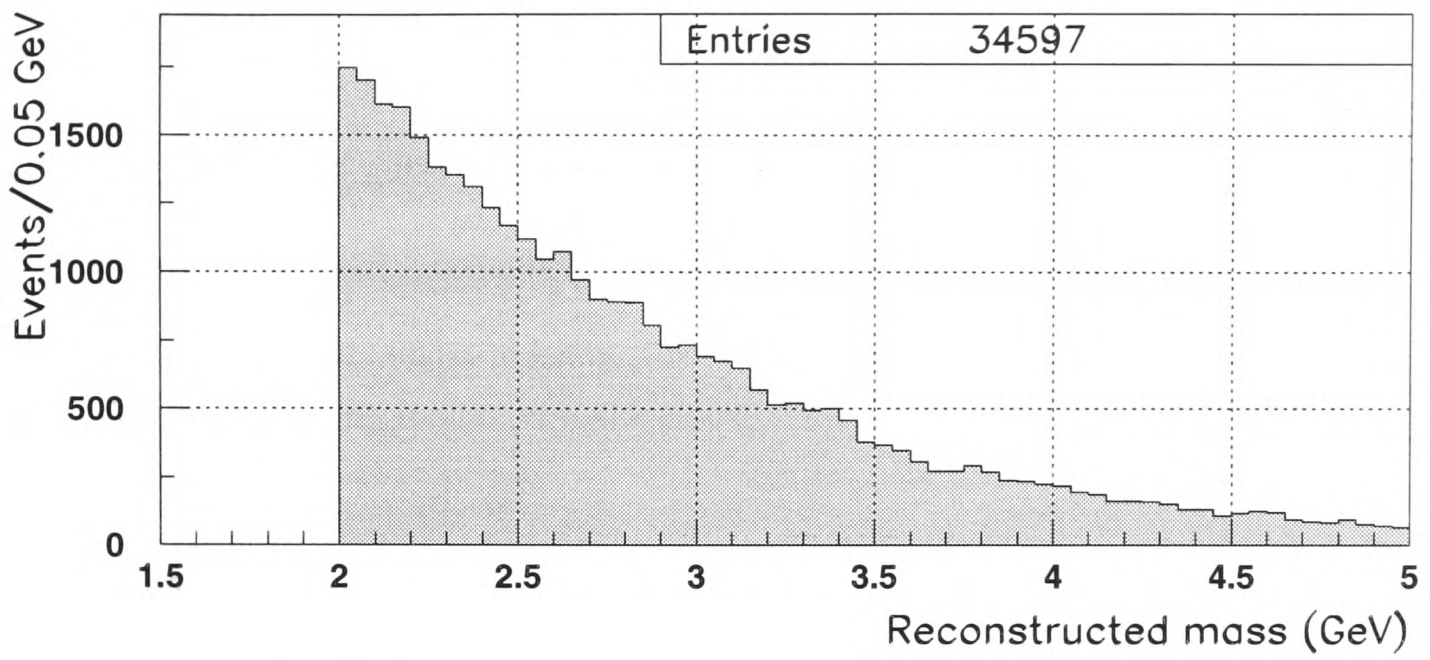

Figure 5.2: Reconstructed mass of the pre–selected candidate J/ψ events from 1993 data. No enhancement in the J/ψ mass region is seen.

5.3 Elastic $J/\psi \to e^+e^-$ selection

The selection procedure for the elastic J/ψ sample from the 1993 data is described in this section. J/ψ photoproduction through the elastic channel should lead to only the decay electron and positron tracks in the CTD with the incident proton and electron remaining intact and being lost down the beam pipe. Therefore a multiplicity[10] cut of two tracks can be applied, which is very effective in removing background events and a very clean elastic J/ψ sample will be seen.

The purity of this elastic sample then allows it to be used in helping to determine the cuts for the inelastic J/ψ sample. For example, looking at the size distribution of calorimeter deposits from the decay electrons and positrons provides a useful guide as to where cuts should be placed on these dimensions when looking for electromagnetic energy deposits in the calorimeter. This elastic J/ψ sample together with an inelastic

[10]The event multiplicity is defined as the number of tracks found in an event using the VCTRAK algorithm on the primary vertex.

J/ψ Monte Carlo sample of events will be used in the next section to determine the cuts used to obtain the inelastic J/ψ sample.

Electrons from photon conversions are rejected using the CONVERT2 algorithm [32]. Pairs of tracks with positive DistB and non–zero IGCTAG (see section 3.6) are considered as possible conversion electrons and are rejected as possible J/ψ decay electron tracks.

The cuts applied to the pre–selected sample to obtain the elastic J/ψ are listed below. These are based on the cuts used in the two 1993 elastic J/ψ analyses, described in [44, 45].

- The J/ψ decay electron tracks are oppositely charged and not identified as conversion electrons by the CONVERT2 algorithm.
- Both electron tracks originate from the main vertex.
- The absolute pseudorapidity $|\eta| \leq 1.5$ for both decay electron tracks. This cut is necessary to place the analysis in an understood region of the CTD reconstruction as defined by the 'Foster cuts' (see footnote 9 in section 5.2).
- Both electron tracks approach within 25 cm of their respective clusters when the tracks are extended into the calorimeter as described in section 5.2 and at least one electron track approaches within 6.5 cm of its cluster.
- The ratio of energy in the EMC (including HAC0 cells) to the total energy > 0.99 for both electron clusters.
- The ratio of calorimeter energy to track momentum of both decay electrons < 1.1 (note that the pre–selection already requires this ratio to lie between 0.4 and 1.6).

- The mass, reconstructed from the two candidate electron tracks after being fitted to the main vertex, lies in the range 2.2 – 4.2 GeV.

- The track multiplicity is equal to two. This is the only cut used to select the physics process producing the J/ψ.

Figure 5.3 shows the reconstructed mass of the two tracks of the elastic J/ψ sample. The decay electrons from the J/ψ may radiate photons as discussed in section 3.5.2. If a measurement of the track momentum is made after a photon is radiated, the track will have a lower momentum hence giving a lower reconstructed mass for the two tracks and a bremsstrahlung tail in the mass spectrum. The reconstructed mass in figure 5.3 is fitted to a gaussian with a bremsstrahlung tail and the background is fitted to a second order polynomial shown as the dashed line. A clear signal is seen at the reconstructed mass 3.08 ± 0.01 GeV with a width of 0.051 ± 0.009 GeV and containing 86 ± 11 events.

There are no like–signed events passing the cuts described above despite the fact that there are over 40 background events in this opposite–signed sample below the J/ψ mass peak. This can be explained by the bias towards opposite–signed events in the charm, elastic and inelastic J/ψ third level triggers BGF03, BGF04 and BGF05 respectively, described in section 5.1.2. Since this elastic sample has a track multiplicity cut of two, there is no possibility of a third oppositely charged track to the like–signed events satisfying the trigger requirements.

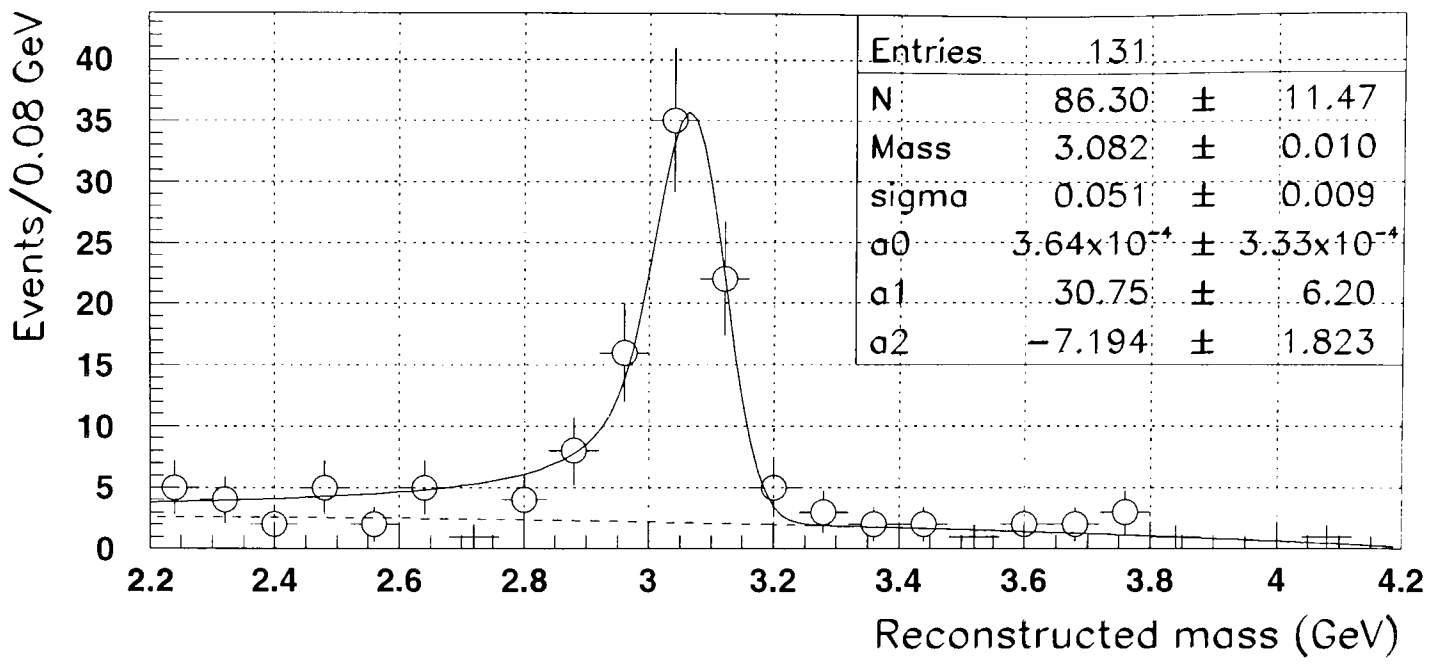

Figure 5.3: Reconstructed mass of the elastic J/ψ sample from 1993 data.

5.4 Inelastic $J/\psi \rightarrow e^+e^-$ selection

This section describes the tighter cuts applied to the pre–selected sample to obtain an inelastic J/ψ sample of events. These cuts are based on studies of inelastic J/ψ Monte Carlos and on the sample of elastic J/ψ events from the 1993 data obtained in the previous section.

In this analysis, each event vertex is re–fitted by the 'FITV' algorithm which uses only the two J/ψ decay electron tracks. Thus for events with more than two candidate electron tracks, a new vertex is calculated for each pair of electron tracks. The electron track variables are then re–calculated using this new vertex. This is especially important for inelastic J/ψ events where event multiplicities are typically high (as shown in figure 5.4) so that the event vertex can be pulled away from the vertex formed by the two decay electron tracks alone. This would then give rise to shifts in the energies and momenta of the decay electron tracks from their true values. J/ψ candidates are rejected if the fitting of the vertex did not converge. Events in the elastic J/ψ sample have

a track multiplicity of two, therefore, the FITV algorithm would make no difference to the reconstructed mass distribution of this sample.

Only events in the reconstructed mass range 2.2 – 4.2 GeV are considered. The reconstructed mass is calculated from the decay electron track variables, after fitting to this new vertex. The energy deposits in the calorimeter are not used to reconstruct the mass due to the poorer resolution of the calorimeter at these low electron energies (typically below 3 GeV – see equations 1.1, 1.2 and 1.3).

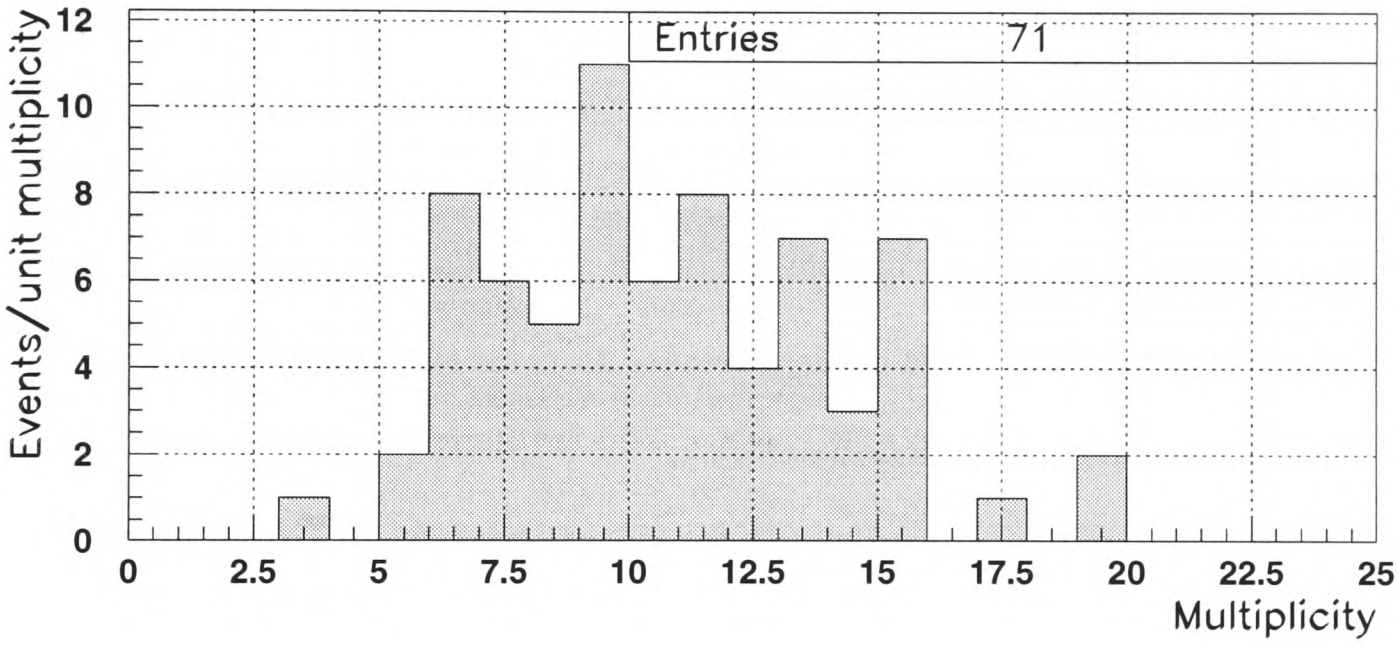

Figure 5.4: Multiplicity distributions of the inelastic J/ψ sample in 1993 data. Tracks contribute to this multiplicity measurement only if they originate from the main vertex.

The cuts applied to the pre–selected sample are now listed. Figures 5.5a – p show the reconstructed mass of the J/ψ candidates as the cuts listed below are applied sequentially. Figures 5.7 – 5.13 and 5.16 further justify some of the cuts. A series of three plots (a – c) are shown for each of these figures. The first plot shows the effect of a particular cut on the pre–selected sample of 1993 data (where cuts are always sequential). In the second of the three plots, the effect of the cut on a HERWIG[11] inelastic J/ψ

[11] The HERWIG Monte Carlo generator is described in section 3.7.

Monte Carlo sample of events is shown after passing all the cuts listed below (except the one being illustrated). The third plot shows the effect of the cut on the 1993 elastic J/ψ sample described in the previous section (with an additional mass cut of 2.85 – 3.15 GeV to further clean up the elastic J/ψ sample).

1. The J/ψ decay electron tracks are oppositely charged and not identified as conversion electrons by the CONVERT2 algorithm.

2. Both electron tracks originate from the main vertex and the fitting of a vertex to the two decay electron tracks using the FITV algorithm (described above) converges.

3. The absolute pseudorapidity, $\mid \eta \mid \leq$ 1.5 for both decay electron tracks (see figures 5.6a-c). This cut is necessary to place the analysis within the 'Foster cuts' (see footnote 9 in section 5.2).

4. Both electron track vertices are within 20 cm of the main vertex along the beam axis (see figures 5.7a-c).

5. The shower radii of both electron clusters $\leq$ 15 cm (see figures 5.8a-c).

6. The shower length[12] of at least one electron cluster $\leq$ 3 cm. These are plotted in figures 5.9a-c and it is seen that there is an excess of events with near zero shower length in the data compared to the Monte Carlo. This is due to noise in the calorimeter which produces energy in single isolated cells which the Monte Carlo does not model.

7. Both electron tracks approach within 20 cm of their respective clusters when

[12]The shower length is defined in equation 3.8 in section 3.4.

the tracks are extended into the calorimeter as described in section 5.2 (see figures 5.10a-c).

8. The ratio of cluster energy in the calorimeter to track momentum of both decay electrons < 1.1 (see figures 5.11a-c). The distributions are centred around 0.8 rather than unity as might be expected for relativistic particles. This is due to the dead material (CTD walls and magnet coil) in front of the calorimeters. Particles lose a fraction of their energy in this dead material and hence the energy deposited in the calorimeters is reduced.

9. At least one of the decay electron tracks has a transverse momentum, $P_t > 1.2$ GeV (see figures 5.12a-c). The pre–selection cuts already require both electron tracks to have $P_t > 0.6$ GeV.

10. The neural network[13] output value for both electron clusters ≤ 0 (see figures 5.13a-c).

11. The sum of the pressure corrected $\frac{dE}{dx}$ values for both decay electrons > 100. The effect of this cut on the pre–selected 1993 data is seen in figure 5.14a. More will be said about this later in section 5.5.

12. Since a low Q^2 photoproduction cross–section is required, the scattered electron should be lost down the beam pipe and there should not be a large deposit of energy near the beam pipe in the rear calorimeter. To ensure this is the case, a cut of 1 GeV is put on the maximum total energy in the first calorimeter ring around the rear beam pipe. In figure 5.15b, this energy is shown for HERWIG inelastic J/ψ Monte Carlo events and one sees that very few events are lost by

[13] See chapter 4 for a description of the neural network used in this analysis.

the cut whereas significantly more real data events rejected (figure 5.15a).

13. The energy in the calorimeter not belonging to the J/ψ decay electron islands in a cone of 35° around the forward beam pipe is summed and required to be greater than 1 GeV (see figures 5.16a-c). The purpose of this cut is to remove J/ψ's produced through mechanisms where the incident proton does not break up such as the elastic and diffractive inelastic channels (see figures 2.13 and 2.15). It is seen in figure 5.16c, that all of the elastic data sample lies well within this cut and is therefore rejected.

14. Elasticity, $z \leq 0.9$ (defined in section 3.1). This cut is required to remain in a safe region for the acceptance calculations as the HERWIG Monte Carlo only generates events with $z \leq 0.95$. It is shown as a dotted line in conjunction with the next cut in figures 5.17a-d.

15. In the elasticity – J/ψ transverse momentum plane, a cut is made removing events with high z and low $P_t^{J/\psi}$ defined by $P_t^{J/\psi} \geq (8.75z - 7)$ as shown in figures 5.17a-d. The reason for this cut is to remove proton dissociative J/ψ events where the incident proton breaks up after emitting a colourless object to interact with the photon (see figure 2.14 in section 2.6.2). Since the emitted colourless object is typically soft, the J/ψ has little transverse momentum and an elasticity close to unity. Cut 13 above, is not effective in removing these events since the incident proton breaks up after the interaction and deposits energy in the forward part of the calorimeter. In figure 5.17b, one sees that most of the HERWIG inelastic J/ψ events are unaffected by this cut. The Pythia Monte Carlo is used to generate 5700 proton dissociative J/ψ events and these are passed through the pre–selection

code, trigger selection and cuts 1 – 13 above. 227 events remain and these are shown in figure 5.17c. It is seen that the majority of these events are rejected by the cuts in the $(z\,P_t^{J/\psi})$ plane. There is another source of background from resolved photon events (see section 2.6.2). In figure 5.17d, resolved photon J/ψ events produced using the EPJPSI[14] Monte Carlo generator are shown. These lie at low elasticities, typically below 0.5 and so are unaffected by this or the previous elasticity cut. The problem of resolved photon J/ψ events entering the signal will be addressed in section 5.7.1.

The elasticity, z, is calculated with calorimeter information using $z = \frac{(E-P_z)_{J/\psi}}{(E-P_z)_{total}}$. Using this method ensures that the loss of energy in the dead material as particles enter the calorimeter (mentioned above in cut 8) cancels out from the numerator and denominator of the fraction. Track information cannot be solely used to calculate the elasticity because neutral particles, which should contribute to $(E - P_z)_{total}$, will not show up as tracks.

In figure 5.18, a plot of the reconstructed γp invariant mass[15], W, against reconstructed mass is shown after all the cuts described above have been applied. A cluster of events around the J/ψ mass is seen at W values below 140 GeV. In section 5.6, it will be established from the Monte Carlo studies, that the acceptance for inelastic J/ψ Monte Carlo events becomes very small for W values outside the range 100 – 140 GeV. In order to reduce the background and to avoid these low acceptances a W cut of 100 – 140 GeV is applied as indicated by the parallel lines in figure 5.18. Note that these results are not biased by choosing a W cut to remove the background since W is a physical variable which will be quoted with the cross–section measurement. The

[14] The EPJPSI Monte Carlo generator is described in section 3.7.
[15] Calculated as described in section 3.2 using only calorimeter information.

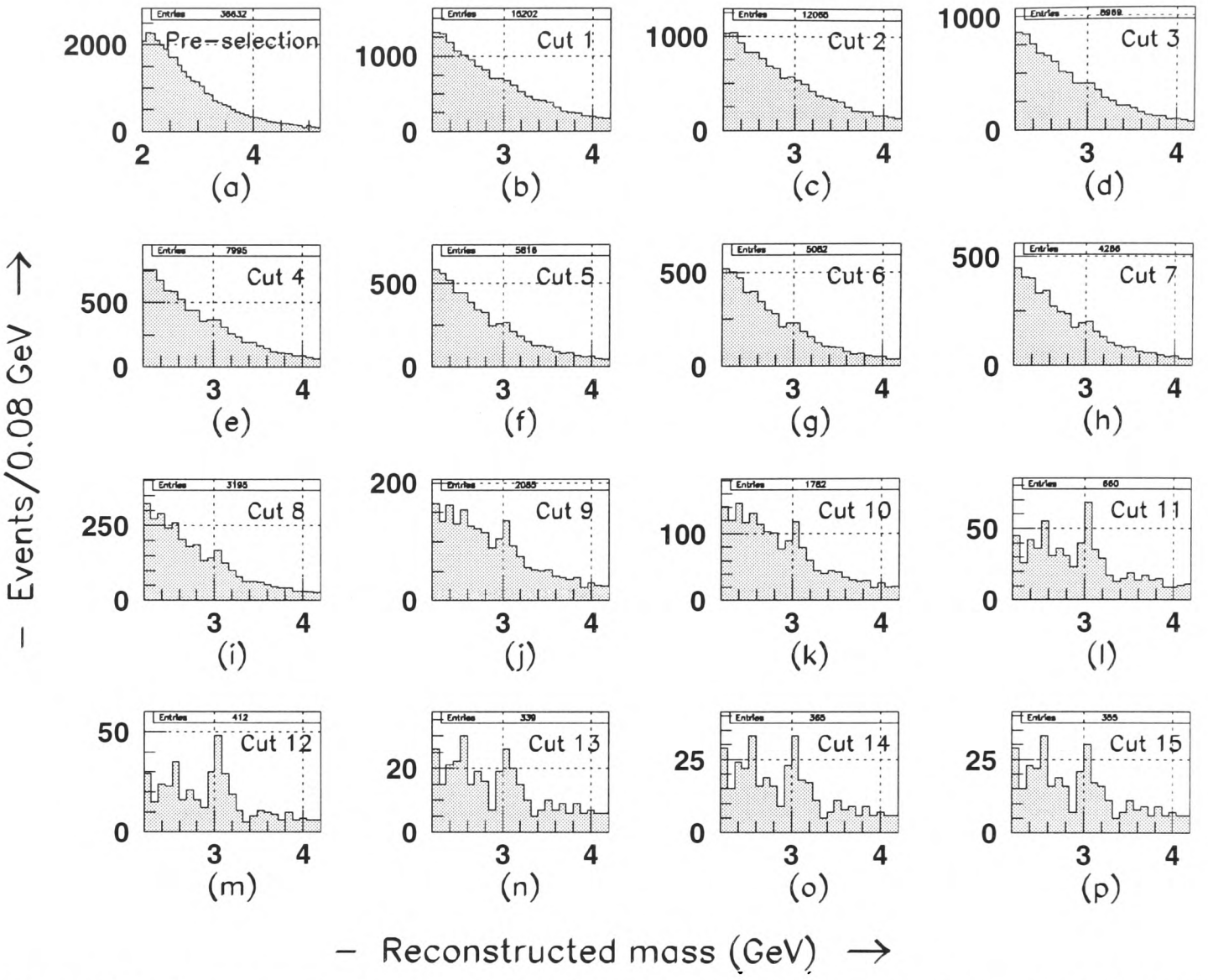

Figure 5.5: Reconstructed mass (GeV) of the J/ψ candidates as cuts are applied in the following order: a) Pre–selection cuts, b) Oppositely charged, non-conversion tracks, c) e^+e^- tracks fitted to vertex, d) Pseudorapidity $|\eta| \leq 1.5$, e) z vertices within 20 cm, f) Shower radii ≤ 15 cm, g) At least one shower length ≤ 3 cm, h) Track–cluster distances ≤ 20 cm, i) $E_{island}/P_{track} \leq 1.1$, j) One track with $P_t \geq 1.2$ GeV, k) Neural net ≤ 0.0, l) $\Sigma \frac{dE}{dx} \geq 100$, m) Rear beam pipe energy ≤ 1 GeV, n) Forward 35° cone energy ≥ 1 GeV, o) $z \leq 0.9$ and p) $P_t^{J/\psi} \geq (8.75z - 7)$.

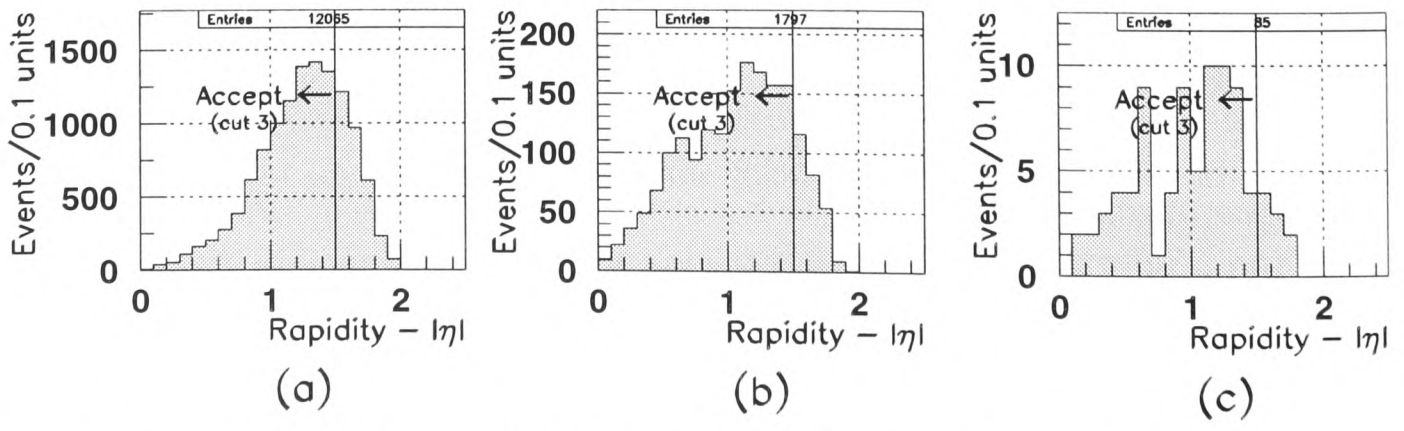

Figure 5.6: Largest absolute η of the two decay electron tracks for a) pre–selected 1993 data, b) HERWIG Monte Carlo and c) elastic J/ψ 1993 data.

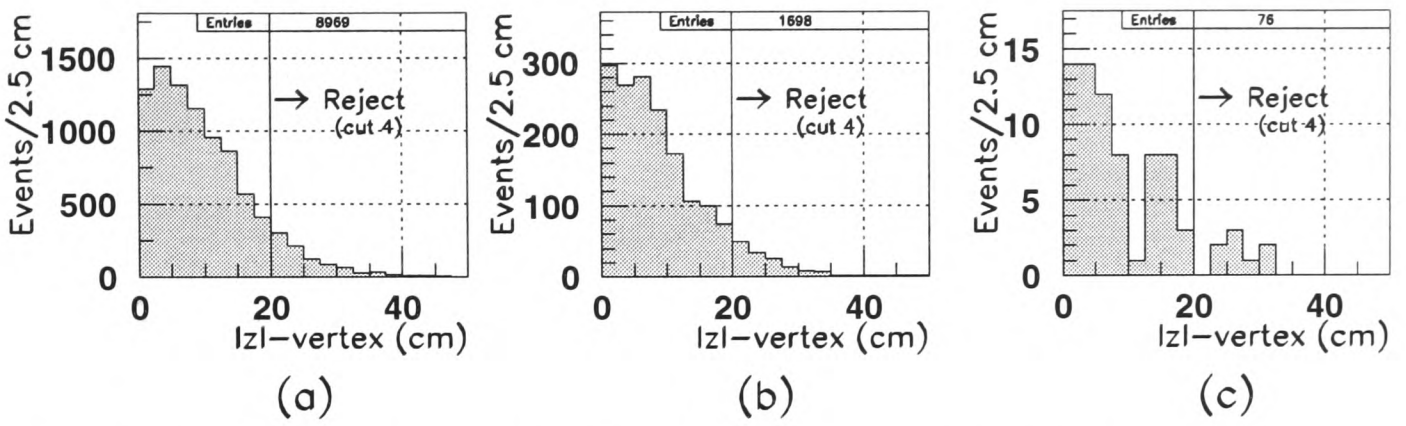

Figure 5.7: Largest absolute z vertex of the two decay electron tracks for a) pre–selected 1993 data, b) HERWIG Monte Carlo and c) elastic J/ψ 1993 data.

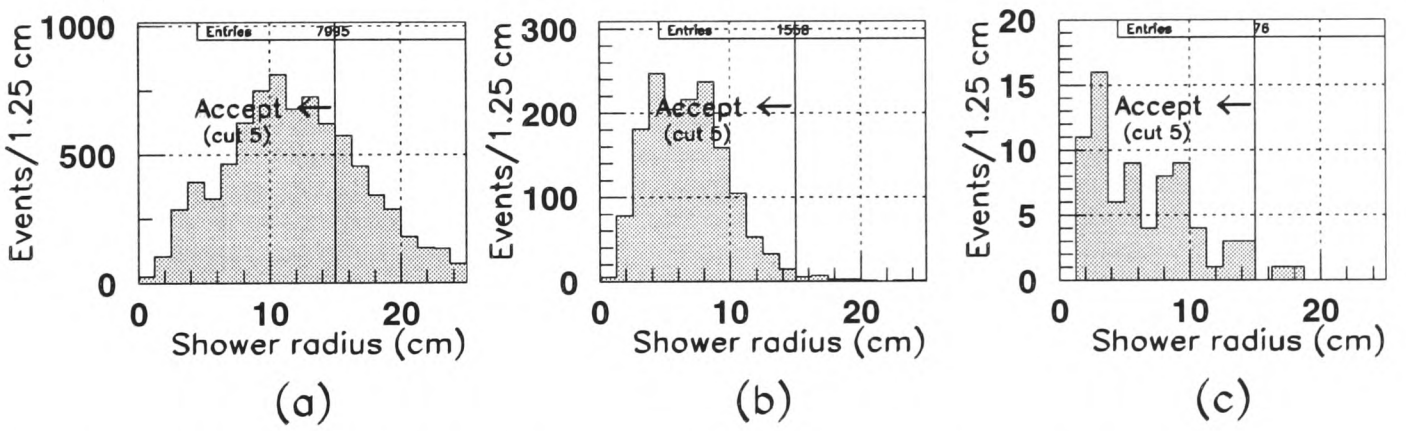

Figure 5.8: Largest shower radius of the two decay electron clusters for a) pre–selected 1993 data, b) HERWIG Monte Carlo and c) elastic J/ψ 1993 data.

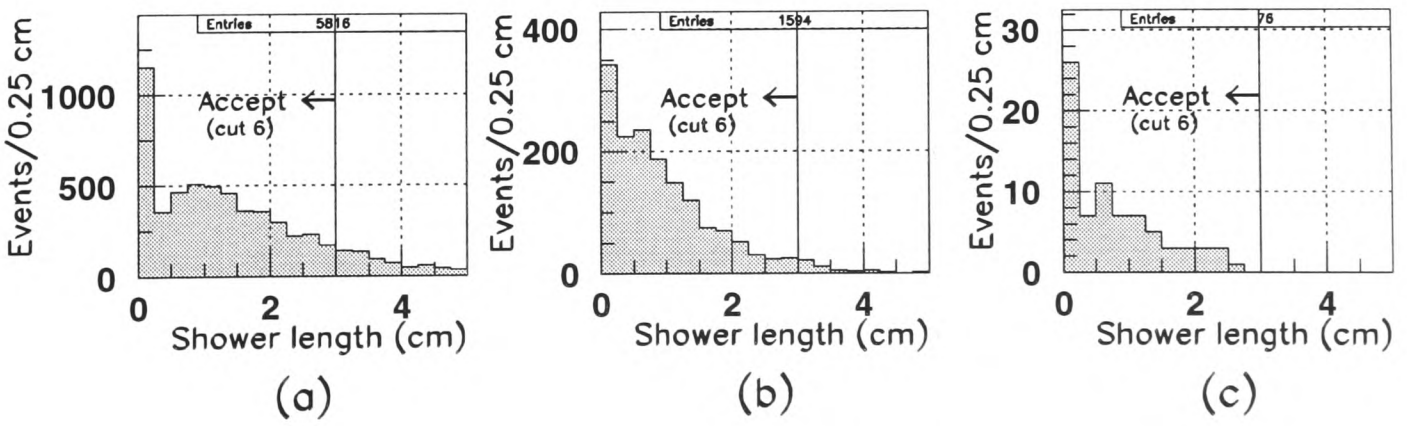

Figure 5.9: Smallest shower length of the two decay electron clusters for a) pre–selected 1993 data, b) HERWIG Monte Carlo and c) elastic J/ψ 1993 data.

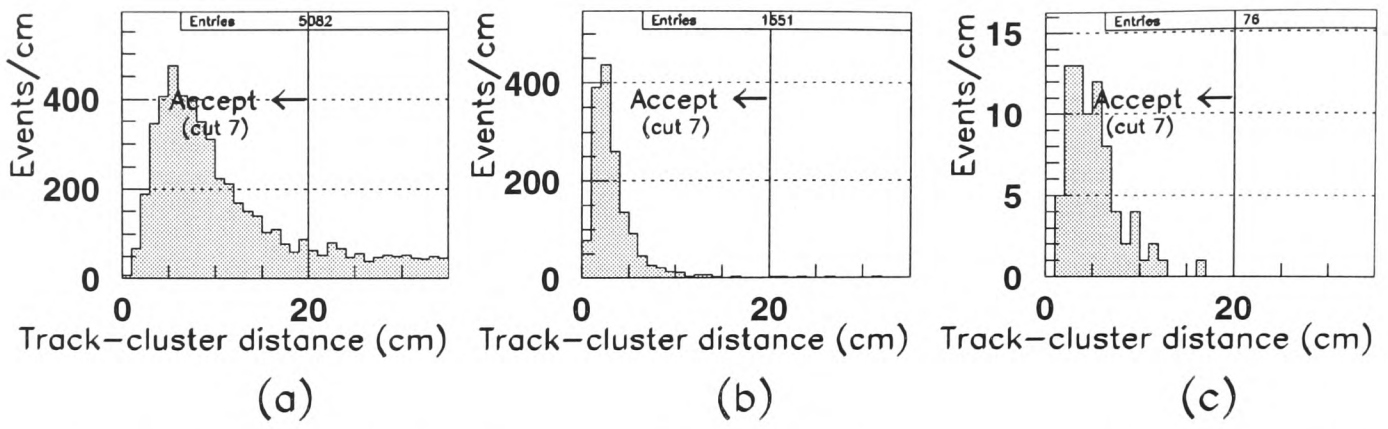

Figure 5.10: Largest track–cluster distance of the two decay electrons for a) pre–selected 1993 data, b) HERWIG Monte Carlo and c) elastic J/ψ 1993 data.

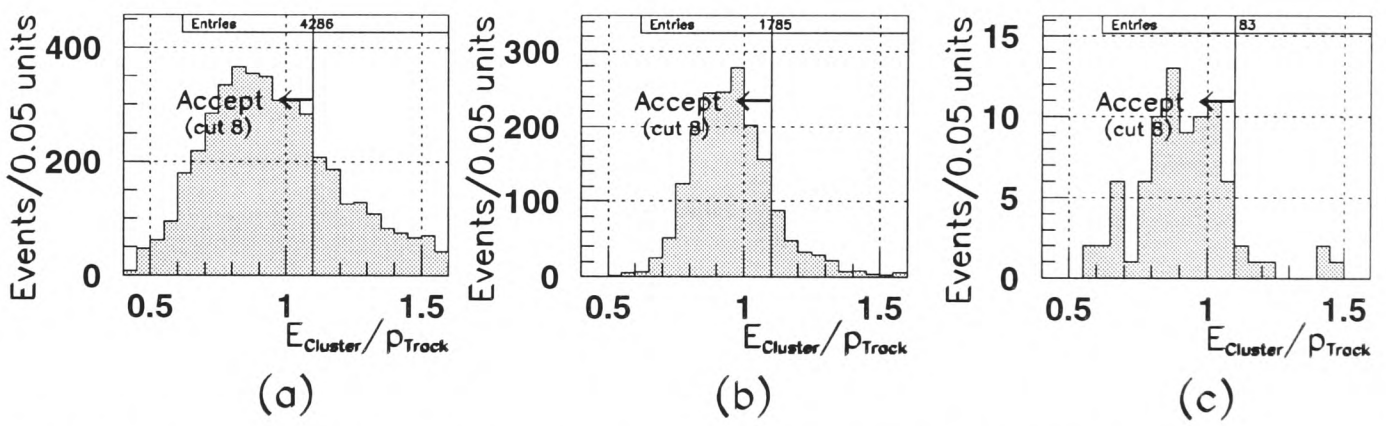

Figure 5.11: Largest calorimeter energy/track momentum of the two decay electrons for a) pre–selected 1993 data, b) HERWIG Monte Carlo and c) elastic J/ψ 1993 data.

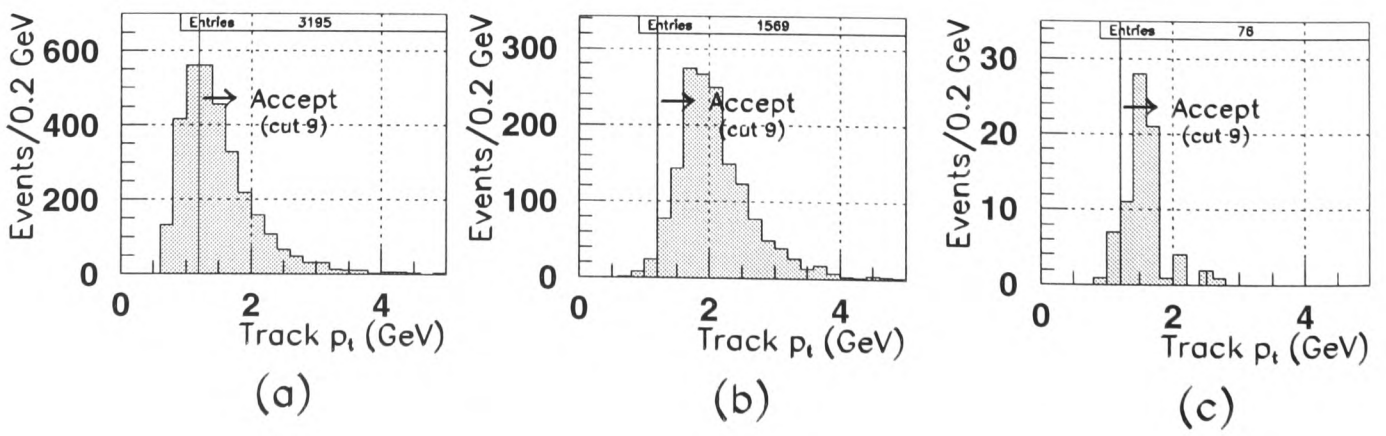

Figure 5.12: Largest transverse momentum, P_t, of the two decay electron tracks (GeV) for a) pre–selected 1993 data, b) HERWIG Monte Carlo and c) elastic J/ψ 1993 data.

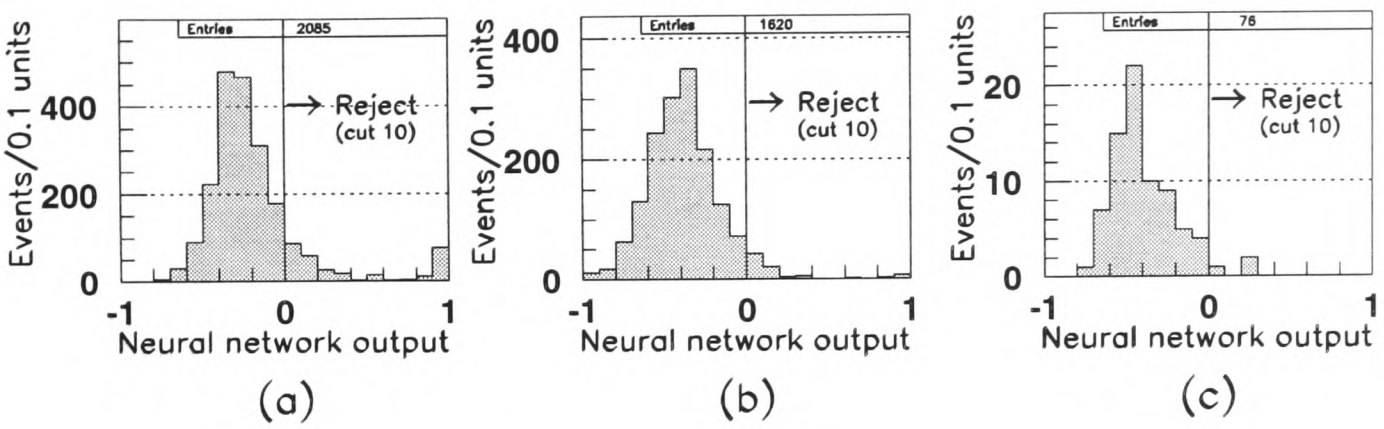

Figure 5.13: Largest neural net output value for the two decay electron clusters for a) pre–selected 1993 data, b) HERWIG Monte Carlo and c) elastic J/ψ 1993 data.

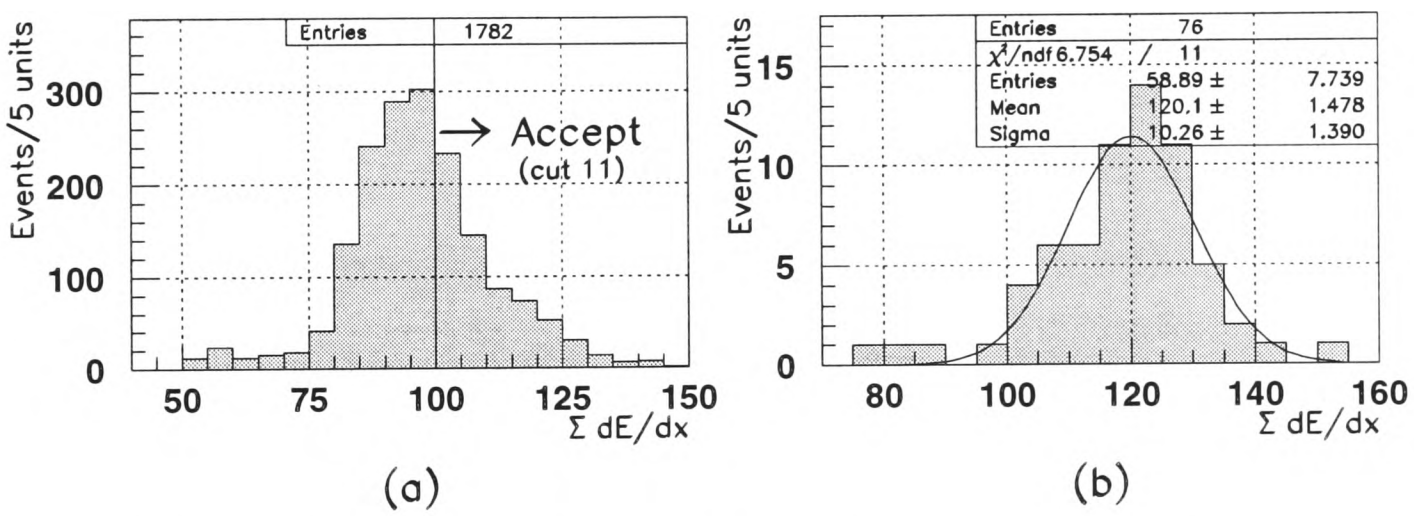

Figure 5.14: a) Sum of pressure corrected $\frac{dE}{dx}$ values for a) the two decay electrons in the pre–selected 1993 data and b) the 1993 elastic J/ψ sample fitted to a gaussian.

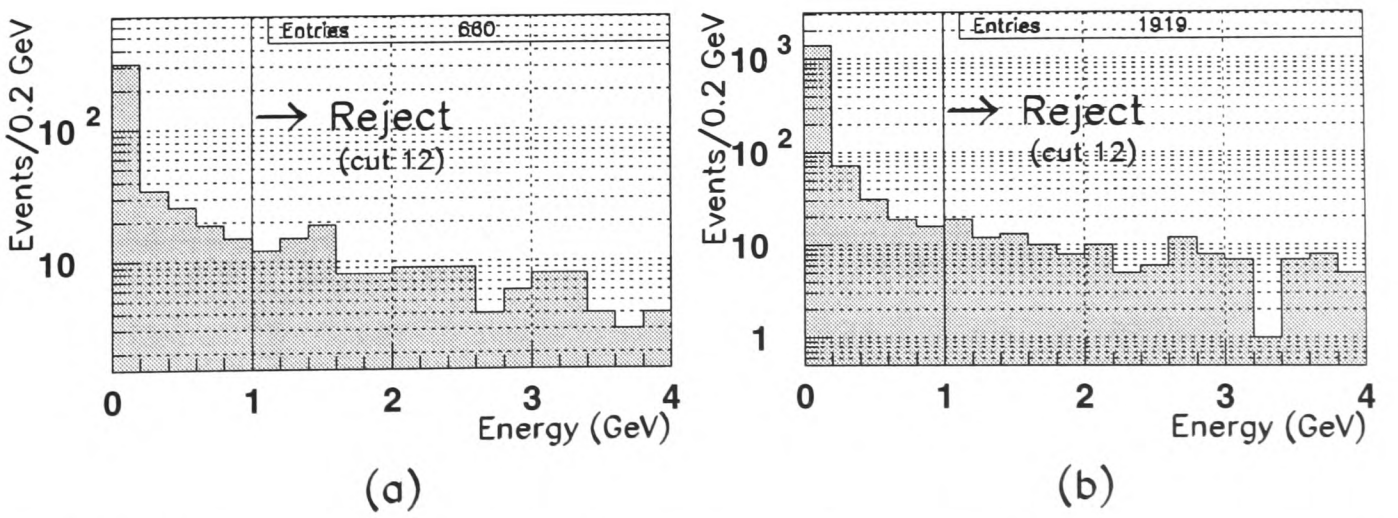

Figure 5.15: Energy in the first ring around the rear beam pipe for a) pre–selected 1993 data and b) HERWIG Monte Carlo.

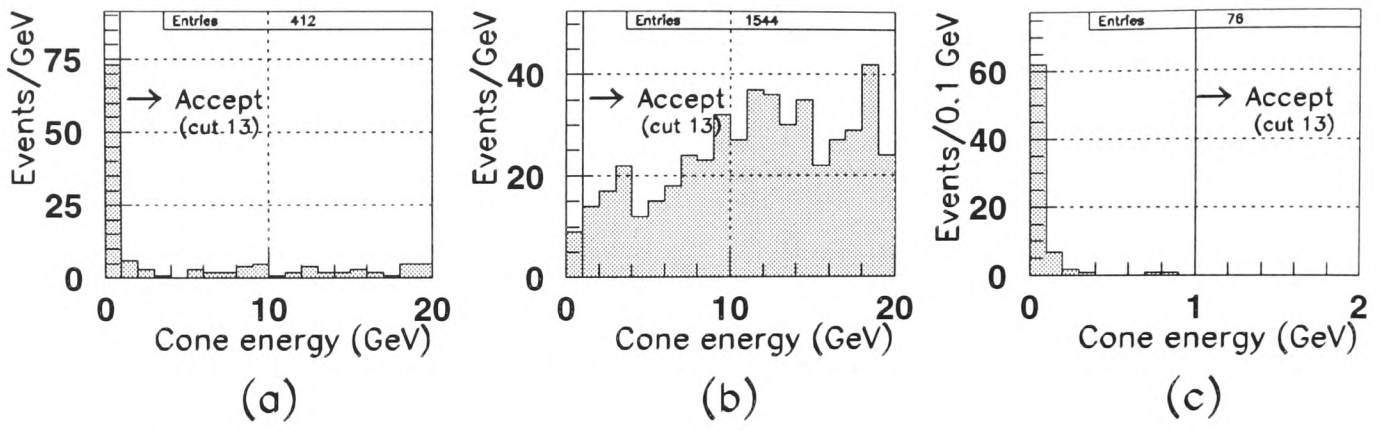

Figure 5.16: Energy in a 35° cone around the forward beam pipe for a) pre–selected 1993 data, b) HERWIG Monte Carlo and c) elastic J/ψ 1993 data.

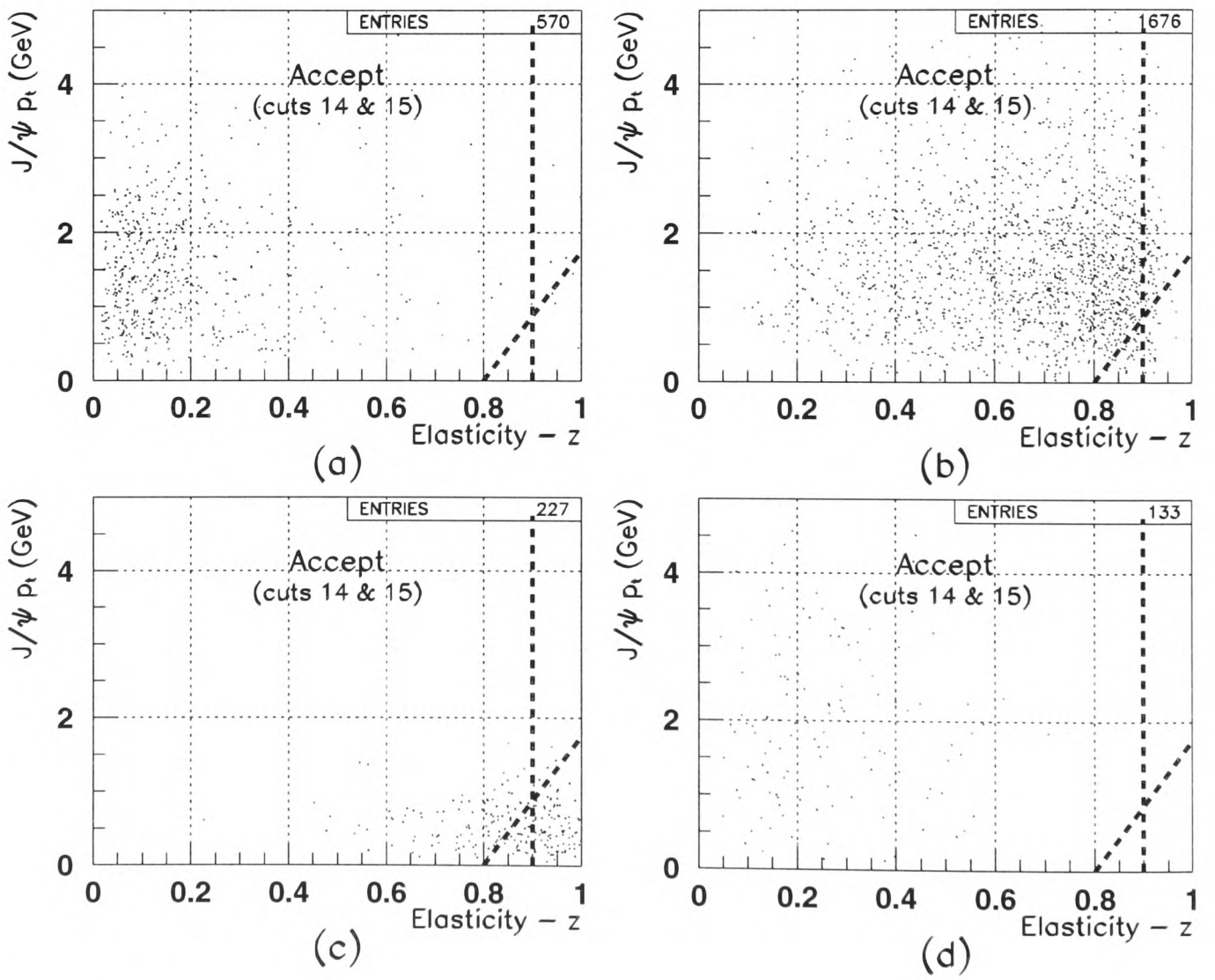

Figure 5.17: Transverse J/ψ momentum vs. elasticity showing the $z \leq 0.9$ cut and the corner cut to reduce proton dissociative J/ψ events for a) pre–selected 1993 data, b) HERWIG Monte Carlo, c) Pythia proton dissociative Monte Carlo and d) EPJPSI resolved photon Monte Carlo.

reconstructed mass distribution in this W region is shown in figure 5.19a. A straight line is fitted to the background and a gaussian fitted to the signal. A clear signal is seen at 3.03±0.03 GeV with a width of 52±15 MeV and containing 13.3±4.6 events. The like–signed background is shown as the hatched area. Due to the bias towards oppositely charged events in the third level trigger as described in section 5.1.2, the levels of like and oppositely–signed background cannot be directly compared, however, it is noted that there is no signal in the like–signed background.

After these cuts, there are no events triggered uniquely by the FLT bits 50 or 58 (elastic J/ψ) or by the TLT bit BGF04 and these are removed from the trigger selection. The elastic ρ FLT trigger, bit 54, is also removed from the sample at this stage – this trigger has an upper cut on the energy around the FCAL beam pipe (see section 5.1.1) and so will contribute little to photon gluon fusion events. A further 6 events are removed from this selection with the removal of the ρ trigger and the resulting reconstructed mass distribution is shown in figure 5.19b. A straight line and gaussian are again fitted giving a clear signal at 3.03±0.03 GeV with a width of 55±16 MeV and containing 12.5±4.6 events. The like–signed background is again shown as the hatched area.

5.5 dE/dx

The $\frac{dE}{dx}$ cut (cut 11 in section 5.4) is very powerful in the search for inelastically produced J/ψ's. The use of $\frac{dE}{dx}$ values for particle identification is discussed in section 3.5.1. The effect of this cut is seen in figure 5.5l where a clear signal is seen at the J/ψ mass region after its application. However, the Monte Carlo does not reproduce $\frac{dE}{dx}$ values, so in order to calculate a cross–section, some other means of estimating the efficiency of this

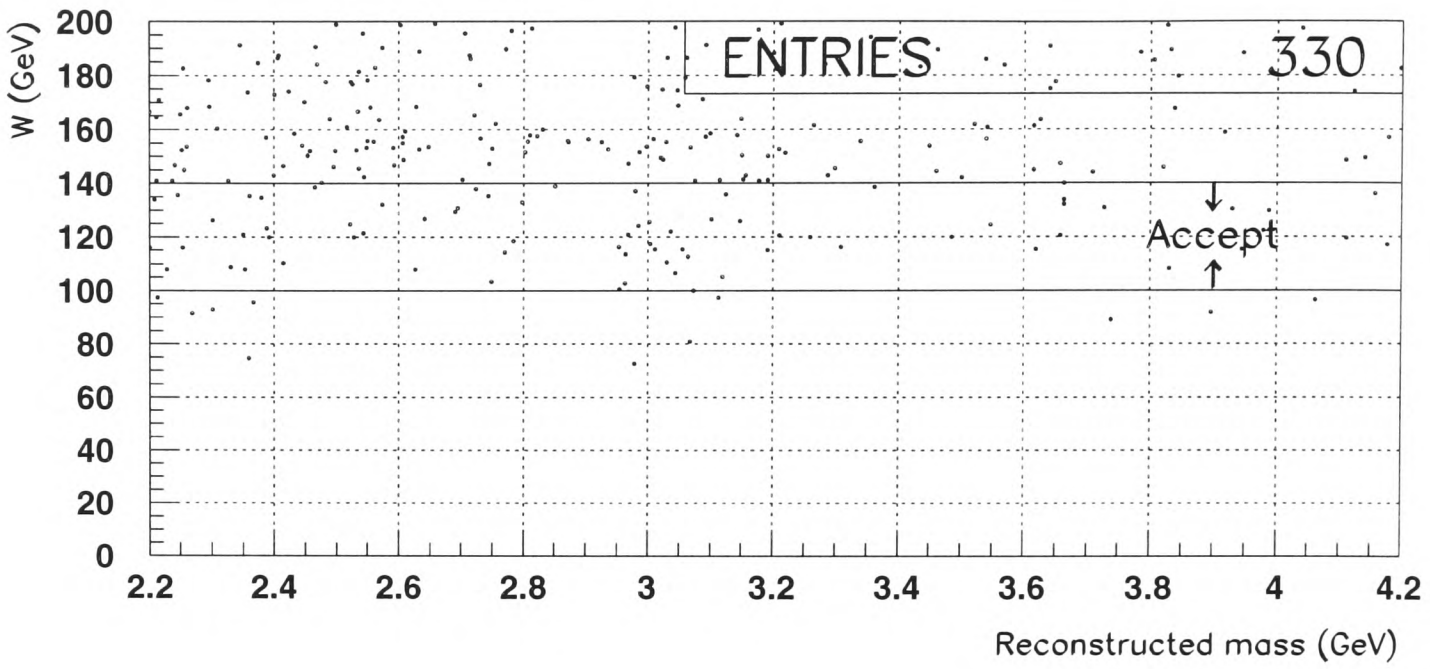

Figure 5.18: W vs. reconstructed mass plot for the inelastic J/ψ selection.

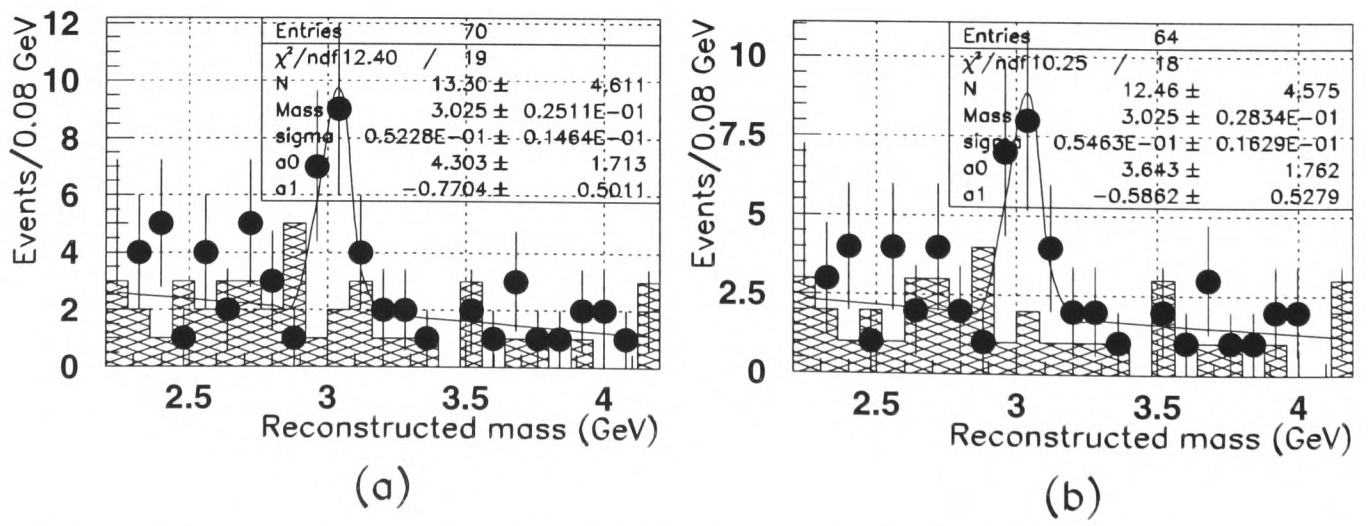

Figure 5.19: Reconstructed mass a) with all selected trigger bits and b) with only FLT bits 40, 41 and 45 and TLT bits BGF03 and BGF05. The like–signed background is shown as the hatched area.

cut is required. A very clean elastic J/ψ signal in the 1993 data is seen in figure 5.3. In figure 5.14b, the sum of the pressure corrected $\frac{dE}{dx}$ values for both decay electrons in this sample is plotted in the mass range 2.85 – 3.15 GeV. This is then fitted to a gaussian, and using the fit parameters the efficiency for the $\frac{dE}{dx}$ cut is estimated to be $97.5^{+0.7}_{-0.9}\%$.

However, before using this method for calculating the efficiency, checks must be made to see if there are differences in the distributions of track momentum, pseudorapidity or the number of hits for decay electron tracks from elastically and inelastically produced J/ψ's. The reason this must be done is because the $\frac{dE}{dx}$ value of an electron track may itself depend on these track variables. If this is the case, the efficiency calculation might be incorrect if tracks from elastically and inelastically produced J/ψ have different distributions in these track variables. Figure 5.20a shows the momentum distribution of both decay electron tracks from the inelastic J/ψ sample with an additional invariant mass cut of 2.85 – 3.15 GeV so as to reduce the background contamination. A similar plot is shown for the elastic J/ψ sample in figure 5.20b. In figures 5.21a and b similar plots are shown for the track pseudorapidity and for the number of hits per track in figures 5.22a and b. Despite the lack of statistics there certainly seem to be some differences in the elastic and inelastic J/ψ samples, particularly in the number of hits and the track momentum distributions. However, one must bear in mind that there are still background events in both the elastic and inelastic J/ψ samples (despite the tighter cut of 2.85 – 3.15 GeV in the reconstructed mass) which could alter the shapes of these distributions.

Having established the distributions of some of the track variables for decay electron tracks from elastically and inelastically produced J/ψ are not quite the same, checks are

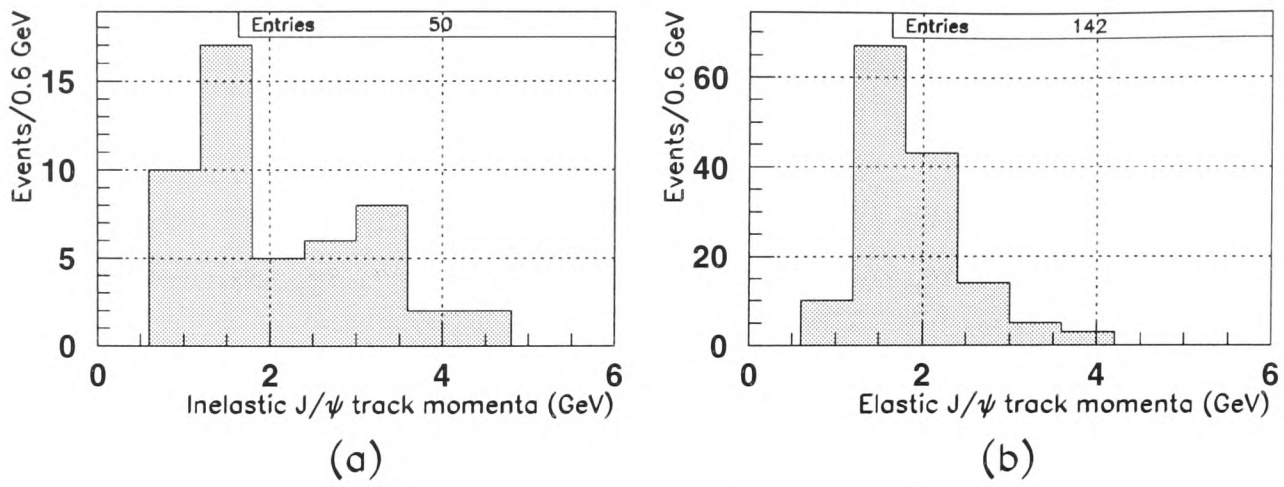

Figure 5.20: Momentum distribution of tracks from the a) inelastic and b) elastic J/ψ samples with an invariant mass in the range 2.85 – 3.15 GeV.

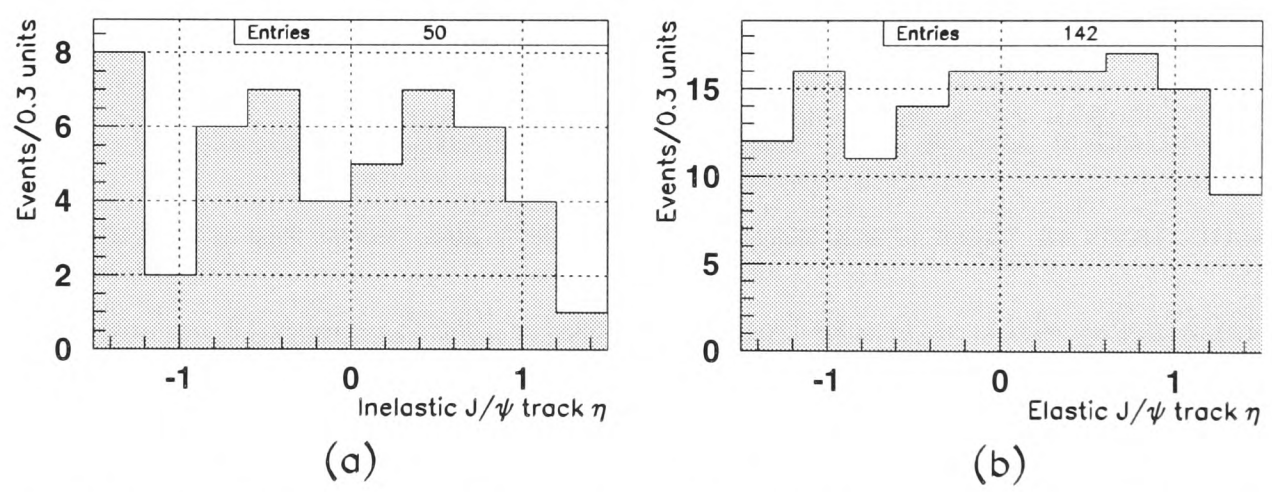

Figure 5.21: Pseudorapidity, η, distribution of tracks from the a) inelastic and b) elastic J/ψ samples with an invariant mass in the range 2.85 – 3.15 GeV.

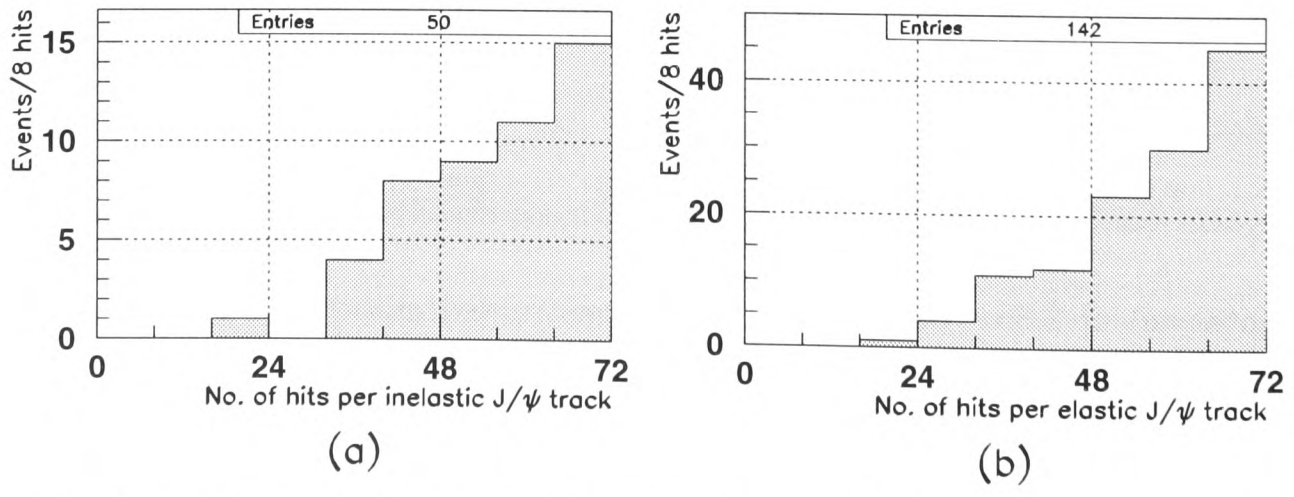

Figure 5.22: Number of hits per track in the a) inelastic and b) elastic J/ψ samples with an invariant mass in the range 2.85 – 3.15 GeV.

now made to see if the $\frac{dE}{dx}$ value of an electron track depends on these track variables. To do this, a large and clean sample of electron tracks is required. The sample of elastic J/ψ's in the 1993 data is not large enough to check that there are no systematic shifts in the mean $\frac{dE}{dx}$ values as a function of these track variables. Therefore, conversion electrons in the 1993 data are studied.

The CONVERT2[16] algorithm is used to select conversion electrons. Running over all the 1993 data, 68,978 candidate conversion pairs are found by requiring the quality cut, IGCTAG = 3. The DistB distribution of all these events is shown in figure 5.23a. The CONVERT2 algorithm only considers pairs with |DistB|$\leq$ 25. There are 6532 like–signed background pairs (with $-25 \leq$ DistB < 0) which are flat as a function of DistB. In order to minimise the background contamination, pairs in the peak: $0 \leq$ DistB < 1, are chosen for our electron sample. The cuts which are applied to the elastic J/ψ electron tracks are also applied to these conversion electrons, namely that both must start in the vertex detector or superlayer 1 of the CTD and extend to at least superlayer 3. Both tracks must have pseudorapidity, $|\eta| \leq 1.5$ and transverse momentum $P_t > 0.6$ GeV. For several runs taken during 1993, no pressure corrections were available or the CTD hi–voltage was low, giving very low $\frac{dE}{dx}$ values. These runs are excluded from the conversion electron sample and also from the inelastic J/ψ analysis. They had a total luminosity of 26.2 nb^{-1} or around 5% of the 1993 data.

After the cuts, 291 conversion pairs remain and the $\frac{dE}{dx}$ values of both their tracks are plotted in figure 5.23b. The $\frac{dE}{dx}$ distribution of the like–signed background pairs ($-25 \leq$ DistB < 0) with the same track cuts is shown in figure 5.23c. As expected, these tracks tend to have lower $\frac{dE}{dx}$ values suggesting that there is a larger hadron component in

[16] See section 3.6 for a description of the CONVERT2 algorithm and the variables IGCTAG and DistB.

the like–signed background. Assuming the level of background to be the same in the opposite–signed conversion pairs (with $0 \leq \text{DistB} < 1$), the background $\frac{dE}{dx}$ distribution (with $-25 \leq \text{DistB} < 0$) is scaled by 1/25 and subtracted from peak distribution in figure 5.23b to give the corrected $\frac{dE}{dx}$ distribution for conversion electrons shown in figure 5.23d.

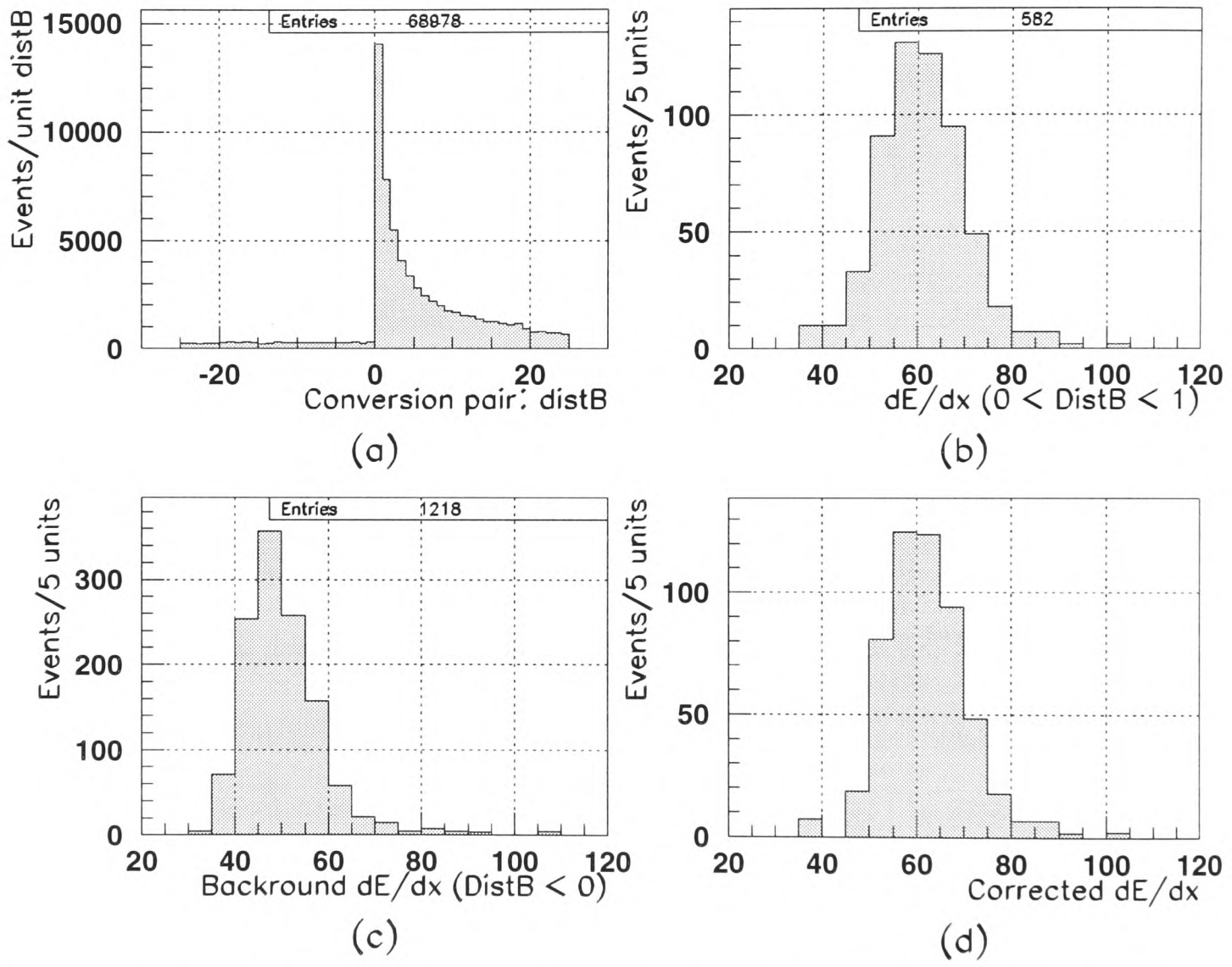

Figure 5.23: a) DistB for all the conversion pair candidates in the 1993 data with IGCTAG = 3, b) $\frac{dE}{dx}$ distribution of conversion tracks with $0 \leq \text{DistB} < 1$, c) $\frac{dE}{dx}$ distribution of tracks from the like-signed background pairs with $-25 \leq \text{DistB} < 0$, d) background subtracted $\frac{dE}{dx}$ distribution.

In figure 5.24a, the $\frac{dE}{dx}$ of the two conversion tracks (with $0 \leq \text{DistB} < 1$) is plotted against their track momenta. The mean $\frac{dE}{dx}$ value is calculated in six bins of track momenta by fitting a gaussian to the background subtracted histogram for each bin.

The background subtraction is performed using the same method as for figure 5.23d. The width of the gaussian fit is taken as the error on the mean and this is plotted in figure 5.24b. The mean $\frac{dE}{dx}$ is flat with respect to the track momentum up till around 3 GeV and then there are signs of a small rise at higher momenta. Since the decay electrons from elastically and inelastically produce J/ψ generally have momenta of less than 3 GeV (see figure 5.20), this small rise does not worry us. Figures 5.25a and b show similar plots for the track pseudorapidity, η, and the mean $\frac{dE}{dx}$ value shows a very small dip near $\eta = 0$ in figure 5.25b. There are more tracks from elastically produced J/ψ in this region, which would tend to push their mean $\frac{dE}{dx}$ values lower. However, the deviation in the mean binned $\frac{dE}{dx}$ values is less than 10% and there are around 20% more tracks from elastically produced J/ψ around the $\eta = 0$ region, than from inelastically produced J/ψ. This will therefore give an error of less than 2% in calculating the efficiency. Figures 5.26a and b show plots for the number of hits per track. Figure 5.26b shows that the mean $\frac{dE}{dx}$ is almost flat in the region 40 – 80 hits per track. The majority of tracks from elastically and inelastically produced J/ψ lie in this region, so differences in their distributions in this variable will not give rise to errors in the $\frac{dE}{dx}$ efficiency calculation.

As a final check on the efficiency calculation of this $\frac{dE}{dx}$ cut, the efficiency is calculated using this sample of conversion electrons. In figure 5.27, the sum of the $\frac{dE}{dx}$ values for each conversion pair is plotted with a) $0 \leq \text{DistB} < 1$ and b) $-25 \leq \text{DistB} < 0$ (like–signed background) and in c) the background has been subtracted and the resulting distribution fitted to a gaussian. Using the fit parameters, the efficiency of the $\frac{dE}{dx}$ cut is estimated to be $96.0^{+0.2}_{-0.4}\%$, just over one standard deviation away from the value obtained using the elastic J/ψ sample of $97.5^{+0.7}_{-0.9}\%$.

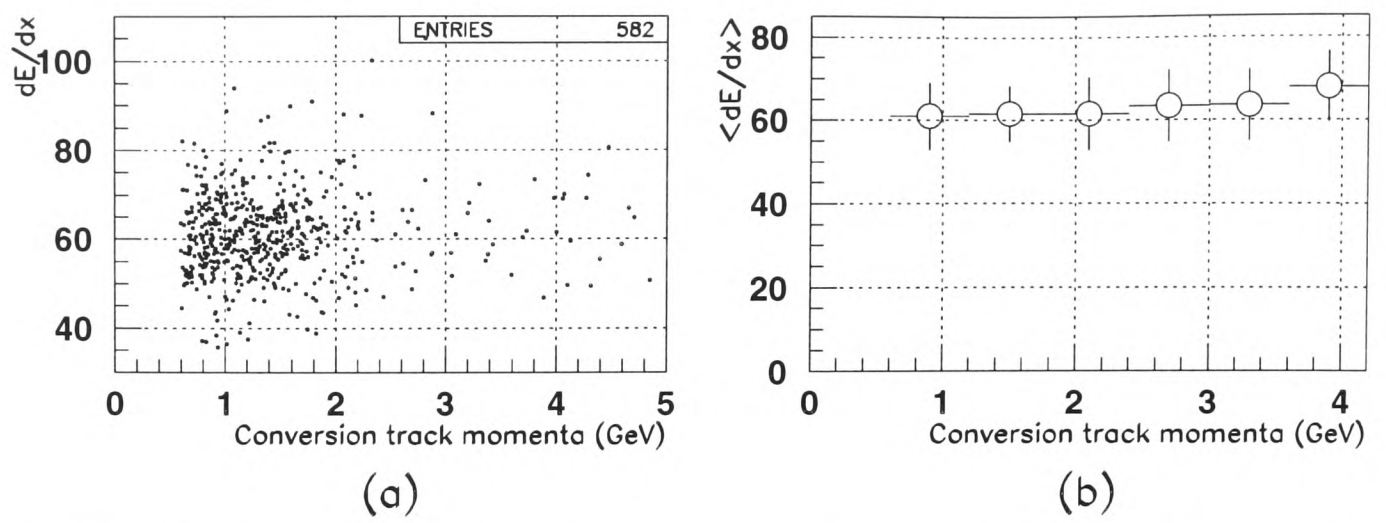

Figure 5.24: a) $\frac{dE}{dx}$ vs. track momenta for conversion tracks with $0 \leq \text{DistB} < 1$ and b) mean background subtracted $\frac{dE}{dx}$ in momentum bins.

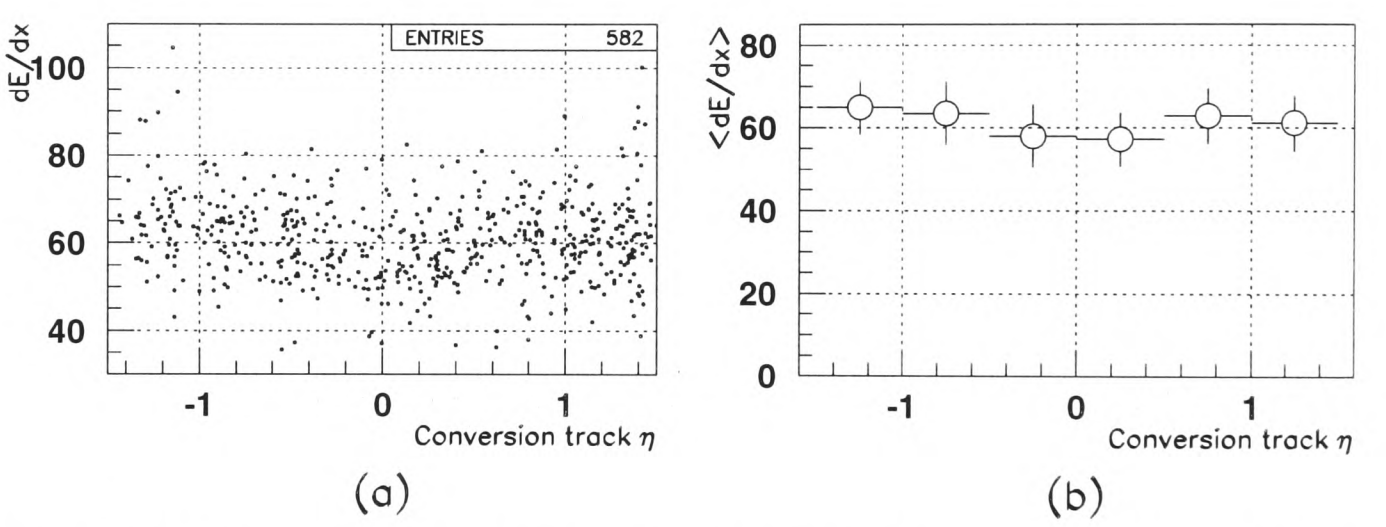

Figure 5.25: a) $\frac{dE}{dx}$ vs. track pseudorapidity, η, for conversion tracks with $0 \leq \text{DistB} < 1$ and b) mean background subtracted $\frac{dE}{dx}$ in pseudorapidity bins.

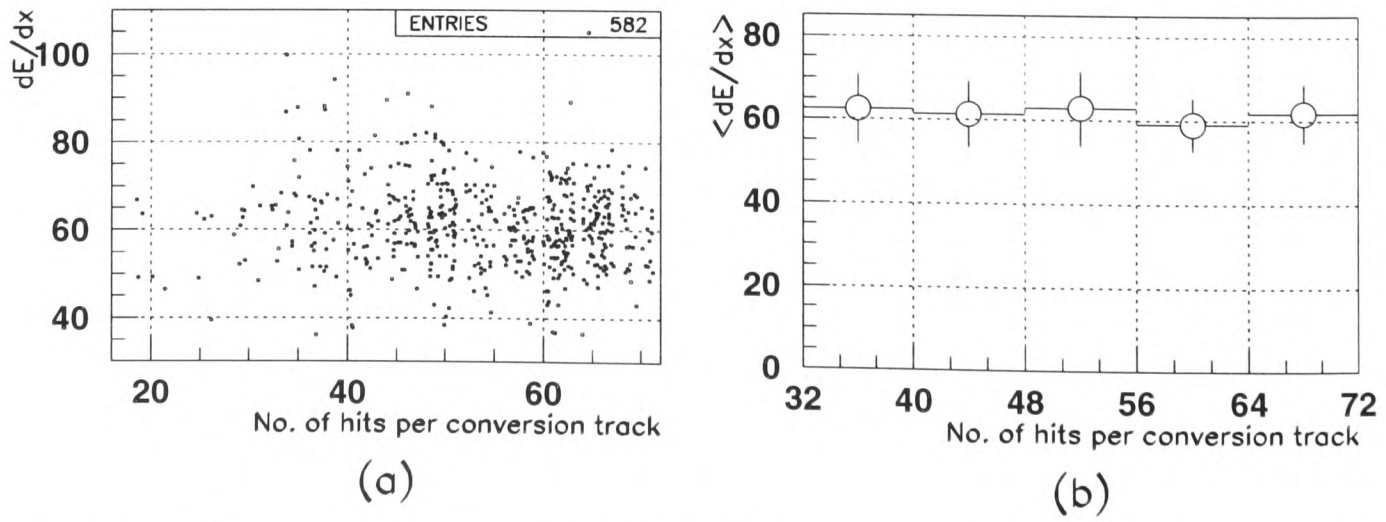

Figure 5.26: a) $\frac{dE}{dx}$ vs. number of hits per conversion track with $0 \leq \text{DistB} < 1$ and b) mean background subtracted $\frac{dE}{dx}$ in bins of number of hits.

Since the distributions of the track variables from the elastic J/ψ sample match those from the inelastic J/ψ sample more closely than those from conversion electrons, the efficiency calculated from the elastic J/ψ tracks will be used later in the cross–section calculation. This study with the conversion electrons will allow us to estimate the systematic error on the efficiency calculation arising from the differences in the distributions of the track variables between the elastic and inelastic J/ψ samples.

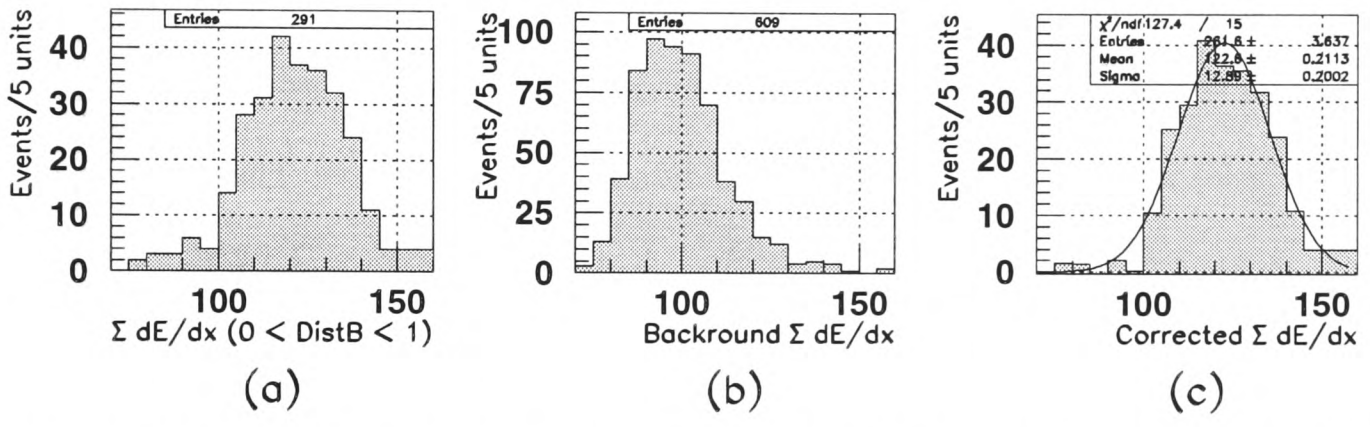

Figure 5.27: Sum of $\frac{dE}{dx}$ values for candidate conversion pairs with a) $0 \leq \text{DistB} < 1$ and b) $-25 \leq \text{DistB} < 0$ (like–signed background) and c) the background subtracted distribution.

5.6 Monte Carlo studies

In this section, the acceptance of the detector to J/ψ events is calculated using the HERWIG inelastic J/ψ Monte Carlo. Figure 5.28a shows the generated W distribution of the 34,319 generated events. Of these, 14039 (41%) are found by the pre–selection code described above, without the trigger and DST bits set. Figure 5.28b shows the reconstructed against generated W for these events. A significant number of events are seen with a much larger reconstructed than generated W. These are events where the assumption that the scattered incident electron does not enter the calorimeter is not valid (used in the calculation of W, see equation 3.4 in section 3.2). Figures 5.29a and b show the reconstructed W distribution and acceptance for these events.

The reconstructed W distribution and acceptance with the FLT, TLT triggers and DST bit 23 set are shown in figures 5.30a and b with the acceptance of the pre–selected sample shown as a dotted line for reference in figure 5.30b. It is seen that events are lost predominantly in the lower W ranges because with a lower γp centre–of–mass energy, these events deposit less energy, particularly in the rear part of the calorimeter and so do not have sufficient energy to pass the FLT triggers.

In figures 5.31a and b, the W distribution and acceptance are shown with all the decay electron selection cuts (except the $\frac{dE}{dx}$ cut since this is not well reproduced in Monte Carlo) applied (namely cuts 1 – 10 detailed in section 5.4). The previous acceptance of figure 5.30b is shown as a dotted line in figure 5.31b. A large decrease in acceptance is seen indicating that the cuts needed to be very tight to separate the signal.

Finally, the cuts 12 – 15 used to select the physics process are applied. The corresponding W distribution and acceptance are shown in figures 5.32a and b with the acceptance of figure 5.31b shown as a dotted line. The acceptance is significantly reduced at high W where the low Q^2 cut 12 removes events where the scattered electron enters the calorimeter, invalidating the assumption used to calculate W, as explained above. Below 200 GeV, the acceptance is not greatly reduced, which is to be expected since these further cuts are designed to keep inelastic J/ψ events and reject other J/ψ production mechanisms.

For the purpose of a cross–section calculation, only two W bins between 100 and 140 GeV are considered since the acceptance is too low outside this range. For this final HERWIG sample, the elasticity, z, and the J/ψ transverse momentum are shown in figures 5.33a and b respectively.

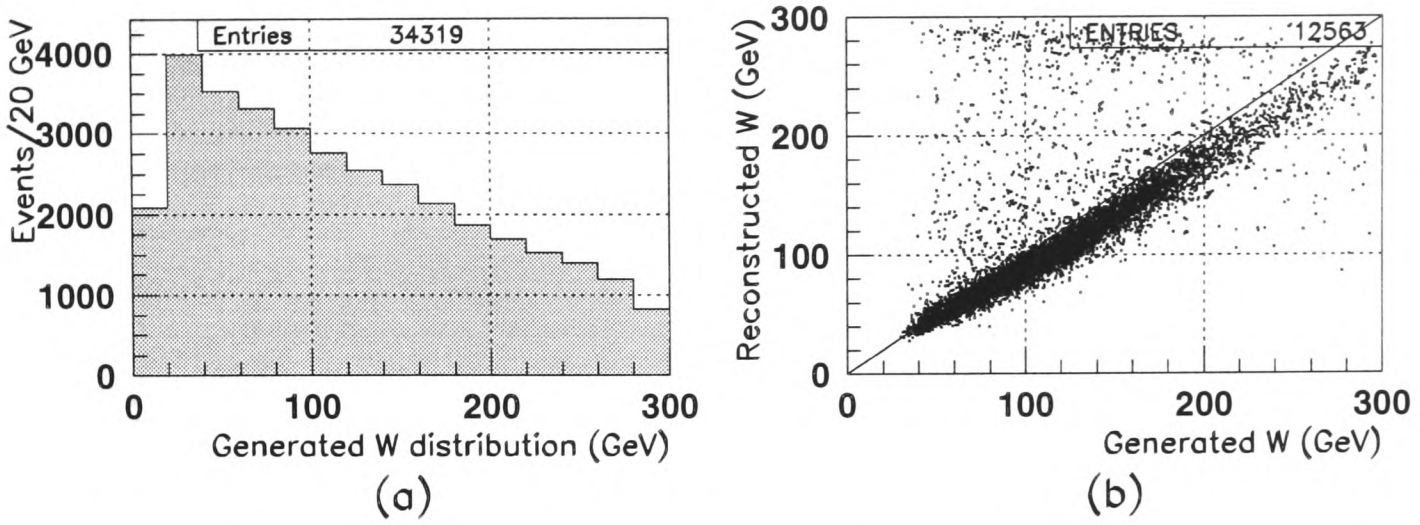

Figure 5.28: a) W distribution (GeV) of HERWIG generated events b) Correlation between reconstructed and generated W for pre–selected HERWIG events.

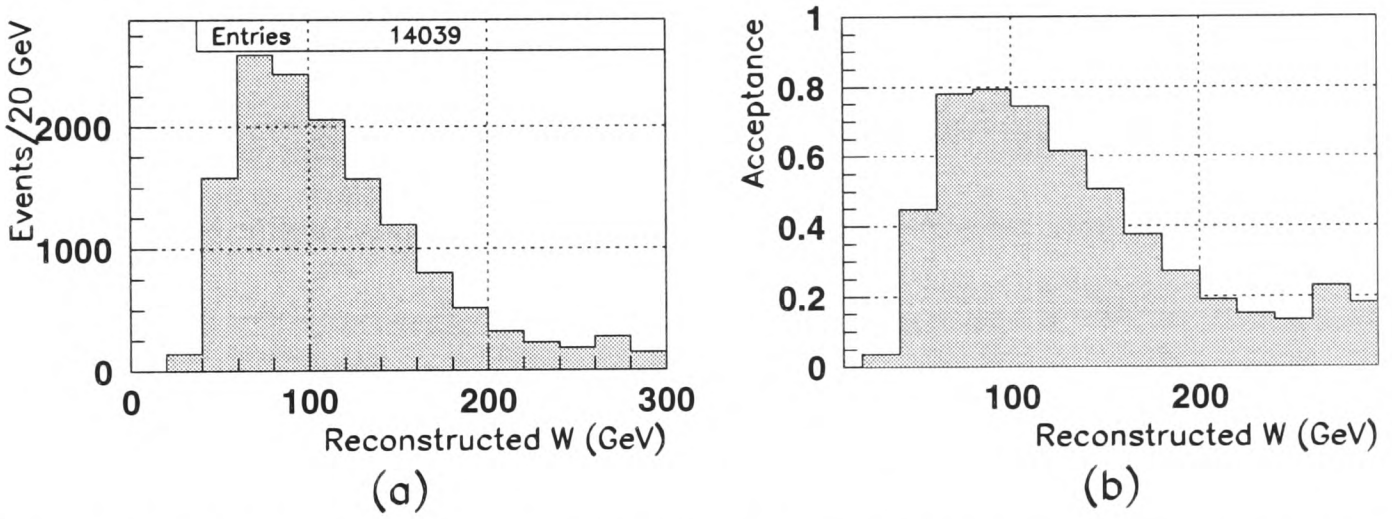

Figure 5.29: a) W distribution (GeV) and b) W acceptance of pre–selected HERWIG generated events (without trigger or DST bits set).

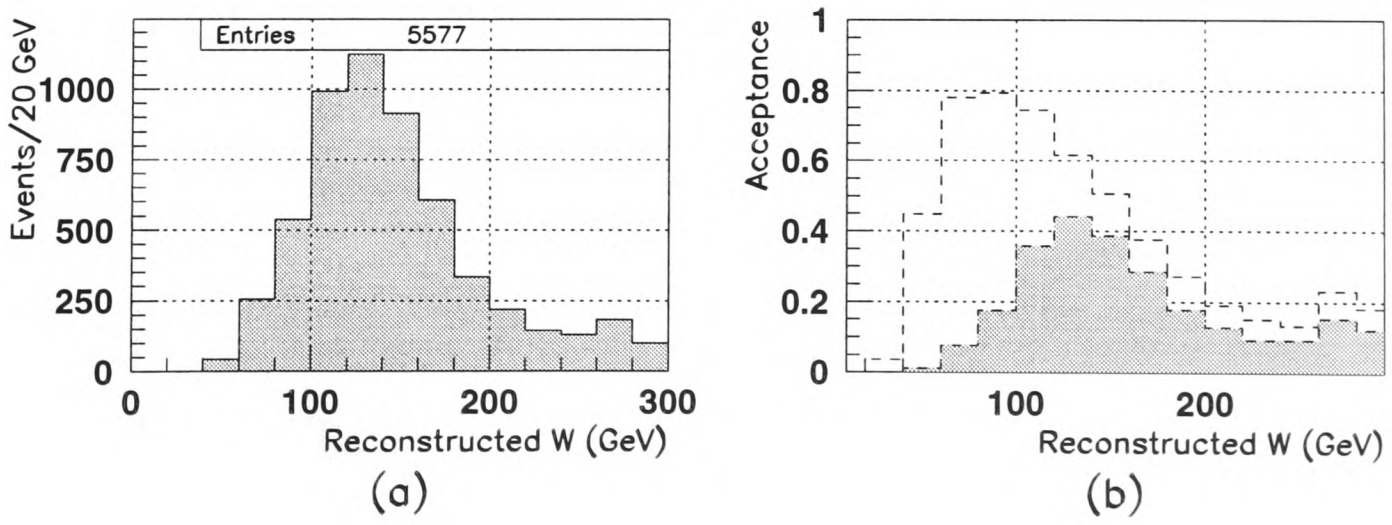

Figure 5.30: a) W distribution (GeV) and b) W acceptance of pre–selected HERWIG generated events with trigger and DST bits set. The previous acceptance without trigger and DST bits set is shown as the dotted line.

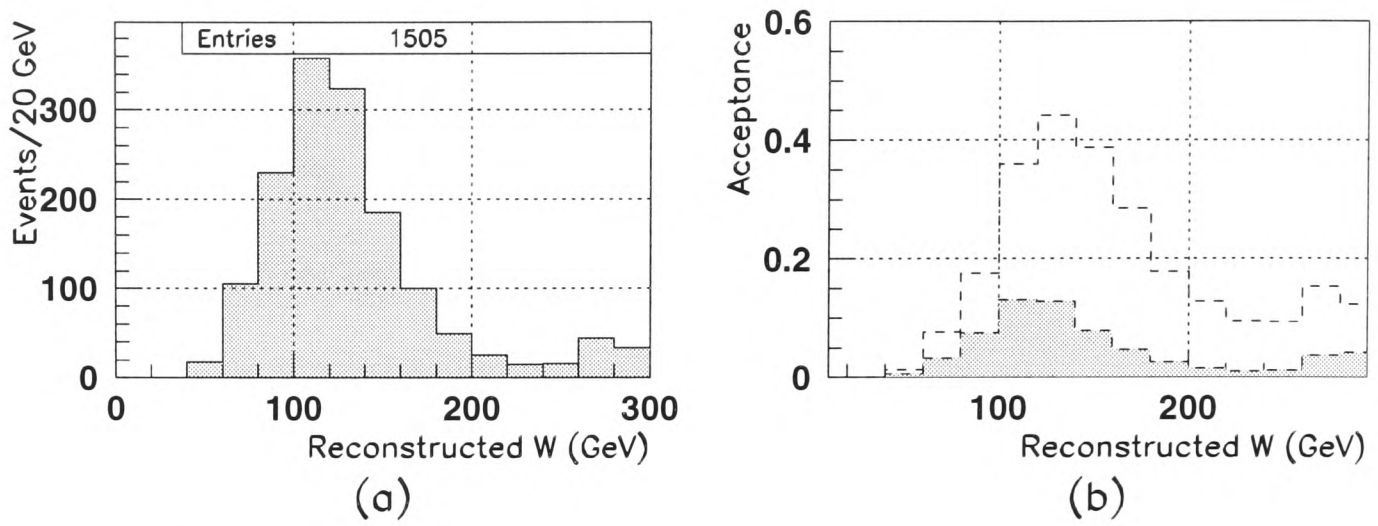

Figure 5.31: a) W distribution (GeV) and b) W acceptance of HERWIG generated events with trigger and DST bits set and all decay electron identifying cuts applied. The previous acceptance with just the trigger and DST bits set is shown as the dotted line.

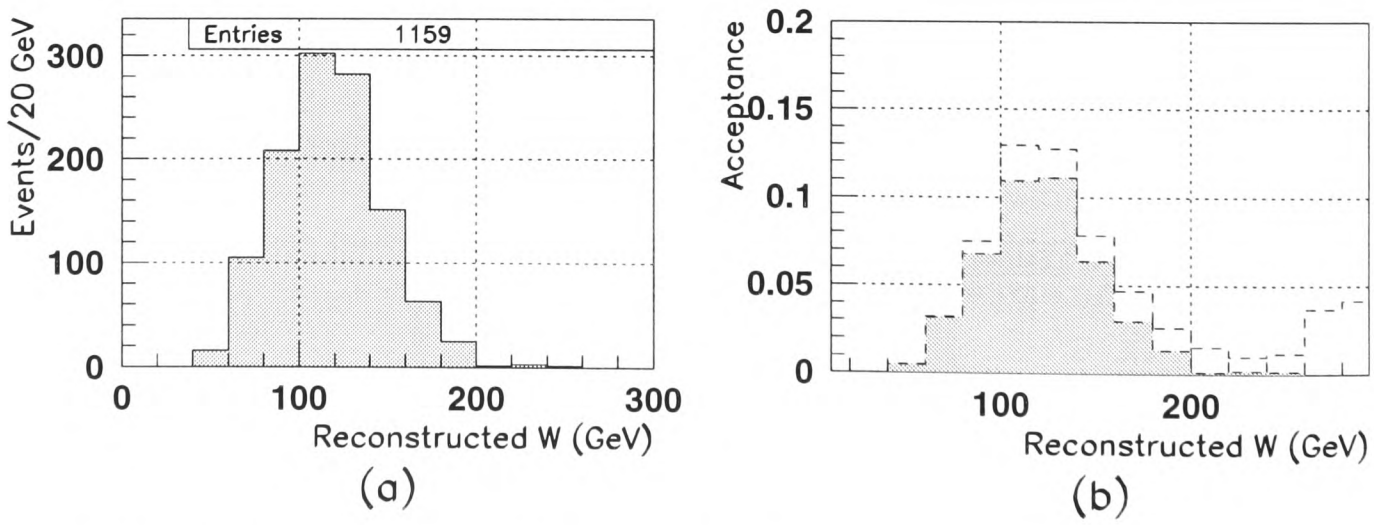

Figure 5.32: a) W distribution (GeV) and b) W acceptance of the final selection of HERWIG generated events after all the cuts have been applied. The previous acceptance with the trigger and DST bits set and the decay electron identifying cuts applied is shown as the dotted line.

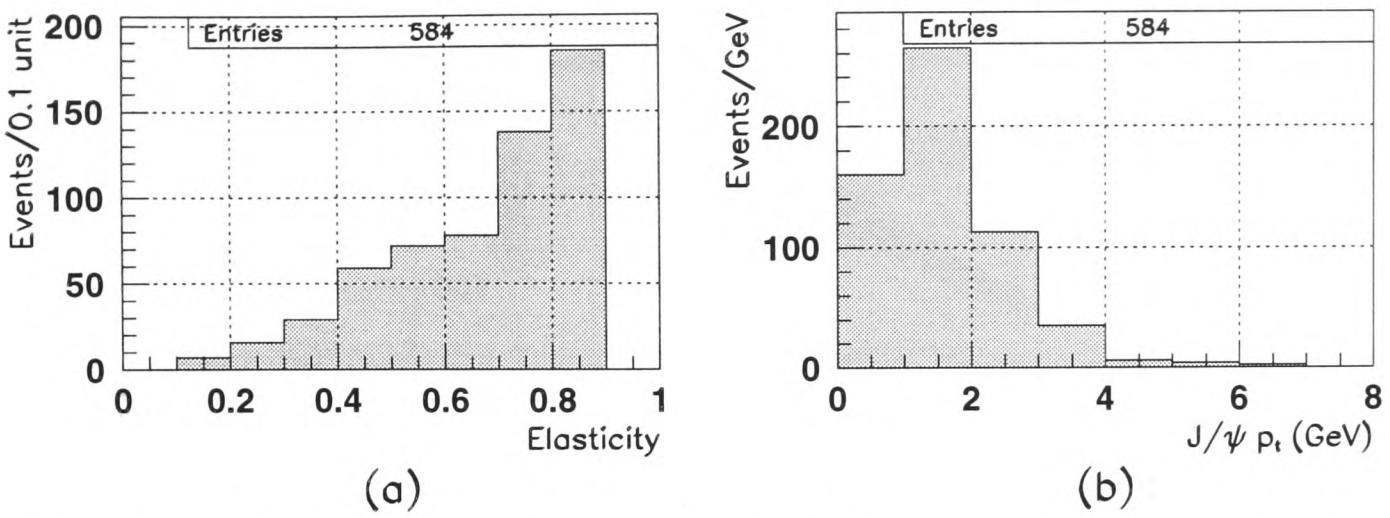

Figure 5.33: Distribution of a) elasticity and b) J/ψ transverse momentum of the final selection of HERWIG generated events with $100 \leq W \leq 140$ GeV.

In figure 5.34a, the correlation between the reconstructed and generated W is shown for the whole W range, and in figure 5.34b, $(W^{rec} - W^{gen})/W^{gen}$ is plotted for $100 \leq W \leq 140$ GeV and fitted a gaussian, giving a $(6.3 \pm 0.2)\%$ width. A systematic shift of $(11.9 \pm 0.3)\%$ is also seen in the reconstructed value. Similar plots for the W range 100 – 140 GeV are shown for the J/ψ transverse momentum in figures 5.35a and b where the width is $(6.1 \pm 0.2)\%$ and for the elasticity, z, in figures 5.36a and b with a width of $(12.2 \pm 0.5)\%$ and a systematic shift of $(6.4 \pm 0.6)\%$. These systematic shifts will be accounted for when calculating the acceptance for the inelastic J/ψ selection cuts.

5.7 Production mechanisms entering the signal

5.7.1 Resolved photon J/ψ production

Contributions to the signal from resolved photon channel J/ψ events are studied in this section. Figure 2.19 in section 2.6.2 shows the diagram for one such process. Resolved photon channel J/ψ events are produced using the Monte Carlo generator EPJPSI 3303 with the DG proton structure function. It is found that a significant number of

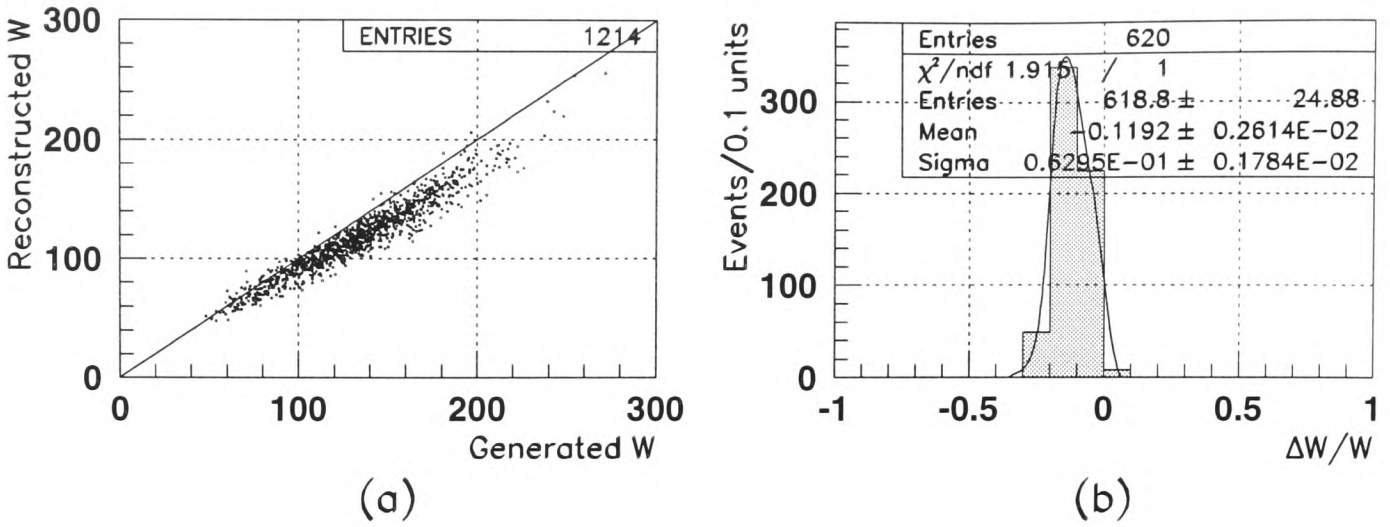

Figure 5.34: a)Reconstructed against generated W (GeV) and b) $(W^{rec} - W^{gen})/W^{gen}$ for the final selection of HERWIG events with $100 \leq W \leq 140$ GeV in (b).

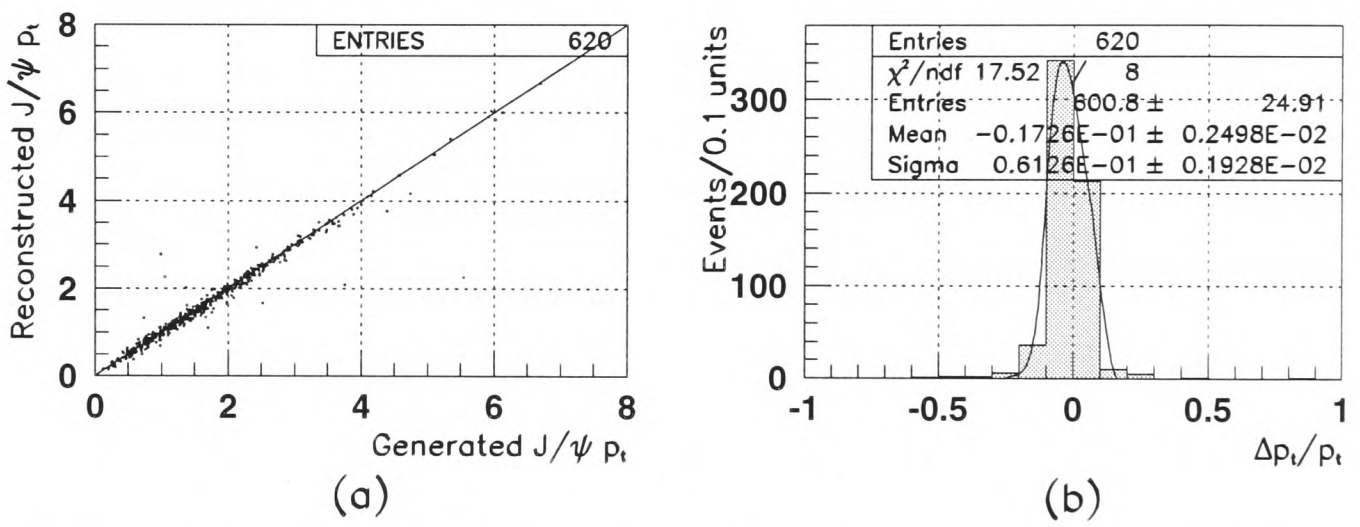

Figure 5.35: a)Reconstructed against generated J/ψ transverse momentum (GeV) and b) $(P_t^{rec} - P_t^{gen})/P_t^{gen}$ for the final selection of HERWIG events with $100 \leq W \leq 140$ GeV.

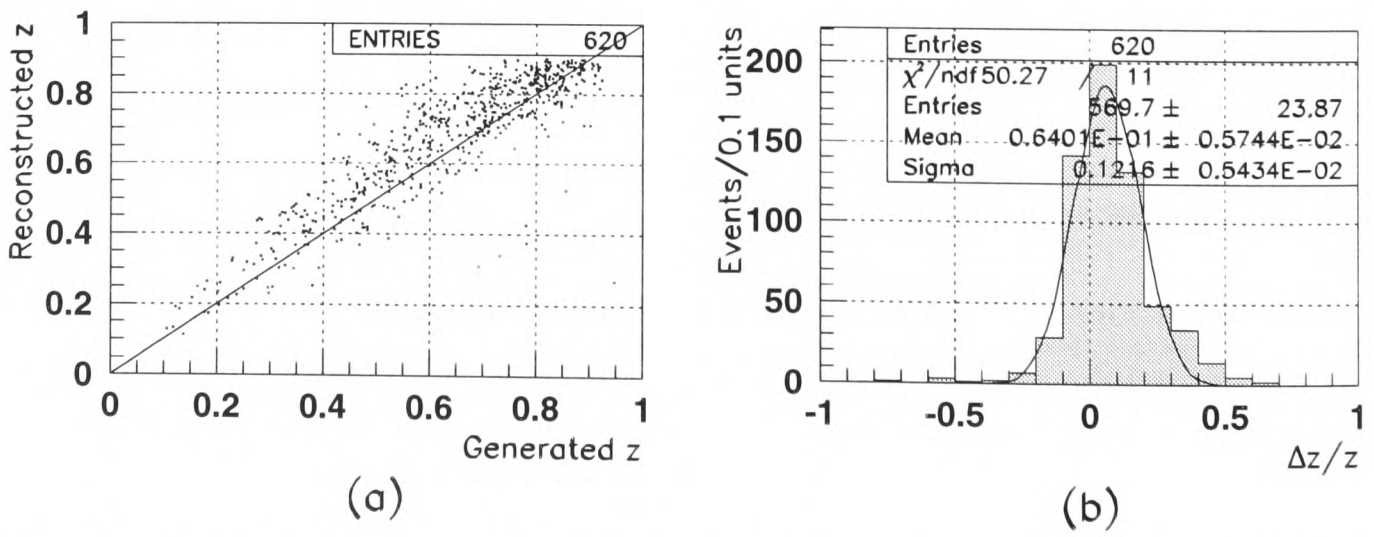

Figure 5.36: a)Reconstructed against generated elasticity, z, and b) $(z^{rec} - z^{gen})/z^{gen}$ for the final selection of HERWIG events with $100 \leq W \leq 140$ GeV.

these events passed all the cuts detailed in section 5.4. The acceptance for resolved photon Monte Carlo events is shown as a function of W in figure 5.37a. In the range $100 \leq W \leq 140$ GeV, the acceptance, of around 5%, is of the same order of magnitude as for HERWIG direct inelastic Monte Carlo events (approximately 13%).

In this channel, the rearward heading incident photon breaks up before interacting to produce the J/ψ. The photon remnant is then expected to deposit most of its energy in the RCAL, thus contributing to the $(E - p_z)_{total}$ and lowering the elasticity of the event (see equation 3.5). In figure 5.37b, the elasticity distribution for EPJPSI resolved photon J/ψ Monte Carlo is shown and the events lie in the low elasticity region. This is to be compared to figure 5.33a showing the same distribution for HERWIG direct inelastic J/ψ Monte Carlo where events tend to lie at a higher elasticity.

In figures 5.38a and b, the elasticity for 1993 data events is shown in the signal reconstructed mass range 2.85 – 3.15 GeV and in the sideband ranges 2.4 – 2.7 GeV and 3.3 – 3.6 GeV respectively. Of the 26 events in the signal mass range, there are expected to be 7.1 background events from the fit of the reconstructed mass distribution in figure 5.19b. The sideband z distribution is scaled to this number of events and subtracted from the signal z distribution, leaving what is expected to be the z distribution of the accepted J/ψ events in figure 5.38c. Comparing this with the z distribution of HERWIG direct inelastic J/ψ Monte Carlo in figure 5.33a, it is seen that there is an excess of events in the low z region suggesting contamination of the signal from resolved photon J/ψ events.

In order to isolate the direct inelastic process, another cut demanding that the elasticity, $z \geq 0.5$ is introduced, as indicated in the reconstructed mass vs. elasticity scatter plot, figure 5.39a. This cut also helps reduce the combinatorial background,

since low z events tend to have more calorimeter energy outside the J/ψ decay leptons, and hence more tracks in the event. The reconstructed mass distribution after this cut is fitted to a gaussian and straight line in a tighter mass region 2.6 – 4.2 GeV as shown in figure 5.39b. The fit gives 6.0 ± 3.7 signal events and there are now only four like–signed background events shown as the hatched area.

The W acceptances of the direct and resolved photon Monte Carlos after this elasticity cut are shown in figures 5.40a and b respectively. In the range $100 \leq W \leq 140$ GeV, the acceptance of direct inelastic events is 10.1% and so this lower elasticity cut has an 81.0% efficiency. However, for resolved photon events, the efficiency has dropped to 0.8% in the same W range as intended.

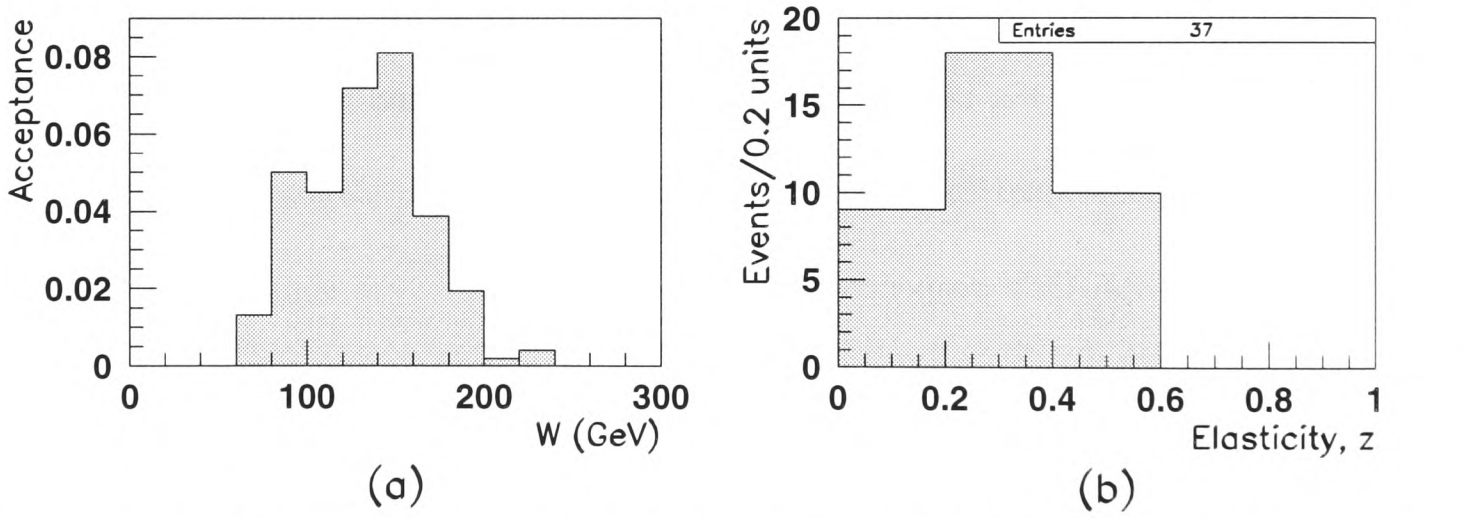

Figure 5.37: a) W acceptance (GeV) and b) elasticity distributions for EPJPSI resolved photon Monte Carlo events.

5.7.2 Elastic ψ' production

Another possible source of background to the inelastic J/ψ sample comes from the ψ' which is the excited 2^3S state of the $c\bar{c}$ system with a mass of 3686.00 ± 0.09 MeV. It therefore lies below the mass threshold required for the decay to $D\bar{D}$. One of the possible decay modes is via $(J/\psi + \textit{anything})$ with a $(57 \pm 4)\%$ branching ratio. The J/ψ then

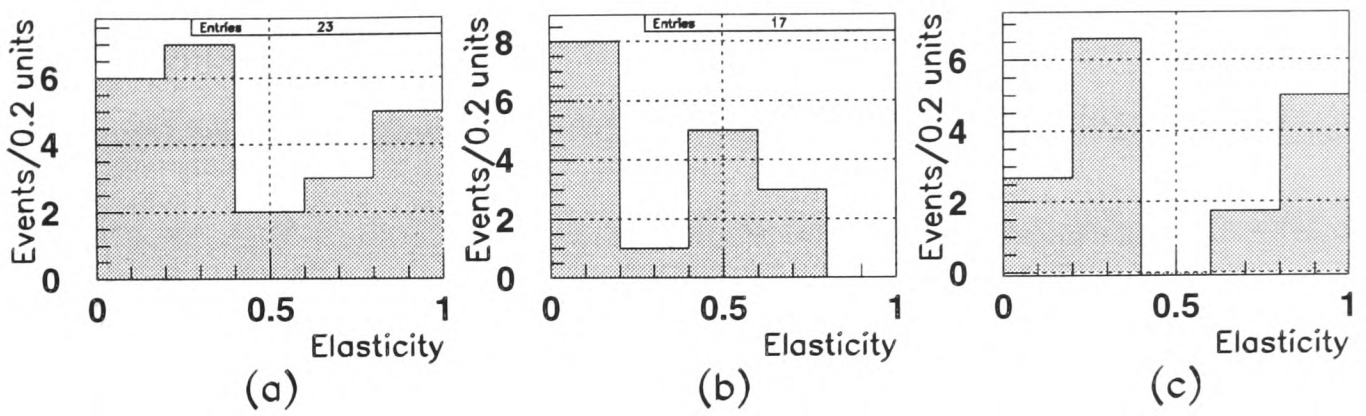

Figure 5.38: z distribution of J/ψ candidate events in the a) signal reconstructed mass region, 2.85 – 3.15 GeV and b) sideband mass region 2.4 – 2.7 and 3.3 – 3.6 GeV. c) z distribution in signal region after background subtraction.

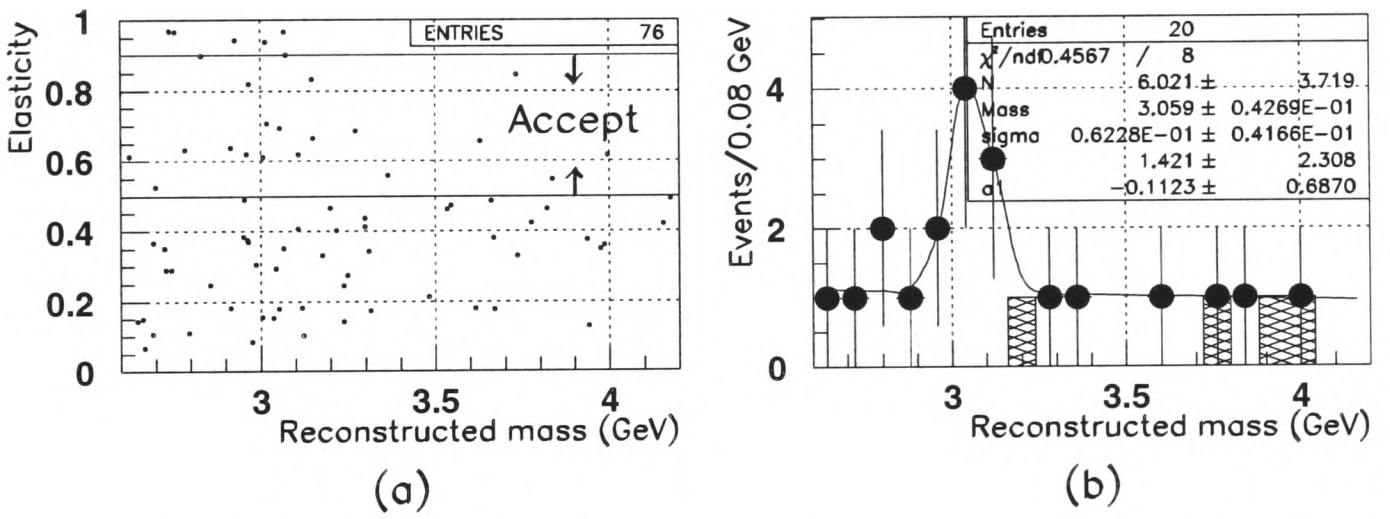

Figure 5.39: a) Scatter plot of reconstructed mass vs. elasticity and b) reconstructed mass distribution of events fitted to a gaussian plus a straight line after $0.5 \leq z \leq 0.9$ cut with the like–signed background shown as the hatched area.

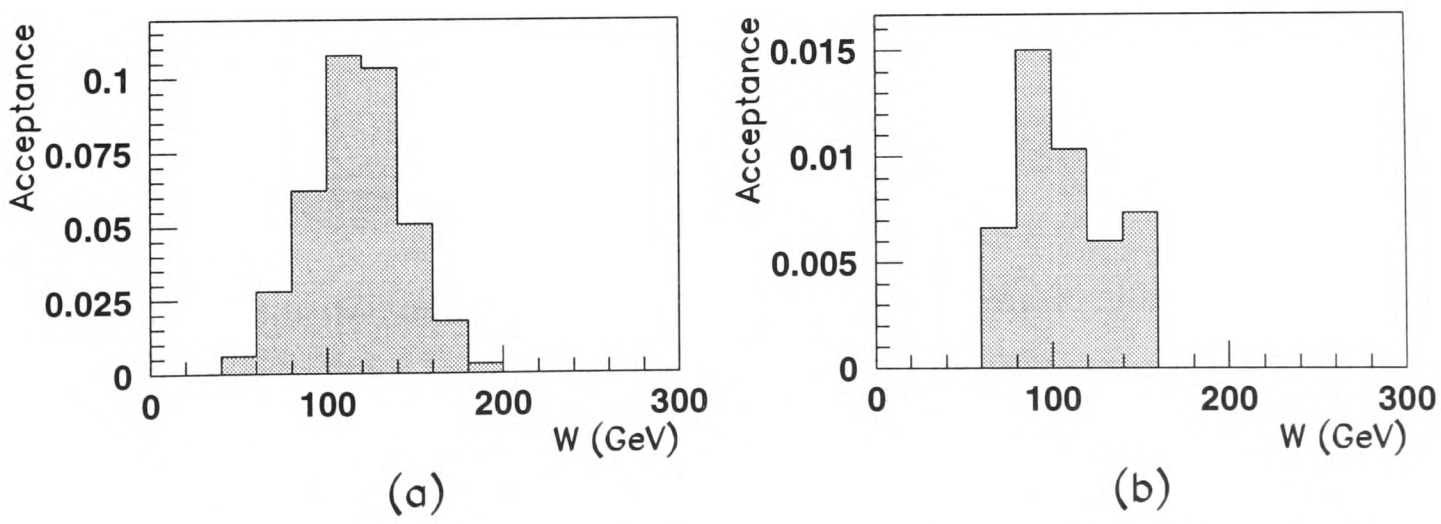

Figure 5.40: W acceptances for a) HERWIG direct and b) resolved photon inelastic J/ψ Monte Carlos.

has a $(5.99 \pm 0.25)\%$ branching ratio to decay via the electron channel and contribute to the inelastic J/ψ signal with the other decay products of the ψ' contributing to the energy required to pass the inelasticity requirement (cut 13 in section 5.4).

The strong decays of the ψ' dominate leaving only a branching ratio of $\sim 0.01\%$ for the decay $\psi' \rightarrow e^+e^-$. However, one of the possible decay modes of the ψ' is $\psi' \rightarrow J/\psi\, \pi^+\, \pi^-$ which has a branching ratio of $(32.4 \pm 2.6)\%$. If an elastically produced ψ' decayed through this channel, and the J/ψ subsequently decayed via the electron channel, then there would be four tracks in the detector belonging to the e^+, e^-, π^+ and π^- with nothing else seen in the detector. This could then fake an inelastic J/ψ event with the two pions providing sufficient energy to pass cut 13 in section 5.4, designed to remove elastic J/ψ events.

Checks were made for such events by scanning through the inelastic J/ψ sample by hand and looking for four track events. The reconstructed mass of the four tracks could then be calculated and this should correspond to the ψ' mass, however, no such events were found. Therefore, it is assumed using Poisson statistics with a 90% confidence level, that in the inelastic J/ψ sample, there is an upper limit of 2.3 elastic ψ' events decaying to $J/\psi\ \pi^+\pi^-$ with the J/ψ subsequently decaying via the electron channel. Multiplying this limit by:

$$\frac{\mathcal{B}.\mathcal{R}.(\psi' \rightarrow J/\psi\ +\ anything)}{\mathcal{B}.\mathcal{R}.(\psi' \rightarrow J/\psi\ \pi^+\pi^-)} = \frac{57\%}{32.4\%} \tag{5.1}$$

an upper limit of around five elastic ψ' events decaying into $(J/\psi\ +\ anything)$ is set with 90% confidence. From figure 5.3, it is seen that there are around 80–90 elastic J/ψ events in the 1993 data. Thus, the upper limit for the ratio of elastic J/ψ and ψ' cross–sections can be estimated to be around 6%.

Contamination of the inelastic J/ψ sample from inelastically produced ψ's is a possibility. If the upper limit on the ratio of the inelastic J/ψ and ψ' cross–sections is assumed to be the same as for the elastic case, then combining this with the branching ratio $\mathcal{B}.\mathcal{R}.(\psi' \to J/\psi\, X) = (57 \pm 4)\%$, an upper limit of around 3% is obtained for inelastic ψ' contamination into the total cross–section.

5.8 Results

5.8.1 Acceptance and cross–section calculations

A total of 4116 events have been generated in the ranges $100 \leq W \leq 140$ GeV and $0.5 \leq z \leq 0.9$, using the HERWIG direct inelastic J/ψ Monte Carlo and the MRSD$-'$ [35, 36] proton structure function. Of these, 560 events passed the final series of cuts thus giving an acceptance $\mathcal{A}(0.5 \leq z \leq 0.9) = (13.6 \pm 0.6)\%$. There are 5074 events generated in this W range with elasticities up to 0.9, giving an acceptance in this elasticity range of $\mathcal{A}(z \leq 0.9) = (11.0 \pm 0.5)\%$.

These acceptances are combined with the $\frac{dE}{dx}$ efficiency calculated in section 5.5 to get the values shown in table 5.1. In figure 5.39b, the reconstructed mass of the final 1993 data sample is fitted to a gaussian and exponential. There are 6.0 ± 3.7 signal events from the fit parameters. The branching ratio of $J/\psi \to e^+e^-$ is $(5.99 \pm 0.25)\%$. The ep cross–section is calculated for the direct process using equation 5.2 and the γp cross–section is obtained by dividing by the integrated photon flux (see appendix A). The results are summarised in table 5.1.

$$\sigma_{ep} = \frac{N}{\mathcal{L} \times \mathcal{B}.\mathcal{R}. \times \mathcal{A}} \tag{5.2}$$

where :

N	=	number of J/ψ signal events
$\mathcal{L}$	=	integrated luminosity
$\mathcal{B.R.}$	=	branching ratio of $J/\psi \to e^+e^-$
$\mathcal{A}$	=	total acceptance of inelastic J/ψ selection

In the quoted cross–sections, the first error is statistical and the second is systematic. A detailed explanation of the systematic errors follows in the next sub–section. The uncertainty in the number of events in the fitting of the mass peak provides the largest contribution to the statistical error. A sufficient number of Monte Carlo events are generated to ensure that the statistical error on the acceptance is small in comparison. The error on the integrated photon flux is systematic and arises from the assumption that the γp cross–section is independent of y and Q^2 as explained in appendix A.

$ep \to e\,J/\psi\,X$	$100 \leq W \leq 140$ GeV
Number of J/ψ events, N	6.0 ± 3.7
Luminosity,	456.7 nb^{-1}
Acceptance $(0.5 < z \leq 0.9)$	$(13.3 \pm 0.6)\%$
Acceptance $(z \leq 0.9)$	$(10.8 \pm 0.5)\%$
$J/\psi \to e^+e^-$ branching ratio	$(5.99 \pm 0.25)\%$
Integrated photon flux	$0.025^{+0\%}_{-10\%}$
$\sigma_{ep}(0.5 < z \leq 0.9)$ (nb)	$1.7 \pm 1.0 \pm 0.5$
$\sigma_{ep}(z \leq 0.9)$ (nb)	$2.0 \pm 1.2 \pm 0.6$
$\sigma_{\gamma p}(z \leq 0.9)$ (nb)	$82 \pm 48 \pm 23$

Table 5.1: Summary of the results including the γp and ep cross–sections.

5.8.2 Systematic uncertainties

In table 5.2, the systematic errors associated with this analysis are listed.

- The gluon density in the proton strongly affects the distribution of the invariant hadronic mass, W and events are partly triggered on the hadronic production. A systematic error is obtained by comparing the MRSD$-'$ and MRSDO$'$ structure functions and using two different Monte Carlo generators to calculate the acceptances.

- The error on the forward cone energy cut is obtained by varying the value of the cut and comparing the loss of real and Monte Carlo events.

- The systematic error on the $z \leq 0.9$ and the $P_t^{J/\psi} \geq (8.75z - 7)$ cuts in the $(z\, P_t^{J/\psi})$ plane used to remove the diffractive component are estimated in exactly the same way (as the forward cone energy cut).

- The resolution on the elasticity reconstruction near $z \sim 0.5$ (see figure 5.36b) is used to estimate the systematic error on the minimum elasticity cut $z \geq 0.5$.

- The efficiency of the $\frac{dE}{dx}$ cut is checked using electrons from conversion photons.

- The fit to the reconstructed mass peak is sensitive to the polynomial chosen to fit the background giving rise to a mass fitting error which is obtained by using different polynomials in the fit.

- The resolution in the reconstruction of W is used to estimate the corresponding systematic error.

- By fitting the J/ψ transverse momentum distribution to that predicted by photon–gluon fusion model, an upper limit of 10% is estimated for the contamination from diffractive processes such as the process illustrated in figure 2.15 which have lower transverse momenta.

- The inelastic ψ' contamination of the J/ψ signal was estimated in section 5.7.2.

These systematic errors have been added in quadrature to give a total error of $^{+26\%}_{-36\%}$ as shown in the table.

Systematic errors:	
Branching fraction	4%
Luminosity	3.3%
Input gluon density	16%
Forward 35° cone cut	2.5%
Cuts in the $(z\, P_t^{J/\psi})$ plane	14%
$z \geq 0.5$ cut	8%
$\frac{dE}{dx}$ cut	1.5%
Reconstructed mass fitting error	10%
$100 \leq W \leq 140$ GeV cut	6%
Diffractive background subtraction	$+0\% - 10\%$
Inelastic ψ' contamination	$+0\% - 3\%$
Total systematic error	$+26\% - 28\%$

Table 5.2: List of systematic errors for $ep \to e\, J/\psi\, X$ cross–section measurement.

5.9 Conclusions

It is clear that the statistics are very poor for the inelastic J/ψ channel with only around 6 events in the signal region after all the cuts. This has enabled the calculation of the inelastic J/ψ cross–section with relatively large statistical errors. The lack of statistics makes the extraction the gluon density in the proton impossible.

The next chapter describes the analysis of the data from the 1994 running period. With six times more data accumulated than during 1993, a far more substantial signal

will be seen and an attempt to extract the gluon density in the proton will be made in chapter 7 using this data.

Chapter 6

The search for $J/\psi \to e^+e^-$ in 1994 data

In this chapter, the analysis of J/ψ photoproduction using the 1994 data is described. There are many similarities with the 1993 analysis but also some significant differences. The most notable being the six–fold increase in the total luminosity collected from ~ 0.5 pb^{-1} in 1993 to ~ 3 pb^{-1} in 1994. Other differences include changes in the triggers to handle this increased luminosity and an improved $\frac{dE}{dx}$ measurement allowing better separation between electron and hadron tracks and giving a better signal–to–background ratio.

6.1 Pre–selection of 1994 data

For the first part of the 1994 running period, HERA continued colliding electrons with protons as in 1993. Thereafter, positrons were used instead of electrons for reasons of increased luminosity. The synchrotron radiation[1] from the bending of the electron beam hit the beam walls to produce gas in the beam pipe, mainly consisting of positive ions. This then tended to diverge the electron beam thus shortening the electron lifetime. This effect was removed by switching to a positron beam.

[1] See section 3.5.2.

The switch from electrons to positrons should make no difference to this analysis since the photon flux[2] is the same for both the particle and antiparticle. Both the electron and positron data are therefore combined. Three shifted vertex runs were also taken in the 1994 running period. The interaction vertex was shifted around 60 cm in the positive z–direction. This allowed the study of very low Q^2 events, since the rearward angular acceptance of the calorimeter increased, allowing the scattered electrons from these very low Q^2 events to be measured. These three shifted vertex runs, with a total luminosity of around 57 nb^{-1}, are excluded from this analysis. As in the 1993 analysis, runs not passing the EVTAKE routine (see footnote 4 in section 5.2) are rejected, however, all the trigger bits are accepted in the pre–selection. The trigger selection will be done at a later stage in the analysis.

Electron candidates in the calorimeter and tracks[3] are found in the same way as in the 1993 pre–selection (see section 5.2), except that the cut on the absolute pseudorapidity of the tracks is slightly tightened from $|\eta| \leq 2.0$ to $|\eta| \leq 1.75$. This change is intended to reduce the number of events passing the pre–selection and has been influenced by the 'Foster cuts' for 1994 data. These state that tracks with transverse momentum $P_t >$ 0.15 GeV and absolute pseudorapidity $|\eta| \leq 1.75$ are within an understood region of the CTD. The loosening of these cuts from the 1993 values (see footnote 9 in section 5.2) reflects the improved resolution and understanding of the CTD in 1994.

Selected electron candidates in the calorimeter are matched to the selected tracks with the same techniques used in 1993 (see section 5.2). A loop is performed over all track–cluster pairs and an event is accepted if it satisfies the same conditions as in 1993.

[2] See appendix A.

[3] Tracks are found using the VCTRAK algorithm described in section 3.3 and [22] and this algorithm will be used in the rest of the analysis.

A total of 3.2 pb^{-1} is analysed and 346,461 out of a total of 16.4 million events pass the pre–selection cuts. Amongst these, there are 467,729 J/ψ candidates. These numbers cannot be compared to those in the 1993 analysis until the actual cross–sections are calculated since the cuts and triggers are different. The reconstructed mass distribution of these J/ψ candidates is shown in figure 6.1 between 2.0 and 5.0 GeV. There is no sign of a J/ψ signal at this stage.

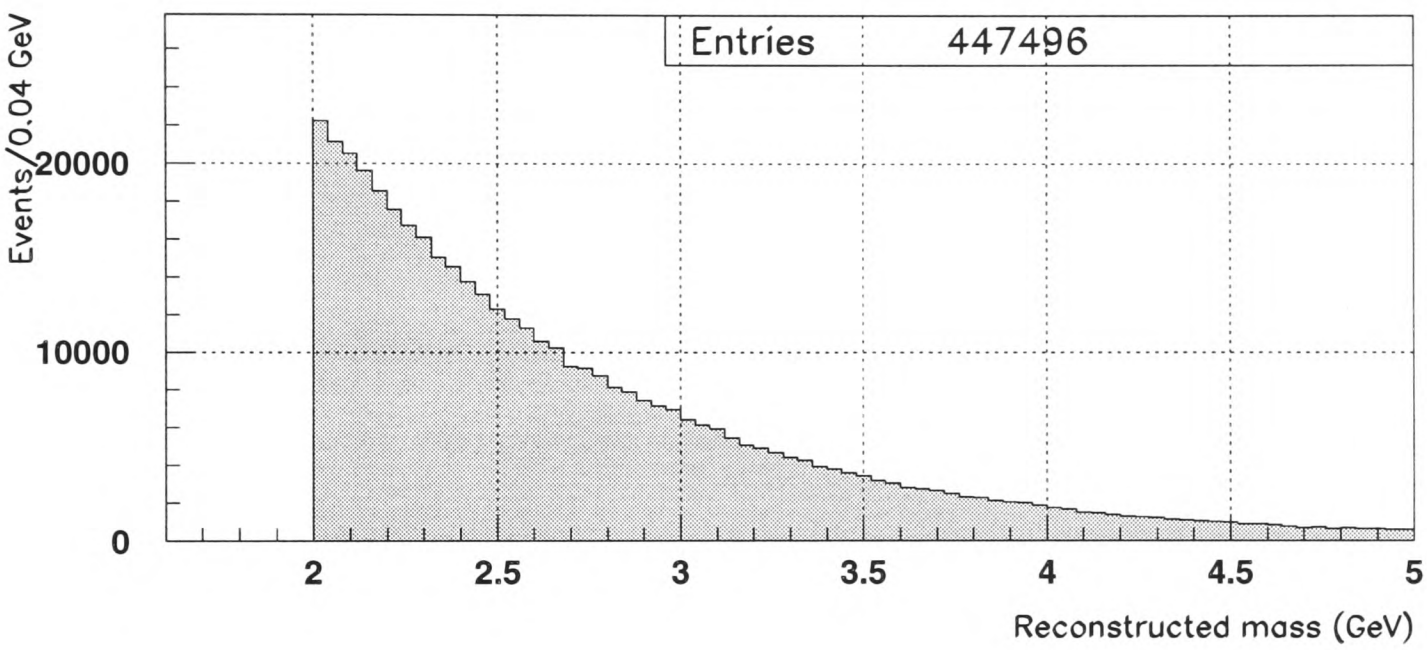

Figure 6.1: Reconstructed mass of the pre–selected J/ψ candidates from 1994 data.

6.2 Elastic $J/\psi \to e^+e^-$ selection

The elastic J/ψ sample from the 1994 data is obtained using exactly the same cuts on the pre–selected data as the cuts used in section 5.3 to obtain the 1993 elastic sample. In summary, an event must have a track multiplicity of two, with the two tracks being matched to electron–like calorimeter clusters. Figure 6.2 shows the reconstructed mass of the two tracks in the range 2.25 – 4.25 GeV. A clear signal is seen around the J/ψ mass together with a bremsstrahlung[4] tail. A gaussian with a bremsstrahlung tail is

[4]Section 3.5.2 discusses the radiation of photons by high energy electrons.

used to fit the signal and a second order polynomial to fit the background. The fit gives a reconstructed mass of 3.083 ± 0.004 GeV with a width of 0.046 ± 0.004 GeV and 443 ± 25 events in the signal compared to 86 ± 11 events in 1993. The background, fitted with a second order polynomial is shown as the dashed line in figure 6.2.

Figure 6.3 shows an actual candidate elastic J/ψ event from the 1994 running period. Two clean oppositely charged tracks are seen matched to energy clusters in the calorimeter. These clusters lie completely in the EMC part of the calorimeter as expected for the $J/\psi \to e^+e^-$ decay. The reconstructed mass of the two tracks was found to be 3.085 GeV, close to the nominal J/ψ mass. Aside from noise, no other activity is seen in the calorimeter with the incident electron and proton being lost down the beam pipe after the interaction.

Again, because of the purity of this elastic J/ψ sample, it will be used together with Monte Carlo to help determine the cuts used to obtain the inelastic J/ψ sample in the next section.

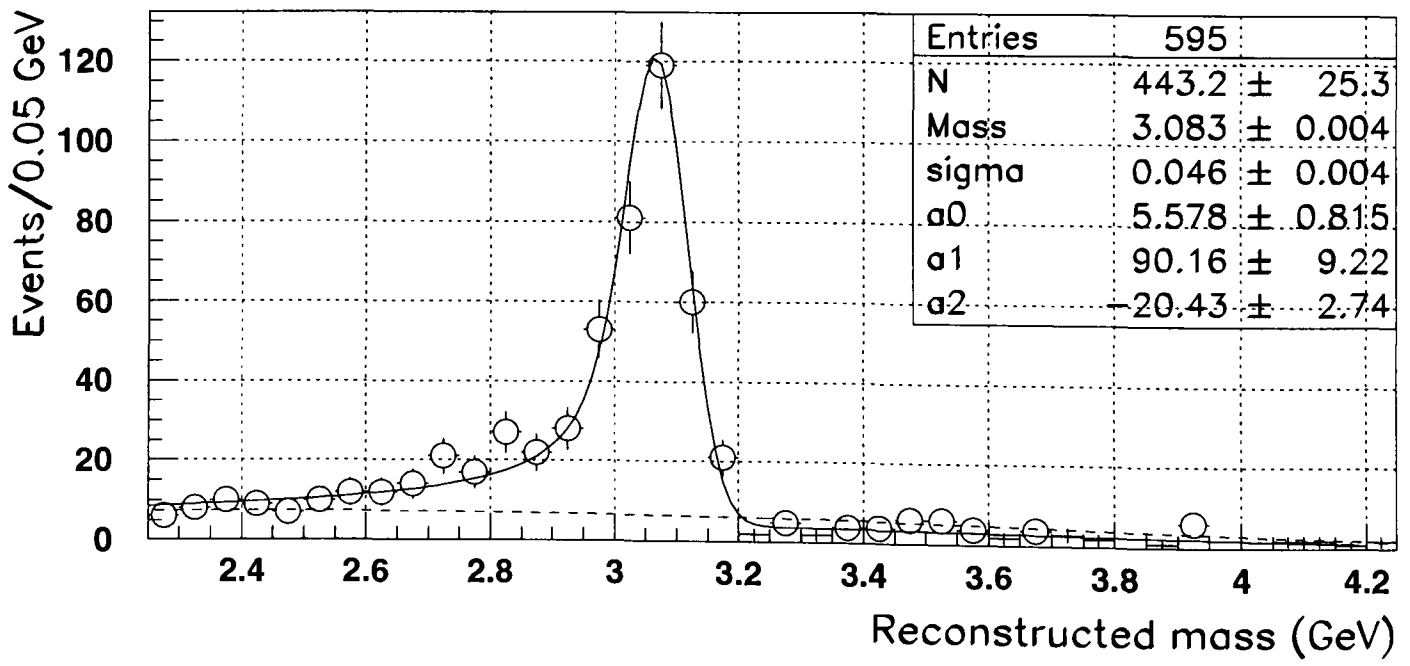

Figure 6.2: Reconstructed mass of the elastic J/ψ sample from the 1994 data fitted to a gaussian with a bremsstrahlung tail. A second order polynomial, shown as the dashed line, is used to fit the background.

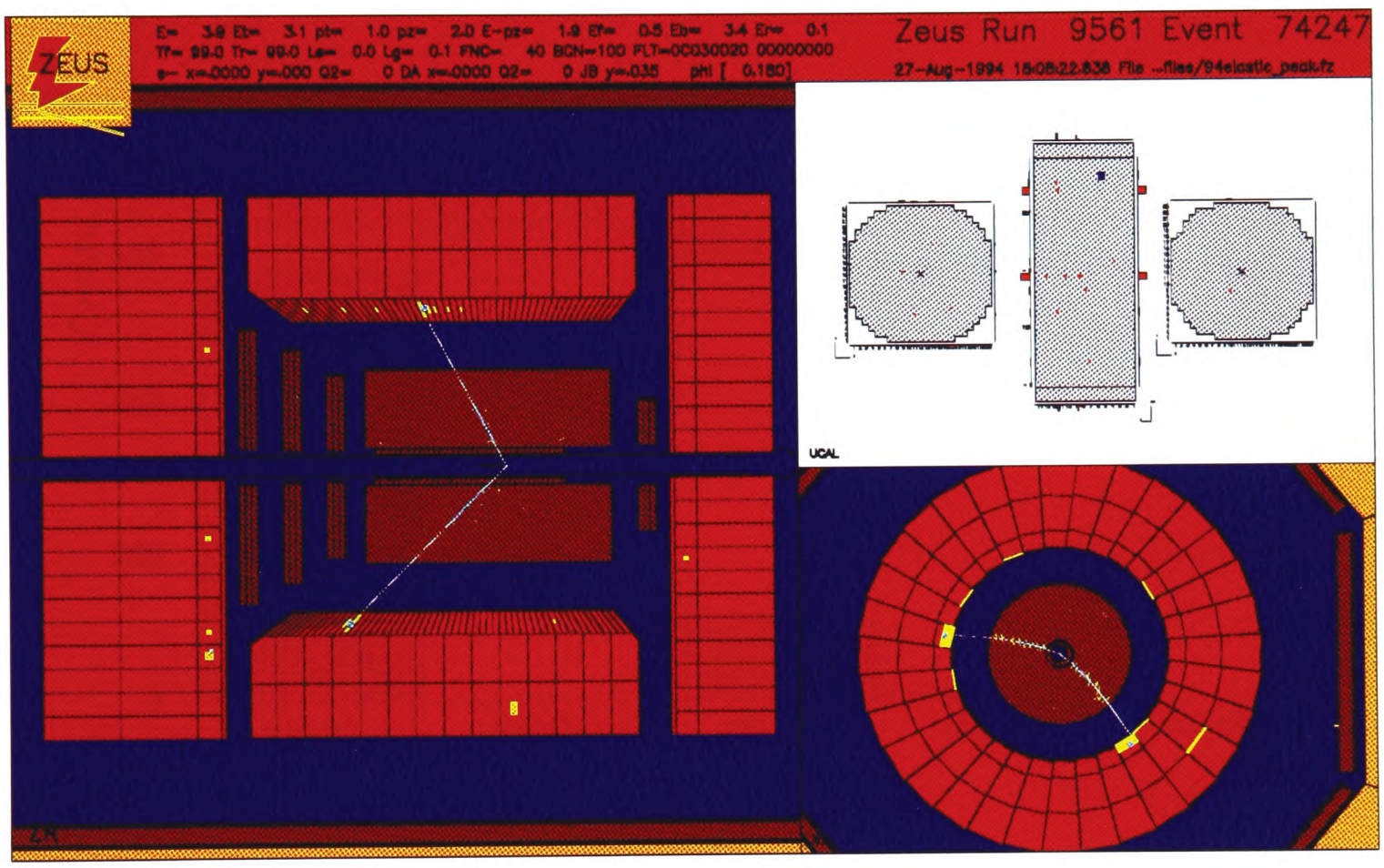

Figure 6.3: Candidate elastic J/ψ event where two tracks are clearly seen matched to electromagnetic energy clusters in the calorimeter. The bottom right picture shows the two tracks bending in opposite directions in the magnetic field. The main picture shows the event in the ZR projection and the top right picture shows the energy deposits in the uranium calorimeters. The reconstructed mass of the two tracks was calculated to be 3.085 GeV. Aside from noise, no other activity is seen in the detector.

There are only two events in the like–signed background due to the third level trigger algorithms. In figure 6.4, the third level heavy flavour triggers set by the elastic sample are shown. Of the 595 events, 579 (over 97%) trigger the J/ψ HFL01 trigger (the trigger bits will be described later in section 6.4.3). This trigger bit requires two oppositely charged electron candidates, and so a two track like–signed electron pair will not pass this trigger. Therefore, almost all of the like–signed background events are rejected by this filter and are not saved onto tape, hence the low ratio of like–signed to opposite–signed background events.

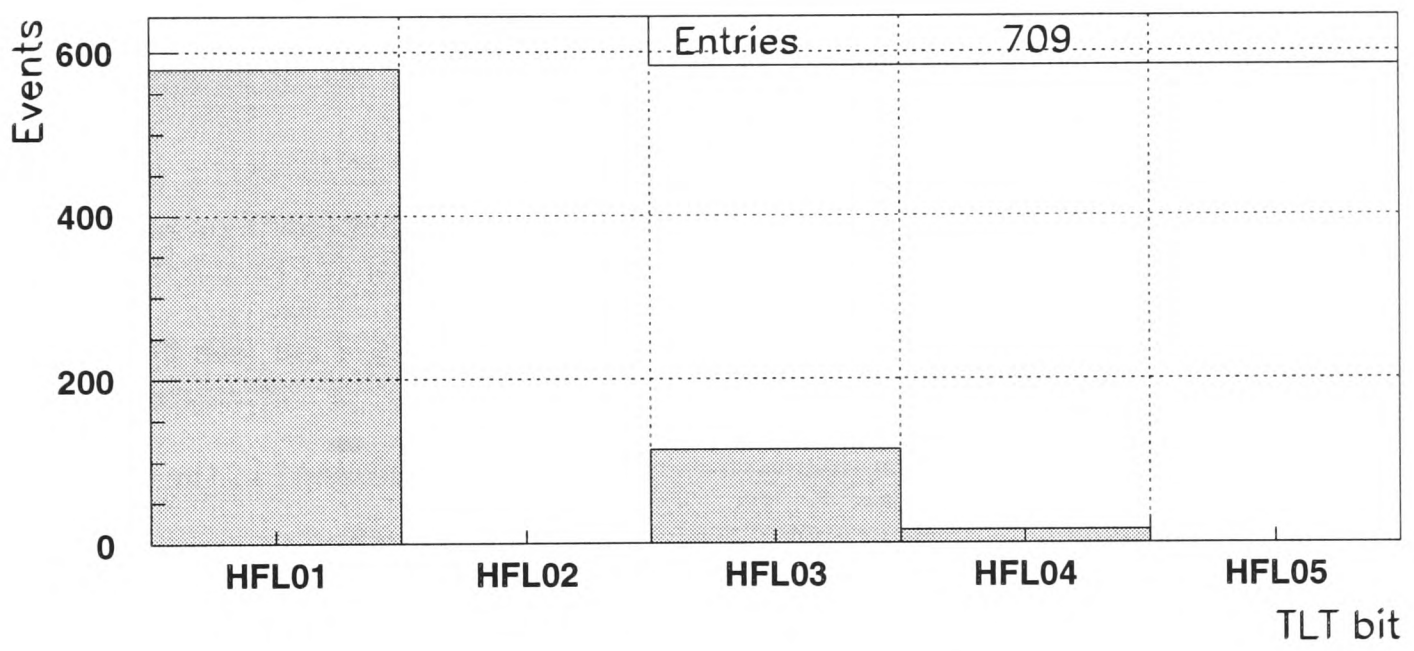

Figure 6.4: Heavy flavour TLT bits set by the 1994 elastic sample.

6.3 Inelastic $J/\psi \rightarrow e^+e^-$ selection

There are a number of changes from the cuts applied to the 1993 data to select the decay electrons from inelastic J/ψ. Therefore all of the cuts will be restated below with the new or changed cuts marked with an asterisk. Figures 6.5 – 6.17 show the effect of some of these cuts applied sequentially to the pre–selected 1994 data sample. They also show the cuts applied to events generated using various Monte Carlos and to the 1994

elastic J/ψ sample described in section 6.2 with an additional mass cut of 2.8 – 3.15 GeV to further improve the signal to background ratio.

1. The J/ψ decay electron tracks are oppositely charged and not identified as conversion electrons by the CONVERT2 algorithm.

2. Both electron tracks originate from the main vertex.

3. The absolute pseudorapidity, $|\eta| \leq 1.5$ for both decay electron tracks (see figures 6.5a–c).

4.* The $z-$coordinate of the main event vertex lies in the range $-50 \leq z_{vtx} \leq 40$ cm (see figures 6.6a–c).

5.* The shower widths[5] of both electron clusters ≤ 7 cm (see figures 6.7a–c).

6.* The shower length of at least one electron cluster ≤ 4 cm (see figures 6.8a–c).

7.* All the energy of both decay electron clusters is contained in the EMC and HAC0 part of the calorimeter, with none extending into the HAC1 or HAC2 parts (see figures 6.9a–c).

8.* Both electron tracks approach within 10 cm of their respective clusters when the tracks are extended into the calorimeter as described in section 5.2 (see figures 6.10a–c).

9.* The ratio of cluster energy in the calorimeter to track momentum of both decay electrons < 1.2 (see figures 6.11a–c).

10.* Both the decay electron tracks have transverse momentum, $P_t > 0.7$ GeV (see figures 6.12a–c).

[5]Defined in section 3.4.

11. At least one of the decay electron tracks has a transverse momentum, $P_t > 1.2$ GeV (see figures 6.13a–c).

12*. The $\frac{dE}{dx}$ values of both electron tracks divided by the average $\frac{dE}{dx}$ value of the pion band in each run ≥ 1.25. It is seen in figure 6.14a, that a large fraction of the 1994 J/ψ candidates are removed by this cut. Section 6.8 looks at this cut in more detail.

13. To select low Q^2 events, a cut of 1 GeV is put on the maximum total energy in the first calorimeter ring around the rear beam pipe (see figures 6.15a–b).

14. The energy in the calorimeter not belonging to the J/ψ decay electron islands within a cone of 35° around the forward beam pipe must be greater than 1 GeV. This removes the elastic J/ψ events from the sample (see figures 6.16a–c).

15. The elasticity, $z \leq 0.9$. This cut is required since the HERWIG Monte Carlo only generates events with elasticities up to 0.95. It is shown with cut 16 in figures 6.17a–d.

16. A cut is made in the elasticity – J/ψ transverse momentum plane defined by $P_t^{J/\psi} \geq (8.75z - 7)$ in order to remove proton dissociative J/ψ events. In such events, the incident proton breaks up after emitting a colourless object to interact with the incident photon as shown in figure 2.14 in section 2.6.2. The colourless object is typically soft, so the momentum of the J/ψ originates principally from the incident photon and therefore, the elasticity is close to unity (see equation 3.3 in section 3.1). The J/ψ has a low transverse momentum. Very few data and HERWIG inelastic J/ψ Monte Carlo events are removed by this cut as seen in figures 6.17a and b. 20,300 proton dissociative J/ψ events are produced using the

Pythia Monte Carlo generator. 2263 remain after the pre–selection, trigger and the above cuts are applied. These are shown in figure 6.17c where it is seen that the cuts in the $(z, P_t^{J/\psi})$ plane remove most of these, as expected. Another source of background, identified in the analysis of the 1993 data, comes from the resolved photon production mechanism. Figure 6.17d shows that these events, generated using the EPJPSI Monte Carlo, typically lie at low elasticities and hence are not affected by these cuts in the $(z, P_t^{J/\psi})$ plane. The resolved photon production mechanism will be addressed later in section 6.6.

The cuts to select the physics process entering the sample (cuts 13 – 16), remain the same as for the 1993 analysis and a detailed explanation of the reasoning behind them can be found in section 5.4. The most significant difference between the 1993 and 1994 analyses is the much improved reconstruction of the track $\frac{dE}{dx}$ values. In 1993, the $\frac{dE}{dx}$ values of the tracks were corrected for run–by–run variations by a simple pressure correction. In 1994, the $\frac{dE}{dx}$ values of tracks are divided by the average $\frac{dE}{dx}$ value of the pion band, calculated on a run–by–run basis. This modification is done to take into account other variations which might affect the $\frac{dE}{dx}$ values of tracks such as changes in the gas composition. Several runs during the 1994 running period had no average $\frac{dE}{dx}$ value for the pion band and these are excluded from the analysis.

The improved $\frac{dE}{dx}$ reconstruction in the 1994 analysis has meant that the $\frac{dE}{dx}$ cut (number 12) is now more powerful in removing background from hadron tracks faking electrons. Figures 6.18a–p show the reconstructed mass of the two tracks as the cuts are applied sequentially and a clear signal in the J/ψ mass region appears when the $\frac{dE}{dx}$ cut is applied in figure 6.18l. The signal–to–background ratio decreases in figure 6.18n when the elastic J/ψ component is removed with cut 14 and again in figure 6.18p when

J/ψ's from proton dissociative events are removed with cut 16. After these cuts, there are 360 J/ψ candidates remaining from an original 467,729.

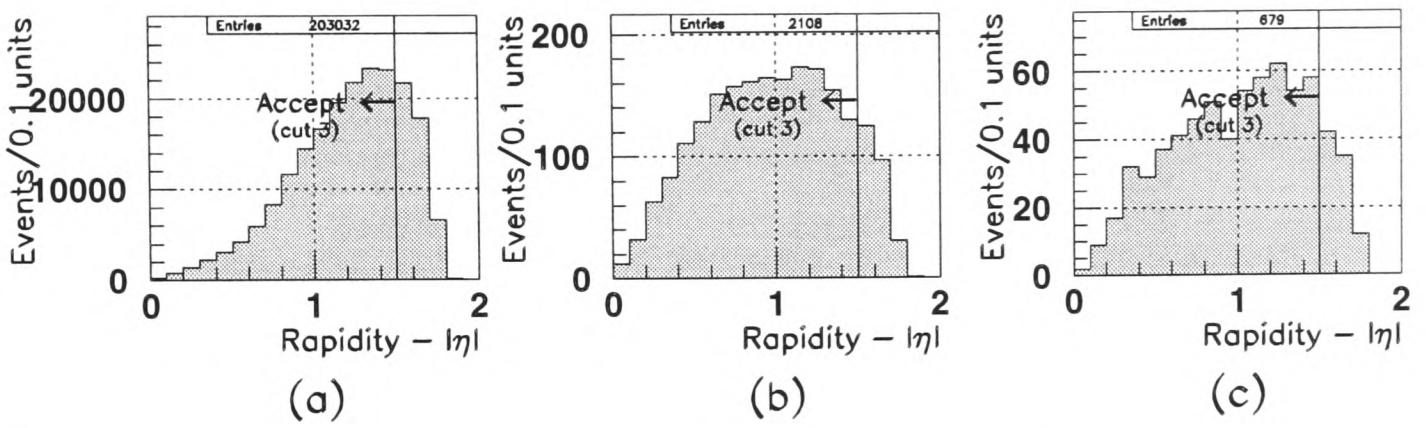

Figure 6.5: Largest absolute η of the two decay electron tracks for a) pre–selected 1994 data, b) HERWIG Monte Carlo and c) elastic J/ψ 1994 data.

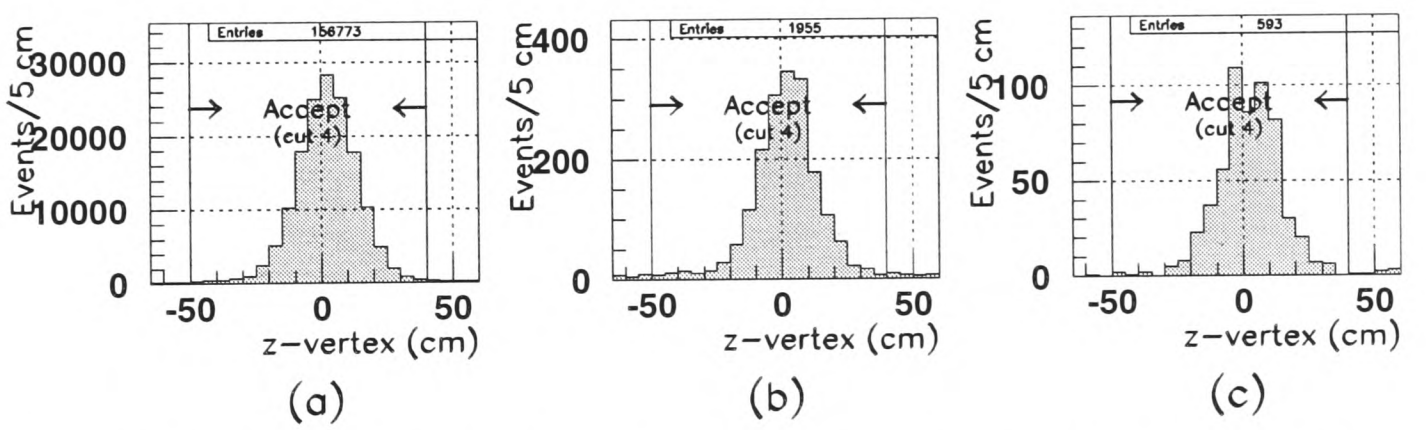

Figure 6.6: Largest absolute $z-$vertex of the two decay electron tracks for a) pre–selected 1994 data, b) HERWIG Monte Carlo and c) elastic J/ψ 1994 data.

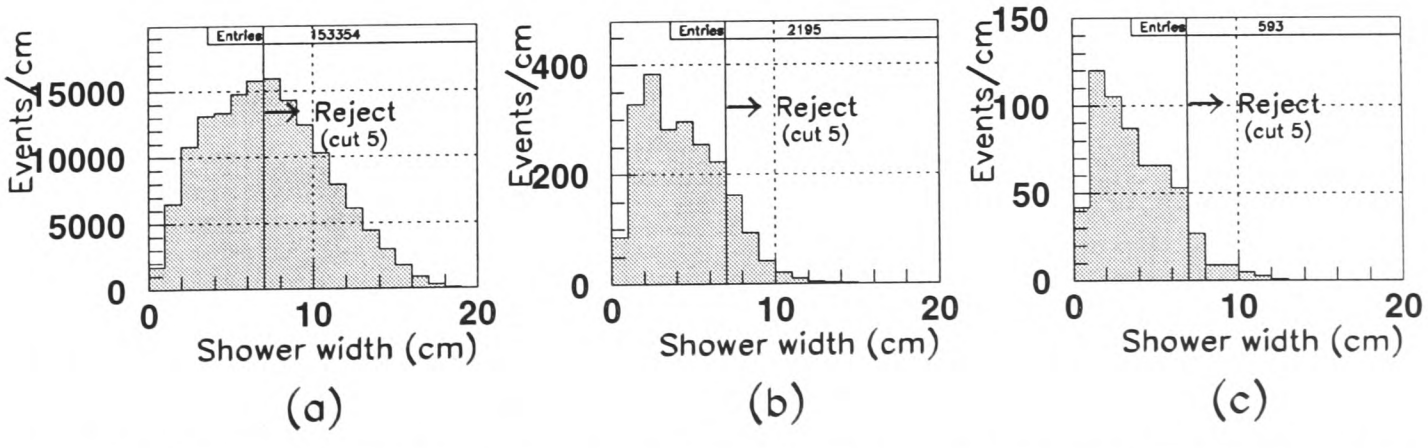

Figure 6.7: Largest shower width of the two decay electron clusters for a) pre–selected 1994 data, b) HERWIG Monte Carlo and c) elastic J/ψ 1994 data.

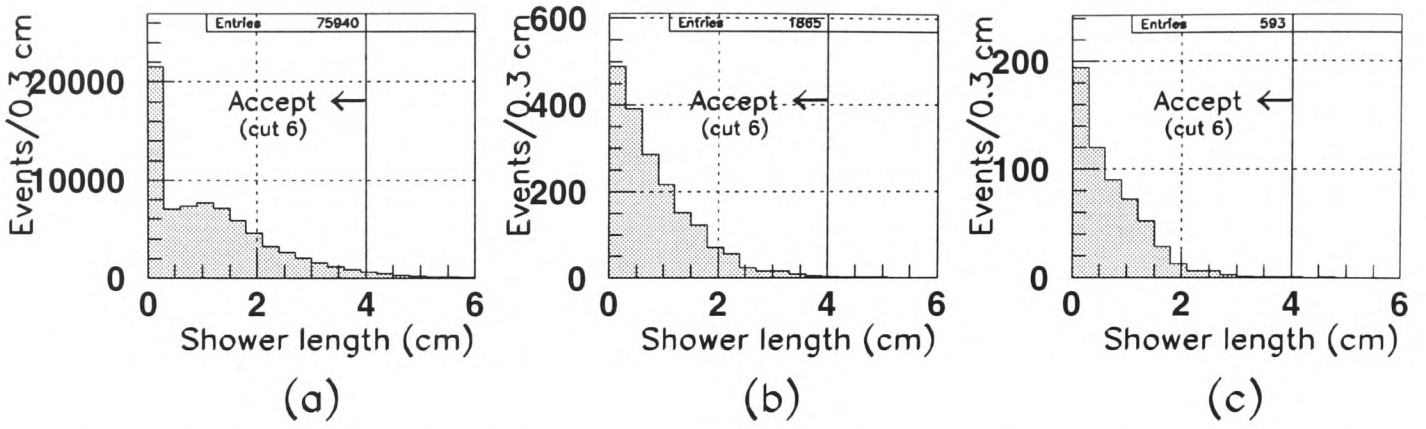

Figure 6.8: Smallest shower length of the two decay electron clusters for a) pre–selected 1994 data, b) HERWIG Monte Carlo and c) elastic J/ψ 1994 data.

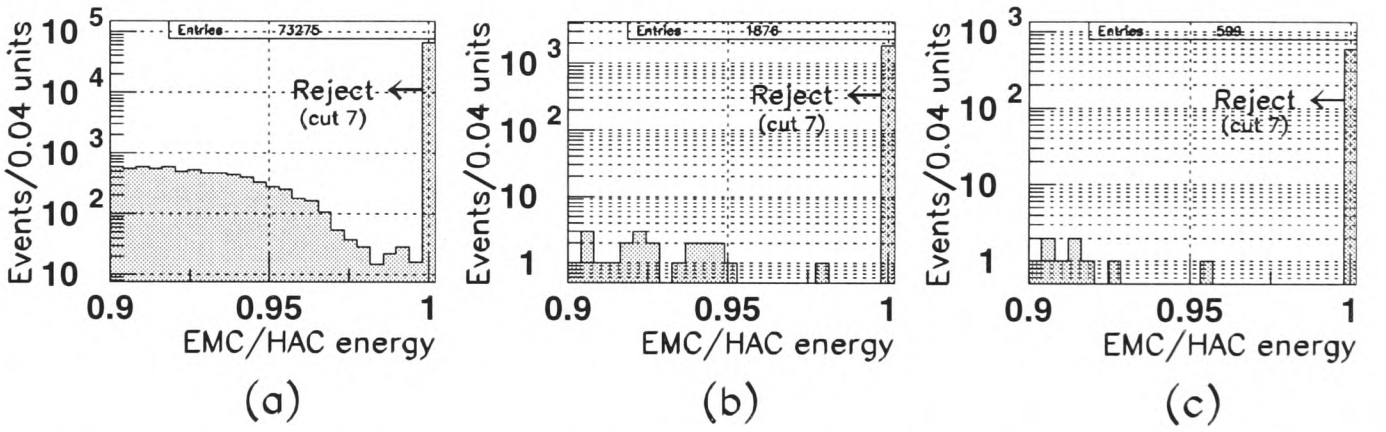

Figure 6.9: Smallest ratio of EMC and HAC0 to total energy of the two decay electron clusters for a) pre–selected 1994 data, b) HERWIG Monte Carlo and c) elastic J/ψ 1994 data.

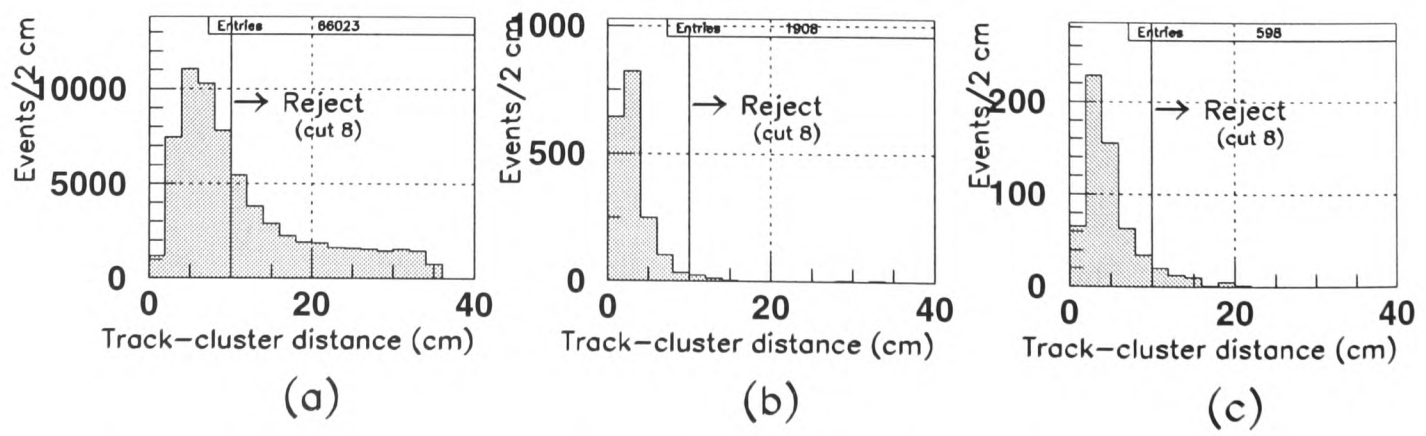

Figure 6.10: Largest track-cluster distance of the two decay electrons for a) pre–selected 1994 data, b) HERWIG Monte Carlo and c) elastic J/ψ 1994 data.

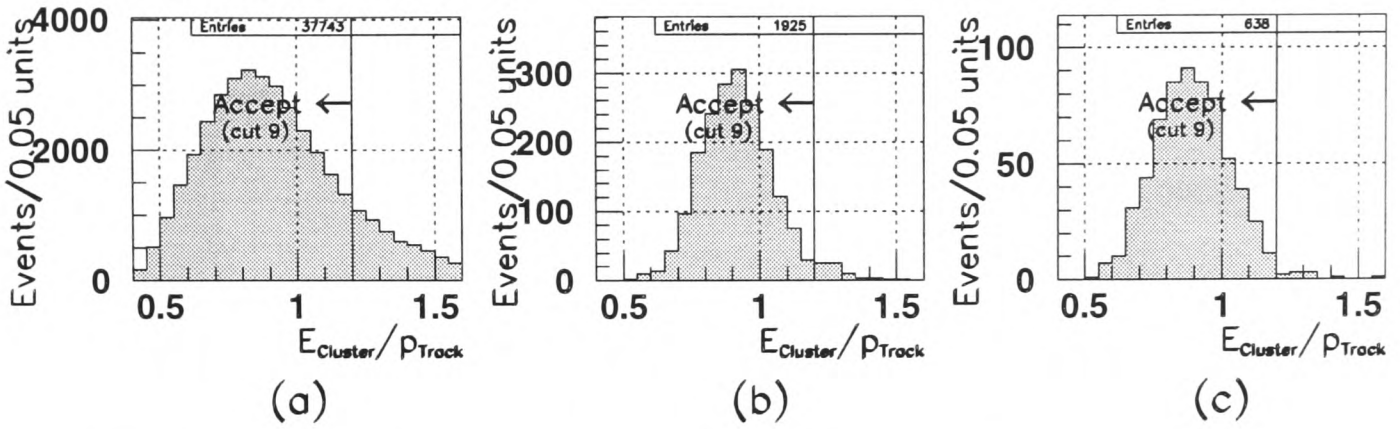

Figure 6.11: Largest calorimeter energy/track momentum of the two decay electrons for a) pre–selected 1994 data, b) HERWIG Monte Carlo and c) elastic J/ψ 1994 data.

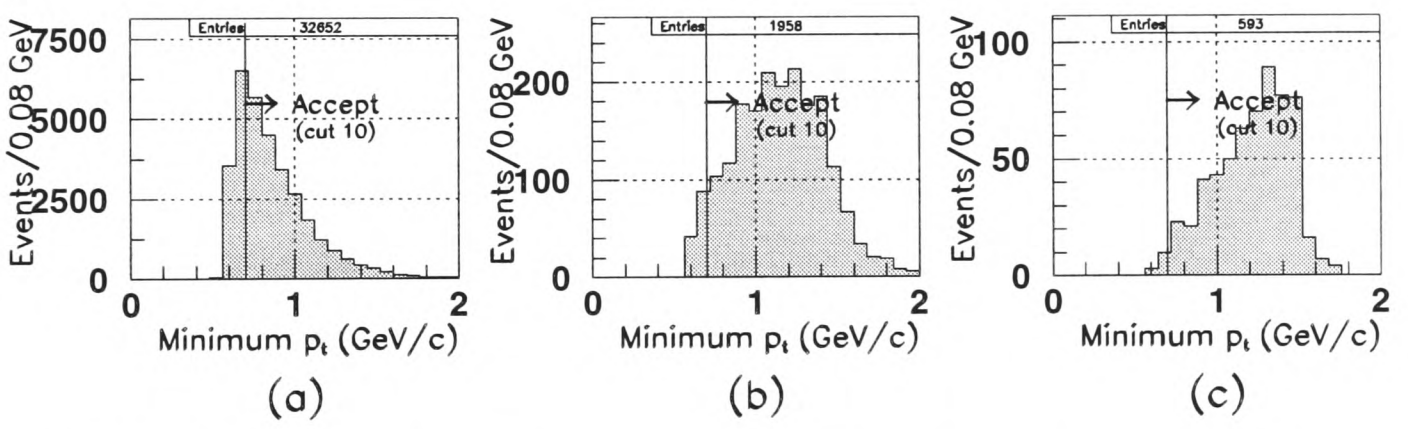

Figure 6.12: Smallest transverse momentum, P_t, of the two decay electron tracks (GeV) for a) pre–selected 1994 data, b) HERWIG Monte Carlo and c) elastic J/ψ 1994 data.

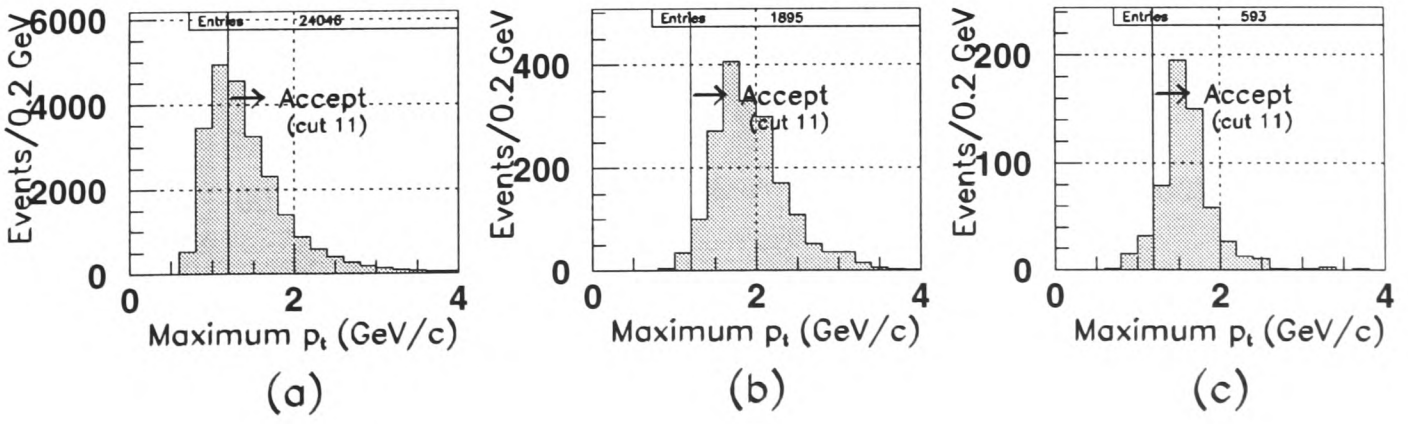

Figure 6.13: Largest transverse momentum, P_t, of the two decay electron tracks (GeV) for a) pre–selected 1994 data, b) HERWIG Monte Carlo and c) elastic J/ψ 1994 data.

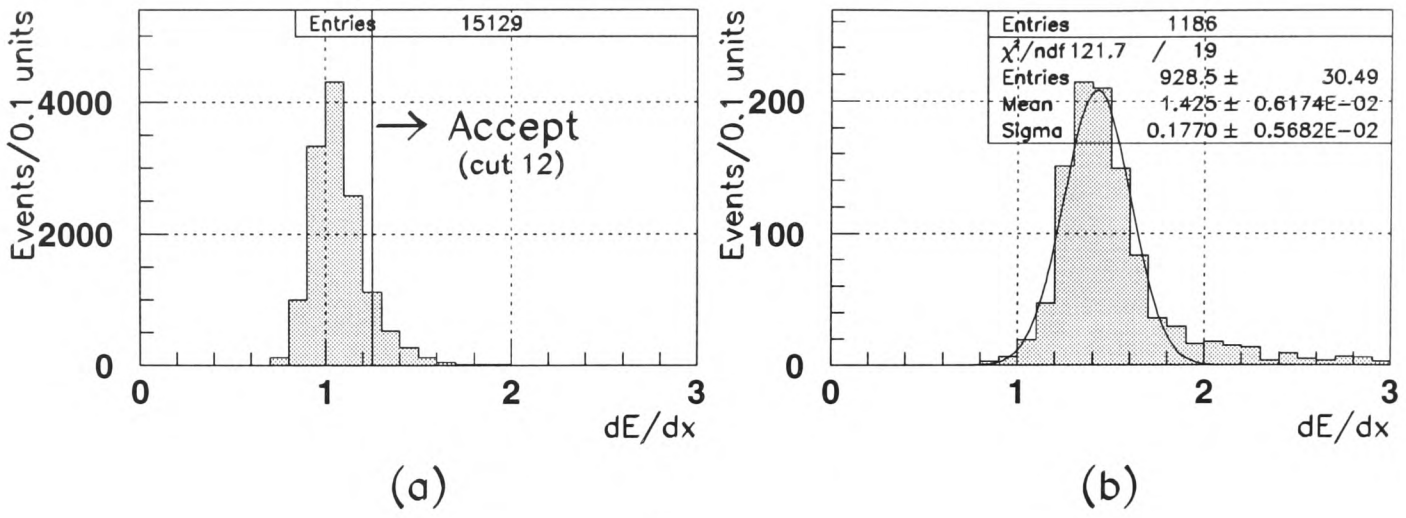

Figure 6.14: a) The pressure corrected $\frac{dE}{dx}$ values for the two decay electrons in the a) pre–selected 1994 data and b) the 1994 elastic J/ψ sample fitted to a gaussian.

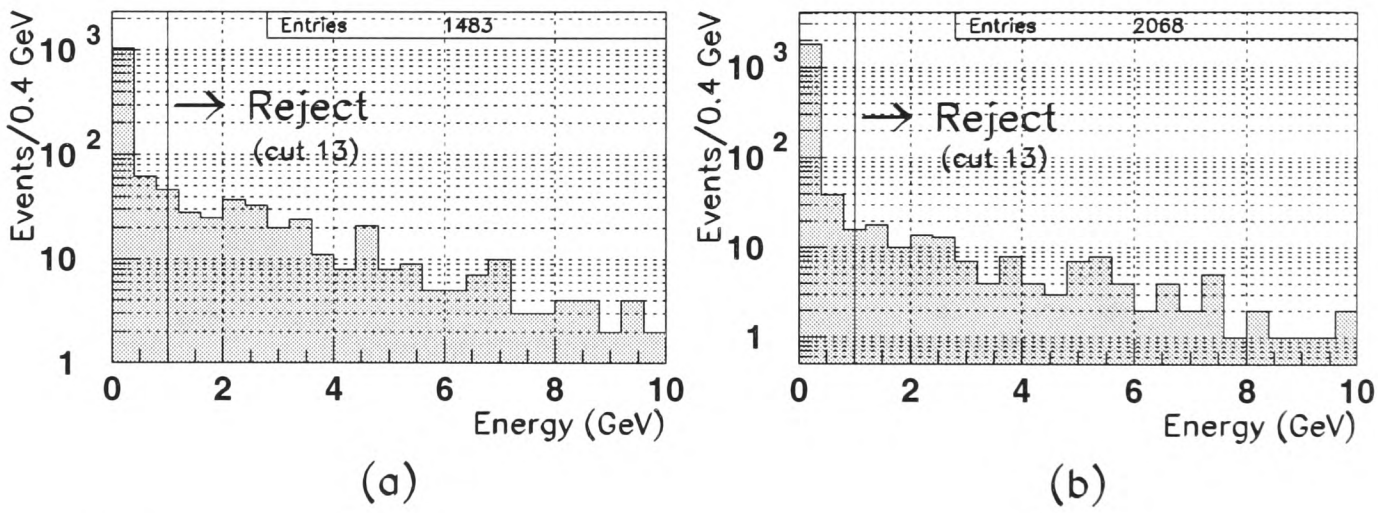

Figure 6.15: Energy in the first ring around the rear beam pipe for a) pre–selected 1994 data and b) HERWIG Monte Carlo.

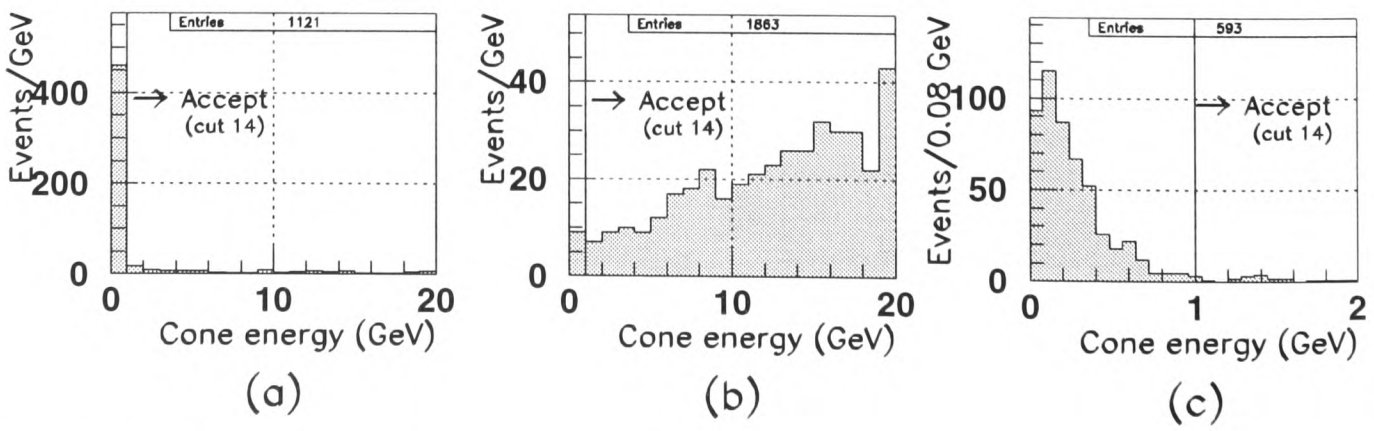

Figure 6.16: Energy in a 35° cone around the forward beam pipe for a) pre–selected 1994 data, b) HERWIG Monte Carlo and c) elastic J/ψ 1994 data.

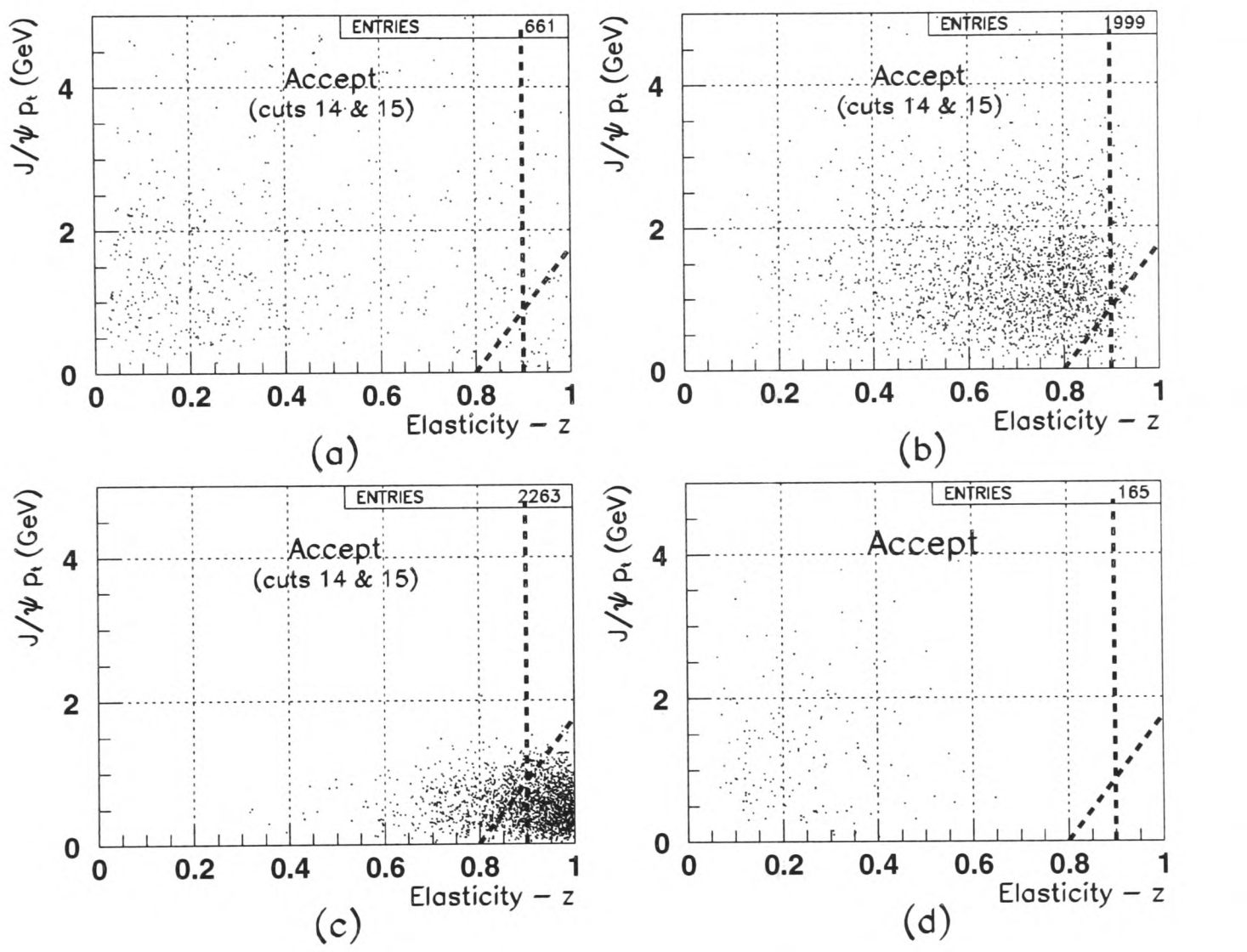

Figure 6.17: Transverse J/ψ momentum vs. elasticity showing the $z \leq 0.9$ cut and the corner cut to reduce proton dissociative J/ψ events for a) pre–selected 1994 data, b) HERWIG Monte Carlo, c) Pythia proton dissociative Monte Carlo and d) EPJPSI resolved photon Monte Carlo.

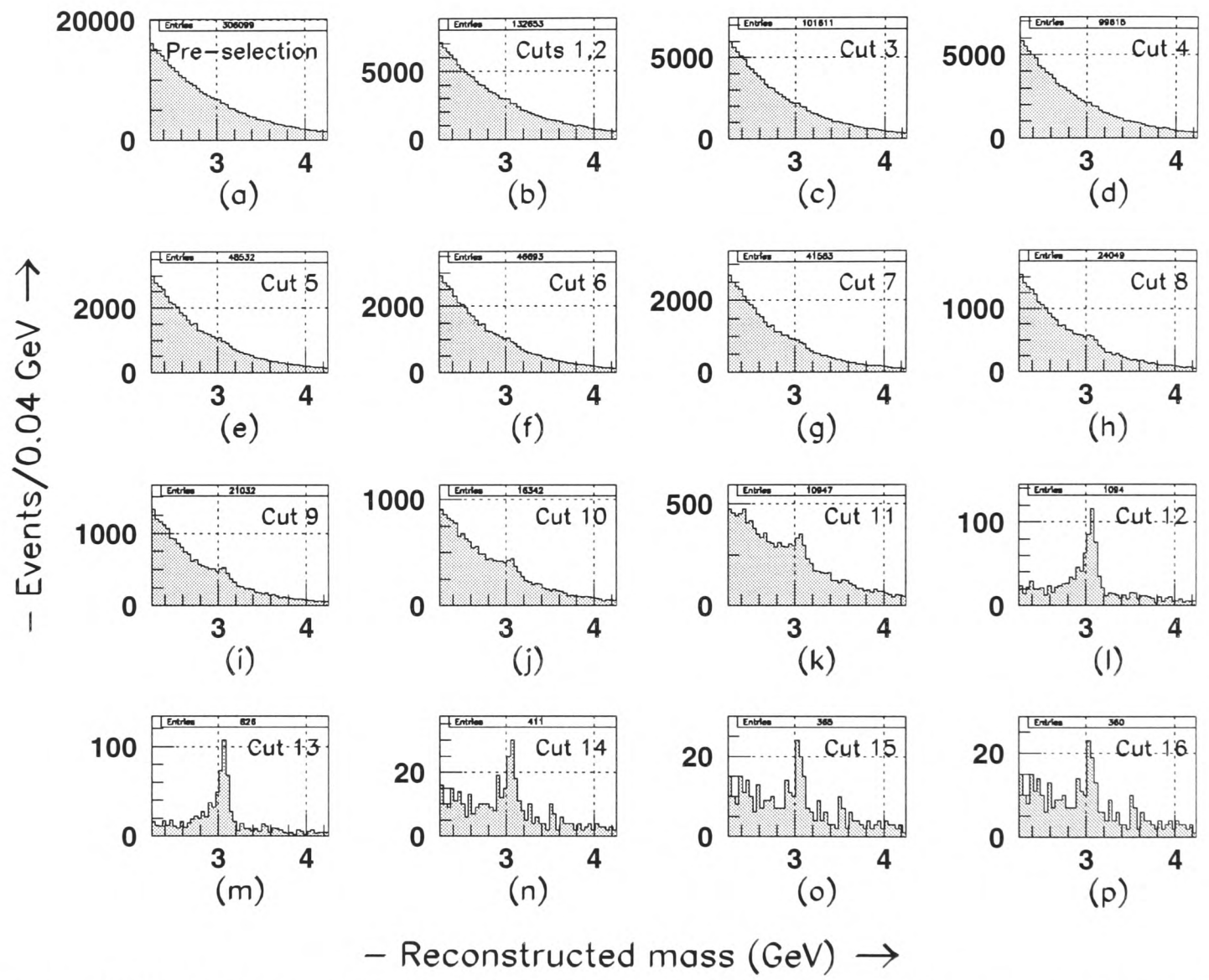

Figure 6.18: Reconstructed mass (GeV) of the J/ψ candidates as cuts are applied in the following order: a) Pre–selection cuts, b) Oppositely, non-conversion, vertexed tracks, c) Pseudorapidity $|\eta| \leq 1.5$, d) Main vertex $-50 \leq z_{vtx} \leq 40$ cm, e) Shower widths $\leq$ 7 cm, f) At least one shower length ≤ 4 cm, g) All energy of electron clusters in EMC and HAC0, h) Track–cluster distances ≤ 10 cm, i) $E_{island}/P_{track} \leq 1.2$, j) Both tracks with $P_t \geq 0.7$ GeV, k) At least one track with $P_t \geq 1.2$ GeV, l) $\frac{dE}{dx} \geq 1.25$, m) Rear beam pipe energy ≤ 1 GeV, n) Forward 35° cone energy ≥ 1 GeV, o) $z \leq 0.9$ and p) $P_t^{J/\psi} \geq (8.75z - 7)$.

6.4 1994 Triggers and Selection

As mentioned at the start of the chapter, the trigger algorithms have been changed from the 1993 configuration to cope with the increased luminosity in 1994. Below, the relevant triggers will be described and those to be used in the analysis will be selected, so that an acceptance calculation and hence a cross–section measurement can be made later in this chapter.

6.4.1 First Level Trigger (FLT)

The FLT rejects beam related background using the C5 and VETO detectors described in sections 1.2 and 1.7 respectively. The following FLT slots will be referred to in the trigger selection, and a full description of them follows.

- **Slot 43:**

  The FLT only looks at hits in the CTD in the innermost superlayer 1. This slot has a track quality requirement which plots the ratio $z/r = cot\ \theta$ of the tracks against the wire number. For straight tracks originating from the vertex, this ratio will be constant for all eight wires in superlayer 1. Also, the following calorimeter energy cuts must be satisfied:

  - Total energy $>$ 14968 MeV
  - Total EMC energy $>$ 10068 MeV
  - Total transverse energy $>$ 11574 MeV
  - Total barrel EMC energy $>$ 3404 MeV
  - Total rear EMC energy $>$ 2032 MeV

- **Slot 46:**

  This slot is the same as slot 43 above except that there is no track quality requirement.

- **Slot 51:**

  The REMC_threshold_sum > 3750 MeV (calculated as in FLT slot 50 of the 1993 trigger, detailed in section 5.1.1).

- **Slot 56:**

  This slot requires the barrel EMC energy $\geq$ 3404 MeV or the rear EMC energy $\geq$ 2032 MeV.

Of the original 49,907 HERWIG generated inelastic J/ψ Monte Carlo events, 6508 pass all the cuts described in the previous section. Figure 6.19a shows the FLT bits triggered by these events and since there are 11,880 entries, it can be deduced that each event sets on average, around 2 FLT triggers. It is also seen that bits 43, 46, 51 and 56 are important, however, these were pre–scaled[6] to 1, 16, 128 and 4 respectively during most of the 1994 running period and so only bit 43 is of real use. Figure 6.19b shows the trigger bits set by the same HERWIG events but without the 2471 events triggered by bit 43 in order to see what other FLT bits might be of use. Bit 51 is now the most regularly triggered however, due to its pre–scaled factor, it is of no use. Also of interest are bits 38 and 39. These are LUMI[7] tagged events, but these are rarely triggered by the HERWIG Monte Carlo events and so they are also not used.

[6]The pre–scale factor specifies what fraction of events passing a particular trigger algorithm are accepted by the trigger as described in section 1.9.

[7]The LUMI detector is described in section 1.6.

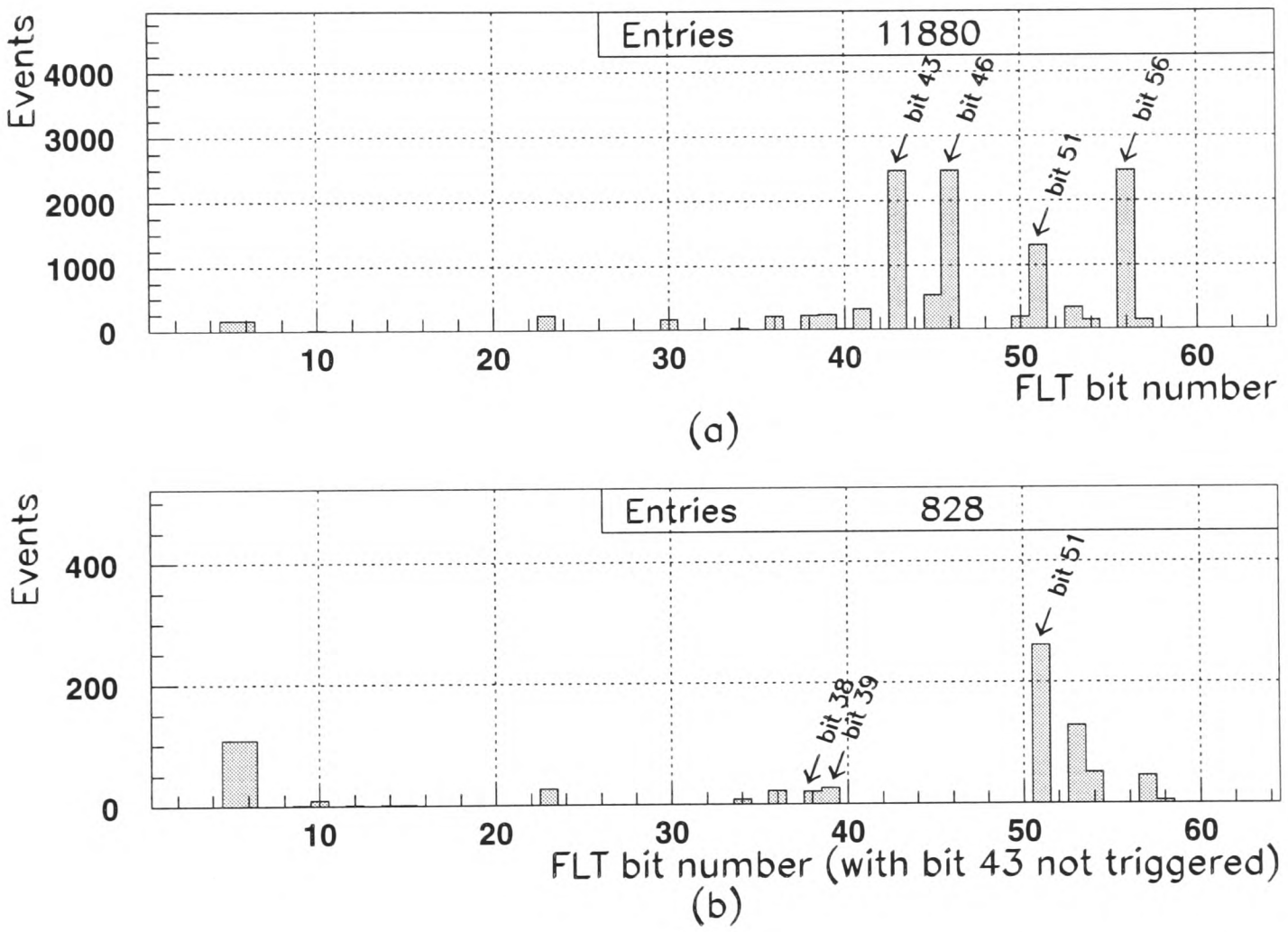

Figure 6.19: FLT bits triggered by HERWIG inelastic J/ψ Monte Carlo events a) passing the J/ψ selection cuts and b) in addition, requiring bit 43 is not triggered.

6.4.2 Second Level Trigger (SLT)

Of the 49,907 HERWIG inelastic J/ψ Monte Carlo events generated, 2471 pass all the cuts in the previous section and the FLT bit 43. Figure 6.20a shows which SLT bits are triggered by these 2471 events and it is seen that HPP4, HFL3 and HFL5 are most regularly triggered. Figure 6.20b shows the SLT bits triggered by the 587 events, not triggered by the heavy flavour inelastic J/ψ bit HFL3, and only the HPP4 and HFL5 triggers remain. HPP4 is the hard photoproduction pre–scale branch and, as the name suggests, it was pre–scaled to 16 during the 1994 running period. The heavy flavour D* bit HFL5 was only introduced in the latter part of the 1994 running period. Therefore both the HPP4 and HFL5 bits are of no use in this analysis and only the J/ψ inelastic trigger, HFL3 from the SLT bits, is selected:

HFL3, the inelastic J/ψ trigger:

This trigger was designed to accept inelastic J/ψ candidates. The trigger requirements are:

- The ratio $P_z/E < 0.92$ calculated by summing over all the calorimeter cells.
- The total calorimeter $(E - P_z) > 4$ GeV
- The number of SLT CTD tracks is non–zero and the event does not have a beam gas vertex. However, in 1994, the SLT CTD was not operational and this requirement was not demanded.
- The total energy in the rear and barrel EMC sections of the calorimeter > 3 GeV

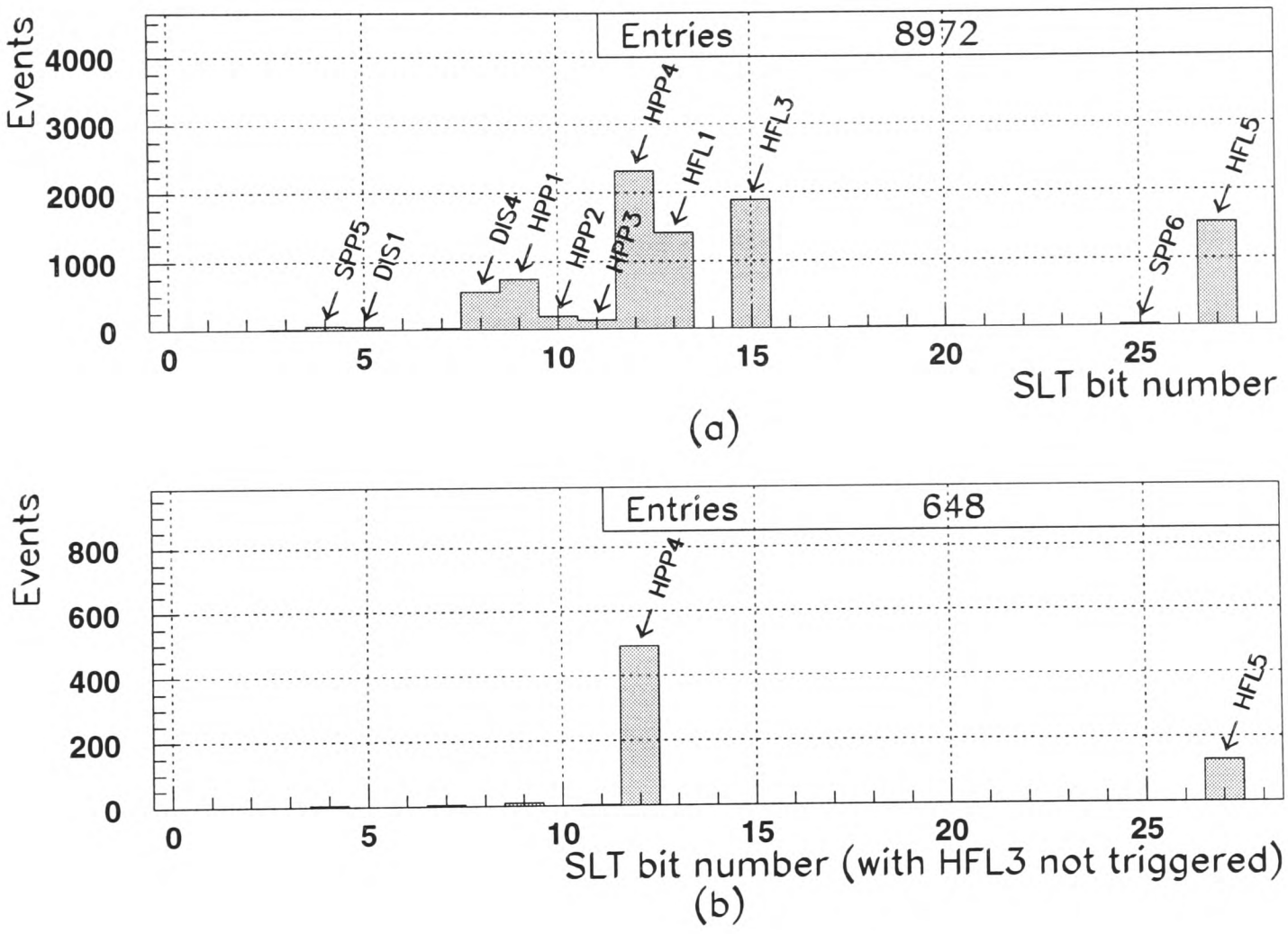

Figure 6.20: SLT bits triggered by HERWIG inelastic J/ψ Monte Carlo events a) passing the J/ψ selection cuts, FLT bit 43 and b) in addition, requiring SLT HFL3 is not triggered.

6.4.3 Third Level Trigger (TLT)

The relevant TLTs to this analysis are:

The J/ψ trigger, HFL01:

This trigger was designed to select events with two oppositely charged electron or muon candidates provided there are no more than 20 tracks in the event.

A loop is performed over all tracks with a transverse momentum > 0.4 GeV and the closest island is found by extending the track into the calorimeter, making sure that the distance between the island and the entry point of the track into the calorimeter is less than 200 cm to prevent tracks being matched to islands on the opposite side of the calorimeter. The track and island are said to be matched if the track approaches within 30 cm of the island.

These track–island pairs are classified as electrons or positrons provided the islands satisfy the following conditions:

- EMC energy / island energy > 0.9
- EMC energy > 0.3 GeV
- number of EMC cells ≤ 8
- number of HAC cells ≤ 3

Alternatively, track–island pairs might be classified as muons which tend to travel further through the calorimeter. The islands of muon candidates must satisfy the following conditions:

- EMC energy / island energy < 0.9

- EMC energy < 3 GeV
- $0.3 <$ HAC energy < 8 GeV
- number of EMC cells in the island < 5
- number of HAC cells in the island ≤ 6

A loop is then performed over all oppositely–signed e^+e^- and $\mu^+\mu^-$ pairs and the invariant mass is calculated. The event is saved if at least one pair has an invariant mass > 2 GeV.

The charm $c\bar{c}$ trigger, HFL04:

This trigger looks for two oppositely–signed, high transverse momentum tracks consistent with the decay of two charmed mesons due to their large mass. All the following conditions have to be satisfied for an event to pass this trigger:

- Absolute $z-$component of the main vertex $|z_{vertex}| < 75$ cm
- $P_z/E_{total} < 0.9$
- Total transverse energy in the calorimeter, $E_t > 6$ GeV
- At least one positive and one negative track lies in the angular range $15^o < \theta < 165^o$ and has transverse momentum $P_t > 0.4$ GeV.

For the Third Level Trigger (TLT), only the heavy flavour bits interest us. Figure 6.21a shows the five heavy flavour bits triggered by the 1884 remaining Monte Carlo J/ψ candidates after passing the cuts in the previous section and the FLT and SLT

selection. The J/ψ (HFL01) and charm $c\bar{c}$ (HFL04) branches are most regularly triggered. Only 17 J/ψ candidates are not accepted by either of these two triggers, and these candidates are shown in figure 6.21b. Only four out of the 17 J/ψ candidates trigger one of the other heavy flavour triggers and the remaining 13 candidates do not trigger any bits. Therefore, only the HFL01 and HFL04 TLT bits are used in this analysis.

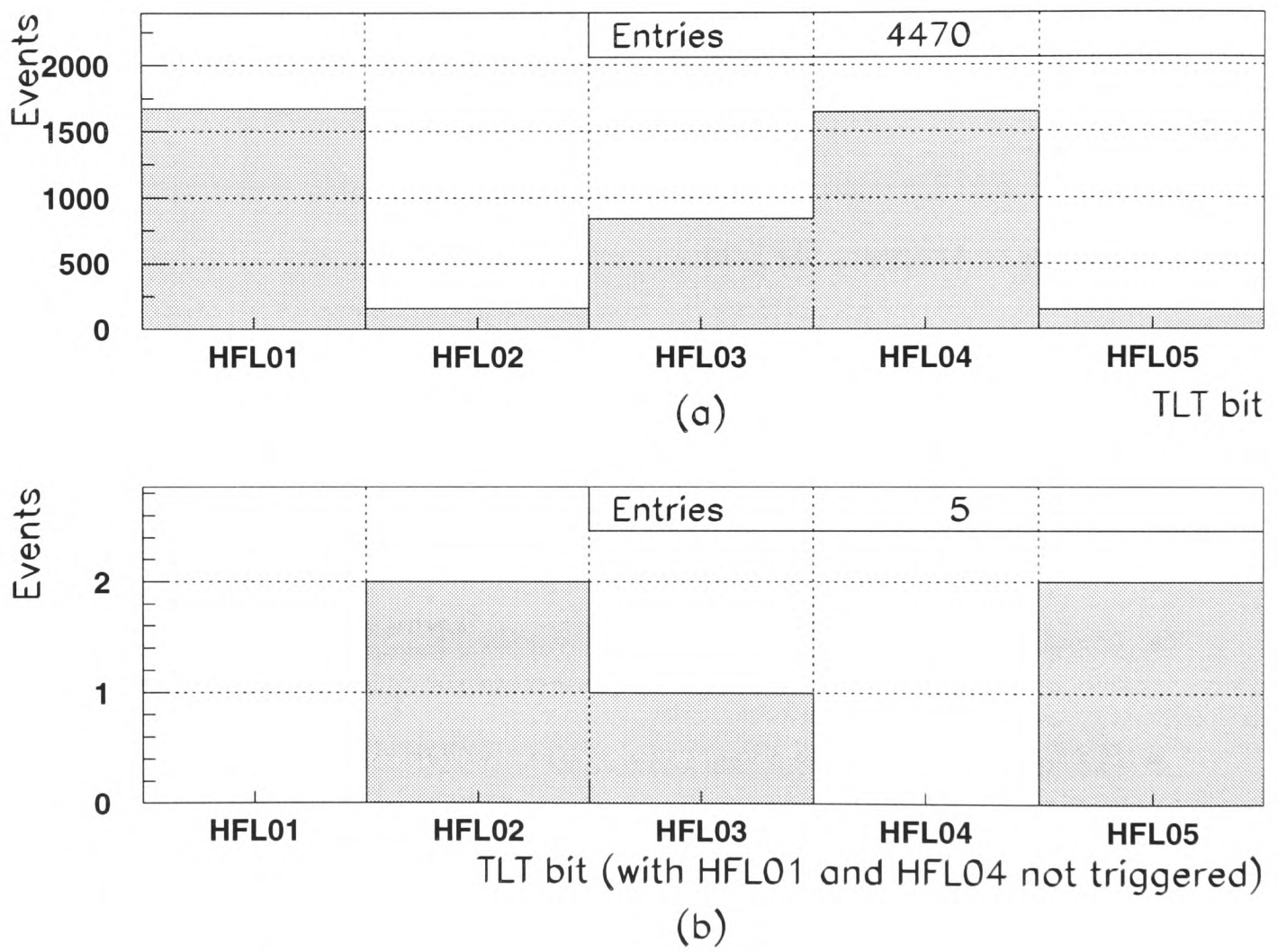

Figure 6.21: TLT bits triggered by HERWIG inelastic J/ψ Monte Carlo events a) passing the J/ψ selection cuts, FLT bit 43, SLT bit HFL3 and b) in addition, requiring TLT HFL01 and HFL04 are not triggered.

In summary, the trigger selection used in this analysis is:

- FLT slot 43
- SLT HFL3 (J/ψ inelastic)

- TLT HFL01 (J/ψ) or HFL04 (charm $c\bar{c}$)

6.5 γp centre–of–mass energy, W, cut

The γp centre–of–mass energy is reconstructed, as described in section 3.2 using $W = \sqrt{2E_p(E-p_z)_{total}}$. The quantity $(E-p_z)_{total}$ is calculated by summing the $(E-p_z)$ for all of the calorimeter cells (using the main event vertex) except those belonging to the J/ψ decay electron island clusters. The $(E-p_z)$ of these decay electrons is calculated using the track variables since the resolution of the track variables is better for the energies of the decay electrons (the track variables cannot be solely used to reconstruct the $(E-p_z)_{total}$ since neutral particles do not leave tracks).

In figure 6.22, a plot of the reconstructed W, against the reconstructed mass is shown for the 287 J/ψ candidates from the 1994 data after passing all the cuts in section 6.3 and the trigger selection in section 6.4. A cut in the W range 80–150 GeV is applied since it will be seen later in the Monte Carlo studies that the acceptance becomes small for W outside this range. In figure 6.23, the reconstructed mass of the events within these W cuts is shown fitted to a gaussian with a bremsstrahlung tail and a second order polynomial background shown as the dashed line. A clear signal is seen at a reconstructed mass of 3.073 ± 0.010 GeV with a width of 0.030 ± 0.008 GeV and 39.7 $\pm$ 8.3 events as determined from the fit parameters.

The like–signed background is shown as the hatched area in the plot. As expected there is no signal in the J/ψ mass region. Also, the like–signed background is considerably lower than the opposite–signed background with 39 like–signed events (in the reconstructed mass range 2.25 – 4.25 GeV) compared to around twice the number of background events in the opposite–signed plot. This discrepancy is due to the third

level trigger selection described in section 6.4.3. The J/ψ HFL01 trigger requires two oppositely charged electron candidates and the charm HFL04 trigger has a minimum transverse momentum cut on both the positive and negative tracks. Much of the like-signed background is therefore rejected by these triggers.

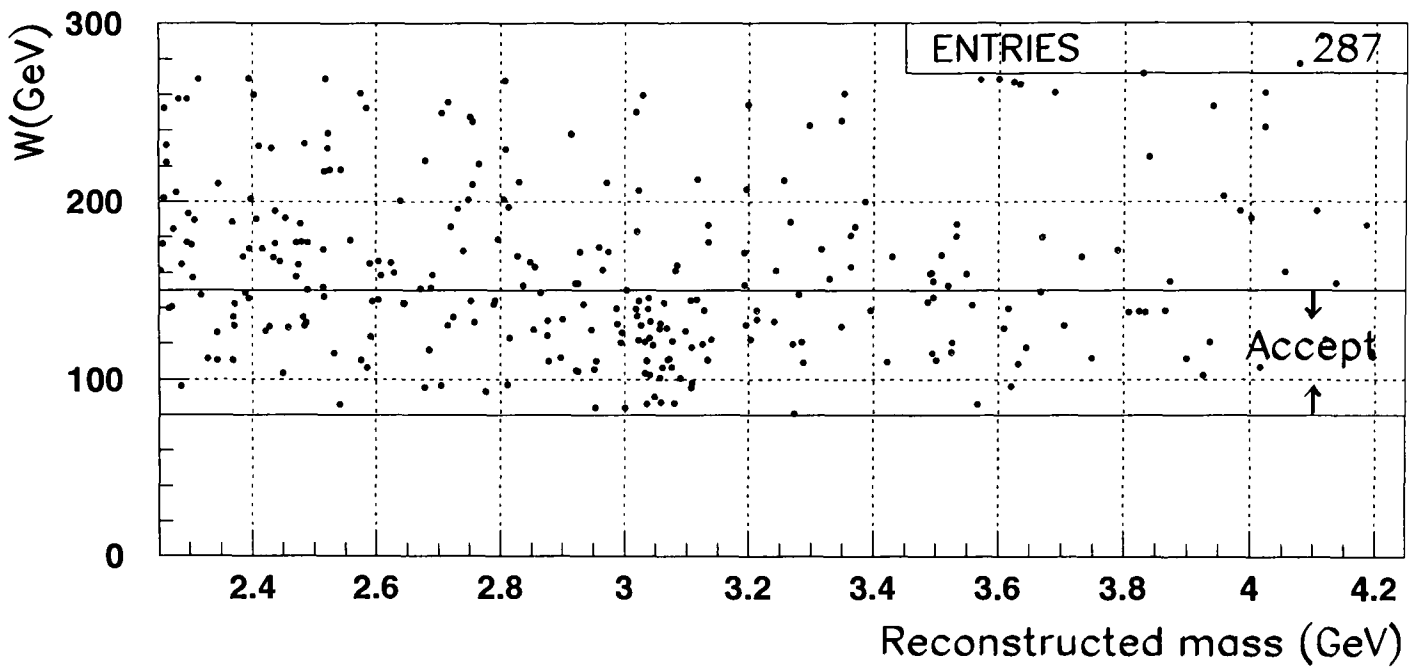

Figure 6.22: W vs. reconstructed mass plot for the inelastic J/ψ candidates selected using the J/ψ selection cuts and the selected triggers.

6.6 Production mechanisms entering the signal

This section checks for J/ψ's produced through mechanisms other than direct inelastic photoproduction. In the 1993 analysis, there was a resolved photon component entering the J/ψ signal which was removed by applying a lower elasticity cut, $z \geq 0.5$. We searched for four track events which might be candidate elastic ψ's decaying to $J/\psi\ \pi^+\pi^-$, but none were found.

6.6.1 Resolved photon J/ψ production

5000 resolved photon channel J/ψ events were produced using the EPJPSI generator. Of these, 165 events passed the inelastic J/ψ selection cuts in section 6.3 as seen in

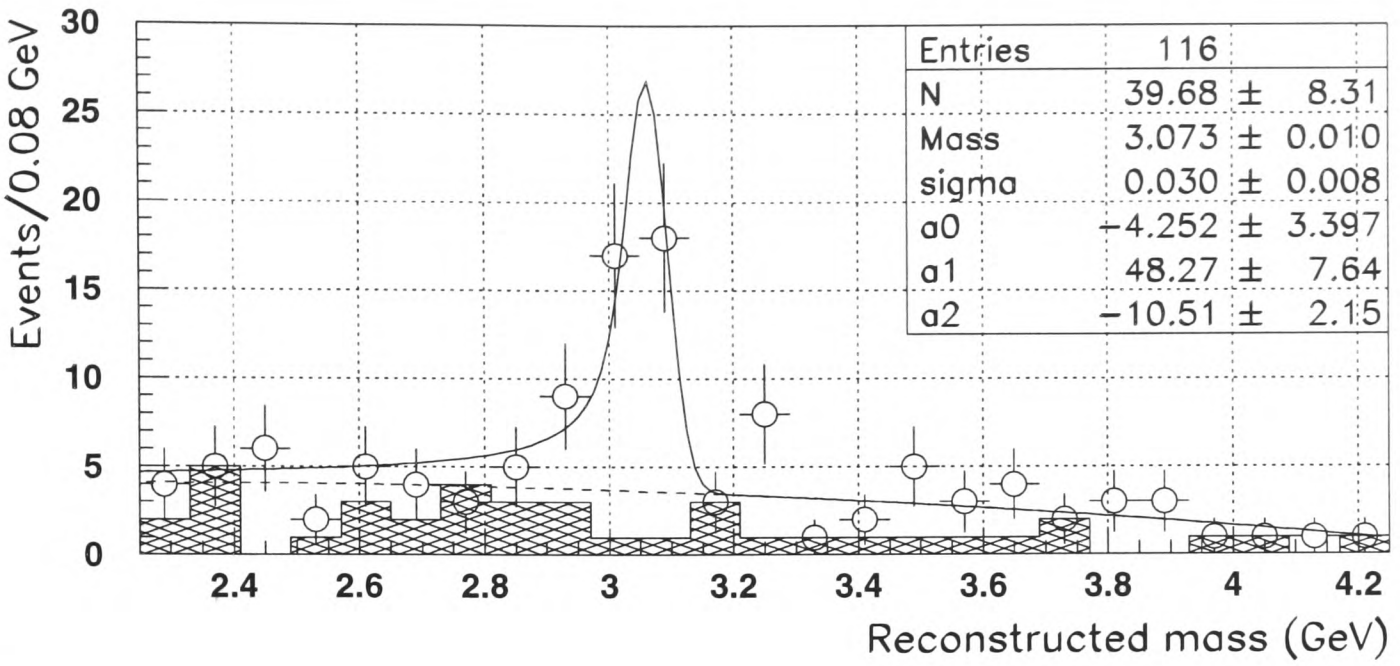

Figure 6.23: Reconstructed mass of the inelastic J/ψ candidates with $80 \leq W \leq 150$ GeV fitted to a gaussian with a bremsstrahlung tail. A second order polynomial, shown as the dashed line, is fitted to the background and the hatched area shows the like–signed background.

figure 5.17d. However, it was found that none of these went on to pass the trigger selection described in section 6.4. This is in contrast to the 1993 analysis where resolved photon channel J/ψ events were entering into the signal. This difference reflects the raising of the energy cuts in the FLT because the increased luminosity in 1994 required a more selective trigger.

Figures 6.24a, b and c show the elasticity distribution of the 1994 inelastic J/ψ data sample after passing the cuts and triggers listed in sections 6.3 and 6.4, for events in the signal region ($2.8 \leq M \leq 3.15$ GeV), and the lower ($2.3 \leq M \leq 2.65$ GeV) and upper ($3.35 \leq M \leq 3.7$ GeV) sideband regions respectively. Note the elasticity cut $z \leq 0.9$ has not been applied in these plots (cut 15 in section 6.3). The elasticity peaks close to unity in the signal region, whereas there is no such peak in the two sideband regions. Due to lack of statistics, differences in the elasticity distributions of the two sideband regions cannot be claimed with any degree of significance.

The two sideband distributions are added together and weighted to the 16.2 background events in the signal mass range (calculated using the fit parameters in figure 6.23). This is subtracted from the signal elasticity distribution to get the background corrected elasticity distribution of the J/ψ events shown in figure 6.24d. This peaks close to unity as in the HERWIG elasticity distribution shown in figure 6.39a in contrast to the elasticity distribution for the 1993 inelastic J/ψ data sample (shown in figure 5.38c) where there was an excess of events in the low z region from the resolved photon channel. This confirms the findings above, from the resolved photon Monte Carlo events which do not pass the trigger selection imposed on the data. Therefore, there is no need for the lower elasticity cut of $z \geq 0.5$ used in the 1993 analysis.

Note that the sideband regions are used for the background subtraction because there are only around 10 like–signed background events in the signal region (compared to 35 in the sideband regions) and using the like–signed events would therefore give an unreliable background estimate.

6.6.2 Elastic ψ' production

A possible source of background to the inelastic J/ψ sample has been identified in section 5.7.2 from the ψ' meson, decaying to the J/ψ with a $(57 \pm 4)\%$ branching ratio.

As in the 1993 analysis, ψ's produced via the elastic photoproduction channel and decaying via $\psi' \to J/\psi \;\; \pi^+\pi^-$ (with the J/ψ subsequently decaying via the electron channel) are removed by looking for four track events with no other activity in the detector and with a reconstructed mass of the two electron and of all four tracks corresponding to the J/ψ and ψ' masses respectively.

Figure 6.25 shows such a candidate elastic ψ' event with two oppositely charged

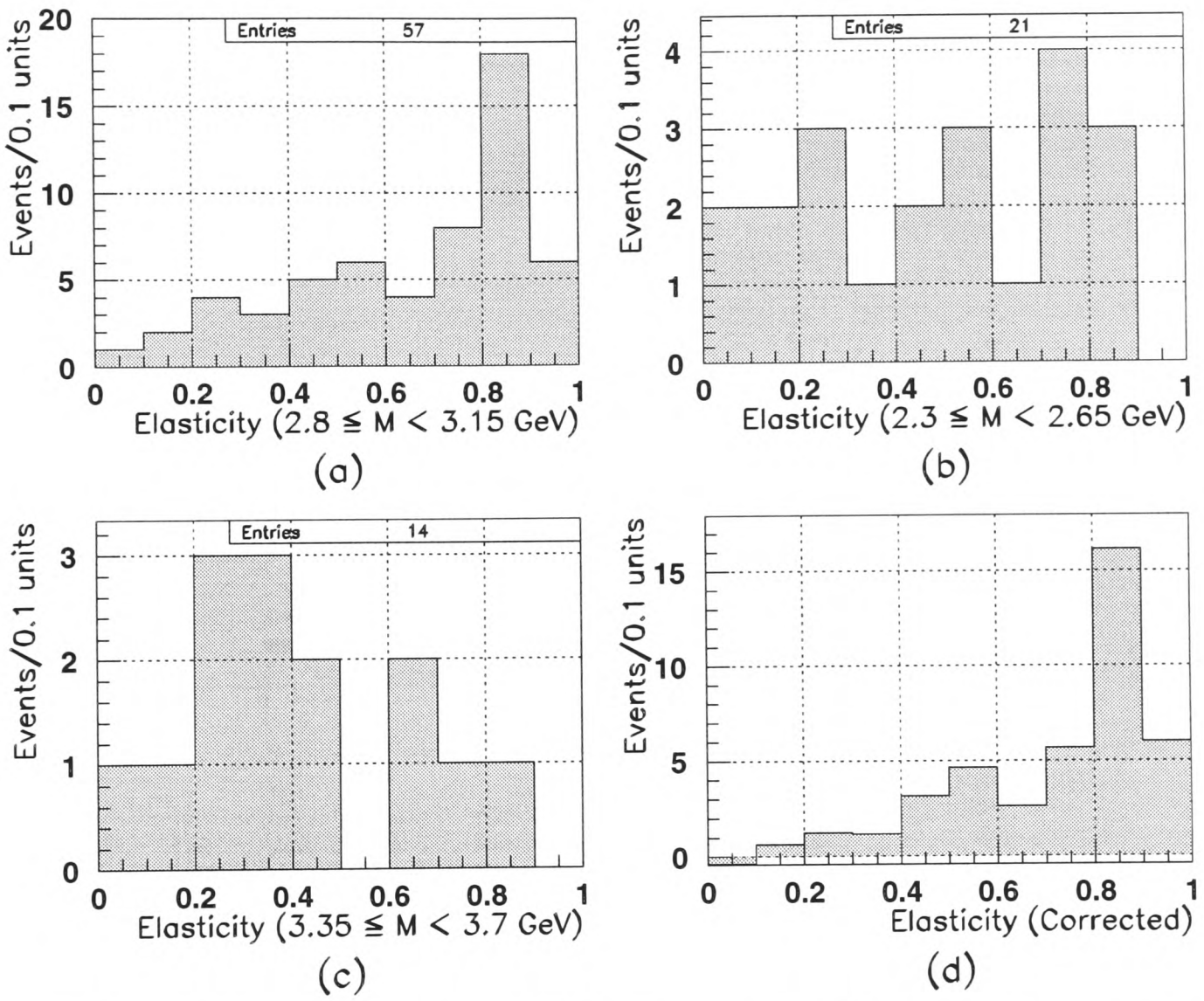

Figure 6.24: Elasticity distribution of J/ψ candidate events in the a) signal reconstructed mass region, 2.8 – 3.15 GeV, b) lower sideband mass region 2.3 – 2.65 GeV and c) upper sideband mass region 3.35 – 3.7 GeV. d) Elasticity distribution in the signal region after background subtraction.

tracks in addition to the two identified e^+e^- tracks and no other tracks in the CTD. However, the invariant mass of the four tracks is found to be 7.0 GeV and so this event is not considered to be via a ψ', which has an invariant mass of 3.686 GeV.

No other candidate ψ' meson, produced via elastic photoproduction and decaying to $J/\psi\ \pi^+\pi^-$ with the subsequent decay $J/\psi \to e^+e^-$ was found in the 1994 inelastic J/ψ data sample.

An upper limit on the contamination from inelastically produced ψ's is estimated in an identical manner to the 1993 analysis. Using Poisson statistics with a 90% confidence level, an upper limit of around five elastic ψ' events decaying into $(J/\psi + \textit{anything})$ is set. From figure 6.2, it is seen that around 440 elastic J/ψ events are found in the 1994 data. Thus, the ratio of elastic J/ψ and ψ' cross–sections has an upper limit of around 1.1%.

The upper limit for this ratio is assumed to be the same for the inelastic J/ψ and ψ' cross–sections. It is multiplied by the branching ratio $\mathcal{B}.\mathcal{R}.(\psi' \to J/\psi\, X) = (57 \pm 4)\%$, an upper limit on inelastic ψ' contamination of 0.6% is obtained.

6.7 In–depth view of an inelastic J/ψ event

In figure 6.26, one of the selected sample of inelastic J/ψ events is shown in three different projections. This is not representative of all events in the sample as some have many more tracks and activity in the detector, making it more difficult to identify the decay electrons from the J/ψ.

A clear interaction vertex, near to the nominal vertex is seen as well as large energy deposits around the forward beam pipe in the ZR and ZX projections which are the remnants of the proton after the interaction. There are no energy deposits around the

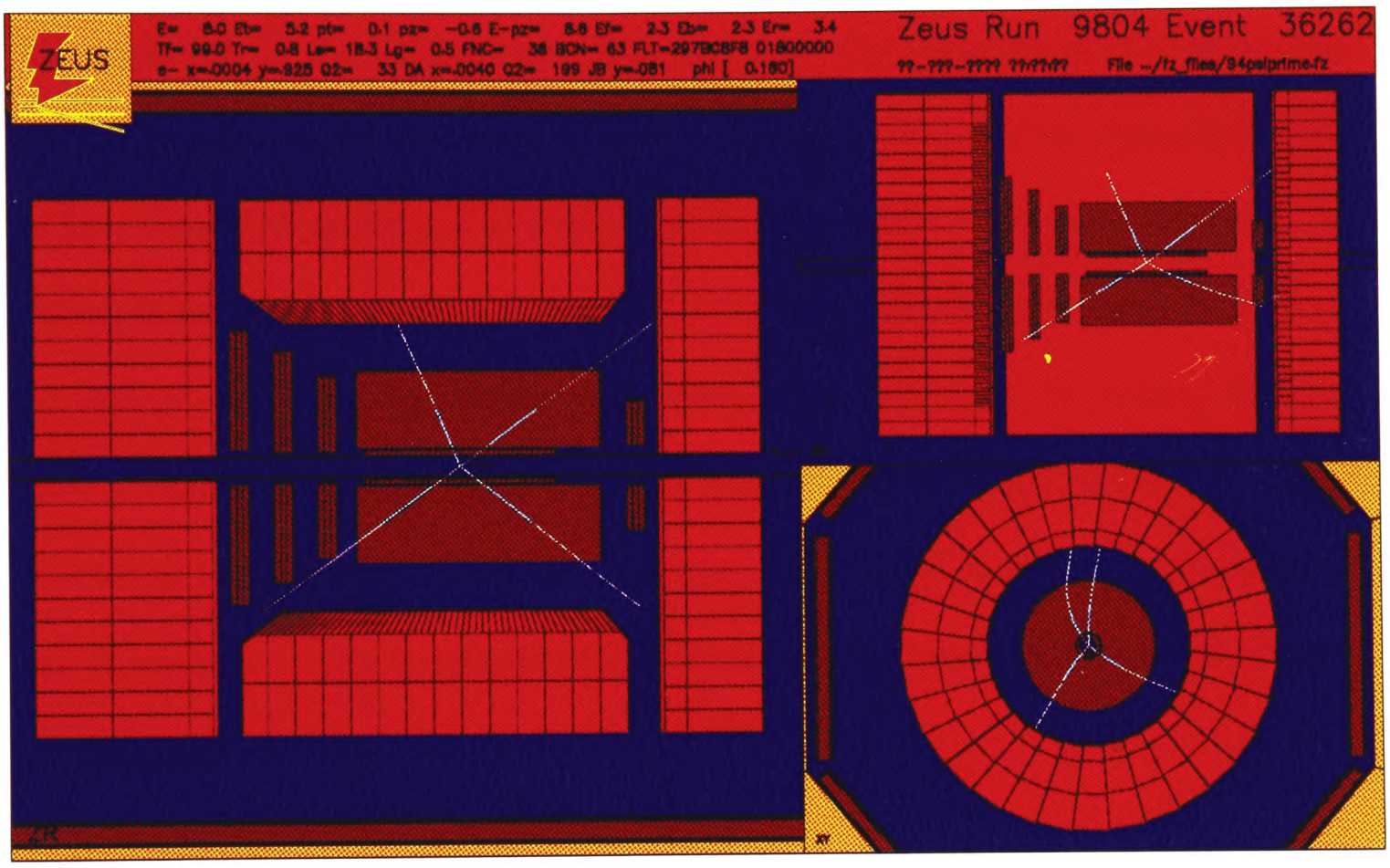

Figure 6.25: Candidate elastic ψ' event from the 1994 data. Two positively and two negatively charged tracks are seen in the detector in accordance with a ψ' produced via elastic photoproduction and decaying via $\psi' \to J/\psi\,\pi^+\pi^-$ followed by $J/\psi \to e^+e^-$. However, the reconstructed mass of the four tracks is 7.0 GeV, almost twice the ψ' mass and so this is not considered to be an elastic ψ' event. The main and top right pictures show the event in the ZR and ZY projections respectively. The bottom right picture shows the XY projection and the charge of the tracks is seen by their curvature.

rear beam pipe and the incident electron is not seen in the detector, as required for photoproduction events (see cut 13 in section 6.3).

There are one electron and two positron candidates in the event which satisfy the $e^{\pm}$ selection criteria outlined in section 6.3. The tracks corresponding to these candidates are labelled A, B, and C. It is seen in the main ZR projection that these tracks point towards energy deposits which lie entirely in the EMC part of the calorimeter. In the XY projection on the bottom right, it is seen from the curvature of the tracks, that track B is negative whereas tracks A and C are positive. It is possible (ignoring charge) to have three J/ψ candidates with the three electron tracks in the event. However, the pairing B and C gives a reconstructed mass of 2.0 GeV, and so it is rejected by the mass cut of 2.25 – 4.25 GeV, despite the tracks being of opposite sign. The pairing A and C gives a reconstructed mass very close to the nominal J/ψ mass of 3.10 GeV, but this is rejected as the two tracks are of the same sign. Finally, the opposite–signed pairing A and B, combine to give a reconstructed mass of 3.03 GeV and this is accepted into the inelastic J/ψ sample.

6.8 dE/dx

As in the 1993 analysis, the Monte Carlo does not reproduce $\frac{dE}{dx}$ values comparable to the data, so the elastic J/ψ sample is used to calculate an efficiency for the $\frac{dE}{dx}$ cut used in section 6.3. Electrons from photon conversions are used to check on the validity of this method.

In figure 6.2, a very clean elastic J/ψ sample is seen. The $\frac{dE}{dx}$ values of the two decay electron tracks are plotted in figure 6.14b for events in this sample with a reconstructed mass in the range of 2.8 – 3.15 GeV to further improve the signal to background ratio.

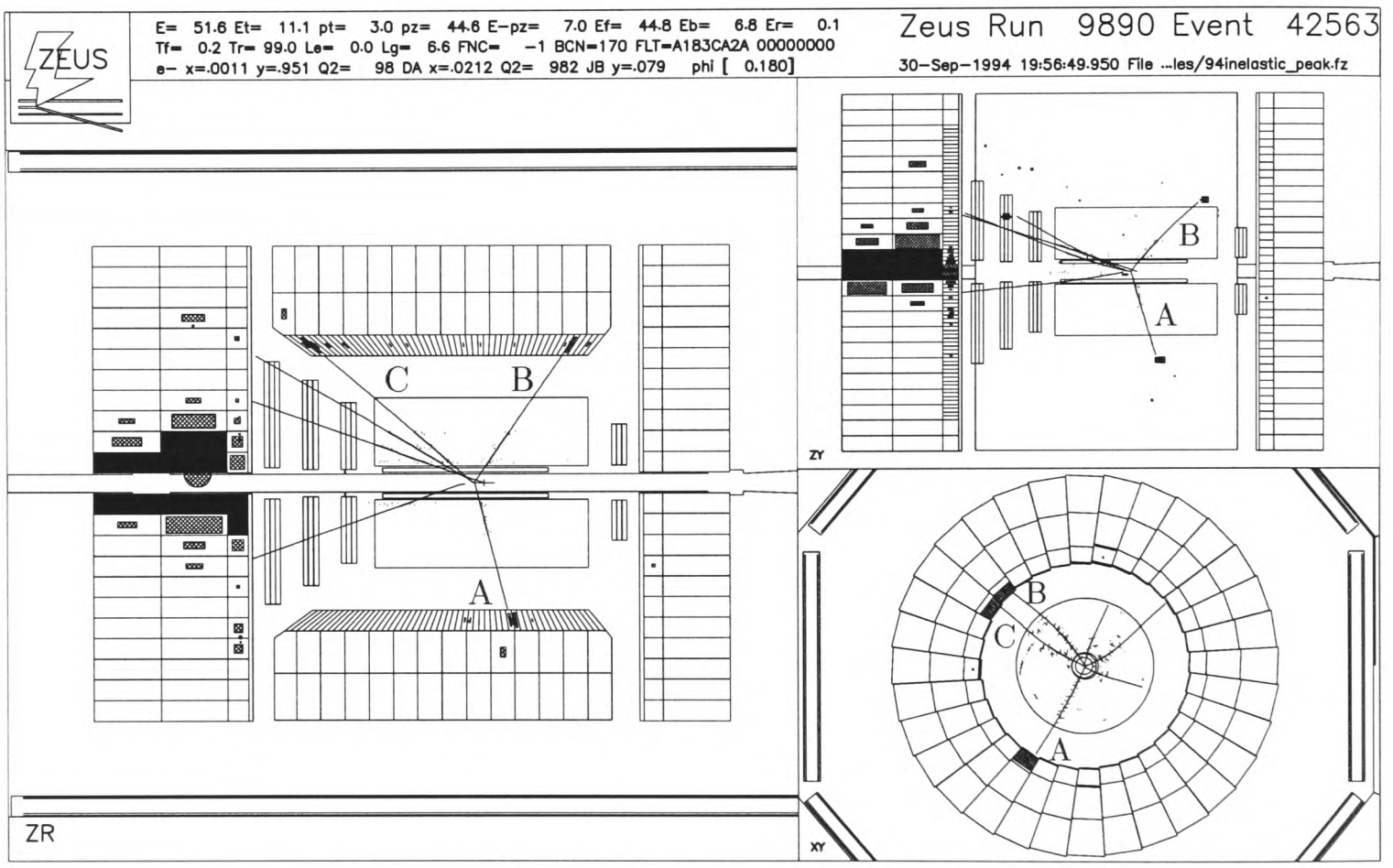

Figure 6.26: Candidate inelastic J/ψ event from the 1994 data in three projections. Three candidate electron tracks are labelled A, B and C. From the track curvatures in the bottom right XY projection, it is seen that track B is negative, whereas tracks A and C are positive. Track C is not labelled in the top right ZX projection because of the density of tracks. The main picture shows the ZR projection.

It is fitted to a gaussian and assuming that these tracks are all electrons, the probability that an electron track has $\frac{dE}{dx} \geq 1.25$ can be calculated from the fit parameters. This is found to be $83.9^{+1.2}_{-1.3}\%$. Therefore, the probability a real J/ψ decaying into a e^+e^- pair passes this $\frac{dE}{dx}$ cut is $70.4^{+2.0}_{-2.2}\%$. For comparison, the efficiency for the $\frac{dE}{dx}$ cut in the 1993 analysis was $97.5^{+0.7}_{-0.9}\%$. The change reflects the tightening of the cut in the 1994 analysis which was not possible in 1993 because of the lack of statistics and the poorer $\frac{dE}{dx}$ reconstruction.

In using this method for calculating the $\frac{dE}{dx}$ efficiency, we must assume that the distributions of electron track variables (such as momentum, pseudorapidity etc.) are the same for the decay electron tracks in both the elastic and inelastic J/ψ samples, or alternatively, we must assume that there is no systematic shift in the $\frac{dE}{dx}$ values for electron tracks as a function of these track variables. In figures 6.27 – 6.29, the distributions for the track momentum, pseudorapidity and number of degrees of freedom per track are shown for the a) inelastic and b) elastic J/ψ decay electron tracks and c) for a sample of electrons from photon conversions in the 1994 data. In the inelastic and elastic J/ψ samples, a further cut on the reconstructed mass of 2.8 – 3.15 GeV is applied to further improve the signal to background ratio.

The distributions of the inelastic and elastic J/ψ samples for the number of degrees of freedom per track are seen to be very similar, but there seem to be differences in the track momentum and pseudorapidity distributions with the decay electrons from inelastic J/ψ tending to have greater momentum and going more in the rearward direction. Thus, we must assess how much the $\frac{dE}{dx}$ values of tracks depend on these three quantities.

Electrons from photon conversions, found using the CONVERT2 algorithm, are again used to see how the $\frac{dE}{dx}$ value of an electron track varies with the track variables

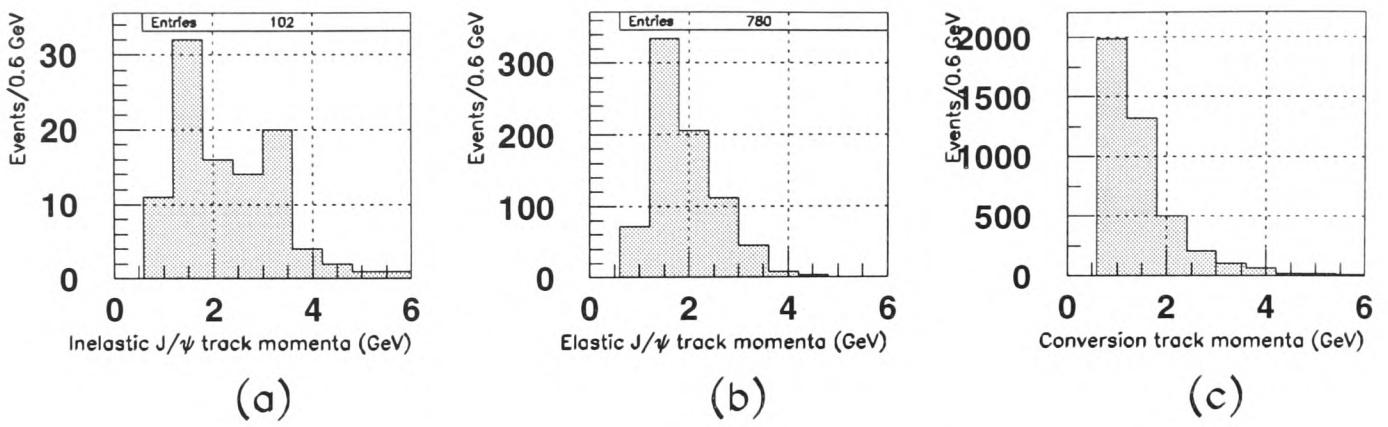

Figure 6.27: Momentum distribution of tracks from the a) inelastic J/ψ b) elastic J/ψ and c) conversion electron samples with an invariant mass cut of 2.8 – 3.15 GeV applied to the J/ψ samples.

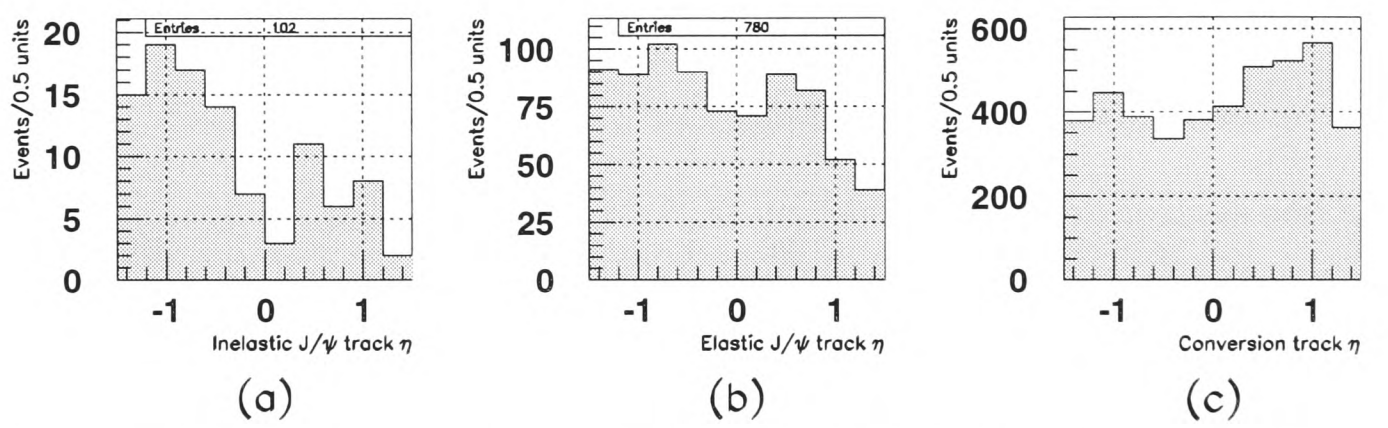

Figure 6.28: Pseudorapidity, η, distribution of tracks from the a) inelastic J/ψ b) elastic J/ψ and c) conversion electron samples with an invariant mass cut of 2.8 – 3.15 GeV applied to the J/ψ samples.

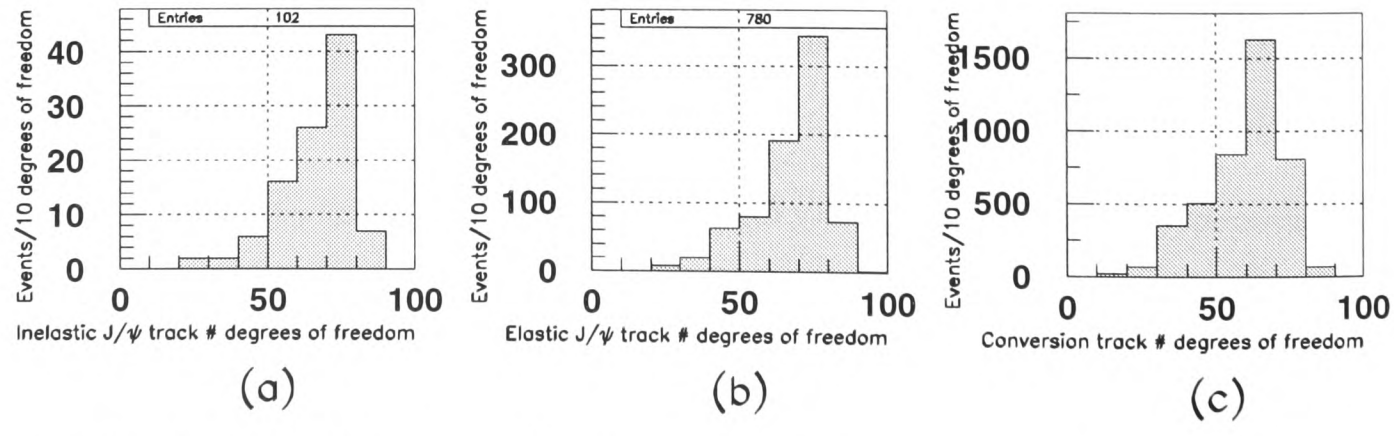

Figure 6.29: Number of degrees of freedom per track in the a) inelastic J/ψ b) elastic J/ψ and c) conversion electron samples with an invariant mass cut of 2.8 – 3.15 GeV applied to the J/ψ samples.

plotted in figures 6.27 – 6.29. This will provide a means of assessing the systematic error on the efficiency of the $\frac{dE}{dx}$ cut.

611,164 conversion electron pairs were found in the 1994 data by requiring IGC-TAG = 3 in the CONVERT2 algorithm (see section 3.6). The variable DistB is plotted in figure 6.30a for all these conversion electron pairs up to $|\text{DistB}| \leq 25$ with the flat distribution in the region $-25 \leq \text{DistB} < 0$ representing the like–signed background pairs.

As in the 1993 analysis, the signal to background ratio of the conversion sample is improved by taking conversion pairs with $0 \leq \text{DistB} < 1$. The cuts used on the elastic J/ψ electron tracks are also applied[8]. These require both tracks to have a transverse momentum $P_t > 0.6$ GeV, absolute pseudorapidity $|\eta| \leq 1.5$ and to start in the vertex detector or superlayer 1 of the CTD and go at least as far as superlayer 3. The $\frac{dE}{dx}$ values of the tracks from the conversion pairs passing these cuts is shown in figure 6.30b with the like–signed background ($-25 \leq \text{DistB} < 0$) $\frac{dE}{dx}$ values shown in figure 6.30c.

The background $\frac{dE}{dx}$ distribution is seen to peak at a lower $\frac{dE}{dx}$ value due to the fact that there will be more hadrons faking electrons in the background sample which tend to have lower mean $\frac{dE}{dx}$ values[9]. Assuming the level of background is the same for the opposite and like–signed conversion pairs, the background $\frac{dE}{dx}$ distribution (with $-25 \leq \text{DistB} < 0$) is scaled by 1/25 and subtracted from the distribution of the conversion sample (with $0 \leq \text{DistB} < 1$) to get a background corrected distribution for the conversion electron pairs shown in figure 6.30d. The fraction of electrons with $\frac{dE}{dx} \geq 1.25$ is used to calculate the probability an electron will pass the $\frac{dE}{dx}$ cut. A value of $(87.7 \pm 0.6)\%$ is obtained. This gives an efficiency for the $\frac{dE}{dx}$ cut used in this inelastic J/ψ analysis

[8] See section 6.2.
[9] See section 3.5.1.

of $(77.0 \pm 1.1)\%$ which is around three standard deviations away from the efficiency calculated using the elastic J/ψ sample.

This difference in the efficiency could be due to differences in the distributions of the track variables, such as the track momentum, pseudorapidity and number of degrees of freedom. These three distributions for the electron tracks from conversion photons are plotted alongside the corresponding distributions for inelastic and elastic J/ψ decay electron tracks in figures 6.27c – 6.29c. The background has been subtracted in the three plots 6.27c – 6.29c using the same method as that described in the preceding paragraph. We see that there are differences between the distributions, especially in the momentum and number of degrees of freedom plots. Because the distributions from the elastic J/ψ sample match those from the inelastic J/ψ sample better than those from conversion photons, we will use the efficiency for the $\frac{dE}{dx}$ cut calculated from the elastic J/ψ sample in a cross–section calculation at the end of this chapter. The efficiency calculated using conversion photons will be used to estimate the error on this efficiency.

The dependence of the $\frac{dE}{dx}$ values of the conversion electron tracks with the track momentum, pseudorapidity and number of degrees of freedom is now considered. The $\frac{dE}{dx}$ values of the tracks in the conversion pairs with $0 \leq \text{DistB} < 1$ are plotted against their momentum in figure 6.31a. These $\frac{dE}{dx}$ values are projected into six bins of momentum. The corresponding background distributions (found as before by binning tracks from the conversion pairs with $-25 \leq \text{DistB} < 0$ and scaling by 1/25) are subtracted. A gaussian is fitted to each of the six resulting background subtracted $\frac{dE}{dx}$ distributions to get the mean $\frac{dE}{dx}$ value in each momentum bin together with the width of the gaussian. These means and widths are plotted in figure 6.31b. The mean $\frac{dE}{dx}$ is seen not to vary significantly over the momentum range of concern in this analysis.

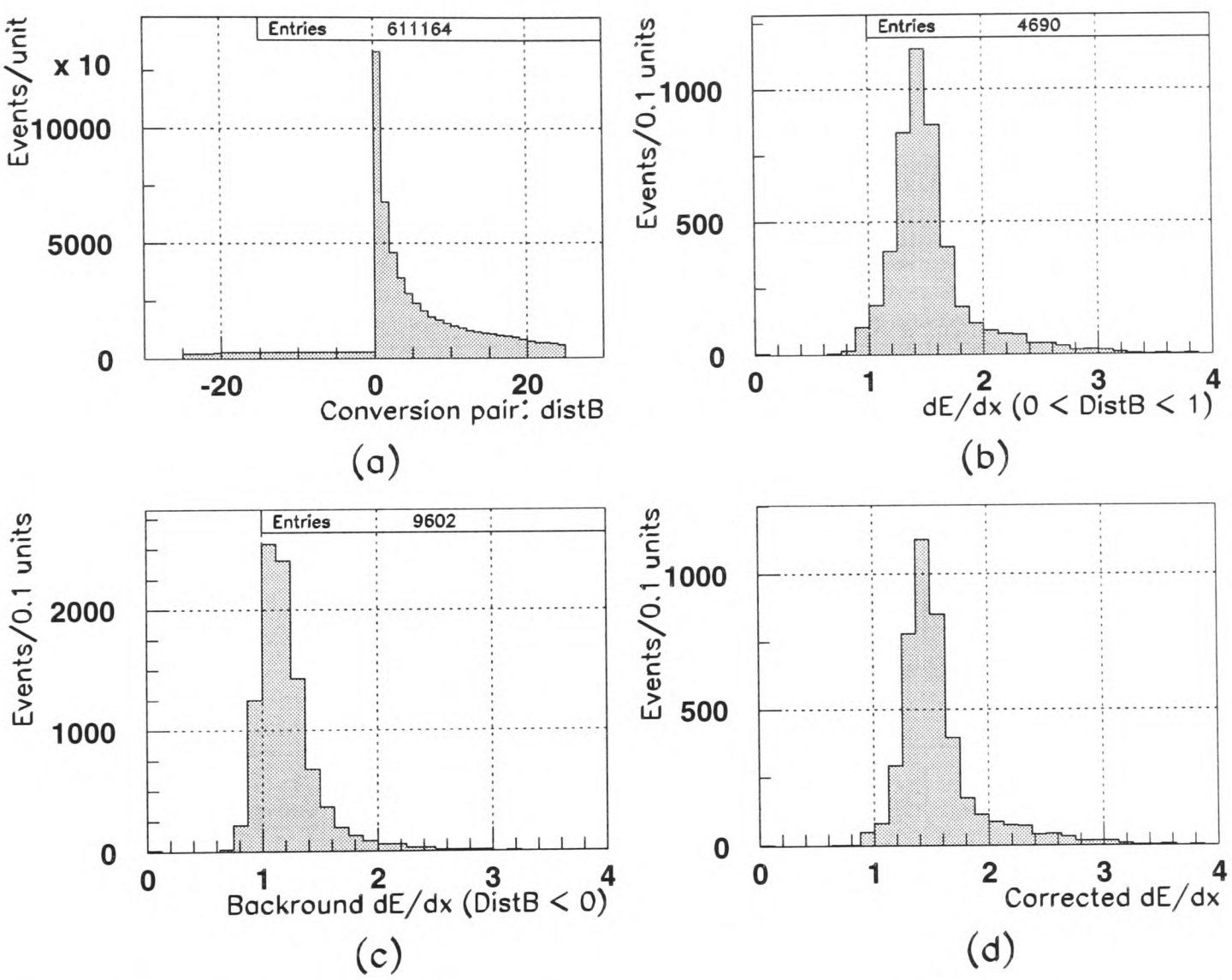

Figure 6.30: a) DistB for all the conversion pair candidates in the 1994 data with IGCTAG = 3, b) $\frac{dE}{dx}$ distribution of conversion tracks with $0 \leq$ DistB < 1, c) $\frac{dE}{dx}$ distribution of tracks from the like-signed background pairs with DistB < 0, d) background subtracted $\frac{dE}{dx}$ distribution.

Similar plots are shown for the track pseudorapidity in figures 6.32a and b. Here, the mean $\frac{dE}{dx}$ value dips near $\eta = 0$ and rises strongly for rearward going tracks. From figures 6.28a and b, it is seen that decay electron tracks from the inelastic J/ψ sample also tend to travel more in the rearward direction than elastic J/ψ tracks. This will result in an underestimation of the efficiency for the $\frac{dE}{dx}$ cut, calculated using the elastic J/ψ sample.

Figures 6.33a and b show similar plots for the number of degrees of freedom on the tracks. Although this shows a slight rise for tracks with fewer degrees of freedom, this is not worrying since there are very few tracks in the inelastic and elastic J/ψ samples with fewer than 50 degrees of freedom as shown in figures 6.29a and b.

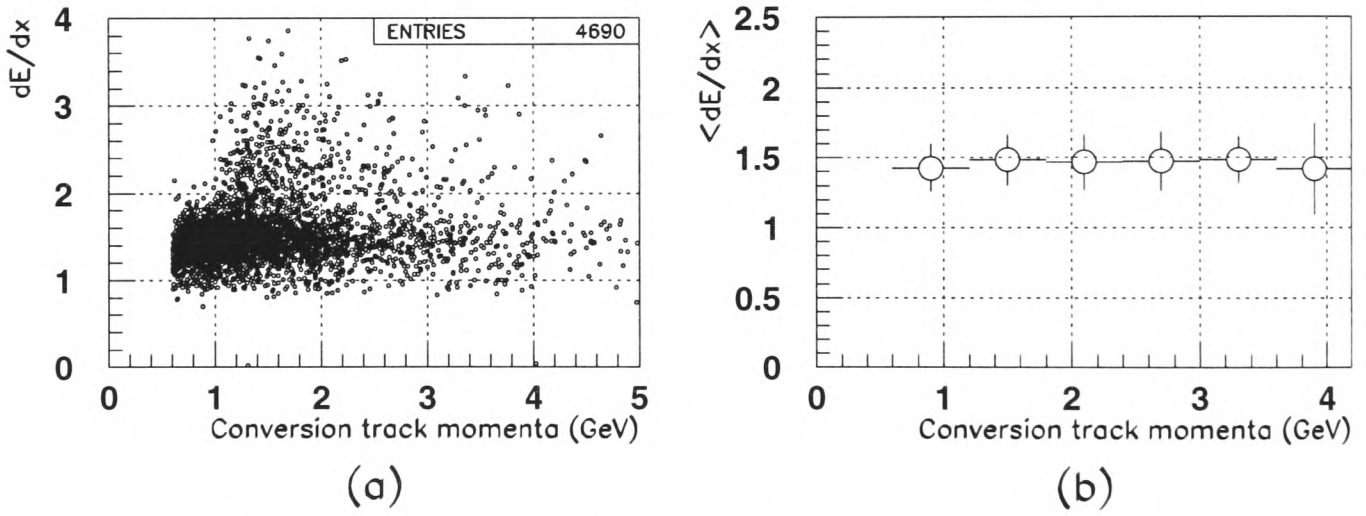

Figure 6.31: a) $\frac{dE}{dx}$ vs. track momenta for conversion tracks with $0 \leq \text{DistB} < 1$ and b) mean background subtracted $\frac{dE}{dx}$ in momentum bins.

6.9 Monte Carlo Studies

The acceptance of the inelastic J/ψ selection procedure is calculated in this section using HERWIG Monte Carlo events with the MRSD$-'$ [35, 36] proton structure function. The Monte Carlo is also used to see how well various physical quantities are reconstructed.

Figure 6.34a, shows the generated W distribution of the 49,907 HERWIG Monte

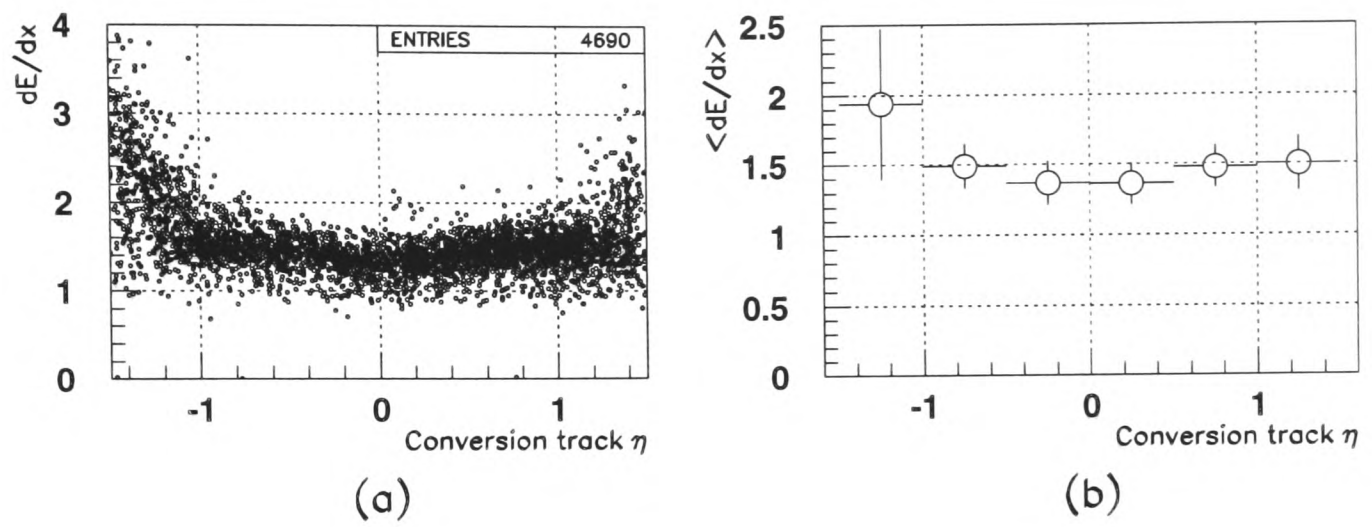

Figure 6.32: a) $\frac{dE}{dx}$ vs. track pseudorapidity, η, for conversion tracks with $0 \leq$ DistB $<$ 1 and b) mean background subtracted $\frac{dE}{dx}$ in pseudorapidity bins.

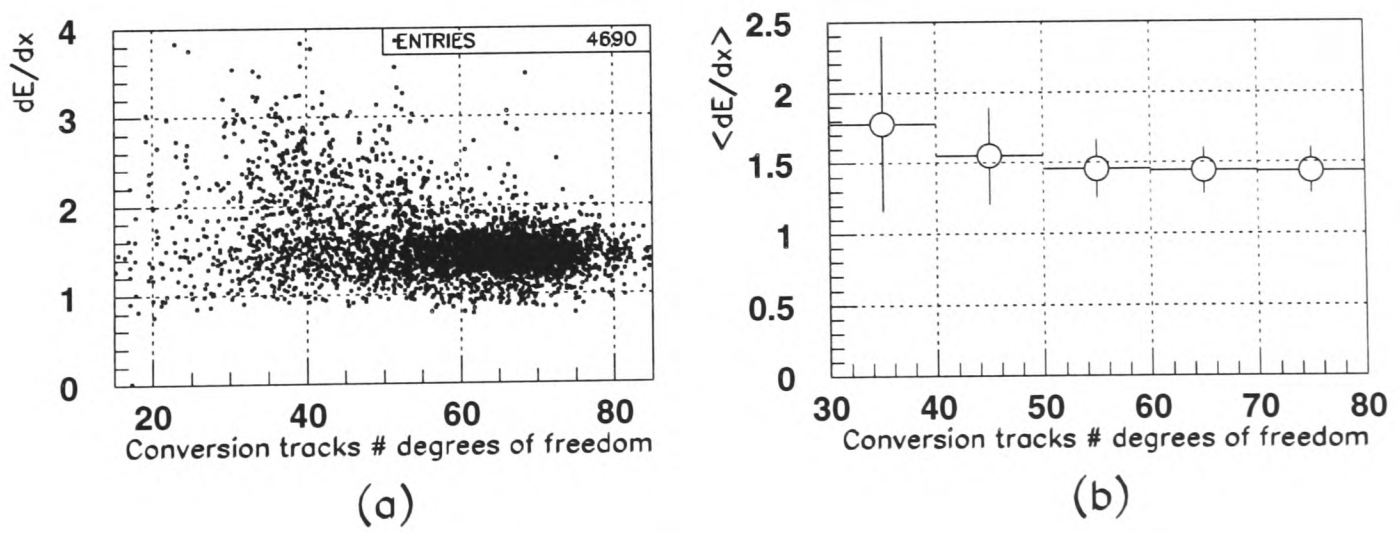

Figure 6.33: a) $\frac{dE}{dx}$ vs. number of degrees of freedom per conversion track with $0 \leq$ DistB $<$ 1 and b) mean background subtracted $\frac{dE}{dx}$ in bins of number of degrees of freedom.

Carlo events. There are 16,847 J/ψ candidates accepted after the pre–selection cuts. In figure 6.34b, the reconstructed against the generated W is shown for these candidates. A general correlation is seen between the two, but there are also a large number of events with a reconstructed W of around 300 GeV for the whole generated W range. This arises from the method for calculating W (see equation 3.4 in section 3.2) where the scattered electron is assumed not to enter the calorimeter. In events where this is not the case, the scattered electron contributes approximately $2 \times E_e = 2 \times 27.5$ GeV (where E_e =electron beam energy) to the $(E - p_z)_{total}$ of the event for low Q^2 events with this contribution decreasing with Q^2. Neglecting the $(E - p_z)$ of the other activity in the calorimeter, W will then be reconstructed as:

$$W = \sqrt{2E_pE_e} = \sqrt{s} \approx 300GeV$$

where : $\sqrt{s}$ = Total centre–of–mass energy

E_e = Incident electron energy

E_p = Incident proton energy

which is exactly what is seen in figure 6.34b. When the low Q^2 cut (up to 1 GeV in the first calorimeter ring around the rear beam pipe – cut 13 in section 6.3) is applied, the reconstructed against true W distribution becomes much cleaner as shown in figure 6.34c. Figure 6.35a shows the reconstructed W distribution of all the pre–selected events and in figure 6.35b, the acceptance of the pre–selection algorithm is shown. Again, a small rise in the number of events and acceptance due to the higher Q^2 events, where the scattered electron enters the calorimeter, is seen, beginning at a W of around 250 GeV since the low Q^2 cut has not yet been applied.

In figures 6.36a and b, the reconstructed W distribution and acceptance are shown for the pre–selected events with the triggers described in section 6.4 applied. The

acceptance in figure 6.35b after only the pre–selection is shown as the dotted line in figure 6.36b. The triggers are seen to remove a large portion of the lower W events because these have lower $(E - p_z)_{total}$ (see equation 3.4) and hence tend not to have enough energy to pass the energy requirements in the trigger cuts.

Next, the J/ψ decay electron identifying cuts 1 to 11 from section 6.3 are applied to the pre–selected, triggered Monte Carlo events. The reconstructed W distribution and acceptance are plotted again in figures 6.37a and b respectively with the dotted line showing the acceptance of the events with just the trigger bits set. The acceptance is seen to fall sharply reflecting the stringency required in the cuts to see a J/ψ signal. Note that the Monte Carlo does not reproduce $\frac{dE}{dx}$ values as mentioned in section 6.8, so cut 12 (in section 6.3) cannot be applied.

Finally, cuts 13 to 16 in section 6.3, used to select the direct inelastic J/ψ production mechanism, are applied. The reconstructed W distribution and acceptance are plotted in figures 6.38a and b respectively with the acceptance of figure 6.37b without cuts 13 to 16 shown as the dotted line. The acceptance drops considerably for W above 200 GeV where the higher Q^2 events, mentioned above, are removed. As expected, below 200 GeV, the acceptance is not so greatly reduced, since these cuts were designed to keep inelastic J/ψ events whilst rejecting other J/ψ production mechanisms.

As stated in section 6.5, the acceptance falls to near zero at around $W = 80$ GeV and the background to the J/ψ signal in the data begins to be significant for $W > 150$ GeV. A cut is therefore placed in the W range 80 – 150 GeV. The number of generated Monte Carlo events in the generated W^{gen} range 80 – 150 GeV with a generated elasticity, $z^{gen} \leq 0.9$, is 10,950 and the number of events accepted in the reconstructed W^{rec} range 80 – 150 GeV with a reconstructed elasticity, $z^{rec} \leq 0.9$, is 1434. The acceptance

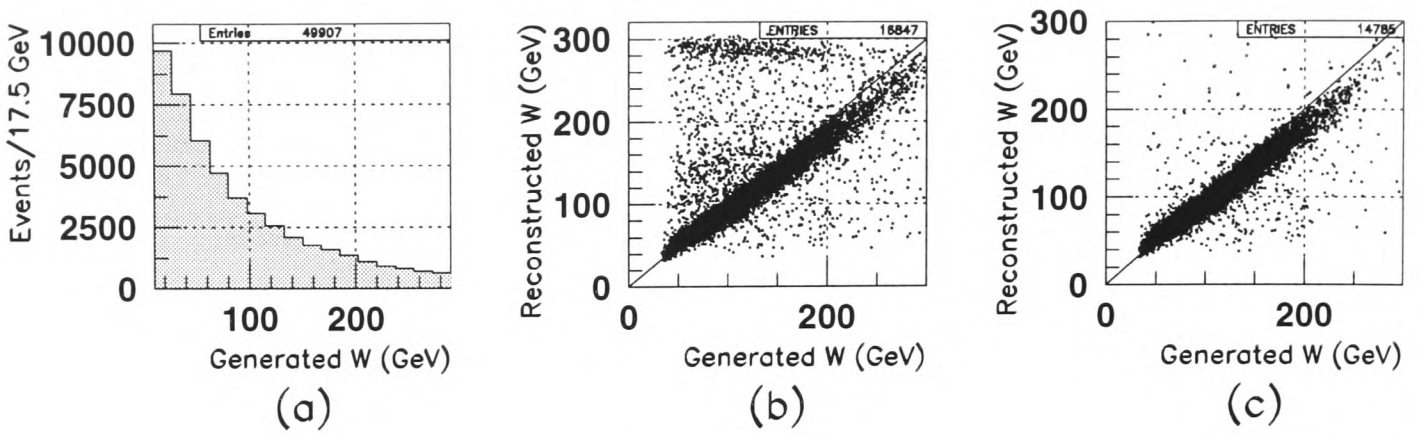

Figure 6.34: a) W distribution (GeV) of HERWIG generated events b) Correlation between reconstructed and generated W for pre–selected HERWIG events and c) with the low Q^2 cut the total energy in the first calorimeter ring < 1 GeV applied.

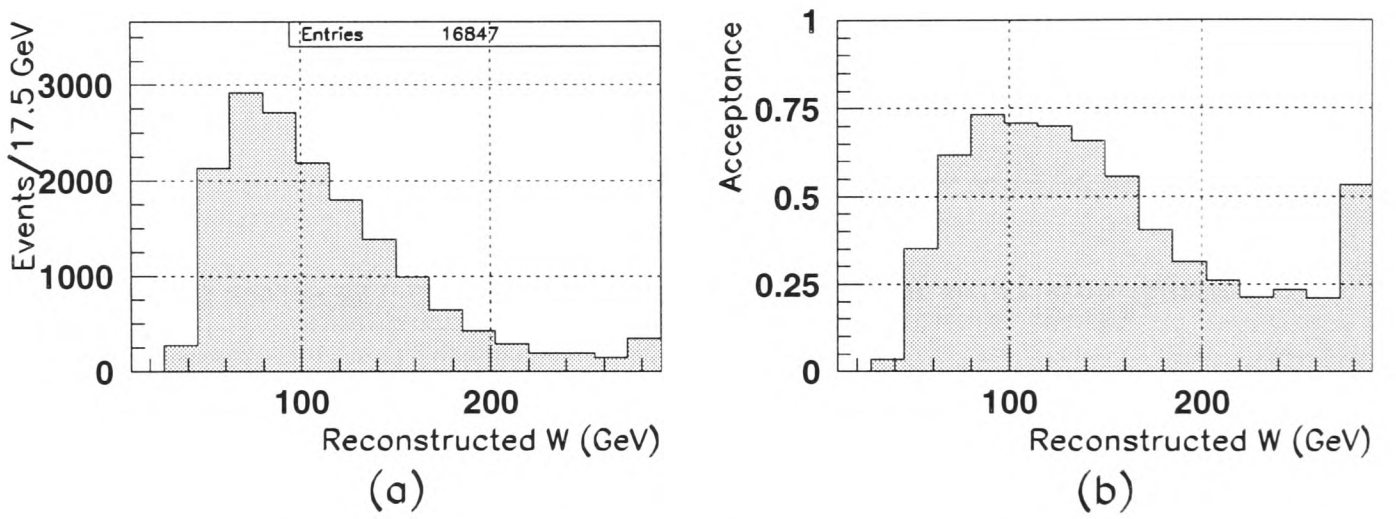

Figure 6.35: a) W distribution (GeV) and b) W acceptance of pre–selected HERWIG generated events.

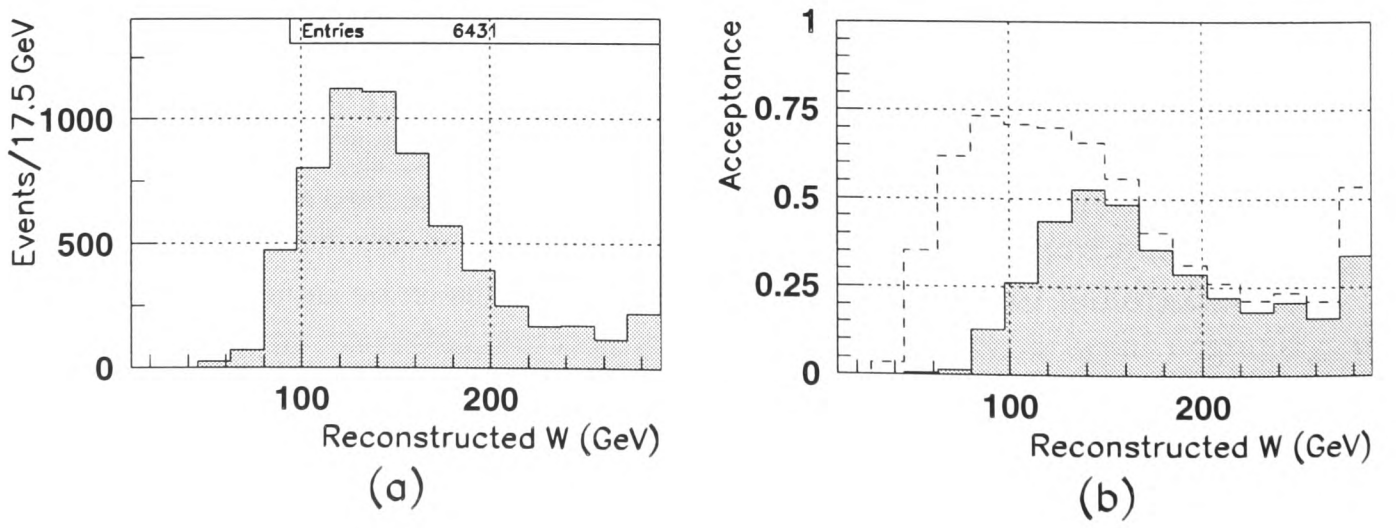

Figure 6.36: a) W distribution (GeV) and b) W acceptance of pre–selected HERWIG generated events with trigger bits set. The previous acceptance without the trigger bits set is shown as the dotted line.

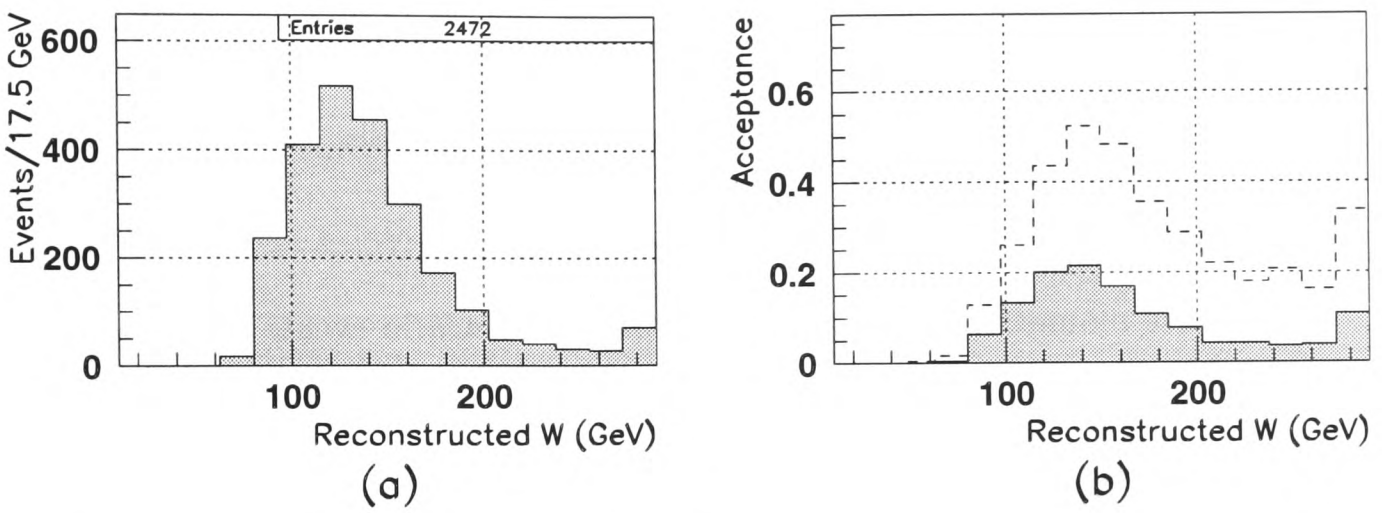

Figure 6.37: a) W distribution (GeV) and b) W acceptance of HERWIG generated events with trigger bits set and all decay electron identifying cuts applied. The previous acceptance with just the trigger bits set is shown as the dotted line.

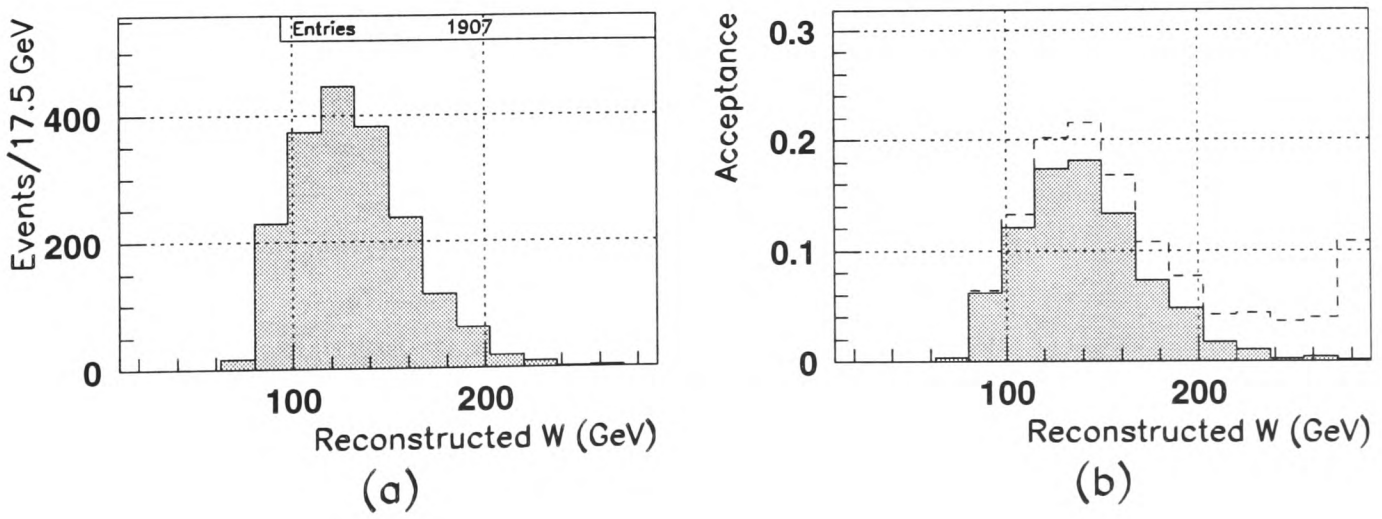

Figure 6.38: a) W distribution (GeV) and b) W acceptance of the final selection of HERWIG generated events after all the cuts have been applied. The previous acceptance with the trigger bits and decay electron cuts applied is shown as the dotted line.

for inelastic J/ψ Monte Carlo events over this W range is then given by:

$$\begin{aligned} \text{Acceptance} &= \frac{(\text{Number of accepted events in } 80 < \text{W}^{\text{rec}} < 150\,\text{GeV})}{(\text{Number of generated events in } 80 < \text{W}^{\text{gen}} < 150\,\text{GeV})} \\ &= (13.10 \pm 0.35)\% \end{aligned} \tag{6.1}$$

This method for calculating the acceptance automatically takes care of any systematic shifts in the reconstruction of W and z. Figures 6.39a and b show the elasticity and J/ψ transverse momentum respectively for the Monte Carlo events within this W range.

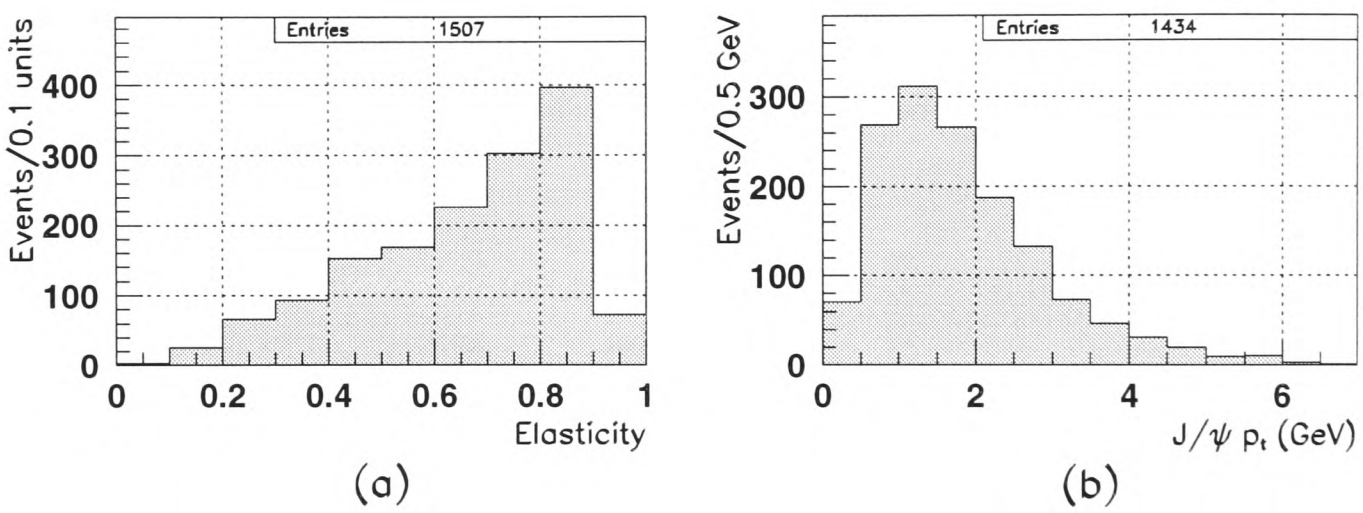

Figure 6.39: Distribution of a) elasticity and b) the J/ψ transverse momentum of the final selection of HERWIG generated events with $80 < W < 150$ GeV.

Having obtained a sample of Monte Carlo events passing the cuts applied to the data, it is now used to see how well various quantities are reconstructed. The reconstructed and generated W are plotted against one another in figure 6.40a (without the W cut applied) and in figure 6.40b, $(W^{rec} - W^{gen})/W^{gen}$ is plotted (with the W cut) and fitted to a gaussian. The fit gives a width of $(5.9 \pm 0.2)\%$ and a systematic shift in the mean of $(6.5 \pm 0.2)\%$.

Similar plots are shown for the J/ψ transverse momentum in figures 6.41a and b. This is reconstructed using the decay electron tracks alone, and as a result, the resolution

is much better than for W with a width of $(2.5 \pm 0.1)\%$ and a systematic shift of less than 1%. Similar plots for the elasticity are shown in figures 6.42a and b. One sees that the reconstruction is poorer than that of both the W and J/ψ transverse momentum distributions, having a width of $(11.8 \pm 0.4)\%$ and a shift of $(6.7 \pm 0.4)\%$. This is because it is calculated entirely using calorimeter measurements (see equation 3.5). The systematic shifts in W and z are accounted for by the acceptance calculation in equation 6.1.

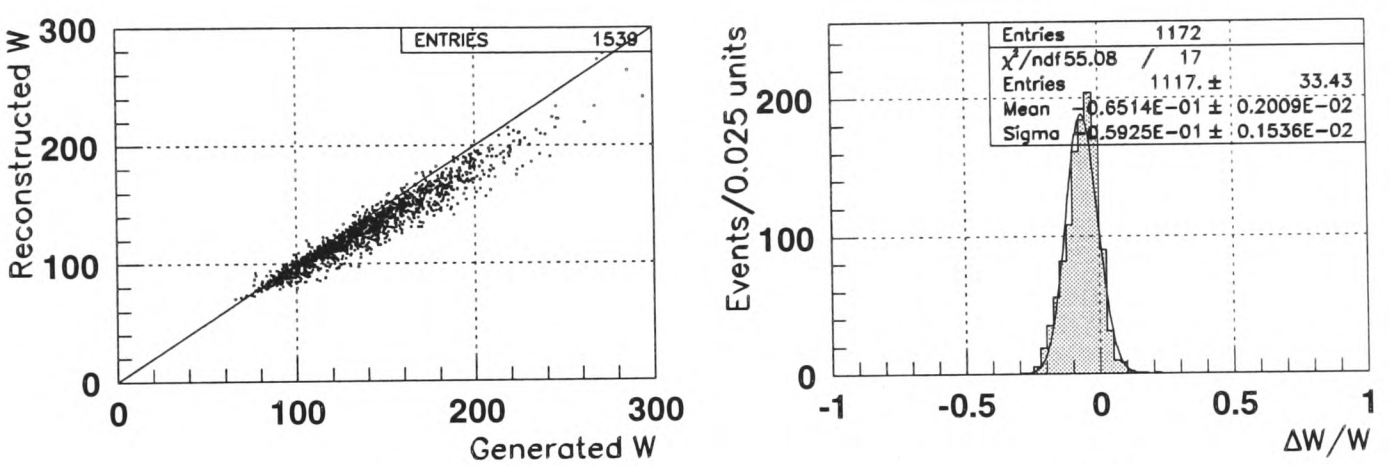

Figure 6.40: a)Reconstructed against generated W (GeV) and b) $(W^{rec} - W^{gen})/W^{gen}$ for the final selection of HERWIG events with $80 < W < 150$ GeV in (b).

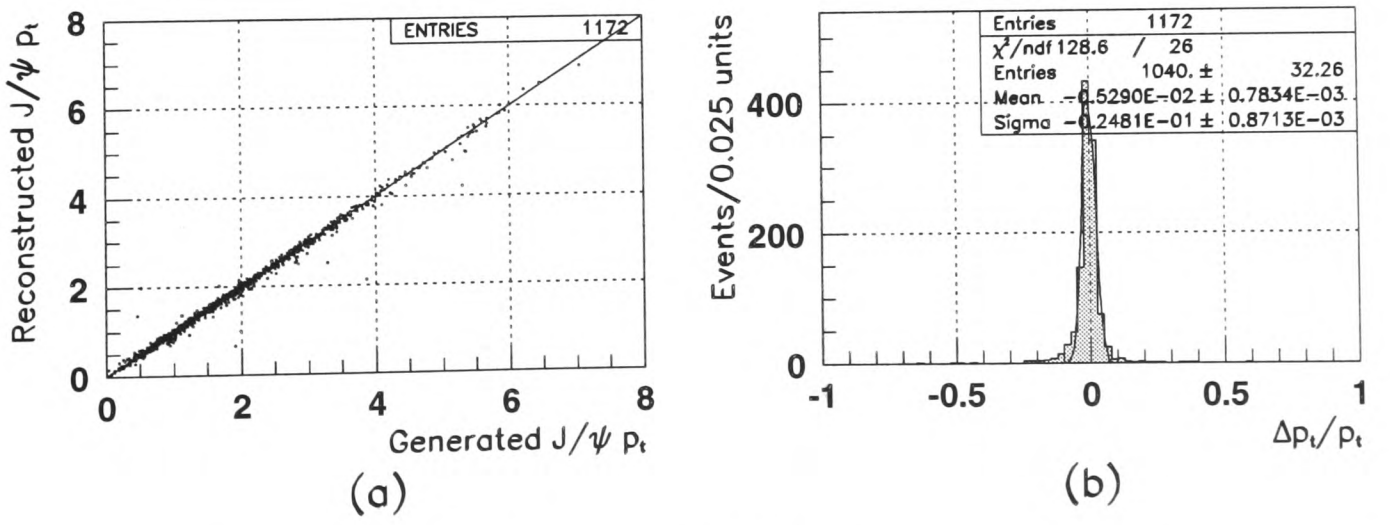

Figure 6.41: a)Reconstructed against generated J/ψ transverse momentum, P_t (GeV) and b) $(P_t^{rec} - P_t^{gen})/P_t^{gen}$ for the final selection of HERWIG events with $80 < W < 150$ GeV.

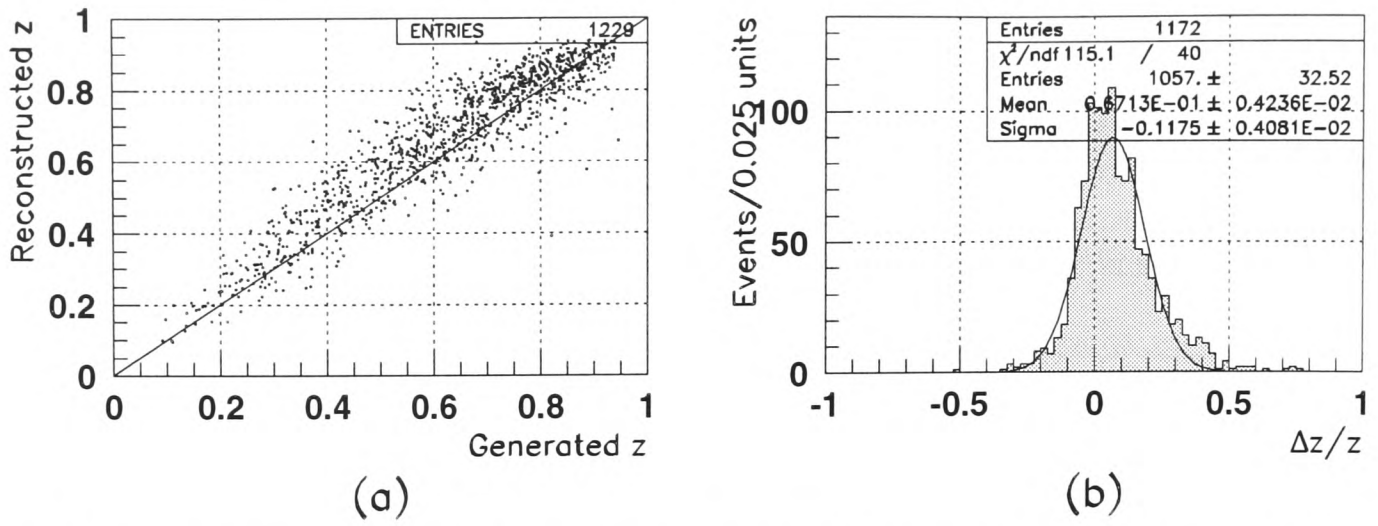

Figure 6.42: a)Reconstructed against generated elasticity, z, and b) $(z^{rec} - z^{gen})/z^{gen}$ for the final selection of HERWIG events with $80 < W < 150$ GeV.

6.10 Results

6.10.1 Cross–section calculation

The acceptance for direct inelastic J/ψ photoproduction events using the HERWIG Monte Carlo generator and the MRSD$-'$ proton structure function was calculated in section 6.9 to be $(13.10 \pm 0.35)\%$. This is combined with the acceptance for the $\frac{dE}{dx}$ cut found in section 6.8 to be $(70.4^{+2.0}_{-2.2})\%$, to give a total acceptance of $(9.22^{+0.36}_{-0.38})\%$.

In figure 6.23, the reconstructed mass of the inelastic J/ψ candidates in the W range 80 – 150 GeV is fitted to a gaussian with a bremsstrahlung tail. From the fit parameters, there are 39.7 ± 8.3 events in the J/ψ mass peak.

This information is used together with the luminosity during the 1994 running period to calculate the ep cross–section using equation 5.2. The γp cross–section is obtained by dividing by the integrated photon flux as explained in appendix A. The results are summarised in table 6.1.

The first error on the cross–sections in table 6.1 is statistical and the second is systematic. The sources of the systematic errors are described in the next section. The

error on the integrated photon flux is systematic and arises from the assumption that the γp cross–section is independent of y and Q^2 as explained in appendix A.

$ep \to e\, J/\psi\, X$	$80 \leq W \leq 150$ GeV
Number of events	39.7 ± 8.3
Luminosity	2,863.11 nb^{-1}
Acceptance ($z \leq 0.9$)	$(9.22^{+0.36}_{-0.38})\%$
$J/\psi \to e^+e^-$ branching ratio	$(5.99 \pm 0.25)\%$
Integrated photon flux	$0.0494^{+0\%}_{-10\%}$
$\sigma_{ep}(z \leq 0.9)$ (nb)	$2.5 \pm 0.54^{+0.63}_{-0.68}$
$\sigma_{\gamma p}(z \leq 0.9)$ (nb)	$51 \pm 11^{+13}_{-14}$

Table 6.1: Summary of the results from the analysis on the 1994 running period including the γp and ep cross–sections.

6.10.2 Systematic uncertainties

Table 6.2 lists the systematic errors associated with the $ep \to e\, J/\psi\, X$ cross–section measurement. Most of the errors are estimated in an identical fashion to the 1993 analysis. They are explained below:

- The gluon density in the proton used in the Monte Carlo simulation affects the distribution of the invariant hadronic mass, W, on which events are partly triggered. A systematic error is obtained by comparing the MRSD$-'$ and MRSD0$'$ structure functions. The error is marginally greater than the 16% found in 1993.

- The error on the forward cone cut is estimated by varying the energy of the cut and comparing the loss of real and Monte Carlo events.

- This same method (as for the forward cone cut) is used to estimate the errors for the cuts in the $(z, P_t^{J/\psi})$ plane: $z \leq 0.9$ and $P_t^{J/\psi} \geq (8.75z - 7)$.

- The studies in section 6.8 with conversion electrons are used to estimate the error on the $\frac{dE}{dx}$ cut. This error is significantly larger than the 1.5% value obtained for the 1993 analysis due to the larger differences between the efficiencies calculated from the elastic J/ψ sample and the conversion electrons.

- The error on the fitting of the reconstructed mass is found by comparing various polynomials used to fit the background distribution.

- The resolution of the W reconstruction in figures 6.40a and b is used to estimate the error in the W cut.

- The J/ψ transverse momentum of the data is compared to that of direct inelastic Monte Carlo events to give an error on the contamination from diffractive processes (see figure 2.15) which tend to have lower transverse momenta.

- The error coming from inelastic ψ' contamination was estimated in section 6.6.2.

The systematic errors have been added in quadrature to give a total systematic error of $^{+26\%}_{-27\%}$, similar to the values obtained in 1993.

6.11 Conclusions

As a result of the increased luminosity and the better understanding of the detector, it is seen that the direct inelastic J/ψ analysis using data taken during the 1994 running period has produced a far cleaner and larger sample of J/ψ events than when the 1993 running period was used in chapter 5. This has resulted in a large decrease in the statistical errors of the cross–section from $\sim 60\%$ in 1993 to $\sim 20\%$.

It has been possible to measure the ep cross–section over a larger W range. This makes direct comparisons of the results from the two years of data taking invalid. How-

Systematic errors:	
Branching fraction	4%
Luminosity	1%
Input gluon density	18%
Forward 35° cone cut	2%
Cuts in the $(z, P_t^{J/\psi})$ plane	12%
$\frac{dE}{dx}$ cut	8%
Reconstructed mass fitting error	8%
$80 \leq W \leq 150$ GeV cut	6%
Diffractive background subtraction	$+0\% - 9\%$
Inelastic ψ' contamination	$+0\% - 0.6\%$
Total systematic error	$+26\% - 27\%$

Table 6.2: List of systematic errors for $ep \to e\, J/\psi\, X$ cross–section measurement.

ever, the γp cross–sections can be compared since they are both measured at a similar $< W >$. In 1993, the cross–section $\sigma_{\gamma p}(z \leq 0.9) = 82 \pm 48 \pm 23$ nb was measured which lies well within one standard deviation from the 1994 result given in table 6.1.

The final chapter of this thesis deals with the extraction of the gluon density within the proton using this 1994 inelastic J/ψ sample. It will be seen that even larger statistics will be required to obtain a useful measurement of the gluon.

Chapter 7

Extraction of the gluon density in the proton

In section 2.6, various J/ψ production mechanisms, possible at HERA, were described. This thesis is primarily based on the direct inelastic J/ψ photoproduction mechanism as illustrated in figure 2.18. This offers an excellent handle on directly measuring the gluon structure function of the proton as a function of the momentum fraction carried by the gluon, x_g, at very small values of x_g. The colour singlet model [46] is used to describe direct inelastically produced J/ψ's via the photon–gluon subprocess $\gamma g \rightarrow J/\psi g$. It was found [19] that this model gave a good description of data from the European Muon Collaboration (EMC), reproducing the z, $P_t^{J/\psi}$ and Q^2 distributions for sufficiently inelastic J/ψ's defined by the kinematical region:

$$z = \frac{p.p_{J/\psi}}{p.q} < 0.8 \tag{7.1}$$

$$P_t^{J/\psi} > 1\,\mathrm{GeV} \tag{7.2}$$

In this chapter, the colour singlet model is described. A description of the method used to extract the gluon density inside the proton using direct inelastic J/ψ lepto-production follows and then this is applied to data collected by the ZEUS detector in 1994.

7.1 Colour singlet model

In the photon–gluon–fusion mechanism, describing direct inelastic J/ψ production, a photon emitted from the incident electron interacts with the gluon content of the incident proton, producing a bare c and $\bar{c}$ quark via the subprocess $\gamma g \rightarrow c\bar{c}$. The $c\bar{c}$ system is not in a colour singlet state and does not have the spin–parity, $J^P = 1^-$, of the J/ψ. Colour must be shed and the spin–parity of the $c\bar{c}$ system must change before the bound $c\bar{c}$ state of the J/ψ can emerge. This is assumed to occur via the emission of a gluon, g_2, as illustrated in figure 7.1a. Also shown are five other diagrams required by gauge invariance.

The binding energy of the J/ψ is ignored to leading order and it is treated as an S–wave of a $c\bar{c}$ system with each spin–$\frac{1}{2}$ constituent carrying half the mass and half the four–momentum of the J/ψ, so it is assumed that $m_c = \frac{1}{2}M_{J/\psi}$. The J/ψ system is represented by a $J^P = 1^-$ wavefunction which is normalised using the J/ψ leptonic decay width, $\Gamma(J/\psi \rightarrow e^+e^-) = \Gamma_{ee}$. The three helicity states of the charm fermion–antifermion pair can be written in terms of the charm spinors as follows:

$$v(\uparrow)\bar{u}(\uparrow) = \frac{1}{\sqrt{2}}\not{\epsilon}(\uparrow)\frac{\not{p}_{J/\psi} + M_{J/\psi}}{2} \tag{7.3}$$

$$v(\downarrow)\bar{u}(\downarrow) = \frac{1}{\sqrt{2}}\not{\epsilon}(\downarrow)\frac{\not{p}_{J/\psi} + M_{J/\psi}}{2} \tag{7.4}$$

$$\frac{1}{\sqrt{2}}\left[v(\uparrow)\bar{u}(\downarrow) + v(\downarrow)\bar{u}(\uparrow)\right] = \frac{1}{\sqrt{2}}\not{\epsilon}(0)\frac{\not{p}_{J/\psi} + M_{J/\psi}}{2} \tag{7.5}$$

where : ϵ = polarisation vector

$p_{J/\psi}$ = four–momentum of the J/ψ

The constant, A, is used to denote the overall coupling strength between the J/ψ

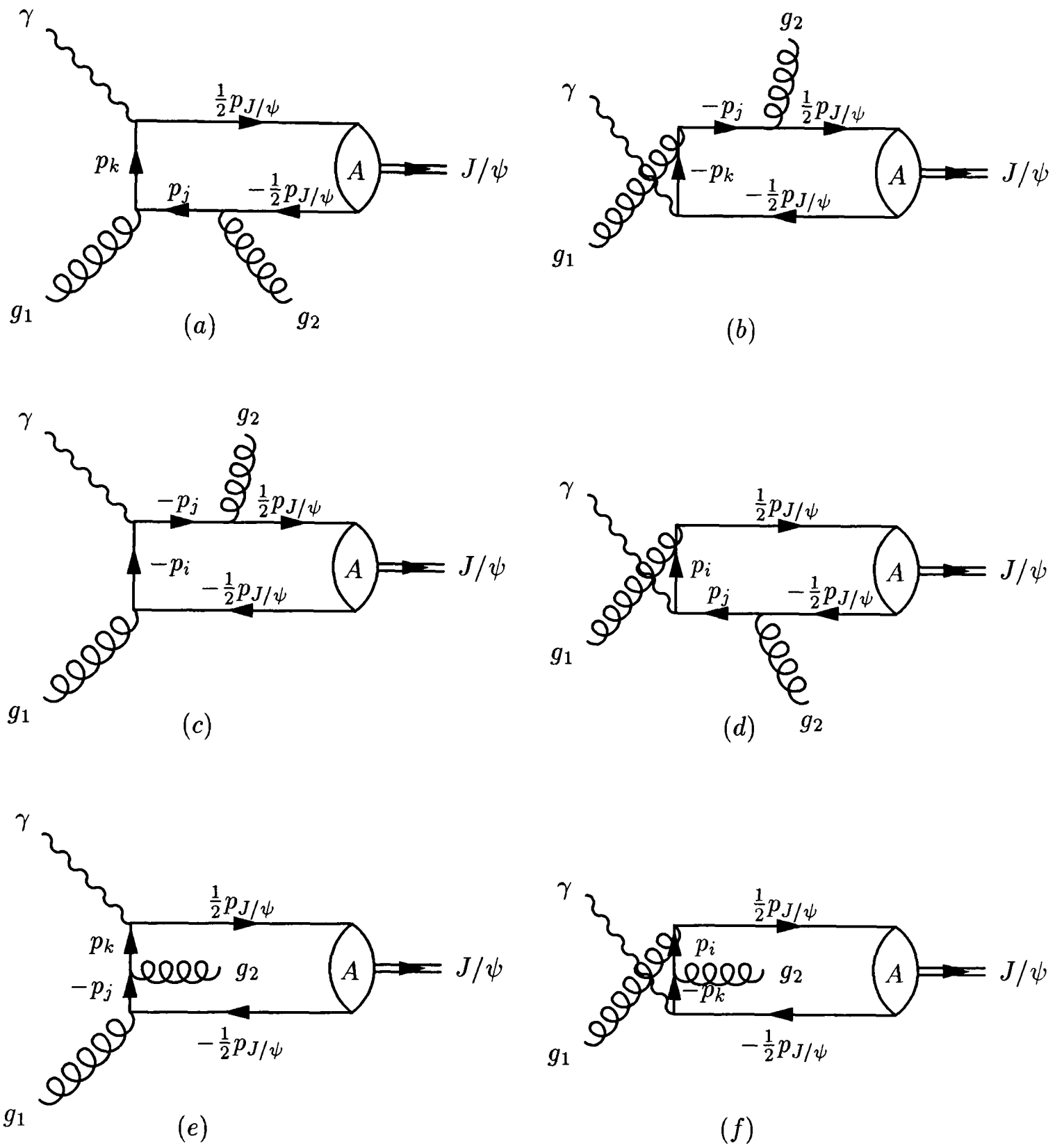

Figure 7.1: The six first order Feynman diagrams required by gauge invariance for the sub–process $\gamma g_1 \rightarrow J/\psi\, g_2$. The constant, A, denotes the coupling strength between the $c\bar{c}$ system and the J/ψ.

and the $J^P = 1^-, c\bar{c}$ state so that a J/ψ state of helicity h can be written as:

$$|J/\psi >= A\, N_h \sum_{\lambda_i} v_{\lambda_1}(-p_{J/\psi}/2)\bar{u}_{\lambda_2}(p_{J/\psi}/2) \tag{7.6}$$

$$\begin{aligned} \text{where :} \quad \lambda_i &= \pm 1/2 \\ h &= \lambda_1 + \lambda_2 \\ N_{\pm 1} &= 1 \\ N_0 &= 1/\sqrt{2} \end{aligned}$$

The coupling constant, A, can be written in terms of the $J/\psi \rightarrow e^+e^-$ and the $J/\psi \rightarrow$ *hadrons* decay widths, Γ_{ee} and Γ_h respectively. The total electronic and hadronic decays are assumed to proceed via a virtual photon and three gluons[1] as illustrated in figures 7.2a and b respectively. These widths can be calculated using first order QCD and are found to be [47]:

$$\Gamma_{ee} = \frac{A^2 e_q^2 e^2}{2\pi M_{J/\psi}} \tag{7.7}$$

$$\Gamma_h = \frac{5(\pi^2 - 9)}{36\pi^2} \frac{A^2 e_q^2 e^2}{M_{J/\psi}} \frac{\alpha_s^3}{\alpha^2} \tag{7.8}$$

$$\begin{aligned} \text{where :} \quad e &= \text{electronic charge} \\ e_q &= \text{charm quark charge} \end{aligned}$$

This then gives a ratio of the hadronic to leptonic widths of:

$$\frac{\Gamma_h}{\Gamma_{ee}} = \frac{5(\pi^2 - 9)}{18\pi} \frac{\alpha_s^3}{\alpha^2} \tag{7.9}$$

Experimentally, the ratio of the hadronic to leptonic decay widths is $\Gamma_h/\Gamma_{ee} = 86.0\%/6\% \simeq 14$ which from equation 7.9 gives $\alpha_s \simeq 0.2$ at a momentum scale of the

[1]This is the lowest order strong decay of the J/ψ as explained in sub–section 2.6.1.

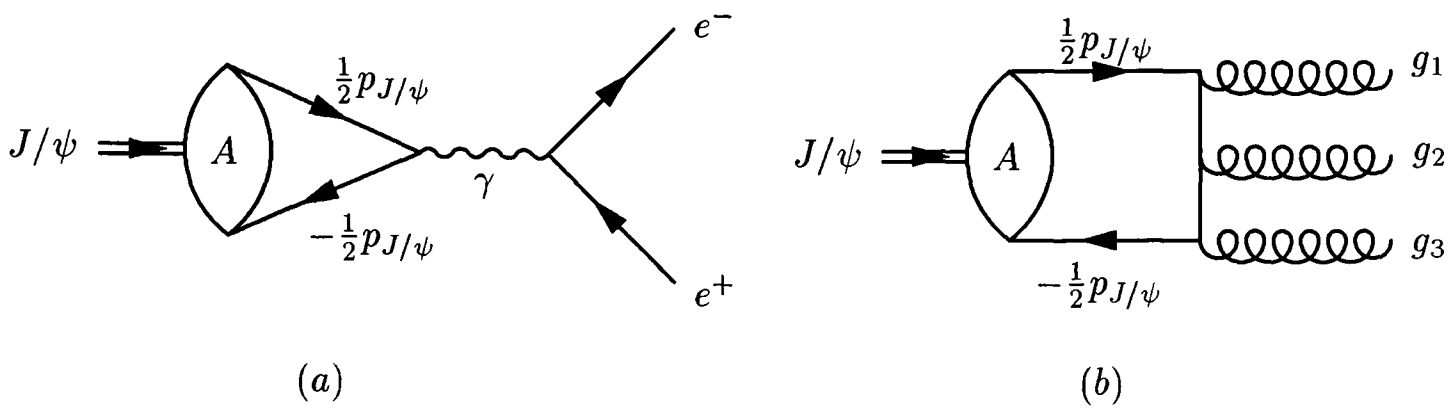

Figure 7.2: Diagrams showing the electronic and hadronic decays of the J/ψ assumed to proceed via a) a virtual photon and b) three gluons respectively.

order of $M^2_{J/\psi}$. The reasonable agreement between this first order result and experiment gives credibility to the rate for $\gamma g \to J/\psi\, g$ calculated using this model, despite the fact that higher order QCD corrections have not been included.

In the six diagrams shown in figures 7.1a–f, the initial and final gluons are on–shell. It will be shown below that the final gluon, g_2, may become soft as the sub–process threshold, $s_{\gamma g_1} \to M^2_{J/\psi}$, is approached. However, this possibility is removed by working in the inelastic domain, $z < 0.9$. The initial and final gluons have the same colour charge in all six diagrams of figure 7.1. The quark lines carrying momenta $\frac{1}{2}p_{J/\psi}$ in figure 7.1 are on–shell whereas those with momenta p_i, p_j and p_k are off–shell.

7.2 Kinematics

This section defines some kinematical variables required to handle the extraction of the gluon density in addition to those defined in section 3.1.

In figure 7.3, the four–momenta for the lowest order sub–process, $\gamma g_1 \to J/\psi\, g_2$, are defined.

In the Quark Parton Model (see section 2.3), the struck gluon, g_1, in the proton

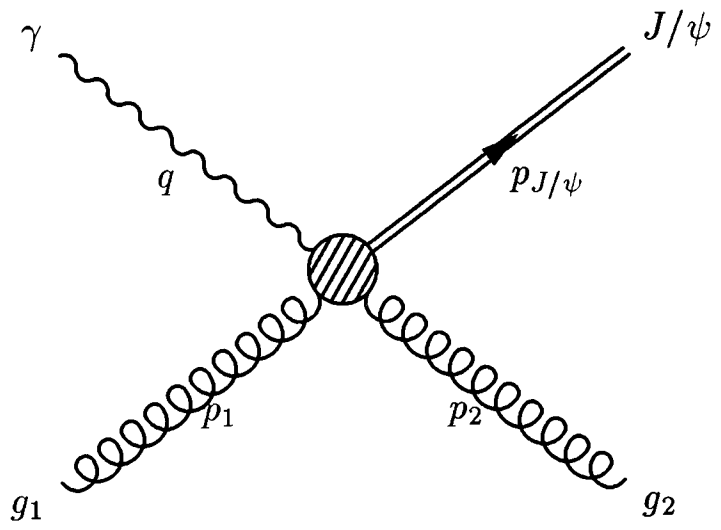

Figure 7.3: Feynman diagram showing the four–momenta for the sub–process $\gamma g_1 \rightarrow J/\psi\, g_2$.

carries a fraction, x_g, of the incident proton momentum, p, so that:

$$p_1 = x_g p \qquad (0 < x_g \leq 1) \tag{7.10}$$

The invariant variables $\hat{s}$, $\hat{t}$ and $\hat{u}$ for the sub–process $\gamma g_1 \rightarrow J/\psi\, g_2$ are defined as:

$$\hat{s} = (q + p_1)^2 = (p_{J/\psi} + p_2)^2 \tag{7.11}$$

$$\hat{t} = (p_{J/\psi} - q)^2 = (p_2 - p_1)^2 \tag{7.12}$$

$$\hat{u} = (p_{J/\psi} - p_1)^2 = (p_2 - q)^2 \tag{7.13}$$

We define $Q^2 = -q^2$ and since the initial and final gluons are on–shell, then:

$$p_1^2 = p_2^2 = 0 \tag{7.14}$$

and:

$$\begin{aligned} \hat{s} + \hat{t} + \hat{u} &= q^2 + p_1^2 + p_2^2 + p_{J/\psi}^2 \\ &= -Q^2 + M_{J/\psi}^2 \end{aligned} \tag{7.15}$$

The variable, $p_\perp$, is defined as the transverse momentum of the J/ψ with respect to the photon direction in the γg_1 centre–of–mass frame. At HERA, this is equivalent to

$P_t^{J/\psi}$, the transverse momentum of the J/ψ in the laboratory frame, since the photon and gluon (emitted from the incident electron and proton respectively), are assumed to be travelling parallel to the beam line and hence the γg_1 centre–of–mass frame is also travelling along the beam line.

It is shown in appendix B that x_g and $\hat{s}$ may be written as:

$$x_g = \frac{\hat{s} + Q^2}{s_{\gamma p} + Q^2} = \frac{\hat{s} + Q^2}{ys} \tag{7.16}$$

$$\hat{s} = \frac{p_\perp^2 + (1-z)M_{J/\psi}^2}{z(1-z)} \tag{7.17}$$

and this allows the reconstruction of x_g in terms of the measurable variables, z, $P_t^{J/\psi}$, y and Q^2.

7.2.1 Kinematical limits

The four–momenta of all the internal quark lines for the sub–process $\gamma g_1 \to J/\psi\, g_2$ are defined in figure 7.1. They satisfy:

$$p_i^2 - m_c^2 = (\frac{1}{2}p_{J/\psi} - p_1)^2 - m_c^2 = \frac{1}{2}(\hat{u} - M_{J/\psi}^2) \tag{7.18}$$

$$p_j^2 - m_c^2 = (\frac{1}{2}p_{J/\psi} + p_2)^2 - m_c^2 = \frac{1}{2}(\hat{s} - M_{J/\psi}^2) \tag{7.19}$$

$$p_k^2 - m_c^2 = (\frac{1}{2}p_{J/\psi} - q)^2 - m_c^2 = \frac{1}{2}(\hat{t} - M_{J/\psi}^2) \tag{7.20}$$

where the effective charm mass has been taken to be $m_c = \frac{1}{2}M_{J/\psi}$. The kinematical limits on $\hat{s}$, $\hat{t}$ and $\hat{u}$ are:

$$M_{J/\psi}^2 \leq \hat{s} \leq s_{\gamma p} \tag{7.21}$$

$$-\hat{s} + M_{J/\psi}^2 \leq \hat{t} \leq 0 \tag{7.22}$$

$$-\hat{s} + M_{J/\psi}^2 \leq \hat{u} \leq 0 \tag{7.23}$$

Therefore, when $\hat{s} \to M^2_{J/\psi}$, then $\hat{t}$, $\hat{u} \to 0$, and from equations 7.18 – 7.20, $p_j^2 \to m_c^2$ and p_i^2, $p_k^2 \to m_c^2 - \frac{1}{2}M^2_{J/\psi}$. Thus in this limit, the quark with four–momentum label p_j becomes on–shell, whereas the quarks with labels p_i and p_k remain off–shell. Therefore, in figures 7.1a, b, c and d, both quarks coupled to the final gluon, g_2, become on–shell and this gluon becomes soft. However, using equation 7.17:

$$\hat{s} - M^2_{J/\psi} = \frac{p_\perp^2}{z(1-z)} + M^2_{J/\psi}\frac{1-z}{z} \tag{7.24}$$

so, by considering only the inelastic domain where $z < 1$, $\hat{s} - M^2_{J/\psi}$ is restricted to positive values and the limit $\hat{s} \to M^2_{J/\psi}$ is avoided. Also, as this limit is approached, diagrams with multiple soft gluon emissions become significant, and may compete with the diagrams shown in figure 7.1.

7.3 Extraction of the gluon density in leptoproduction

The inelastic J/ψ photoproduction cross–section is directly proportional to the gluon density in the proton:

$$\sigma_{\gamma p} \approx \frac{BH}{M^2_{J/\psi}}\,\bar{x}G(\bar{x}) \tag{7.25}$$

where :

$$B = \frac{\alpha_s^2 \Gamma_{ee}}{\alpha M_{J/\psi}} \tag{7.26}$$

$$\bar{x} = \frac{3.4\, M^2_{J/\psi}}{s_{\gamma p}} \tag{7.27}$$

and H is a dimensionless constant. The derivation of this expression is somewhat lengthy and is consigned to appendix C. Thus, it can be seen that the inelastic J/ψ photoproduction cross–section is directly proportional to the gluon density in the proton and by measuring this cross–section as a function of the centre–of–mass energy, $s_{\gamma p}$, and hence of $\bar{x}$, the gluon density can be measured.

In order to make use of these results for inelastic J/ψ leptoproduction, encountered at HERA, the relationship between the γp and ep cross–sections must be found. The one–photon exchange differential cross–section in ep interactions can be written as a sum of the transverse and longitudinal photon–proton cross–sections, $\sigma_T^{\gamma^* p}$ and $\sigma_L^{\gamma^* p}$ respectively [48]:

$$\frac{d^2\sigma_{ep}}{dx_g dy} = \frac{\alpha}{\pi}\left(\frac{1-x_g}{x_g y}\right)\left[\left(1-y+\frac{y^2}{2}\right)\sigma_T^{\gamma^* p}+(1-y)\sigma_L^{\gamma^* p}\right] \tag{7.28}$$

Taking the limit as $Q^2 \to 0$, the longitudinal photon cross–section vanishes and the transverse photon cross–section approaches the photoproduction cross–section:

$$\begin{aligned}\sigma_T^{\gamma^* p} &\to \sigma_{\gamma p}\\ \sigma_L^{\gamma^* p} &\to 0\end{aligned}$$

so that using equation 7.25:

$$\begin{aligned}\frac{d^2\sigma_{ep}}{dx_g dy} &= \frac{\alpha}{\pi}\left(\frac{1-x_g}{x_g}\right)\left(\frac{1+(1-y)^2}{y}\right)\sigma_{\gamma p}\\ &\approx \frac{BH\alpha}{M_{J/\psi}^2\pi}\left(\frac{1-x_g}{x_g}\right)\left(\frac{1+(1-y)^2}{y}\right)\bar{x}G(\bar{x})\end{aligned} \tag{7.29}$$

This last equation is integrated with respect to x_g, between the minimum, x_{min}, and maximum, x_{max}, kinematically accessible values of x_g. This gives:

$$\begin{aligned}\frac{d\sigma_{ep}}{dy} &\approx \frac{BH\alpha}{M_{J/\psi}^2\pi}\left\{ln\left(\frac{x_{max}}{x_{min}}\right)-(x_{max}-x_{min})\right\}\left(\frac{1+(1-y)^2}{y}\right)\bar{x}G(\bar{x})\\ &\approx K\left(\frac{1+(1-y)^2}{y}\right)\bar{x}G(\bar{x})\end{aligned} \tag{7.30}$$

where K is some constant. Changing the variables in the differential cross–section from y to $log_{10}\bar{x}$ with the use of $\bar{x} = 3.4\,M_{J/\psi}^2/s_{\gamma p} = 3.4\,M_{J/\psi}^2/ys$, we obtain:

$$\frac{d\sigma_{ep}}{d\,log_{10}\bar{x}} \approx \frac{K}{ln\ 10}\left\{1+\left(1-\frac{3.4\,M_{J/\psi}^2}{\bar{x}s}\right)^2\right\}\bar{x}G(\bar{x}) \tag{7.31}$$

Thus, we arrive at the result that the differential cross–section, $d\sigma_{ep}/d\,log_{10}\,x_g$ is dependent on the gluon density, $x_g G(x_g)$, in the proton to leading order. This result has been used in [49] to extract the gluon density in the proton using the formula:

$$x_g G(x_g) = \mathcal{F}(x_g)|_{MC} \left(\frac{d\sigma_{ep}}{d\,log_{10}\,x_g}\right)_{data} \tag{7.32}$$

where :

$$\mathcal{F}(x_g)|_{MC} = \frac{(x_g G(x_g))_{MC}}{(d\sigma_{ep}/d\,log_{10}\,x_g)_{MC}} \tag{7.33}$$

It is seen that $\mathcal{F}(x_g)|_{MC}$ is a weighting factor and is determined from Monte Carlo data. It was found in [49] that $d\sigma_{ep}/d\,log_{10}\,x_g$ is sensitive to the gluon density put into the Monte Carlo generator. This method has the advantage over parameterising $\mathcal{F}(x_g)$ directly (as in equation 7.31) in that higher order diagrams to those shown in figure 7.1 are taken into account and approximations such as the integral of equation C.14 are not required. However, the method does require a complete understanding of the Monte Carlo used to find $\mathcal{F}(x_g)|_{MC}$.

Also, we must be confident that the variable $log_{10}\,x_g$ can be reconstructed with sufficient accuracy using equations 7.16 and 7.17. Around 50,000 HERWIG inelastic J/ψ Monte Carlo events are generated. The cuts applied to the 1994 data to obtain the 1994 inelastic J/ψ sample (described in sections 6.3 – 6.5) are applied to these Monte Carlo events and around 1100 are accepted by the selection. Figure 7.4a shows a plot of the reconstructed against the generated $log_{10}\,x_g$ for the accepted Monte Carlo events. A correlation is seen between the two variables which is also seen in figure 7.4b, where $(log_{10}\,x_g^{rec} - log_{10}\,x_g^{gen})/log_{10}\,x_g^{gen}$ is plotted and fitted to a gaussian. The fit gives a width of $(6.3 \pm 0.2)\%$ and a systematic shift in the mean of $(5.7 \pm 0.2)\%$.

It is also seen that events lie approximately in the range $10^{-3.3} < x_g < 10^{-2.2}$. The lower limit arises from the limited acceptance of the variable $y \approx W^2/s$ where the

approximation holds for low Q^2 events (see equations B.3 and B.4 in appendix B). Since a cut of $80 \leq W \leq 150$ GeV has been applied in section 6.5, then $0.07 \leq y \leq 0.25$. Using equation 7.16 and the minimum value of $\hat{s}$ given in equation 7.21, the minimum value of x_g is given by:

$$\begin{aligned} x_g|_{min} &\simeq \frac{\hat{s}_{min}}{s\, y_{max}} \\ &\simeq \frac{M^2_{J/\psi}}{0.25 \times 4 E_e E_p} \\ &\simeq 10^{-3.4} \end{aligned}$$

The upper limit of $x_g < 10^{-2.2}$ arises from the acceptance of the inelastic J/ψ selection code. It will be seen later in figure 7.7b, that the acceptance of inelastic J/ψ events is very low beyond $x_g \simeq 10^{-2.2}$. This is because the proton remnant from events with large x_g will have lower momenta and hence may not have enough energy to pass the energy cuts of the triggers.

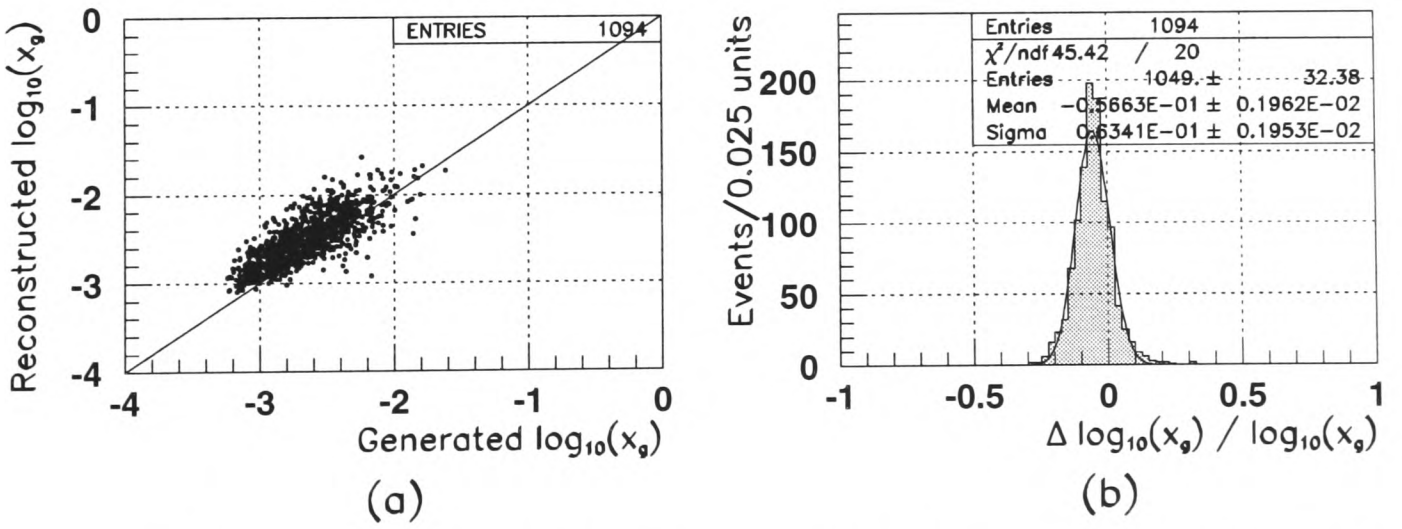

Figure 7.4: a) Reconstructed against generated $log_{10}\, x_g$, and b) $(log_{10}\, x_g^{rec} - log_{10}\, x_g^{gen})/log_{10}\, x_g^{gen}$ fitted to a gaussian for HERWIG inelastic J/ψ Monte Carlo events.

7.4 Extracting the gluon density using 1994 data

In this section, the results of the previous section are applied to the inelastic J/ψ sample obtained from data taken during the 1994 running period as described in chapter 6. The gluon density inside the proton will be extracted but because of the lack of statistics, the results are expected to have large statistical errors.

An additional minimum $P_t^{J/\psi}$ cut of 1 GeV, is applied to the 1994 inelastic J/ψ sample as suggested in equation 7.2. It is seen in figures 6.41a and b, that this quantity is well reconstructed within $(2.5 \pm 0.1)\%$. This cut excludes diagrams where soft–gluon emissions become significant. A gaussian with a bremsstrahlung tail is re–fitted to the mass spectrum of the J/ψ sample and this is shown in figure 7.5.

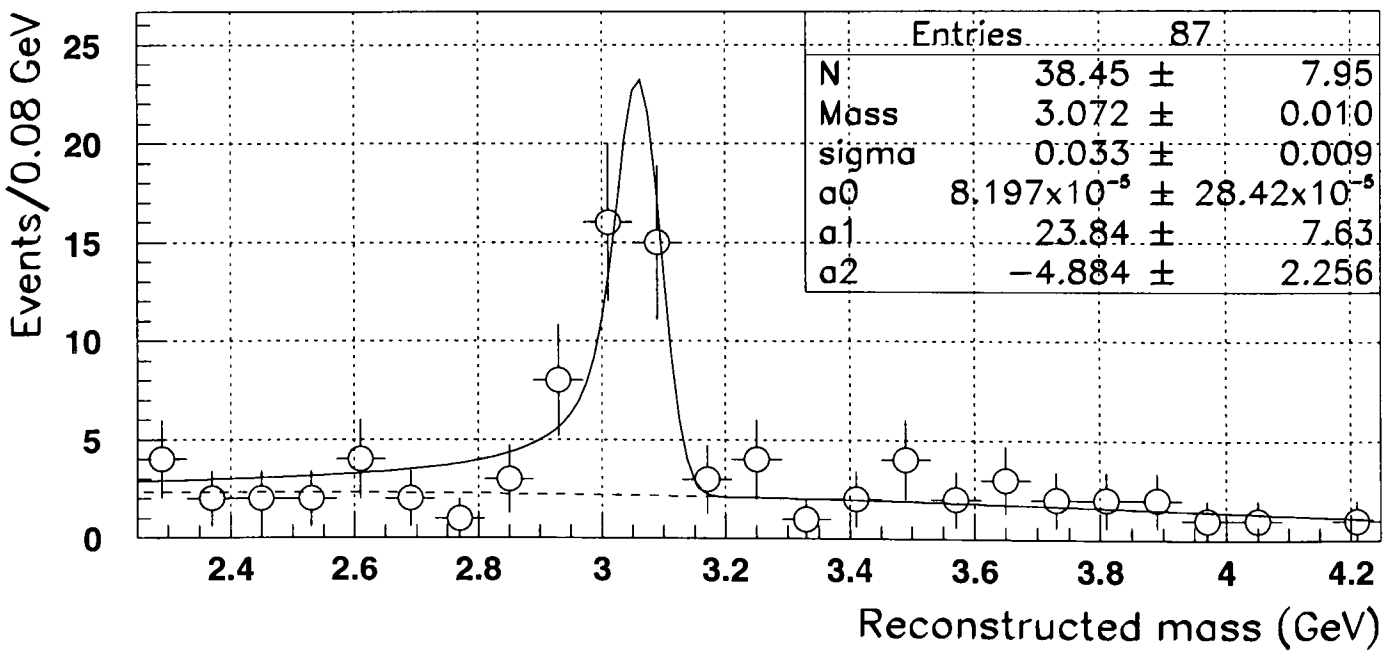

Figure 7.5: Reconstructed mass distribution of the 1994 inelastic J/ψ sample with an additional $P_t^{J/\psi} > 1$ GeV cut. The distribution is fitted to a gaussian with bremsstrahlung tail and a second order polynomial for the background.

Figures 7.6a, b and c show the $log_{10} x_g$ distribution of events in the J/ψ signal region $(2.8 \leq M \leq 3.15$ GeV) and the lower $(2.3 \leq M \leq 2.65$ GeV) and the upper $(3.35 \leq$

$M \leq 3.7$ GeV) sideband regions respectively. Due to lack of statistics, differences in the distributions of the two sideband regions cannot be claimed with any degree of significance.

The two sideband distributions are weighted equally and added together. The resulting distribution is weighted to the 9.7 background events as calculated from the fit parameters in figure 7.5. This is then subtracted from the $log_{10} x_g$ distribution for the signal region (figure 7.6a) to give a corrected (background subtracted) distribution shown in figure 7.6d.

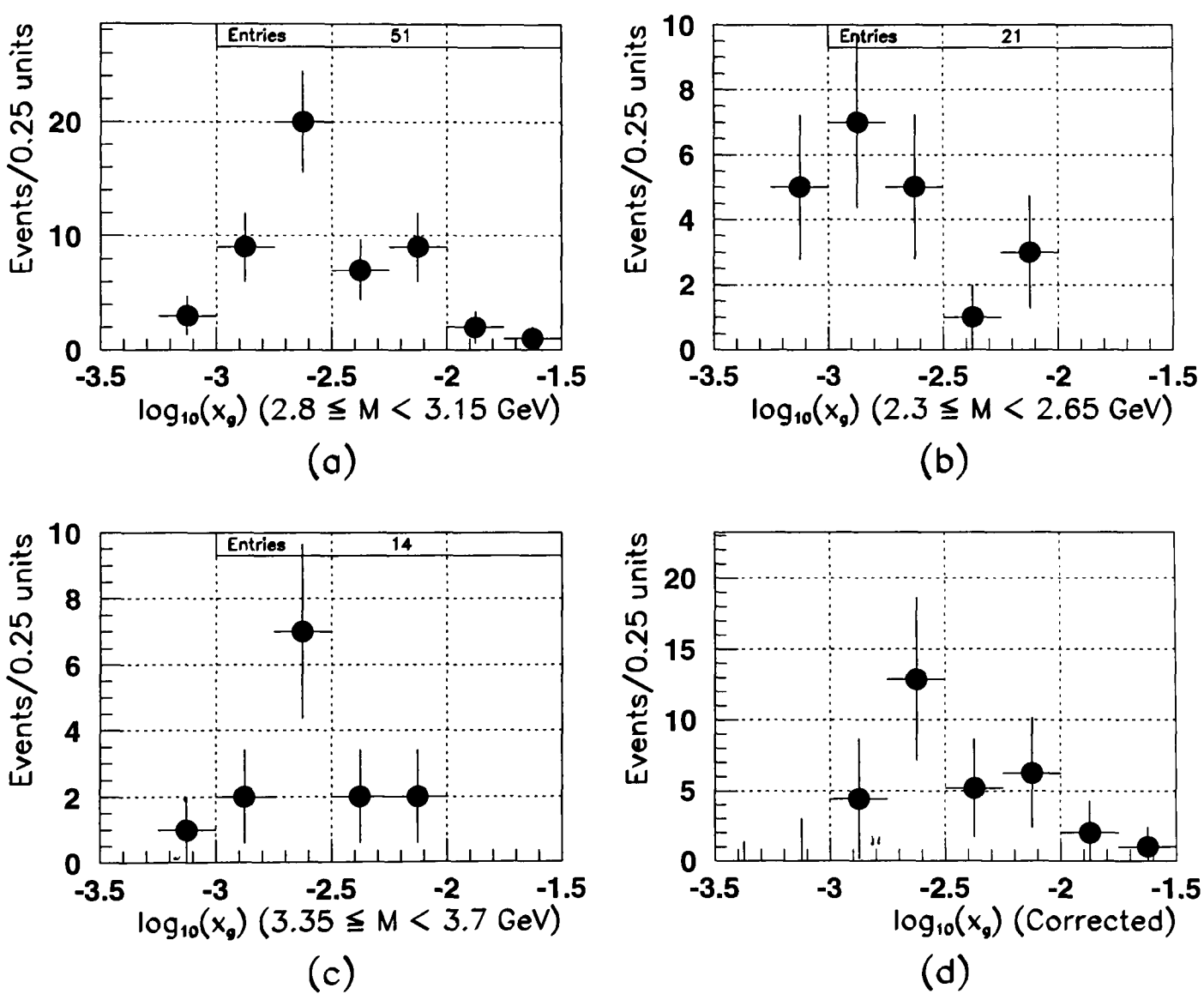

Figure 7.6: $Log_{10} x_g$ distribution of 1994 inelastic J/ψ data events in the a) signal reconstructed mass region $2.8 \leq M \leq 3.15$ GeV, b) lower sideband mass region $2.3 \leq M \leq 2.65$ GeV and c) upper sideband mass region $3.35 \leq M \leq 3.7$ GeV. d) The background subtracted $log_{10} x_g$ distribution. The errors on the points are purely statistical.

Figure 7.7a shows the $log_{10}\, x_g$ distribution for the 50,000 generated HERWIG Monte Carlo inelastic J/ψ events with the minimum $P_t^{J/\psi}$ of 1 GeV applied. Figure 7.7b shows the $log_{10}\, x_g$ distribution for the 1100 events which pass the inelastic J/ψ selection cuts. This is divided by the generated $log_{10}\, x_g$ distribution of the 50,000 generated events to give the acceptance of the J/ψ selection cuts as a function of $log_{10}\, x_g$, shown in figure 7.7c. It is seen that the acceptance drops to well below 5% outside the range $10^{-3} > x_g \leq 10^{-2.25}$ and the rest of this analysis will concentrate only on the events in the three bins within this range.

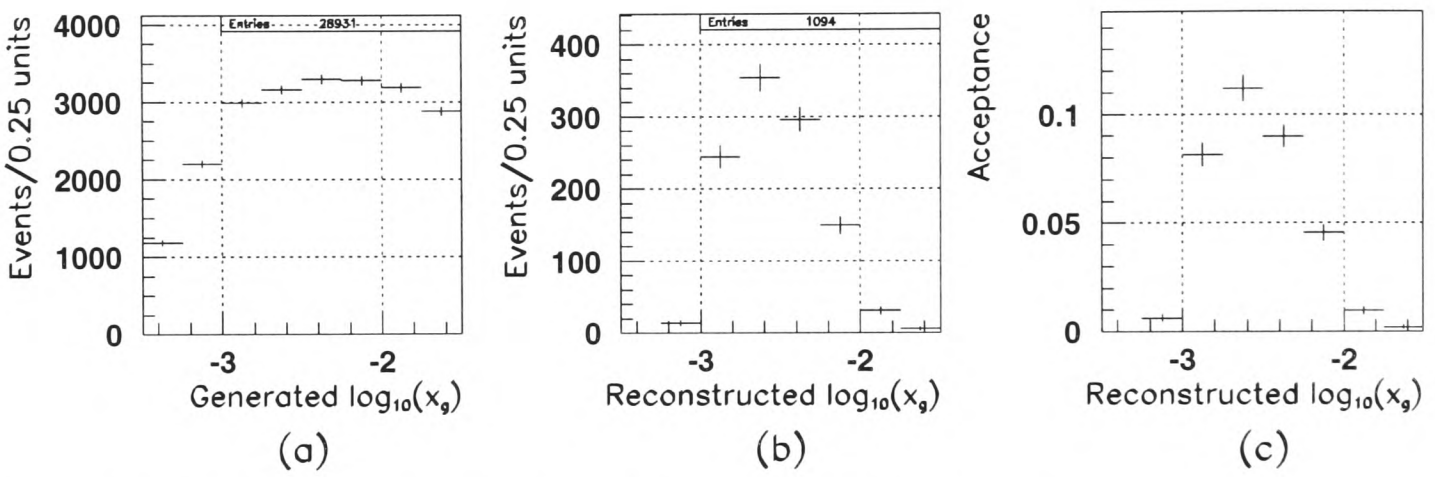

Figure 7.7: a) $Log_{10}\, x_g$ distribution of the generated HERWIG Monte Carlo inelastic J/ψ events with $P_t^{J/\psi} > 1$ GeV, b) the events passing the inelastic J/ψ selection cuts. c) Acceptance of HERWIG Monte Carlo events as a function of $log_{10}\, x_g$. Statistical errors are shown.

The acceptance of the $\frac{dE}{dx}$ cut (see section 6.3) is assumed to be independent of $log_{10}\, x_g$ which is a reasonable assumption given the studies in section 6.8. This acceptance was found to be $(70.4^{+2.0}_{-2.2})\%$. The differential cross–section, is calculated using:

$$\left(\frac{d\sigma_{ep}}{d\, log_{10}\, x_g}\right)_{data} = \left(\frac{dN}{d\, log_{10}\, x_g}\right)_{data} \Big/ \left\{\mathcal{L} \times \mathcal{B}.\mathcal{R}. \times \frac{d\mathcal{A}}{d\, log_{10}\, x_g}\right\} \qquad (7.34)$$

where :	$\left(\frac{dN}{d\,log_{10}\,x_g}\right)_{data}$	=	number of events per $log_{10}\,x_g$ bin
	$\mathcal{L}$	=	integrated luminosity
	$\mathcal{B.R.}$	=	branching ratio of $J/\psi \rightarrow e^+e^-$
	$\frac{d\mathcal{A}}{d\,log_{10}\,x_g}$	=	acceptance of inelastic J/ψ selection per $log_{10}\,x_g$ bin

The resulting distribution is shown in figure 7.8a for the three bins in the range $10^{-3} > x_g \leq 10^{-2.25}$.

The 50,000 HERWIG Monte Carlo events were generated with an integrated luminosity of 181.9 pb^{-1}. Figure 7.8b shows the differential cross–section $(d\sigma_{ep}/d\,log_{10}\,x_g)_{MC}$ of these Monte Carlo events.

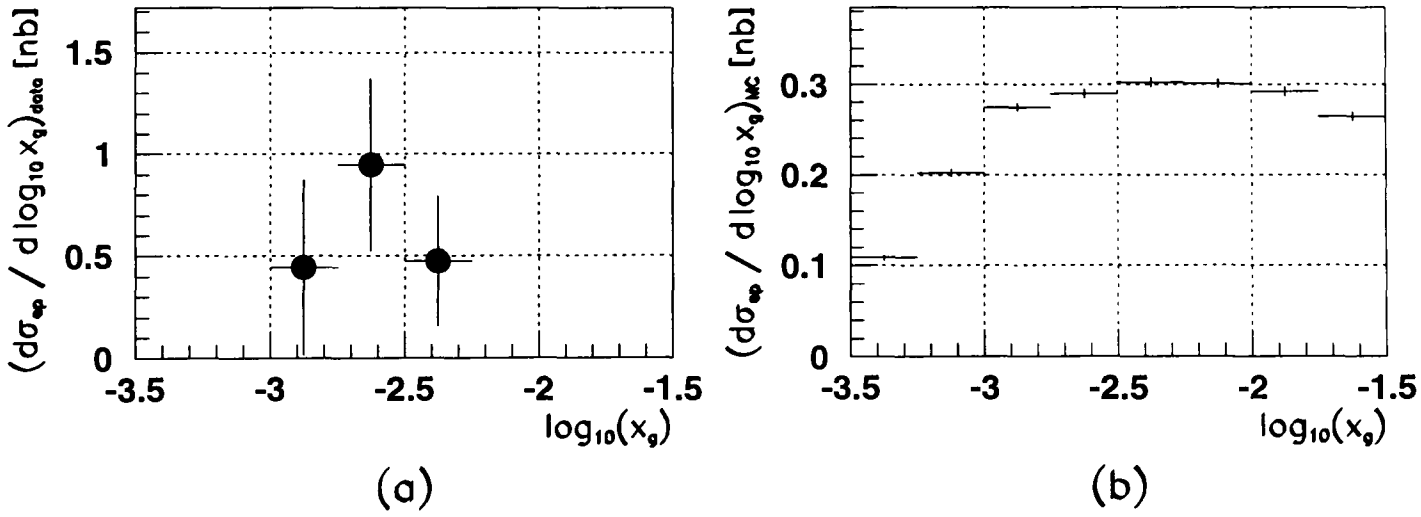

Figure 7.8: Plots showing the differential cross–sections, $(d\sigma_{ep}/d\,log_{10}\,x_g)$, distribution for events with $P_t^{J/\psi} > 1$ GeV from a) 1994 data and b) HERWIG Monte Carlo. Statistical errors are shown.

The gluon density from the MRSD$-'$ proton structure function used in the HERWIG Monte Carlo is shown in figure 7.9a. The ratio of the data to Monte Carlo cross–sections is found for each $log_{10}\,x_g$ bin and this is multiplied by the MRSD$-'$ gluon density to give the gluon density extracted from the data according to equations 7.32 and 7.33. This is shown in figure 7.9b. The errors in the plot are purely statistical and they are too large

to predict the shape of the gluon density with any degree of certainty, as anticipated in the beginning of this section.

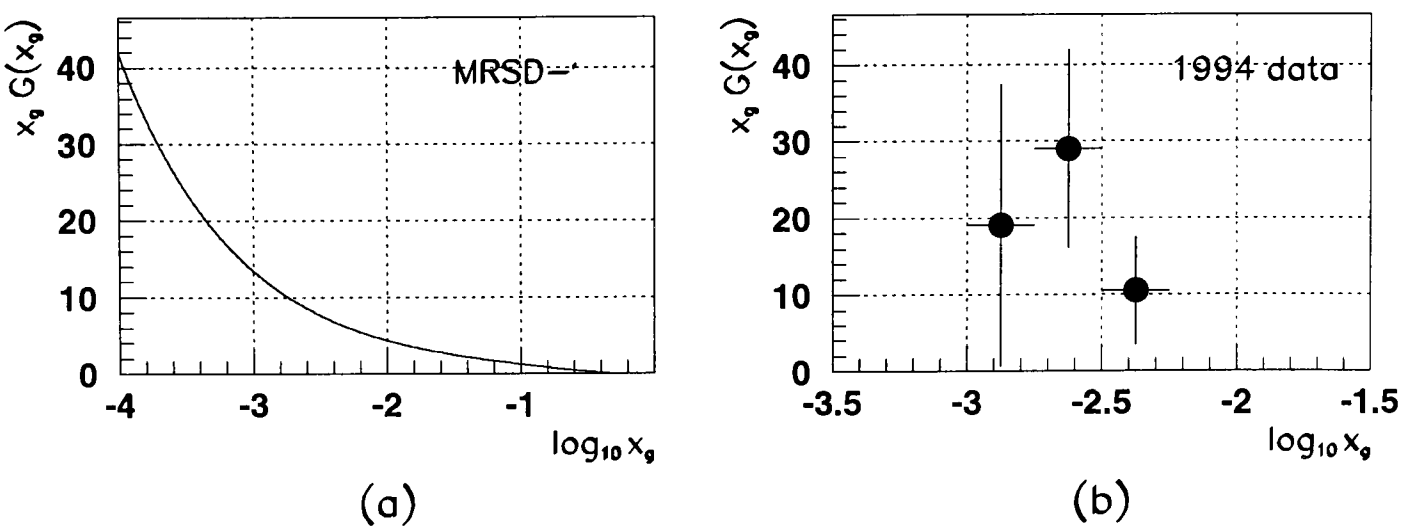

Figure 7.9: The gluon density from a) the MRSD−′ proton structure function and b) the inelastic J/ψ 1994 data.

7.4.1 Possible sources of error

Several possible sources of error for the method used to extract the gluon density are mentioned in this sub–section. These should be carefully considered when a detailed study of the gluon density is performed. However, from figure 7.9b, it is seen that these errors will all be secondary to the error arising from the lack of statistics in this analysis. Therefore, these additional errors will only be mentioned for future use.

Of the 51 events in the signal region $2.8 \leq M \leq 3.15$ GeV, approximately 38 ± 8 are expected to be J/ψ candidates (assuming a negligible number of J/ψ candidates lie outside this mass range – see figure 7.5). This gives a signal–to–background ratio of $3.1^{+5.3}_{-1.2}$. It is therefore clear that there are two potentially large sources of error arising from the background subtraction:

- the number of background events to subtract.
- the $log_{10} x_g$ distribution of the background events. It is seen that the $log_{10} x_g$

distributions of the two sideband regions in figures 7.6b and c have large statistical errors. The background subtraction can only be trusted if these two sideband distributions have the same shape and it is unclear whether this is so, given the lack of statistics.

Other possible sources of error to the gluon density extraction are:

- the function $\mathcal{F}(x_g)|_{MC}$. It should be checked that this function is not dependent on the Monte Carlo generator and the inputed parton distributions used to extract it.

- the reconstruction of $log_{10}\, x_g$. It is seen in figure 7.4b that the $log_{10}\, x_g$ reconstruction has a width of around 6.6% and a systematic shift of 3.8%.

- after the analysis presented in this thesis was completed, it was found that there was a calibration error of up to $(6 \pm 3)\%$ in the ZEUS calorimeter. (Studies have shown that the BCAL energies have been underestimated by $(6 \pm 3)\%$ and the RCAL energies by $(2.5 \pm 3)\%$). Since the tracking variables have been used for the majority of the analysis presented in this thesis, the calibration error does not worry us. However, calculation of variables such as y (equation 3.6) and hence x_g (equation 7.16) rely on calorimeter energy measurements and so could themselves by incorrect by up to $(6 \pm 3)\%$.

7.5 Conclusions

This chapter has served to show how the gluon density within the proton may be extracted using inelastic J/ψ production at HERA. Due to the large statistical errors shown in figure 7.9b and the systematic errors mentioned at the end of the last section,

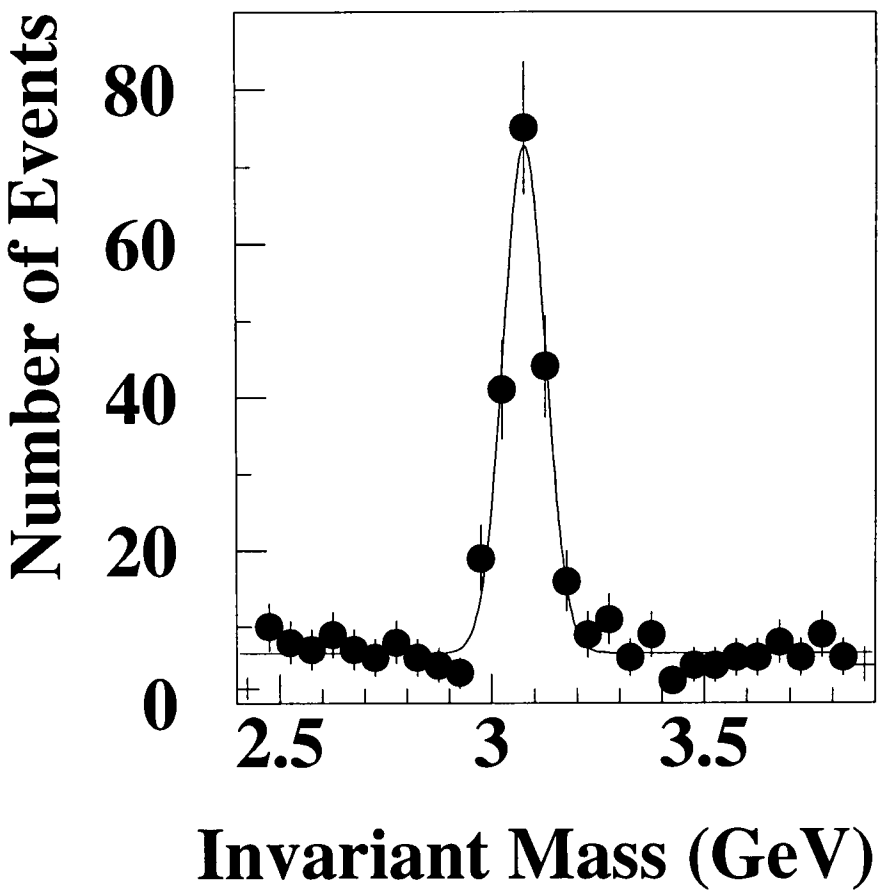

Figure 7.10: Reconstructed mass of the inelastic $J/\psi \to \mu^+\mu^-$ sample from data taken in 1994 with the ZEUS detector.

little information on the gluon density can be deduced from the results extracted using the 1994 data.

With HERA continuing to take more data, and the resolution of the ZEUS detector constantly being improved, it should be possible to obtain a larger and cleaner inelastic J/ψ sample in the future from which better measurements of the gluon density within the proton can be obtained. A clean inelastic J/ψ from the muon decay mode ($J/\psi \to \mu^+\mu^-$) has already been selected from the data taken in 1994. The reconstructed mass of this sample is shown in figure 7.10 where a mass peak is seen above a very low background. The techniques described in this chapter can equally well be applied to these events.

Appendix A

The integrated photon flux

This appendix calculates the integrated photon flux which is used in chapters 5 and 6 to convert a leptoproduction cross–section into a photoproduction result.

For low Q^2 leptoproduction events, the contribution to the J/ψ production cross–section from the exchange of longitudinal virtual photons can be neglected. The J/ψ leptoproduction cross–section, $\sigma(ep \to J/\psi\, X)$ can be written in terms of the J/ψ photoproduction cross–section, $\sigma(\gamma p \to J/\psi\, X)$ as follows [50]:

$$\sigma_{ep}(s) = \int_{y_{min}}^{y_{max}} dy \int_{Q^2_{min}}^{Q^2_{max}} dQ^2 \;\; \Phi(y, Q^2)\, \sigma_{\gamma p}(y, Q^2) \tag{A.1}$$

where :

$$\Phi(y, Q^2) = \frac{\alpha}{2\pi} \frac{1}{y\, Q^2} \left[1 + (1-y)^2 - \frac{2 m_e^2\, y^2}{Q^2} \right] \tag{A.2}$$

is the photon flux factor and m_e is the electron mass. The limits to the y integral are determined by the W range being measured since for low Q^2 photoproduction events, $y = \frac{p.q}{p.l} = W^2/s$ (see equations B.3 and B.4 in appendix B). The upper Q^2 limit is determined by cut 12 in section 5.4 for the 1993 and cut 13 in section 6.3 for the 1994 J/ψ analyses. These demanded the energy in the first ring around the rear beam pipe to be less than 1 GeV and so the scattered electron had to be lost down the rear beam pipe. This limited the maximum Q^2 to around 4 GeV. Because of the $1/Q^2$ factor in

the photon flux, the precise value of Q^2_{max} is not essential in calculating the integral in equation A.1. The lower Q^2 limit is determined by y and is given by $Q^2_{min} = m_e^2 \frac{y^2}{1-y}$ [50].

At these low Q^2 values, the Q^2 dependence of $\sigma_{\gamma p}$ can be neglected. Also, $\sigma_{\gamma p}$ is assumed to be independent of y so that equation A.1 becomes:

$$\sigma_{ep}(s) = \mathcal{P}.\mathcal{F}. \times \sigma_{\gamma p}(y, Q^2) \tag{A.3}$$

where :

$$\mathcal{P}.\mathcal{F}. = \int_{y_{min}}^{y_{max}} dy \int_{Q^2{}_{min}}^{Q^2{}_{max}} dQ^2 \; \Phi(y, Q^2) \tag{A.4}$$

is the integrated photon flux. This is calculated in table A.1 for the W ranges used in the analyses of the data collected during the 1993 and 1994 running periods. The integration was performed once again assuming $\sigma_{\gamma p}$ was not independent of y, but rose linearly with $W = \sqrt{sy}$. The photoproduction cross section was found to increase by around 10%. This is added as a systematic error on the integrated photon flux.

Running period:	1993	1994
W range	100 – 140 GeV	80 – 150 GeV
Centre–of–mass energy, $\sqrt{s}$	296 GeV	300 GeV
y_{min}; y_{max}	0.114; 0.224	0.0709; 0.249
Integrated photon flux,	$0.025^{+0\%}_{-10\%}$	$0.0494^{+0\%}_{-10\%}$

Table A.1: Summary of the integrated photon fluxes for the analyses on the 1993 and 1994 data. The error on the integrated photon fluxes are systematic.

Appendix B

Derivation of kinematic formulae

This appendix derives some of the kinematic formulae used in section 7.2. Using equation 7.10:

$$p_1.q = x_g\ p.q \tag{B.1}$$

and:

$$\hat{s} = (p_1 + q)^2 = 2p_1.q + q^2 = 2p_1.q - Q^2 \tag{B.2}$$

$$p.q = \frac{1}{2}(s_{\gamma p} + Q^2) \tag{B.3}$$

$$p.q = y\ p.l = ys/2 \tag{B.4}$$

where equation B.3 follows from $s_{\gamma p} = (p+q)^2 \simeq 2p.q - Q^2$ and equation B.4 from $s = (p+l)^2 \simeq 2p.l$, neglecting the electron and proton masses. Putting equations B.2 – B.4 into equation B.1, we end up with equation 7.16:

$$x_g = \frac{\hat{s} + Q^2}{s_{\gamma p} + Q^2} = \frac{\hat{s} + Q^2}{ys} \tag{B.5}$$

A proof of equation 7.17 for $\hat{s}$ follows. Writing out the four–momenta explicitly for the sub–process $\gamma(q)\, g_1(p_1) \rightarrow J/\psi(p_{J/\psi})\, g_2(p_2)$ in the γg_1 centre–of–mass frame:

$$q = (K,\ 0,\ 0,\ k) \tag{B.6}$$

$$p_1 = (k,\ 0,\ 0,\ -k) \tag{B.7}$$

$$p_2 = (k',\ -k'sin\,\theta,\ 0,\ -k'cos\,\theta) \tag{B.8}$$

$$p_{J/\psi} = (E_{J/\psi},\ k'sin\,\theta,\ 0,\ k'cos\,\theta) \tag{B.9}$$

where θ is the angle of the J/ψ in the γg_1 centre–of–mass frame relative to the incident photon direction. The following relations also hold:

$$p_\perp = k'sin\,\theta \tag{B.10}$$

$$Q^2 = -q^2 = -K^2 + k^2 \tag{B.11}$$

$$p^2_{J/\psi} = M^2_{J/\psi} = E^2_{J/\psi} - k'^2 \tag{B.12}$$

$$K + k = E_{J/\psi} + k' \tag{B.13}$$

where the last equality follows from the conservation of energy. Using equations 7.11 – 7.13, it is then easy to show:

$$\hat{s} = 2k^2 + 2Kk - Q^2 = (E_{J/\psi} + k')^2 \tag{B.14}$$

$$\hat{t} = -2kk'(1 - cos\,\theta) \tag{B.15}$$

$$\hat{u} = M^2_{J/\psi} - 2E_{J/\psi}k - 2kk'cos\,\theta \tag{B.16}$$

The elasticity parameter, z, (defined in equation 3.3 in section 3.1) can be re–written as follows, using equations 7.10, 7.11 and 7.13:

$$\begin{aligned} z &= \frac{p.p_{J/\psi}}{p.q} \\ &= \frac{p_1.p_{J/\psi}}{p_1.q} \\ &= \frac{p^2_{J/\psi} - (p_{J/\psi} - p_1)^2}{(q + p_1)^2 - q^2} \\ &= \frac{M^2_{J/\psi} - \hat{u}}{\hat{s} + Q^2} \end{aligned} \tag{B.17}$$

Using this last equation and equation 7.15, the variable $\hat{t}$ can now be written:

$$\hat{t} = (M^2_{J/\psi} - \hat{u}) - (\hat{s} + Q^2)$$

$$= z(\hat{s}+Q^2) - (\hat{s}+Q^2)$$

$$= -(1-z)(\hat{s}+Q^2) \qquad \text{(B.18)}$$

From equations B.10, B.15 and B.16:

$$\hat{t}\left[(\hat{u}-M_{J/\psi}^2)+2E_{J/\psi}K-2kk'\right] = [-2kk'(1-cos\,\theta)]\,[-2kk'(1+cos\,\theta)]$$

$$= 4k^2k'^2sin^2\theta$$

$$= 4k^2p_\perp^2$$

Substituting for $\hat{u}$ and $\hat{t}$ on the left hand side using equations B.17 and B.18 respectively:

$$4k^2p_\perp^2 = -(1-z)(\hat{s}+Q^2)\left[-z(\hat{s}+Q^2)+2k(E_{J/\psi}-k')\right] \qquad \text{(B.19)}$$

$$= z(1-z)(\hat{s}+Q^2)^2 - 2k(1-z)(\hat{s}+Q^2)(E_{J/\psi}-k') \qquad \text{(B.20)}$$

But from equation 7.15:

$$(\hat{s}+Q^2)^2 = (M_{J/\psi}^2-\hat{u}-\hat{t})^2$$

$$= \left[(2E_{J/\psi}k+2kk'cos\,\theta)+2kk'(1-cos\,\theta)\right]^2 \qquad \text{– using B.15 and B.16}$$

$$= \left[2k(E_{J/\psi}+k')\right]^2$$

$$= 4k^2\hat{s} \qquad \text{– using B.14}$$

Putting this last equation together with B.14 into equation B.20, we get:

$$4k^2p_\perp^2 = 4k^2\hat{s}z(1-z) - 2k(1-z)(E_{J/\psi}-k')(2k^2+2Kk)$$

$$p_\perp^2 = \hat{s}z(1-z) - (1-z)(E_{J/\psi}-k')(k+K)$$

$$= \hat{s}z(1-z) - (1-z)(E_{J/\psi}-k')(E_{J/\psi}+k') \qquad \text{– using 7.15}$$

$$= \hat{s}z(1-z) - (1-z)(E_{J/\psi}^2-k'^2)$$

$$= \hat{s}z(1-z) - (1-z)M_{J/\psi}^2 \qquad \text{– using B.12}$$

It is then easy to re–arrange this last equation to give equation 7.17 which we originally set out to prove:

$$\hat{s} = \frac{p_\perp^2 + (1-z)M_{J/\psi}^2}{z(1-z)} \tag{B.21}$$

Appendix C

Inelastic J/ψ photoproduction cross–section

In this appendix, the result for the J/ψ inelastic photoproduction cross–section, quoted in equation 7.25, is proved.

On inspection of the six diagrams in figure 7.1, it is seen that the invariant amplitudes for the diagrams can be paired off with $M_a = M_b$, $M_c = M_d$ and $M_e = M_f$. The total amplitude for the sub–process $\gamma g_1 \to J/\psi\, g_2$ to leading order is the sum of these six amplitudes. $|M(\gamma g_1 \to J/\psi\, g_2)|^2$ is calculated using perturbative QCD in [51]. The spin and colour of the initial and final states are averaged and summed respectively and we are left with:

$$\sum_{spins,\, colour} \overline{|M|^2} = \frac{16}{3} g^4 e_q^2 M_{J/\psi}^2 A^2 \, \frac{\hat{s}^2(\hat{s} - M_{J/\psi}^2)^2 + \hat{t}^2(\hat{t} - M_{J/\psi}^2)^2 + \hat{u}^2(\hat{u} - M_{J/\psi}^2)^2}{(\hat{s} - M_{J/\psi}^2)^2(\hat{t} - M_{J/\psi}^2)^2(\hat{u} - M_{J/\psi}^2)^2} \tag{C.1}$$

where :

	$g^2/4\pi$	=	α_s
	e_q	=	charm quark charge
	A	=	coupling strength between the J/ψ and $J^P = -1$, $c\bar{c}$ state

This is related to the differential cross–section for the $\gamma g_1 \rightarrow J/\psi\, g_2$ sub–process via:

$$\frac{d\sigma_{\gamma g_1}}{d\hat{t}} = \frac{1}{16\pi\hat{s}^2} \sum_{spins,\, colour} \overline{|M|^2} \tag{C.2}$$

The differential cross–section for the process $\gamma p \rightarrow J/\psi\, X$ is obtained by convoluting this last equation with the gluon distribution in the proton, $G(x_g, \hat{t})$. In this analysis, the $\hat{t}$ dependence of this gluon density is ignored so that $G(x_g, \hat{t}) = G(x_g)$ and we have:

$$\begin{aligned} \frac{d\sigma_{\gamma p}}{d\hat{t}} &= \int \frac{d\sigma_{\gamma g_1}}{d\hat{t}} G(x_g)\, dx_g \\ &= \frac{1}{3\pi}\, g^4 e_q^2 M_{J/\psi}^2 A^2 \int f(\hat{s},\hat{t}) G(x_g)\, dx_g \\ &= B\, M_{J/\psi}^4 \int f(\hat{s},\hat{t}) G(x_g)\, dx_g \end{aligned} \tag{C.3}$$

where:

$$B = \frac{8\pi}{3}\frac{\alpha_s^2\, \Gamma_{ee}}{\alpha M_{J/\psi}} \tag{C.4}$$

$$f(\hat{s},\hat{t}) = \frac{1}{\hat{s}^2}\left[\frac{\hat{s}^2(\hat{s}-M_{J/\psi}^2)^2 + \hat{t}^2(\hat{t}-M_{J/\psi}^2)^2 + \hat{u}^2(\hat{u}-M_{J/\psi}^2)^2}{(\hat{s}-M_{J/\psi}^2)^2\,(\hat{t}-M_{J/\psi}^2)^2\,(\hat{u}-M_{J/\psi}^2)^2}\right] \tag{C.5}$$

Equation 7.7 has been used to substitute the coupling constant, A, for the $J/\psi \rightarrow e^+e^-$ decay width, Γ_{ee} in the dimensionless constant, B. We have written $f(\hat{s},\hat{t},\hat{u}) = f(\hat{s},\hat{t})$ since only two of the variables $\hat{s}$, $\hat{t}$ and $\hat{u}$ are independent from equation 7.15. Since the gluon density, $G(x_g)$ is assumed to be independent of $\hat{t}$, the integral over $\hat{t}$ may be performed over the limits $-\hat{s} + M_{J/\psi}^2 \leq \hat{t} \leq 0$ whilst keeping $\hat{s}$ constant. For γp photoproduction events, the initial photon is real so that $Q^2 = 0$ and from equation 7.16, $x_g = \hat{s}/s_{\gamma p}$. The differential cross–section with respect to x_g can then be identified as:

$$\frac{d\sigma_{\gamma p}}{dx_g} = B\, M_{J/\psi}^4\, G(x_g)\, I(\hat{s}) \tag{C.6}$$

$$= \frac{B\, M_{J/\psi}^4 s_{\gamma p}}{\hat{s}}\, x_g G(x_g)\, I(\hat{s}) \tag{C.7}$$

where:

$$\begin{aligned} I(\hat{s}) &= \int f(\hat{s},\hat{t})\, d\hat{t} \\ &= \frac{2}{(\hat{s}+M^2_{J/\psi})^2}\left(\frac{\hat{s}-M^2_{J/\psi}}{\hat{s}M^2_{J/\psi}}+\frac{2\,ln(\hat{s}/M^2_{J/\psi})}{\hat{s}+M^2_{J/\psi}}\right) \\ &\quad +\frac{2(\hat{s}+M^2_{J/\psi})}{\hat{s}^2 M^2_{J/\psi}(\hat{s}-M^2_{J/\psi})}-\frac{4\,ln(\hat{s}/M^2_{J/\psi})}{\hat{s}\,(\hat{s}-M^2_{J/\psi})^2} \end{aligned} \tag{C.8}$$

Introducing a new dimensionless variable $r = \hat{s}/M^2_{J/\psi}$, we can write:

$$\frac{I(\hat{s})M^8_{J/\psi}}{\hat{s}} = \frac{2\,(r-1)}{r^2(r+1)^2}+\frac{4\,ln(r)}{r\,(r+1)^3}+\frac{2\,(r+1)}{r^3(r-1)}-\frac{4\,ln(r)}{r^2(r-1)^2} \tag{C.9}$$

$$= h(r) \tag{C.10}$$

so that:

$$\frac{d\sigma_{\gamma p}}{dx_g} = \frac{B\,s_{\gamma p}}{M^4_{J/\psi}}\, x_g G(x_g) h(r) \tag{C.11}$$

where $h(r)$ is a universal function of r. This function is finite over the whole kinematic range $M^2_{J/\psi} \le \hat{s} \le s_{\gamma p}$ or $1 \le r \le s_{\gamma p}/M^2_{J/\psi}$ with:

$$\lim_{r\to 1} h(r) = \lim_{\hat{s}\to M^2_{J/\psi}} h(\hat{s}/M^2_{J/\psi}) = 0$$

The function is peaked at $r = r_0$ with $h(r_0) = h_0$, as shown in figure C.1a.

Assuming $\alpha_s = 0.3$, the dimensionless constant B is calculated to be $B = 1.6\times 10^{-4}$.

Then:

$$\begin{aligned} \frac{d\sigma_{\gamma p}}{dx_g}\Big/ x_g G(x_g) &= \frac{B\,s_{\gamma p}}{M^4_{J/\psi}}\, h(r) \\ &= h(r)\,\left(1.7\times 10^{-6} s_{\gamma p}\right)\ \mathrm{GeV}^{-2} \\ &= h(r)\ (0.66 s_{\gamma p})\ \mathrm{nb} \end{aligned} \tag{C.12}$$

where $s_{\gamma p}$ is measured in units of GeV^2. Figure C.1b shows $\frac{d\sigma_{\gamma p}}{dx_g}\Big/ x_g G(x_g) = \frac{B\,s_{\gamma p}}{M^4_{J/\psi}} h(r)$ plotted against x_g for various values of $s_{\gamma p}$. The peaks for the curves have coordinates:

$$\left(x_g\ ;\ \frac{d\sigma_{\gamma p}}{dx_g}\Big/ x_g G(x_g)\right) = \left(\frac{M^2_{J/\psi} r_0}{s_{\gamma p}}\ ;\ \frac{B h_0}{M^4_{J/\psi}} s_{\gamma p}\right) \tag{C.13}$$

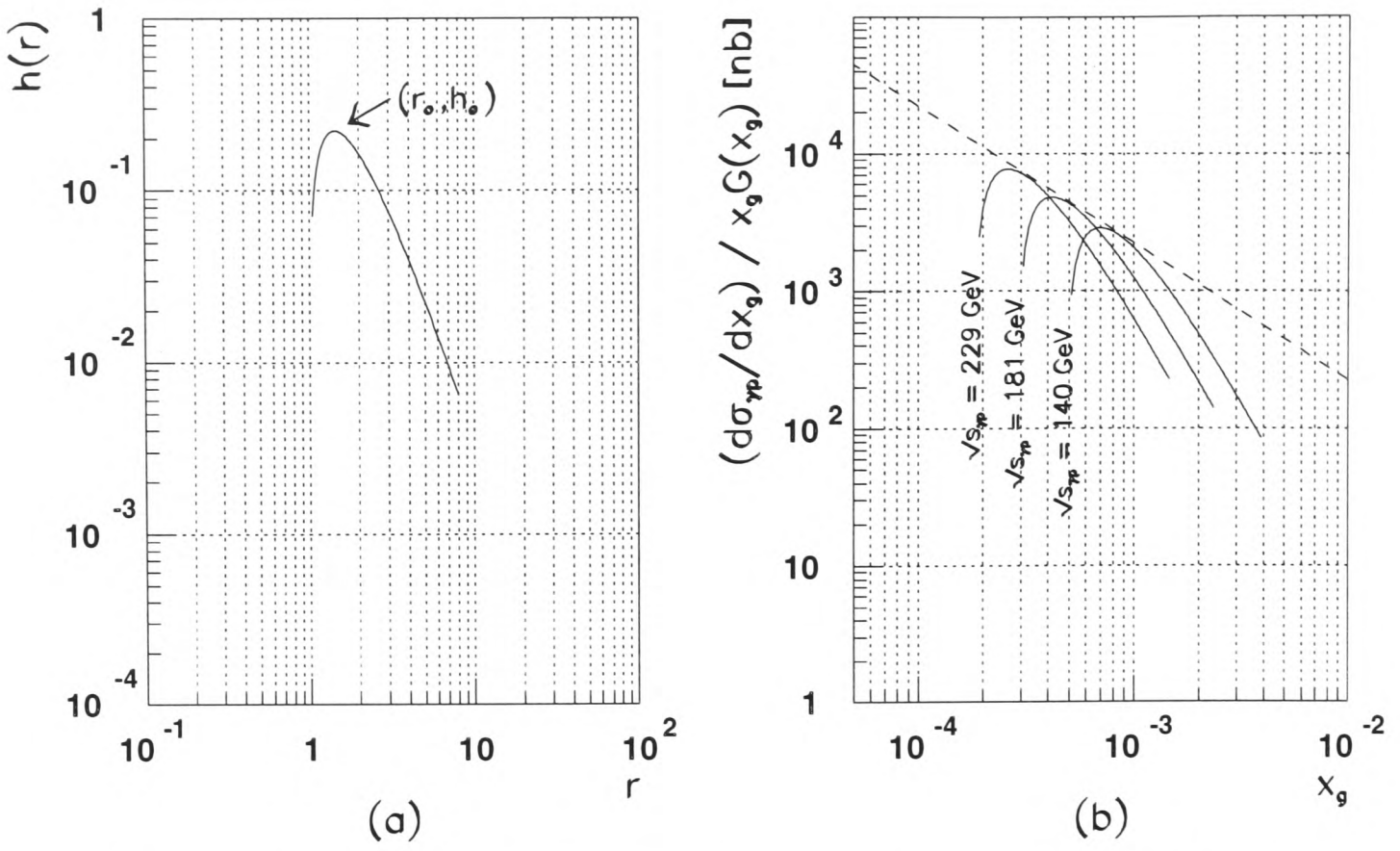

Figure C.1: (a) Plot showing the function $h(r)$ against r and (b) $\frac{d\sigma_{\gamma p}}{dx_g} \Big/ x_g G(x_g) = \frac{B\, s_{\gamma p}}{M^4_{J/\psi}}\, h(r)$ is plotted against x_g for three different values of $s_{\gamma p}$ attainable at HERA. The peaks of the curves lie on a line of gradient -1. The strong coupling constant is assumed to take the value $\alpha_s = 0.3$ in the calculation of B.

and they lie on a straight line of gradient -1 on the logarithmic scales of figure C.1b as $s_{\gamma p}$ is varied. Also, the increase in height of the peaks with $s_{\gamma p}$ is exactly compensated by the decrease in their width.

Due to the peaking in $h(r)$, the observed differential cross–section for inelastic J/ψ photoproduction directly reflects the gluon density, $x_g G(x_g)$, in the region $x_{peak} = r_o M^2_{J/\psi}/s_{\gamma p}$. The total $\gamma p \to J/\psi\, X$ cross–section is obtained by integrating equation C.11 over x_g, to give:

$$\begin{aligned} \sigma_{\gamma p} &= \int \frac{B\, s_{\gamma p}}{M^4_{J/\psi}}\, x_g G(x_g)\, h(r)\, dx_g \\ &\approx \frac{B}{M^2_{J/\psi}}\, \bar{x} G(\bar{x}) \int h(r)\, dr \end{aligned} \qquad \text{(C.14)}$$

where $s_{\gamma p} dx_g = M^2_{J/\psi} dr$ has been used. The nature of the function $h(r)$ means that the

gluon density is probed at $\bar{x} = \mathcal{O}(x_{peak})$. The definite integral in equation C.14 can be replaced by the constant $H = \int h(r)\, dr$ leaving:

$$\sigma_{\gamma p} \approx \frac{BH}{M^2_{J/\psi}}\, \bar{x}G(\bar{x}) \tag{C.15}$$

and we have the important result that the γp cross–section is directly proportional to the gluon density $\bar{x}G(\bar{x})$ in the proton. It is found in [52] that $\bar{x} \simeq 1.5\, x_{peak} \simeq 3.4\, M^2_{J/\psi}/s_{\gamma p}$. Thus by varying the centre–of–mass energy, $s_{\gamma p}$, in photoproduction experiments, the gluon density inside the proton can be directly probed.

Bibliography

[1] The ZEUS detector,
Status Report 1993,
DESY 1993.

[2] B. Foster et al.,
The design and construction of the ZEUS central tracking detector,
Nuclear Instruments & Methods A338:254 (1994).

[3] C. Alvisi et al.,
The ZEUS vertex detector: design and prototype,
Nuclear Instruments & Methods A305:30 (1991).

[4] V.N. Gribov and L.N. Lipatov,
Deep Inelastic Scattering in Perturbation Theory,
Sov. J. Nucl. Phys. 15:78 (1972).

[5] G. Altarelli and G. Parisi,
Asymptotic Freedom in Parton Language,
Nucl. Phys. B216:298 (1977)

[6] ZEUS Collaboration, M. Derrick et al.,
Extraction of the gluon density of the proton at x,
Physics Letters B345:576 (1995).

[7] H1 Collaboration, T. Ahmed et al.,
Hard scattering in γp interactions,
Physics Letters B297:205 (1992).

[8] ZEUS Collaboration, M. Derrick et al.,
Observation of hard scattering in photoproduction at HERA,
Physics Letters B297:404 (1992).

[9] ZEUS Collaboration, M. Derrick et al.,
Dijet cross sections in photoproduction at HERA,
Physics Letters B348:665 (1995).

[10] J.R. Forshaw and R.G. Roberts,
Determining the gluon distributions in the proton and photon from two–jet production at HERA,
Physics Letters B319:539 (1993).

[11] M.G. Ryskin,
Diffractive J/ψ electroproduction in LLA QCD,
Zeitschrift für Physik C57:89 (1993).

[12] S.J. Brodsky, L. Frankfurt, J.F. Gunion, A.H. Mueller, M. Stikman,
Diffractive leptoproduction of vector mesons in QCD,
Physical Review D50:3134 (1994).

[13] B.Z. Kopeliovich, J. Nemchick, N.N. Nikolaev, B.G. Zakharov,
Decisive test of colour transparency in exclusive virtual photoproduction of vector mesons,
Physics Letters B324:469 (1994).

[14] L. Ianotti,
The Gluon Distribution in the Proton from the 1993 J/ψ Elastic Photoproduction Data,
ZEUS–Note 95–048 (May 1995).

[15] M. Aguilar–Benitez et al.,
Review of Particle Properties,
Physical Review D50:1173 (1994).

[16] FTPS collaboration, B.H. Denby et al.,
Inelastic and Elastic Photoproduction of $J/\psi(3097)$,
Physical Review Letters 52:795 (1987).

[17] R. Barate et al., NA–14 Collaboration,
Measurement of J/ψ and ψ' Real Photoproduction of Lithium–6 at a Mean Energy of 90 GeV,
Zeitschrift für Physik C33:505 (1987).

[18] EMC Collaboration, J.J. Aubert et al.,
Production of charmonium in 250 GeV μ^+–iron interactions,
Nuclear Physics B213:1 (1983).

[19] R. Baier, R. Rückl,
Muoproduction of J/ψ and the photon–gluon scattering process: $\gamma_v\, g \to J/\psi\, g$,
Nuclear Physics B218:289 (1983).

[20] M. de Jong, NMC Collaboration,
Ph.D. Thesis,
Utrecht (1991).

[21] D. Allasia et al., NMC Collaboration,
Inelastic J/ψ production in deep inelastic scattering from hydrogen and deuterium and the gluon distributions of free nucleons,
Physics Letters B258:493 (1991).

[22] D. Bandyopadhyay et al.,
VCTRAK Offline Output Information,
ZEUS–Note 93–122 (Nov. 1993).

[23] B. Rossi,
High Energy Particles,
Prentice–Hall Inc., p17 (1961).

[24] J.D. Jackson,
Classical Electrodynamics,
New York: Wiley (1962).

[25] S. Ahlen,
Theoretical and experimental aspects of the energy loss of relativistic heavily ionizing particles,
Reviews of Modern Physics 52:121 (1980).

[26] R.M. Sternheimer,
The density effect for the ionization loss in various materials,
Physical Review 88:851 (1952).

[27] R.M. Sternheimer, S.M. Seltzer and M.J. Berger,
Density effect for the ionization loss in various substances,
Physical Review B26:6067 (1982); erratum B27:6971 (1983).

[28] R.M. Sternheimer, M.J. Berger and S.M. Seltzer,
Density effect for the ionization loss in various substances,
Atomic Data and Nuclear Data Tables 30:261 (1984).

[29] A. Walenta, J. Fischer, H. Okuno and C. Wang,
Measurement of ionisation loss in the region of relativistic rise for noble and molecular gases,
Nuclear Instruments & Methods 161:5 (1979).

[30] J. Burq, M. Chemarin, M. Chevallier et al.,
Observation of the ionisation energy loss of high energy protons and pions in hydrogen gas,
Nuclear Instruments & Methods 187:407 (1981).

[31] H. Bethe and J. Ashkin,
Passage of radiation through matter,
Experimental Nuclear Physics, Volume 1, Part 2, New York: Wiley (1959).

[32] L. Koepke, R. Van Woudenberg,
Photon Conversions in the ZEUS Detector,
ZEUS–Note 94–16 (Feb. 1994).

[33] G. Marchesini, B.R. Webber, et al.,
HERWIG - A Monte Carlo Event Generator for simulating Hadron Emissions Reactions With Interfering Gluons,
DESY 91–048 (1991).

[34] H. Jung,
EPJPSI 2.0: Monte Carlo generator for J/ψ mesons in high energy electron–proton collisions,
in proceedings of the workshop on physics at HERA,
vol. 3:1488, DESY 1991, Eds. W. Buchmuller and G. Ingleman.

[35] A.D. Martin, W.J. Stirling and R.G. Roberts,
New Information of Parton Distributions,
Physical Review D47:867 (1993).

[36] A.D. Martin, W.J. Stirling and R.G. Roberts,
Parton Distributions Updated,
Physics Letters B306:145 (1993).

[37] M.W. van der Heijden, NMC Collaboration,
Thesis, University of Amsterdam (1991).

[38] CCFR Collaboration, S.R. Mishra,
in proceedings of the Joint International Lepton–Photon Symposium and Europhysics Conference on High Energy Physics,
Eds. S. Hegarty, K. Potter and E. Quercigh,
Geneva, Switzerland 135 (1991).

[39] CDHSW Collaboration, J.P. Berge et al.
Zeitschrift für Physik C49:187 (1990).

[40] A. Donnachie and P.V. Landshoff,
Proton structure functions at small Q^2
Zeitschrift für Physik C61:139 (1994).

[41] Y. Balitzki, L.N. Lipatov,
Soviet Journal of Nuclear Physics 28:822 (1978).

[42] E.A. Kuraev, L.N. Lipatov,
Soviet Physics JETP44:443 (1976),
Soviet Physics JETP45:199 (1977).

[43] R. Sinkus, H. Abramowicz,
Electron Identification with Neural Networks at ZEUS,
ZEUS–Note 93–117 (Nov. 1993).

[44] C. Li et al.,
Observation of elastic $J/\psi(\rightarrow e^+e^-)$,
ZEUS–Note 94–54 (April 1994).

[45] F. Wilson, B.H.Y. Hung and K. Long,
Observation of Elastic J/ψ *Production Using the ZEUS Detector at HERA*,
ZEUS–Note 94–70 (July 1994).

[46] W.–K. Keung and I.J. Muzinich,
Beyond the static limit for quarkonium decays,
Physical Review D27:1518 (1983).

[47] V.A. Novikov, L.B. Okun, M.A. Shifman, A.I. Vainshtein, M.B. Voloshin and V.I. Zakharov,
Charmonium and Gluons,
Physics Reports 41C:2 (1978).

[48] Halzen & Martin,
Quarks and Leptons: An Introductory Course in Modern Particle Physics,
John Wiley & Sons, Inc. (1984).

[49] H. Jung, G.A. Schuler, J. Terron,
J/ψ production mechanisms and determination of the gluon density at HERA,
in proceedings of the workshop on physics at HERA,
vol. 2:712, DESY 1991, Eds. W. Buchmuller and G. Ingleman.

[50] V.M. Budnev, I.F. Ginzburg, G.V. Meledin and V.G. Serbo,
The two-photon particle production mechanism. Physical problems. Applications. Equivalent photon approximation,
Physics Reports 15C:181 (1975).

[51] E.L. Berger and D. Jones,
Inelastic photoproduction of J/ψ and Υ by gluons,
Physical Review D23:1521 (1981).

[52] A.D. Martin, C.–K. Ng and W.J. Stirling,
Inelastic leptoproduction of J/ψ as a probe of the small–x behaviour of the gluon structure function,
Physics Letters B191:200 (June 1987).